Charles University in Prague
Faculty of Mathematics and Physics

MASTER THESIS

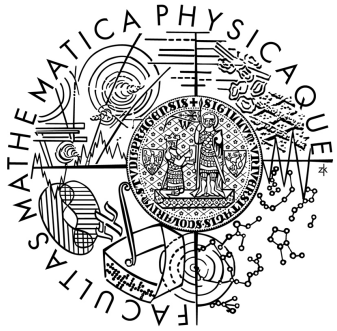

Libor Šachl

Ray-based Born approximation

Department of Geophysics

Supervisor: RNDr. Luděk Klimeš, DrSc.
Study program: Physics

2011

Here at this place I would like to thank all people, who helped with this thesis. In the first place, I would like to thank my supervisor, RNDr. Luděk Klimeš, DrSc., who never refused to consult my recent results and was always willing to answer my questions, no matter how many questions I had. I would also like to thank RNDr. Václav Bucha, CSc. and Mgr. Petr Bulant, Ph.D., who helped me with the software troubles. I would also like to thank doc. RNDr. Ctirad Matyska, DrSc., with whom I discussed the theory of the Born approximation. I should not forget all other people from the Department of Geophysics, the lecturers as well as students. I really appreciate the great atmosphere they created. And of course, I have to thank my family because without them I would probably neither write this thesis nor study the Charles University.

Prohlašuji, že jsem svou diplomovou práci napsal samostatně a výhradně s použitím citovaných pramenů. Souhlasím se zapůjčováním práce.

V Praze dne Libor Šachl

Contents

Název práce: Bornova aproximace založená na paprskové metodě
Autor: Libor Šachl
Katedra: Katedra geofyziky
Vedoucí diplomové práce: RNDr. Luděk Klimeš, DrSc.
e-mail vedoucího: klimes@seis.karlov.mff.cuni.cz

Abstrakt:
Jedním z cílů této diplomové práce bylo vytvoření programu *grdborn.for* pro výpočet 2D a 3D Bornovy aproximace prvního řádu v nehomogenním isotropním prostředí bez útlumu. Výpočet 3D amplitud s pomocí 2D Bornovy aproximace využívá korekční člen, který je odvozen. Program je dále použit při výpočtu Bornovy aproximace v různých modelech. Program testujeme ve třech jednoduchých modelech. Studujeme efekt diskretizace, efekt vzniku falešných vln způsobených konečností výpočetní mřížky atd. V dalším kroku se soustředíme na komplikovanější modely. S pomocí Bornovy aproximace počítáme seismogramy ve 2D heterogeních modelech. Věnujeme se difragovaným vlnám, efektu kaustik atd.
Klíčová slova: Bornova aproximace, paprsková teorie, rychlostní model, perturbace

Title: Ray-based Born approximation
Author: Libor Šachl
Department: Department of Geophysics
Supervisor: RNDr. Luděk Klimeš, DrSc.
Supervisor's e-mail address: klimes@seis.karlov.mff.cuni.cz

Abstract:
One of the aims of this thesis was coding of program *grdborn.for* for computing the 2D and 3D ray-based Born approximation of the first order in an inhomogenous isotropic medium without attenuation. The computation of 3D amplitudes using the 2D Born approximation is based on the correction term, which is derived. The program is further used in computing the Born approximation in various models. We test its performance in three simple models. We study the effect of the discretization, the spurious waves introduced by the finite size of the grid etc. In the next step, we focus on the computations in more complicated models. We compute the Born seismograms in 2D heterogenous models. We study the diffracted waves, the effects of caustics etc.
Keywords: Born approximation, ray theory, velocity model, perturbation

Preface

This master thesis is based on the articles named "3D and 2D computations of 3D synthetic seismograms using the ray-based Born approximation in simple models", "2D computations of 3D synthetic seismograms using the ray-based Born approximation in heterogenous model P1", "Effect of caustics to the ray-based Born approximation" and "Born and ray theory seismograms in 2D heterogenous isotropic models". The first and second article were published in report 21 of consortium SW3D (Seismic waves in complex 3-D structures). These articles were slightly revised for this master thesis. The poster based on the first paper was presented in the 73rd EAGE Conference & Exhibition incorporating SPE EUROPEC 2011 in Vienna in the student section.

The first chapter explains the theory of the Born approximation, provides a short introduction to the ray theory and explains the concepts used in the seismic wave modelling, which are mentioned in the thesis. These information are probably familiar for people working in the seismic wave modelling, but we think that it might be useful to brush them up for somebody working in a slightly different field.

The second, third, fourth and fifth chapter contain the four mentioned articles. The articles focus mainly on the numerical tests of the Born approximation. The important difference between the articles is the use of a homogenous background model in the first article and the use of a heterogenous background model in the remaining articles.

There are several appendices. Appendix A is devoted to the software used during the computations. The programs from SW3D packages which have been already coded are just listed, the programs newly programmed are shortly described.

Appendix B is about program *grdborn.for*. For the direct use of the program, the commentaries at the beginning of the program code should be sufficient. The text in this appendix tries to explain more deeply how the program works, it is not a manual.

Appendix C describes the one of two prepared sample computations. Part C.1. introduces the sample computation and describes its structure. This text together with the commentaries in the data files, history files and program codes could be sufficient to show how to use program *grdborn.for* in cooperation with the certain SW3D programs. Of course, there are many input files and parameters and their settings could be slightly different for a different model. For this reason, part C.2. explains the functionality of the input files and parameters in the computation.

The newly coded programs described in appendix A and appendix B as well as the sample computations from appendix C are available on the attached CD.

Chapter 1

Theory

1.1 Elastodynamic equation

We shall use the Lagrangian description of motion in an elastic continuum. In the Lagrangian description, we study the motion of a particle specified by its original position at some reference time. Assume that the particle is located at the position described by Cartesian coordinates x_i at the reference time. The vector distance of a particle at time t from position $\vec{x}$ at the reference time is called the displacement vector and is denoted by $\vec{u}$. Obviously, $\vec{u} = \vec{u}(\vec{x}, t)$.

In a linear, anisotropic, perfectly elastic solid, the elastodynamic equation has the form

$$(c_{ijkl}u_{k,l})_{,j} + f_i = \rho\ddot{u}_i, \qquad i = 1, 2, 3 \tag{1.1}$$

Here f_i denote the Cartesian components of body forces (force per volume), and ρ is the density. The term with f_i in elastodynamic equation (1.1) will also be referred to as the source term. Quantities $\ddot{u}_i = \partial^2 u_i/\partial t^2, i = 1, 2, 3$, represents the second partial derivatives of u_i with respect to time (that is, the Cartesian components of particle acceleration $\ddot{\vec{u}}$) and c_{ijkl} are components of the elastic tensor. The elastic tensor has, in general, $3 \times 3 \times 3 \times 3 = 81$ components. These components, however, satisfy the following symmetry relations:

$$c_{ijkl} = c_{jikl} = c_{ijlk} = c_{klij},$$

which reduce the number of independent components of the elastic tensor from 81 to 21.

The components c_{ijkl} of the elastic tensor are also often called elastic constants, elastic moduli, elastic parameters or stiffnesses.

In the isotropic solid, the components of elastic tensor c_{ijkl} can be expressed in terms of two independent elastic moduli λ and μ as follows:

$$c_{ijkl} = \lambda\delta_{ij}\delta_{kl} + \mu(\delta_{ik}\delta_{jl} + \delta_{il}\delta_{jk}) \tag{1.2}$$

see (Jeffreys, 1956) and (Aki,2002). Here δ_{ij} is the Kronecker symbol,

$$\delta_{ij} = 1 \text{ for } i = j, \qquad \delta_{ij} = 0 \text{ for } i \neq j$$

Elastic moduli λ, μ are also known as Lamé's elastic moduli; μ is called the rigidity (or shear modulus).

Elastodynamic equation (1.1) is written in the time domain. It can be written in the frequency domain as well. It reads

$$(c_{ijkl}u_{k,l})_{,j} + \rho\omega^2 u_i = -f_i, \qquad i = 1, 2, 3. \tag{1.3}$$

Here $\omega = 2\pi f$ is the circular frequency, where f is frequency. Remark that despite the fact that we use in both forms of elastodynamic equation u_i and f_i, it has different meaning. It means $u_i(\mathbf{x}, t)$ and $f_i(\mathbf{x}, t)$ in the time domain and $u_i(\mathbf{x}, \omega)$ and $f_i(\mathbf{x}, \omega)$ in the frequency domain (Červený, 2001).

1.2 Green function

In order to avoid coefficient $(2\pi)^{-\frac{1}{2}}$ at the force density in the definition of the frequency–domain Green function, we consider here Fourier transform

$$u(\omega) = \int_{-\infty}^{+\infty} \mathrm{d}t\; u(t)\; \exp(\mathrm{i}\omega t),$$

see (Červený, 2001) eq. A.1.2, without coefficient $(2\pi)^{-\frac{1}{2}}$. Then the frequency–domain elastodynamic Green function is the solution of equation

$$\big[c_{ijkl}(\mathbf{x})\, G_{km,l}(\mathbf{x}, \mathbf{x}', \omega)\big]_{,j} + \omega^2 \varrho(\mathbf{x})\, G_{im}(\mathbf{x}, \mathbf{x}', \omega) + \delta_{im}\, \delta(\mathbf{x}-\mathbf{x}') = 0 \tag{1.4}$$

The frequency–domain Green function obeys reciprocity relation

$$G_{im}(\mathbf{x}, \mathbf{x}', \omega) = G_{mi}(\mathbf{x}', \mathbf{x}, \omega) \tag{1.5}$$

Taking scalar product of equation (1.4) with $f_m(\mathbf{x}', \omega)$ and integrating at least over the support V of $f_m(\mathbf{x}', \omega)$, we see that

$$u_i(\mathbf{x}, \omega) = \int_V \mathrm{d}^3\mathbf{x}' \, G_{im}(\mathbf{x}, \mathbf{x}', \omega) \, f_m(\mathbf{x}', \omega)$$

is the solution of the frequency–domain elastodynamic equation (Klimeš, 2009).

It is possible to find the expressions for the elastodynamic Green function for isotropic homogenous media (Červený, 2001, eq. 2.5.54), elastodynamic Green function for anisotropic homogenous media (Červený, 2001, eq. 2.5.73) and the ray-theory Green function for anisotropic heterogenous media, see Klimeš (2011).

1.3 Born approximation

1.3.1 Perturbations

The Born approximation is one of the so called perturbation methods. Perturbation methods play an important role in ray methods. They can be used for fast but approximate solution of forward problems in complicated models. Perturbation methods play an equal or even more important role in inverse problems (Červený et al., 2007).

We introduce perturbation parameters f^α. For $c_{ijkl} = c_{ijkl}(\mathbf{x}, f^\alpha)$, $\varrho = \varrho(\mathbf{x}, f^\alpha)$ and $f_i = f_i(\mathbf{x}, \omega, f^\alpha)$, we obtain wavefield $u_i = u_i(\mathbf{x}, \omega, f^\alpha)$ dependent on perturbation parameters f^α. The background model is given by $f^\alpha = f_0^\alpha$, the perturbed model is given by $f^\alpha = f_1^\alpha$

The wavefield in the perturbed model can be related to the wavefield in the background model using Taylor (perturbation) expansion

$$u_i(\mathbf{x}, \omega, f_1^\alpha) = u_i(\mathbf{x}, \omega, f_0^\alpha) + u_{i,\alpha}(\mathbf{x}, \omega)(f_1^\alpha - f_0^\alpha) + \ldots,$$

where $u_{i,\alpha}$ means derivative of the wavefield with respect to the perturbation parameters f^α computed in the background model (Klimeš, 2009).

1.3.2 General form

We differentiate the frequency–domain elastodynamic equation (1.3) with respect to f^α, and obtain elastodynamic equation for first–order perturbation derivatives $u_{i,\alpha}$:

$$(c_{ijkl} \, u_{k,\alpha l})_{,j} + \omega^2 \varrho \, u_{i,\alpha} + F_{i\alpha} = 0 \tag{1.6}$$

where

$$F_{i\alpha} = (c_{ijkl,\alpha}\, u_{k,l})_{,j} + \omega^2 \varrho_{,\alpha}\, u_i + f_{i,\alpha}$$

For exact background wavefield $u_i(\mathbf{x}, \omega, f_0^\alpha)$, perturbation derivatives $f_{i,\alpha}$ probably vanish.

We may express the solution of this equation in the form of integrals over volume Ω which covers the supports of the perturbation derivatives of c_{ijkl}, ϱ and f_i:

$$u_{i,\alpha}(\mathbf{x}, \omega) = \int\limits_\Omega \mathrm{d}^3\mathbf{x}'\, G_{im}(\mathbf{x}, \mathbf{x}', \omega)\, F_{m\alpha}(\mathbf{x}', \omega)$$

In order to avoid the spatial derivatives of perturbation derivatives of elastic moduli in the integral, we may express

$$\begin{aligned}
&\int\limits_\Omega \mathrm{d}^3\mathbf{x}'\, G_{im}\, (c_{mjkl,\alpha}\, u_{k,l})_{,j} \\
&= \int\limits_\Omega \mathrm{d}^3\mathbf{x}'\, (G_{im}\, c_{mjkl,\alpha}\, u_{k,l})_{,j} - \int\limits_\Omega \mathrm{d}^3\mathbf{x}'\, G_{im,j}\, c_{mjkl,\alpha}\, u_{k,l} \\
&= \int\limits_{\partial\Omega} \mathrm{d}^2\mathbf{x}'\, G_{im}\, c_{mjkl,\alpha}\, u_{k,l} n_j - \int\limits_\Omega \mathrm{d}^3\mathbf{x}'\, G_{im,j}\, c_{mjkl,\alpha}\, u_{k,l} \\
&\approx - \int\limits_\Omega \mathrm{d}^3\mathbf{x}'\, G_{im,j}\, c_{mjkl,\alpha}\, u_{k,l},
\end{aligned}$$

where we used the Green theorem and neglected the surface integral, because we can choose Ω so big that the integrand is sufficiently small.

The first–order perturbation derivatives $u_{i,\alpha}$ then read

$$u_{i,\alpha}(\mathbf{x}, \omega) = \int\limits_\Omega \mathrm{d}^3\mathbf{x}'\, \left[G_{im}(\mathbf{x}, \mathbf{x}', \omega)\, K_{m\alpha}(\mathbf{x}', \omega) - G_{im,j}(\mathbf{x}, \mathbf{x}', \omega)\, L_{mj\alpha}(\mathbf{x}', \omega)\right] \tag{1.7}$$

where

$$K_{i\alpha} = \omega^2 \varrho_{,\alpha}\, u_i + f_{i,\alpha}$$

and

$$L_{ij\alpha} = c_{ijkl,\alpha}\, u_{k,l}.$$

The higher order perturbation derivatives can be obtained similarly (Klimeš, 2009).

Note, that if we have only one perturbation parameter α and if we suppose linear dependence of $c_{ijkl}(\mathbf{x},\alpha)$, $\varrho(\mathbf{x},\alpha)$ on α and put $\alpha = 0$ for the background model and $\alpha = 1$ for the perturbed model, we get eq. (2.6.18) from Červený (2001).

1.3.3 Another view

Matyska (2011) noted that there is another view on this problem. We perform the dot product between vector elastodynamic equation in the time domain (1.1) without body force f_i and time independent vector test function $\mathbf{\Psi}(\mathbf{x})$ and integrate the result over bounded domain Ω with Lipschitz boundary.

$$\int_\Omega (c_{ijkl}u_{k,l})_{,j}\Psi_i \,\mathrm{d}^3\mathbf{x} = \int_\Omega \rho\frac{\partial^2 u_i}{\partial t^2}\Psi_i \,\mathrm{d}^3\mathbf{x}. \tag{1.8}$$

In the case of the perturbed medium we have

$$\int_\Omega \left[(c_{ijkl}+\Delta c_{ijkl})(u_k+\Delta u_k)_{,l}\right]_{,j}\Psi_i \,\mathrm{d}^3\mathbf{x} = \int_\Omega (\rho+\Delta\rho)\frac{\partial^2(u_i+\Delta u_i)}{\partial t^2}\Psi_i \,\mathrm{d}^3\mathbf{x}, \tag{1.9}$$

where the quantities with Δ are the perturbations. Equation (1.9) minus equation (1.8) reads

$$\int_\Omega \left(c_{ijkl}\Delta u_{k,l}\right)_{,j}\Psi_i \,\mathrm{d}^3\mathbf{x} = \int_\Omega \rho\frac{\partial^2\Delta u_i}{\partial t^2}\Psi_i \,\mathrm{d}^3\mathbf{x} + \int_\Omega \left(\Delta\rho\frac{\partial^2 u_i}{\partial t^2} - \left(\Delta c_{ijkl}u_{k,l}\right)_{,j}\right)\Psi_i \,\mathrm{d}^3\mathbf{x}, \tag{1.10}$$

where we neglected terms

$$\int_\Omega \left(\Delta c_{ijkl}\Delta u_{k,l}\right)_{,j}\Psi_i \,\mathrm{d}^3\mathbf{x} \qquad , \qquad \int_\Omega \Delta\rho\frac{\partial^2\Delta u_i}{\partial t^2}\Psi_i \,\mathrm{d}^3\mathbf{x}, \tag{1.11}$$

because each of them contains two "small" quantities. We apply the Green theorem at the most left term in equation (1.10),

$$\int_\Omega c_{ijkl}\Delta u_{k,l}\Psi_{i,j} \,\mathrm{d}^3\mathbf{x} = -\int_\Omega \rho\frac{\partial^2\Delta u_i}{\partial t^2}\Psi_i \,\mathrm{d}^3\mathbf{x} + \int_\Omega \left(-\Delta\rho\frac{\partial^2 u_i}{\partial t^2} + \left(\Delta c_{ijkl}u_{k,l}\right)_{,j}\right)\Psi_i \,\mathrm{d}^3\mathbf{x}, \tag{1.12}$$

where we omitted the surface integral, because it is equal to zero due to the Dirichlet boundary conditions and test functions $\mathbf{\Psi}$ which are zero at the boundary in the sense of trace. Term

$$F_i = -\Delta\rho\frac{\partial^2 u_i}{\partial t^2} + (\Delta c_{ijkl}u_{k,l})_{,j}, \tag{1.13}$$

can be interpreted as the body force. Notice, that if $\Delta c_{ijkl}u_{k,l}$ is not continuous, for example due to the jump in the elastic parameters c_{ijkl} at the interface between two different materials (which happens in the models used in the first paper), $(\Delta c_{ijkl}u_{k,l})_{,j}$ represents the surface force. Then it is necessary to rewrite (1.12) using the Green theorem to obtain (the surface integral is equal to zero again)

$$\int_\Omega c_{ijkl}\Delta u_{k,l}\Psi_{i,j}\ \mathrm{d}^3\mathbf{x} = -\int_\Omega \rho\frac{\partial^2\Delta u_i}{\partial t^2}\Psi_i\ \mathrm{d}^3\mathbf{x} + \int_\Omega \left(-\Delta\rho\frac{\partial^2 u_i}{\partial t^2}\Psi_i - \Delta c_{ijkl}u_{k,l}\Psi_{i,j}\right)\ \mathrm{d}^3\mathbf{x},$$

which is already correct, because $c_{ijkl} \in L^\infty(\Omega)$ and we suppose that u_k is smooth enough, for example $u_k \in C^\infty(\Omega)$ or it is at least a function from Sobolev space $W^{1,2}(\Omega)$, because it is the ray-theory solution. Alternatively, using $c_{ijkl} = c_{klij}$, we may rewrite (1.12)

$$((\mathbf{\Delta u}, \mathbf{\Psi})) = -\left(\rho\frac{\partial^2\mathbf{\Delta u}}{\partial t^2}, \mathbf{\Psi}\right) + (\mathbf{F}, \mathbf{\Psi}), \tag{1.14}$$

where

$$((\mathbf{a}, \mathbf{b})) = \int_\Omega c_{ijkl}\frac{\partial a_i}{\partial x_j}\frac{\partial b_k}{\partial x_l}\ \mathrm{d}^3\mathbf{x},$$

is an elliptical bilinear form due to the fact that $c_{ijkl} \geq 0$ for each combination of i,j,k,$l \in \{1, 2, 3\}$ and

$$(\mathbf{a}, \mathbf{b}) = \int_\Omega a_i b_i\ \mathrm{d}^3\mathbf{x},$$

is a scalar product.

We add that equation (1.14) in the frequency domain has the form

$$((\mathbf{\Delta u}, \mathbf{\Psi})) - \omega^2\rho\,(\mathbf{\Delta u}, \mathbf{\Psi}) = (\mathbf{F}, \mathbf{\Psi}). \tag{1.15}$$

Equations (1.14), (1.15) are suitable for the weak formulation of the problem. They are both hyperbolic. For the properties of the hyperbolic systems like

the existence of the solution or its uniqueness we refer to Rektorys (1982) or Evans (1998).

Note that in Červený (2001) the derivation of the first-order Born approximation starts with subtracting the wave equation in the perturbed medium and in the background medium, i.e. similarly to the derivation of (1.10), but without the multiplication by the vector test function and integration. The author then neglects terms (1.11) (again no multiplication by the vector test function and integration) and obtains equation (1.6), where Δu_i, F_i (see (1.13)) stand instead of $u_{i,\alpha}$, $F_{i\alpha}$. It would be possible to construct the following iteration process: In the first step, we compute the wavefield perturbations in the specified receiver and in our computational grid. In the next step we use them to compute the neglected terms and add them to force F_i. We again compute the wavefield perturbations using the corrected F_i and so on. Unfortunately this algorithm is too time demanding, because it requests the computation of the wavefield perturbations using the Born approximation at each gridpoint.

1.4 Ray theory, a short introduction

We compute the quantities in the background model using the ray theory. This section presents the key ideas of the ray theory. We use Einstein summation convention.

Ray theory ansatz

For each elementary wave, we express the displacement in terms of vectorial amplitude a_i and travel time τ,

$$u_i(x^m, \omega) = a_i(x^m)\, \exp\big[\mathrm{i}\omega\tau(x^m)\big].$$

We insert this ansatz into anisotropic elastodynamic equation (1.3) with $f_i = 0$:

$$(\mathrm{i}\omega)^2\, N_i(a_k, \tau_{,l}) + \mathrm{i}\omega\, M_i(a_k, \tau_{,l}) + L_i(a_k) = 0. \tag{1.16}$$

Terms N_i, M_i, L_i are expressed in Červený (2001, eq. 2.4.41).

Christoffel equation

We wish equation (1.16) to be satisfied for arbitrary frequency ω. Therefore, the coefficients N_i, M_i, L_i should be zero. Three highest–order equations with

respect to ω,

$$N_i(a_k, \tau_{,l}) = 0,$$

constitute the matrix Christoffel equation

$$\Gamma_{ik}\, a_k - a_i = 0$$

(Červený, 2001, eq. 2.4.42). Here

$$\Gamma_{ik} = \frac{c_{ijkl}}{\varrho}\, \tau_{,j} \tau_{,l}$$

(Červený, 2001, eq. 2.4.43) is the Christoffel matrix.

We see that a_i must be a multiple of unit eigenvector g_i of Γ_{ik},

$$a_i = A\, g_i.$$

Vector g_i is called the polarization vector.

Eikonal equation

We select unit eigenvector g_i and the corresponding eigenvalue G of Γ_{ik}. Travel time τ is the solution of eikonal equation

$$G\big(x^m, \tau_{,n}(x^r)\big) = 1$$

(Červený, 2001, eq. 2.4.44), where $G(x^m, \tau_{,n})$ is the eigenvalue of $\Gamma_{ik}(x^m, \tau_{,n})$ corresponding to eigenvector $g_i(x^m, \tau_{,n})$.

This eikonal equation is a special case of the Hamilton–Jacobi equation.

Transport equation

If the eigenspace corresponding to eigenvalue $G(x^m, \tau_{,n})$ is one–dimensional, only one of equations of order ω in (1.16) can be satisfied:

$$a_i\, M_i(a_k, \tau_{,l}) = 0.$$

This transport equation for amplitude A reads

$$(\varrho\, a_{ijkl} g_i g_k \tau_{,l} A^2)_{,j} = 0.$$

Phase–space derivatives

We denote the partial derivatives with respect to spatial coordinates x^i by lower–case Roman subscripts following a comma, and the partial derivatives with respect to components $p_j = \tau_j$ of the slowness vector by lower–case Roman superscripts following a comma,

$$H_{,ij\ldots n}^{,ab\ldots f}(x^r, p_s) = \frac{\partial}{\partial x^i}\frac{\partial}{\partial x^j}\ldots\frac{\partial}{\partial x^n}\frac{\partial}{\partial p_a}\frac{\partial}{\partial p_b}\ldots\frac{\partial}{\partial p_f}H(x^r, p_s).$$

Hamilton–Jacobi equation

The eikonal equation for travel time is a special case of the Hamilton–Jacobi equation. The Hamilton–Jacobi equation is a general first–order partial differential equation

$$H\big(x^m, \tau_{,n}(x^r)\big) = C$$

for travel time $\tau = \tau(x^r)$, where C is a constant. Sufficiently smooth function $H = H(x^m, p_n)$ defined in the phase space is called the Hamiltonian function. The Hamilton–Jacobi equation may be replaced by Hamilton's equations (equations of geodesics, ray–tracing equations)

$$\frac{\mathrm{d}x^i}{\mathrm{d}\gamma} = H^{,i} \tag{1.17}$$

$$\frac{\mathrm{d}p_i}{\mathrm{d}\gamma} = -\,H_{,i}. \tag{1.18}$$

These Hamilton's equations may be used for calculation of the gradient of travel time τ along *rays* (*geodesics*).

Travel time τ is then given by equation

$$\frac{\mathrm{d}\tau}{\mathrm{d}\gamma} = \frac{\partial\tau}{\partial x^i}\frac{\mathrm{d}x^i}{\mathrm{d}\gamma} = p_i\, H^{,i}.$$

Meaning of independent parameter γ along rays depends on the form of the Hamiltonian function.

Ray coordinates

The system of rays corresponding to action $\tau = \tau(x^m)$ is referred to as the orthonomic system of rays. In D–dimensional manifold, the initial conditions

for Hamilton's equations corresponding to the orthonomic system of rays are parametrized by $D-1$ ray parameters

$$\gamma^1,\ \gamma^2,\ ...,\ \gamma^{D-1}.$$

The ray parameters together with independent parameter

$$\gamma^D = \gamma$$

along rays form ray coordinates.

Hamiltonian equations of geodesic deviation

We define matrices

$$Q^i{}_a = \frac{\partial x^i}{\partial \gamma^a}$$

and

$$P_{ia} = \frac{\partial p_i}{\partial \gamma^a}$$

representing the geodesic deviation (ray deviation) corresponding to ray coordinates γ^a. These matrices are often referred to as the paraxial matrices. Matrix $Q^i{}_a$ is called the matrix of geometrical spreading.

The equations for $Q^i{}_a$ and P_{ia} are linear Hamiltonian equations of geodesic deviation (paraxial ray equations, dynamic ray tracing equations) read (Červený, 1972)

$$\frac{\mathrm{d}}{\mathrm{d}\gamma} Q^i{}_a = \quad H^{,i}_{,j}\, Q^j{}_a + H^{,ij}\, P_{ja}$$

$$\frac{\mathrm{d}}{\mathrm{d}\gamma} P_{ia} = -H_{,ij}\, Q^j{}_a - H^{,j}_{,i}\, P_{ja}.$$

The solution of the transport equation can be expressed using the determinant of matrix $Q^i{}_a$:

$$A = A_0 \sqrt{\frac{\varrho_0}{\varrho}\, \frac{H^{,k} p_k}{(H^{,k} p_k)_0}\, \frac{\det \mathbf{Q}_0}{\det \mathbf{Q}}},$$

where quantities with subscript 0 are the initial values at the initial point of the ray.

The second order derivative of travel time can be calculated using

$$\tau_{,ij} = P_{ia} Q^{-1}_{aj},$$

where Q^{-1}_{aj} is the inverse matrix to $Q^j{}_a$.

The third–order and higher–order spatial derivatives of travel time can be calculated by quadratures along rays (Klimeš, 2002).

1.5 Concepts used in the seismic wave modelling

In applications, the whole system of rays is usually needed. The rays are parametrized by two **ray parameters** γ^1 and γ^2. For example, for an elementary wave generated by a point source, the two ray parameters may be chosen as the take–off angles of initial slowness vectors at the source.

The **velocity model** specifies the spatial distribution of the density–reduced elastic moduli in anisotropic media, or the spatial distribution of the P–wave or S–wave propagation velocities in isotropic media. The velocity model should also specify the spatial distribution of the density.

The velocity model specifies the spatial distribution of these medium properties inside the finite **model volume** and in its vicinity. The model volume is usually limited by coordinate surfaces,

$$x^i_{\min} \leq x^i \leq x^i_{\max} \quad ,$$

but may also be limited by other surfaces.

If the n–th derivatives of the travel time are to be continuous, the n–th derivatives of the density–normalized elastic moduli must be continuous. If the amplitudes are to be continuous, the second derivatives of the density–normalized elastic moduli must be continuous. The minimum requirement on a **smooth velocity model** for the zero–order ray theory are the continuous second derivatives of the density–normalized elastic moduli.

The density–normalized elastic moduli may be discontinuous only along interfaces. Interfaces thus divide the velocity model into blocks. The variation of the density–normalized elastic moduli within each block should be smooth in the same sense as in the smooth velocity model. A velocity model composed of these blocks, which are separated by interfaces, may be called the **block velocity model**.

The surfaces forming the interfaces may be defined implicitly, as the zero isosurfaces of given functions $f(x^i)$. Each surface divides the whole model volume into two parts, the positive part, in which $f(x^i) > 0$, and the negative part, in which $f(x^i) < 0$.

As in Červený et al. (1988), we construct the block velocity model from two types of blocks formed by smooth surfaces: simple blocks which are the "building bricks" of the velocity model and have no physical meaning, and complex blocks, which represent the physical units of the velocity model. A **simple block** is defined by two finite sets F^+ and F^- of surfaces $f(x^i) = 0$. A point x^i lies

within the simple block if and only if

$$f(x^i) > 0 \quad \text{for any} \quad f \in F^+ \quad , \qquad f(x^i) < 0 \quad \text{for any} \quad f \in F^- \quad .$$

The simple block is an intersection of the positive parts of the velocity model corresponding to the surfaces from F^+ and the negative parts of the model corresponding to F^-.

A **complex block** is formed as a union of several simple blocks (it may, of course, be also formed by one simple block). While the simple blocks need not form a disjunct system, the complex blocks must form it.

In velocity models with structural interfaces, the ray tracing must be supplemented by the prescription specifying which of the reflected or refracted waves should be considered after incidence at an interface. We refer to this prescription as the **code of the elementary wave**.

Rays of the same ray history pass through an equal sequence of blocks and interfaces. Each sequence of blocks and interfaces encountered during ray tracing thus defines the corresponding **ray history**.

Controlled initial–value ray tracing consists in dividing the ray–parameter domain into regions of the same value of the history function, and in sampling these regions. See e.g. Bulant (1996) and Bulant (1999).

The **two–point ray tracing** means finding all rays of a given elementary wave, which take off from the source and pass through the receiver. The **receiver** is a given point, situated at the **reference surface** (Klimeš, 2009).

3D and 2D computations of 3D synthetic seismograms using the ray-based Born approximation in simple models

Libor Šachl

Charles University, Faculty of Mathematics and Physics, Department of Geophysics,
E-mail: sachl@karel.troja.mff.cuni.cz

Summary

Program *grdborn.for* for computing the 2D and 3D ray-based Born approximation of the first order in an inhomogenous isotropic medium without attenuation has been coded. The program calculates the 3D amplitudes. The computation of 3D amplitudes using the 2D Born approximation is based on the correction term, which is derived in this paper. The 2D computation is, of course, due to the reduction of one dimension, much faster, but the results are very good. Three simple models are used to show the program performance. The P-waves are considered in all computations apart from one numerical example in which we show that the program can compute S-wave seismograms too. The effect of discretization is numerically shown in the 3D computations, and we have also attempted to explain this theoretically. We numerically touch upon the effect of increasing perturbations.

Key words: Born approximation, ray theory, velocity model, perturbation

1 Introduction

In computing seismograms in a complex structure, we can meet a situation for which the method we are using is not suitable, or to which it cannot be even applied. A good example is the ray theory, which has certain advantages when compared with other methods, but is not applicable if the medium is not "smooth enough". A possible solution is to use a model which is "close" to the original one and satisfies the theory requirements. Let us call this model background and the original one perturbed. We know approximately the wavefield in the background model and wish to estimate the wavefield in the perturbed model. The method how to modify the wavefield is using the first-order Born approximation, which requires the quantities computed in the background model and differences between the perturbed and background model called perturbations. The result is a correction of the wavefield.

Seismic Waves in Complex 3-D Structures, Report 21, Charles University, Faculty of Mathematics and Physics, Department of Geophysics, Praha 2011, pp. 69-98

2 The Born approximation in an isotropic medium, with point-source and high-frequency approximation

Consider an isotropic medium. We insert the expression

$$c_{ijkl} = \lambda\delta_{ij}\delta_{kl} + \mu(\delta_{ik}\delta_{jl} + \delta_{il}\delta_{jk})$$

for the components of the elastic tensor in the isotropic solid into the first-order Born approximation (Červený, 2001, eq. 2.6.18)

$$\Delta u_n(\mathbf{x},\omega) = \int\limits_{\Omega} \big[\omega^2 u_i(\mathbf{x}',\omega)\Delta\rho(\mathbf{x}')G_{ni}(\mathbf{x},\mathbf{x}',\omega) - u_{k,l}(\mathbf{x}',\omega)\Delta c_{ijkl}(\mathbf{x}')G_{ni,j}(\mathbf{x},\mathbf{x}',\omega)\big]d^3\mathbf{x}', \tag{1}$$

where ω is the circular frequency, $\Delta c_{ijkl}(\mathbf{x})$ and $\Delta\rho(\mathbf{x})$ are the perturbations of elastic moduli and density, Ω is a domain where these perturbations are non-zero, $u_i(\mathbf{x}',\omega)$ is the solution of the elastodynamic equation for the background medium, $G_{ij}(\mathbf{x},\mathbf{x}',\omega)$ is the Green function in the background medium and $G_{ij,k}(\mathbf{x},\mathbf{x}',\omega)$ is the spatial derivative of the Green function with respect to x'_k. In adition we use the reciprocity of the Green function $G_{ij}(\mathbf{x},\mathbf{x}',\omega) = G_{ji}(\mathbf{x}',\mathbf{x},\omega)$. We obtain

$$\Delta u_i(\mathbf{x},\omega) = \int\limits_{\Omega} \big[\omega^2\Delta\rho(\mathbf{x}')G_{mi}(\mathbf{x}',\mathbf{x},\omega)u_m(\mathbf{x}',\omega) + \Delta\lambda(\mathbf{x}')G_{ji,j}(\mathbf{x}',\mathbf{x},\omega)u_{k,k}(\mathbf{x}',\omega) + \Delta\mu(\mathbf{x}')G_{ki,j}(\mathbf{x}',\mathbf{x},\omega)(u_{k,j}(\mathbf{x}',\omega) + u_{j,k}(\mathbf{x}',\omega))\big]d^3\mathbf{x}', \tag{2}$$

where $G_{ij,k}(\mathbf{x}',\mathbf{x},\omega)$ is the spatial derivative of the Green function with respect to x'_k. Assume further that we have a point source located at point $\mathbf{x}^s$. Let us decompose the wavefield and the Green function into amplitudes a_i, A_{ij} and phase terms $\exp(i\omega\tau)$, $\exp(i\omega T)$. We arrive at

$$u_i(\mathbf{x}',\omega) = a_i(\mathbf{x}')\exp(i\omega\tau), \tag{3}$$

$$G_{ij}(\mathbf{x}',\mathbf{x},\omega) = A_{ij}(\mathbf{x}',\mathbf{x})\exp(i\omega T), \tag{4}$$

where τ is a travel time from $\mathbf{x}^s$ to $\mathbf{x}'$, i.e. from the point source to an integration point, and T is a travel time from $\mathbf{x}$ to $\mathbf{x}'$, i.e. from the receiver to an integration point.

Using the high-frequency approximation of the spatial derivatives,

$$u_{i,j}(\mathbf{x}',\omega) \approx i\omega a_i(\mathbf{x}')p_j\exp(i\omega\tau), \tag{5}$$

$$G_{ij,k}(\mathbf{x}',\mathbf{x},\omega) \approx i\omega A_{ij}(\mathbf{x}',\mathbf{x})P_k\exp(i\omega T), \tag{6}$$

where $\tau_{,i}$ is the spatial derivative of travel time τ with respect to x'_i, which is denoted by p_i. $T_{,i}$ is the spatial derivative of travel time T with respect to x'_i, which is denoted by P_i. $G_{ij,k}(\mathbf{x}',\mathbf{x},\omega)$ is the spatial derivative of the Green function with respect to x'_k.

Using equations (3), (4), (5) and (6), Equation (2) becomes

$$\Delta u_i(\mathbf{x},\omega) = \omega^2 \int_\Omega \exp[i\omega(\tau+T)][\Delta\rho A_{ji} a_j + \Delta\lambda A_{ji} P_j a_k p_k + \Delta\mu A_{mi} P_j (a_m p_j + a_j p_m)] d^3\mathbf{x}', \quad (7)$$

where $\Delta\rho = \Delta\rho(\mathbf{x}')$, $\Delta\lambda = \Delta\lambda(\mathbf{x}')$, $\Delta\mu = \Delta\mu(\mathbf{x}')$, $a_i = a_i(\mathbf{x}')$, $A_{ij} = A_{ij}(\mathbf{x}', \mathbf{x})$. Note that the reciprocity is applied for numerical reasons only. Computing the Green function from the receiver to each gridpoint is much easier than computing the Green function from each gridpoint to the receiver when using SW3D programs.

3 Models

The x_3-axis is oriented downwards in both background and perturbed models. The background model is homogenous without interfaces. The values of the elastic parameters are

$$v_p = 6 \text{ km/s}, \qquad v_s = 3 \text{ km/s}, \qquad \rho = 2000 \text{ kg/m}^3.$$

Each perturbed model contains two homogenous layers. The models differ in the shape of the interface between the layers and in the model volume. The values of the elastic parameters in the upper layer are equal to the values in the background model. The values of the elastic parameters in the lower layer are

$$v_p = 6.01 \text{ km/s}, \qquad v_s = 3.01 \text{ km/s}, \qquad \rho = 2010 \text{ kg/m}^3.$$

Model 1 has a horizontal interface at a depth of 10 km. The model volume is $(0 \text{ km}, 10 \text{ km}) \times (0 \text{ km}, 10 \text{ km}) \times (0 \text{ km}, 20 \text{ km})$. See Figure 1.

Model 2 has an inclined interface with slope 2/5. The model volume is $(-5 \text{ km}, 10 \text{ km}) \times (0 \text{ km}, 10 \text{ km}) \times (0 \text{ km}, 20 \text{ km})$. See Figure 2.

Model 3 has a curved interface. The model volume is $(-5 \text{ km}, 15 \text{ km}) \times (0 \text{ km}, 10 \text{ km}) \times (0 \text{ km}, 20 \text{ km})$. See Figure 3.

4 Numerical examples of 3D computations of 3D seismograms

In all 3 models, the explosive source is situated at point $(2 \text{ km}, 1 \text{ km}, 1 \text{ km})$, the receiver at point $(8 \text{ km}, 9 \text{ km}, 0 \text{ km})$. The source time function is a Gabor signal with a prevailing frequency of 10 Hz, filtered by a frequency filter which is non-zero only for frequencies f, $1 \text{ Hz} < f < 20 \text{ Hz}$. There is a cosine tapering for $1 \text{ Hz} < f < 2 \text{ Hz}$ and $19 \text{ Hz} < f < 20 \text{ Hz}$ while for $2 \text{ Hz} < f < 19 \text{ Hz}$ the filter is equal to one. Just P-waves are considered in all numerical examples except for one numerical example focused on S waves.

In the SW3D programs, the following specification of the grid is used: O_1, O_2, O_3 specify the coordinates of the origin of the grid. N_1, N_2, N_3 are the numbers of gridpoints

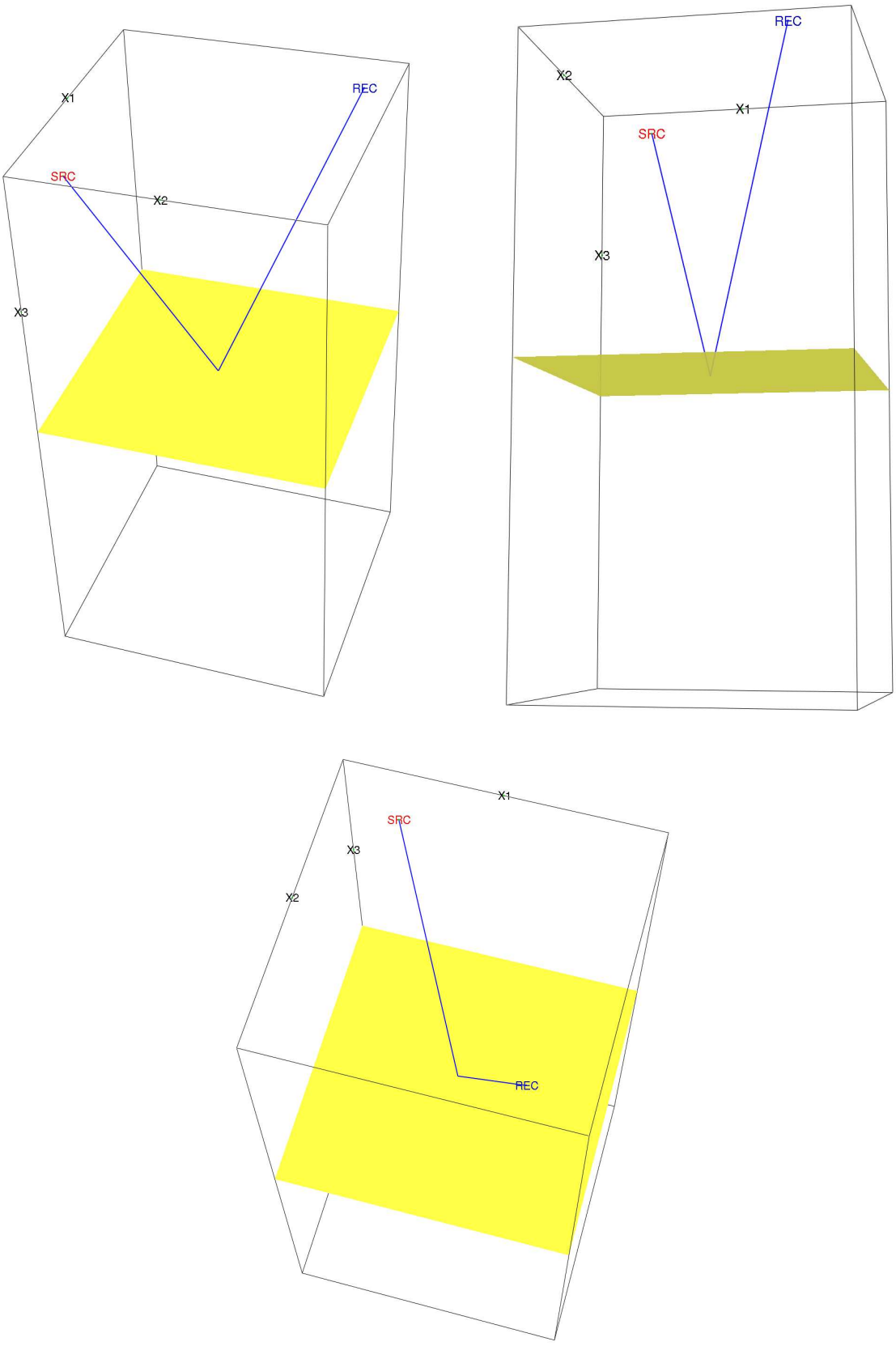

Figure 1: The model volume, the interface and the reflected ray in Model 1. The figures of the models were created in program GOCAD.

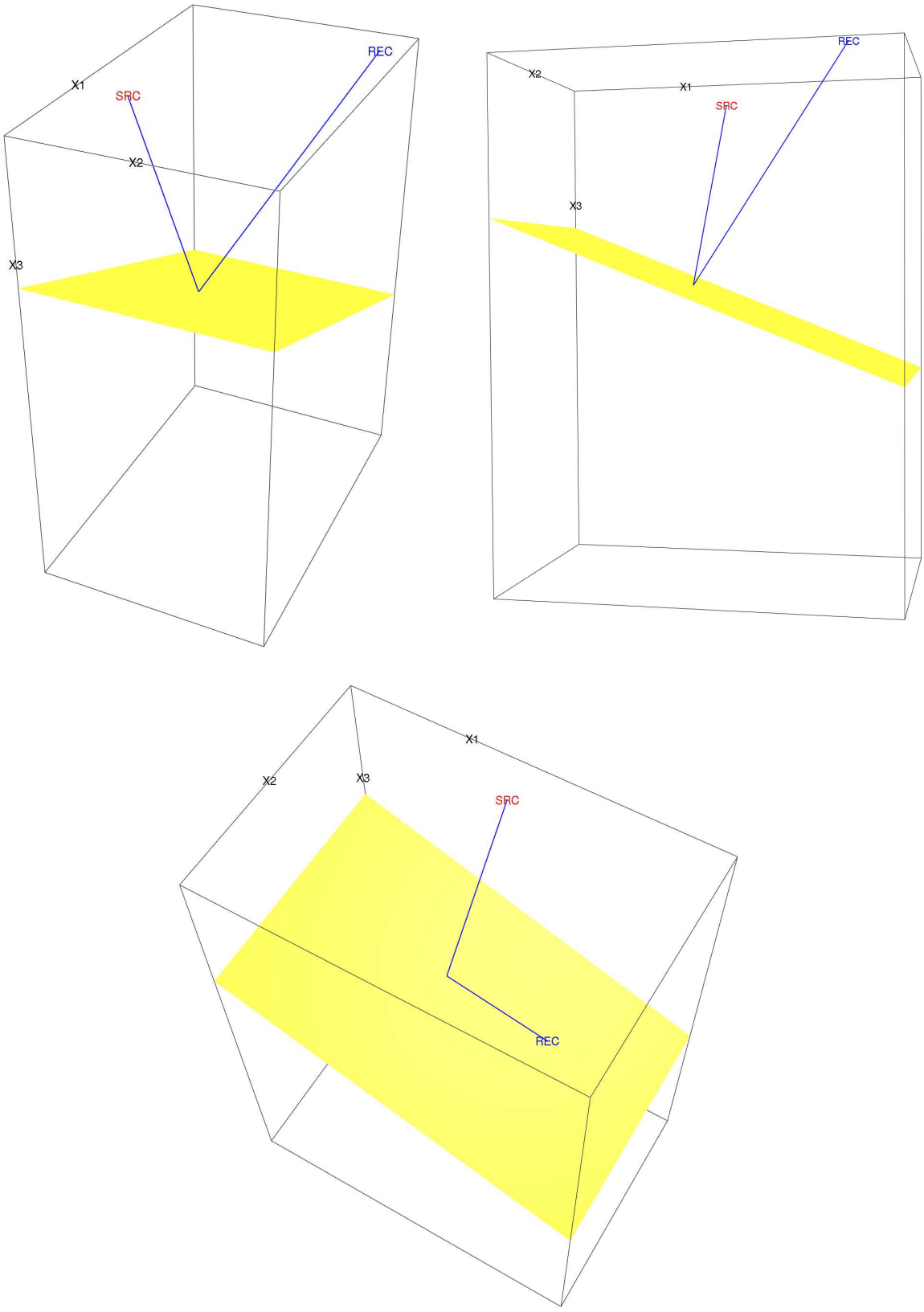

Figure 2: The model volume, the interface and the reflected ray in Model 2.

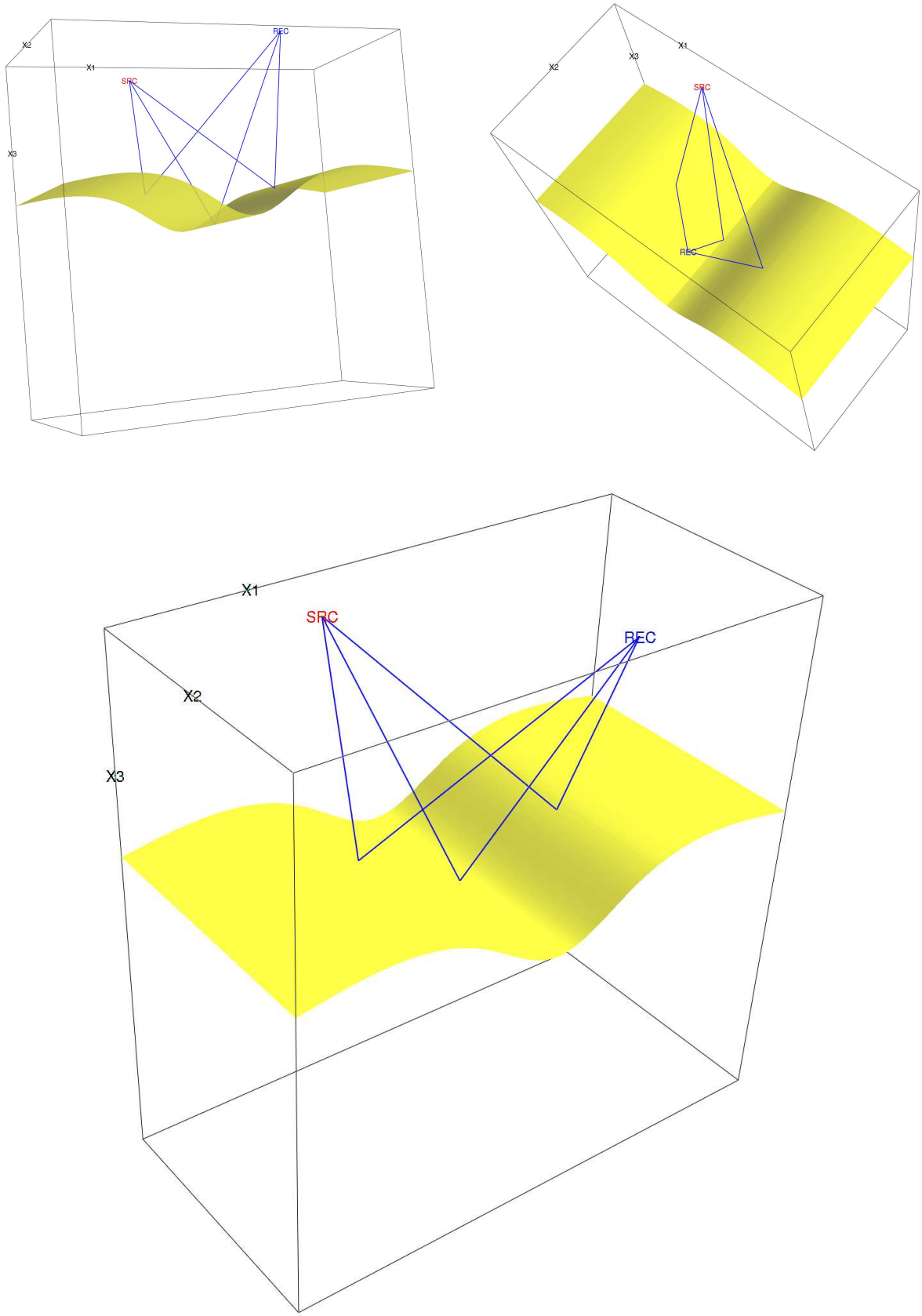

Figure 3: The model volume, the interface and the reflected rays in Model 3.

along the x_1, x_2, x_3 coordinate axes, respectively. D_1, D_2, D_3 are the grid intervals in the directions of the x_1, x_2, x_3 coordinate axes, respectively. We use this notation in this paper.

4.1 Model 1

4.1.1 Model 1 - Grid density

The position of the grid with respect to the horizontal interface is depicted in Figure 4. The white circles represent the gridpoints where perturbations are zero. The interface is situated precisely between two gridpoint planes. The distance between the model boundary and the nearest gridpoint plane is equal to half the grid interval, because the value of any quantity at each gridpoint represents the value in the block centred at the gridpoint with sides equal to the grid intervals.

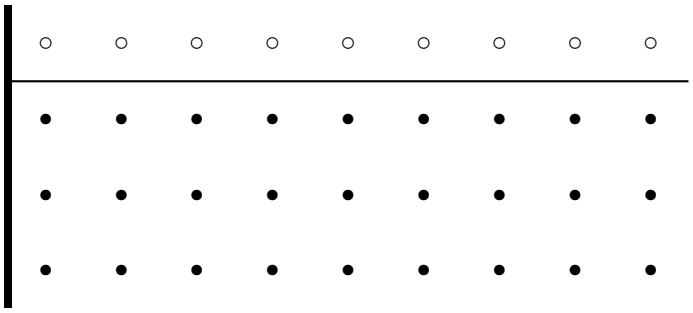

Figure 4: Position of the grid in Model 1, which discretize the interface in the best way. Bold line: Model boundary. Thin line: Interface.

For the position of the coordinate axes, refer to Figure 1 in Section 3. The grid interval is chosen to be 0.1 km, which is smaller than quarter of wavelength $\lambda = v_p/f_d \Rightarrow \frac{\lambda}{4} = \left(\frac{1}{4}\frac{6}{10}\right)$ km $= 0.15$ km, where we have inserted the value of the prevailing frequency of the Gabor signal $f_d = 10$ Hz and P-wave velocity $v_p = 6$ km/s. The size of the grid is $100 \times 100 \times 100$ points and covers only the lower part of the model, where the perturbation is non-zero in order to save memory. Figure 5 shows the resulting seismogram. We can see that the main features have been captured, but obviously some discrepancies are present. In order to get rid of them, we try to densify our grid. First, we densify it twice in the direction of the third axis (For the position of the coordinate axes, refer to Figure 1.). The resulting seismogram displayed in Figure 6 is better than the previous one. Second, we try to densify the grid additionally in the direction of the first axis. It is slightly surprising that it has no impact on the seismogram. Therefore, we step back, use 100 gridpoints in the direction of the first axis, but apply additional densification in the direction of the third axis. The seismogram has improved, see Figure 7. There are virtually no differences between the Born and ray-theory seismogram.

We try to understand the effect of discretization. Let us assume the paraxial approximation with the first-order Taylor expansion of travel with respect to the spatial coordinates. The central point is the point of reflection, therefore, the derivatives of travel time

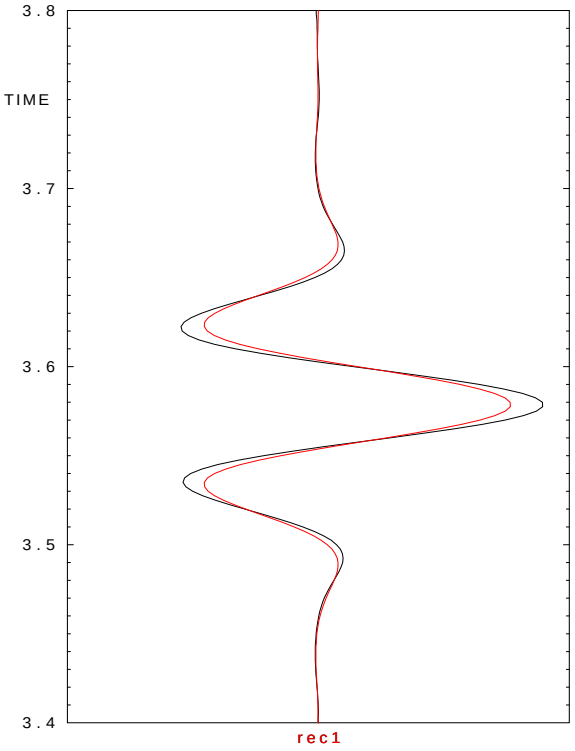

Figure 5: Model 1, grid $100 \times 100 \times 100$ grid-points.

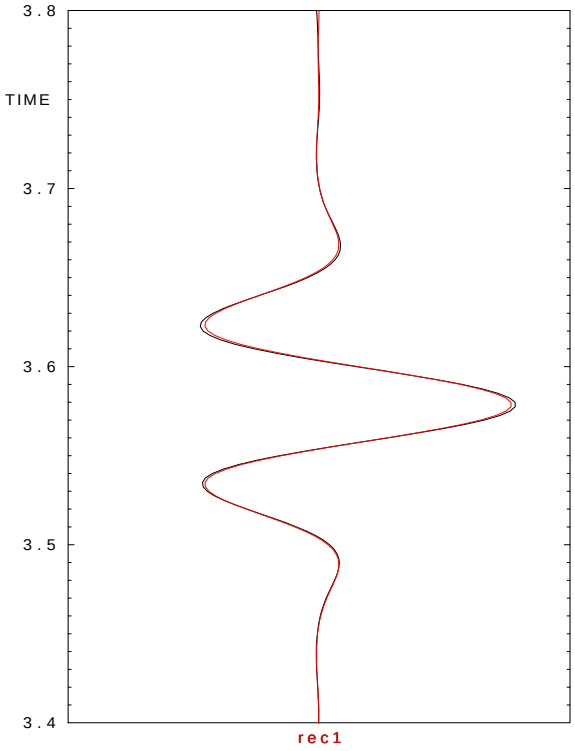

Figure 6: Model 1, grid $100 \times 100 \times 200$ grid-points.

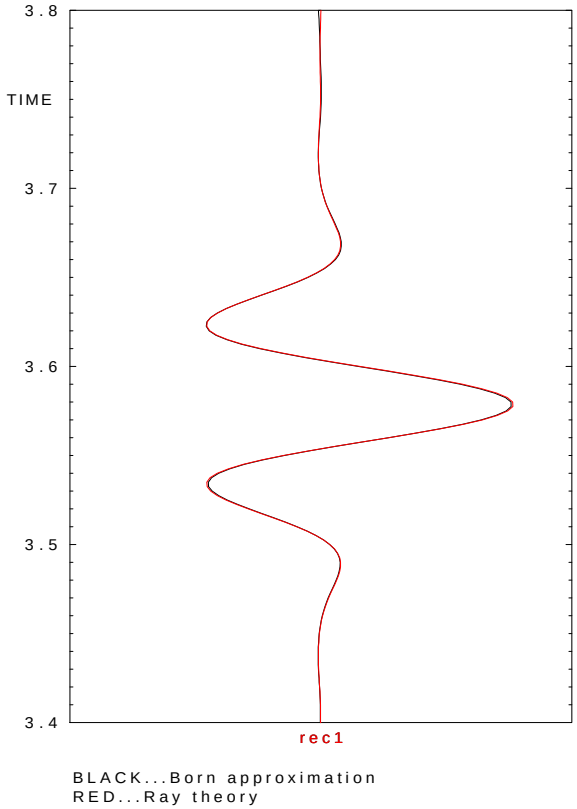

Figure 7: Model 1, grid $100 \times 100 \times 400$ grid-points.

with respect to the first and second coordinate axes are equal to zero and the integral in the Born approximation in the homogenous model can be simplified to

$$I_0 = \int_0^\infty \exp(i\omega\widehat{p_3}x_3)\mathrm{d}x_3 = -\frac{1}{i\omega\widehat{p_3}}, \tag{8}$$

where

$$\omega = \frac{2\pi v}{\lambda} \qquad , \qquad \widehat{p_3} = p_3 + P_3 = \frac{2\cos\alpha}{v}, \tag{9}$$

α being the angle between the slowness vector of the incident wave and the normal to the interface.

Discretization with the grid interval h affects the integral in the following way:

$$I_1 = \sum_{n=0}^{\infty} h\exp\left[i\omega\widehat{p_3}\left(\frac{h}{2}+nh\right)\right] = h\exp\left(i\omega\widehat{p_3}\frac{h}{2}\right)\frac{1}{1-\exp(i\omega\widehat{p_3}h)}. \tag{10}$$

Expressions (8) and (10) yield

$$\frac{I_1}{I_0} - 1 = -i\omega\widehat{p_3}h\frac{\exp\left(i\omega\widehat{p_3}\frac{h}{2}\right)}{1-\exp(i\omega\widehat{p_3}h)} - 1,$$

which becomes

$$\frac{I_1}{I_0} - 1 = \frac{\omega\widehat{p_3}\frac{h}{2}}{\sin(\omega\widehat{p_3}\frac{h}{2})} - 1. \tag{11}$$

The expression in (11) is real and, therefore, the discretization error influences the amplitude of the wave, but not the phase. Equation (11) using (9) becomes

$$\frac{I_1}{I_0} - 1 = \frac{2\pi\frac{h}{\lambda}\cos\alpha}{\sin\left(2\pi\frac{h}{\lambda}\cos\alpha\right)} - 1, \tag{12}$$

which reads approximately

$$\frac{I_1}{I_0} - 1 \approx \frac{1}{6}\left(2\pi\frac{h}{\lambda}\cos\alpha\right)^2. \tag{13}$$

We compare the numerical results with theoretical predictions (12) and (13), see Table 1.

$h = D_3$ [km]	Equation (13) [%]	Equation (12)[%]	Measured [%]
0.1	14	16	17
0.05	3.6	3.7	2.2
0.025	0.89	0.90	0.90

Table 1: Effect of the discretization error on the wave amplitude. Comparison of the theoretical prediction and the numerical results. D_3 is the grid interval in the direction of the third coordinate axis.

Both theoretical predictions (12) and (13) agree well with the numerical modelling in case of the smallest grid interval $D_3 = 0.025$ km. The differences between the theoretical predictions and numerical results are observed for $D_3 = 0.05$ km and 0.1 km. The difference between the full formula (13) and its first approximation (12) is negligible for $D_3 = 0.025$ km. The difference grows for $D_3 = 0.05$ and is important for $D_3 = 0.1$ km.

4.1.2 Model 1 - Spurious waves

In Section 4.1.1, we studied the seismogram in the time window $3.4 - 3.8$ s, and when we used a sufficiently dense grid we observe no differences between the seismograms computed using the Born approximation and the ray theory. However, the differences are apparent when we extend our time window from $3.4 - 3.8$ s to $3.0 - 7.2$ s, see Figure 8. The differences are caused by interfaces artificially introduced by the grid. The perturbed model has one defined interface. The model is defined within the model volume, but it smoothly continues across the model boundaries. The elastic parameters are not zero outside the model volume and the model perturbations can thus be non-zero there, too. In other words, model boundaries (side boundaries, bottom and top boundary) are not interfaces. On the contrary, our choice of the grid is equivalent to putting model perturbations zero elsewhere. In the case of Model 1, the boundaries of the lower part of the model are treated as interfaces. From what was said, we expect various types of reflections present in the seismogram, for example the wave reflected from the bottom model interface, as well as diffractions.

How to distinguish these spurious waves from the genuine? They are sensitive to positions of the grid boundaries. Therefore, if we shift these boundaries, the seismograms should change slightly. A good shift is $\frac{\lambda}{4}$ because the wave has to travel $\Delta l = 2\frac{\lambda}{4} = \frac{\lambda}{2}$ more/less in the case of normal incidence. If the incidence is not normal, the length of the trajectory changes by $\Delta l = \frac{\lambda}{2}\cos\alpha$, where α is the angle between the normal to the interface and the vector tangent to the ray. We decide to reduce the grid, so that $\Delta l < 0$ and the shift present in the seismogram should be towards shorter times. $D_1 = D_2 = 0.1$ km, $D_3 = 0.025$ km, $\frac{\lambda}{4} = 0.15$ km, therefore, we erase 2 side gridpoint planes and 8 bottom gridpoint planes, which is equivalent to $|\Delta l| = 0.2\cos\alpha$ km. This value is larger than $\frac{\lambda}{4}$ for normal incidence, but due to the cosine modification for oblique incidence, a larger value is better than smaller. The seismogram is displayed in Figure 9.

The waves which are shifted in the seismogram should be eliminated. There are at least two ways of doing this. The first one is safe but computationally expensive. It consists in a sufficient extension of the grid. If the grid boundaries (interfaces) are far enough, reflections, etc. arrive sufficiently late. The seismogram depicted in Figure 10 is computed using the grid which covers the volume of $(-10 \text{ km}, 20 \text{ km}) \times (-10 \text{ km}, 20 \text{ km}) \times (10 \text{ km}, 20 \text{ km})$. The grid density is the same as in computing the seismograms in Figures 7 and 8, but the grid contains 9 times more points. Compare the three waves visible in the seismograms in Figures 8, 9, 10. The first wave is obviously the true wave, because we see no shift in the seismogram in Figure 9. The second wave and the third wave are both shifted in the seismogram in Figure 9, but notice that no shift is present in the seismogram in Figure 10 in case of the third wave. We enlarge the model in the horizontal direction, which means that the third wave is the reflection from the bottom of the grid.

One might think that we can use a sparser grid if we are sufficiently far from the source and the receiver. If this were true, we would be able to cover a large volume with only slightly more computational effort using varying grid density. Unfortunately we can be unpleasantly surprised. We try to cover the same volume $(-10 \text{ km}, 20 \text{ km}) \times$

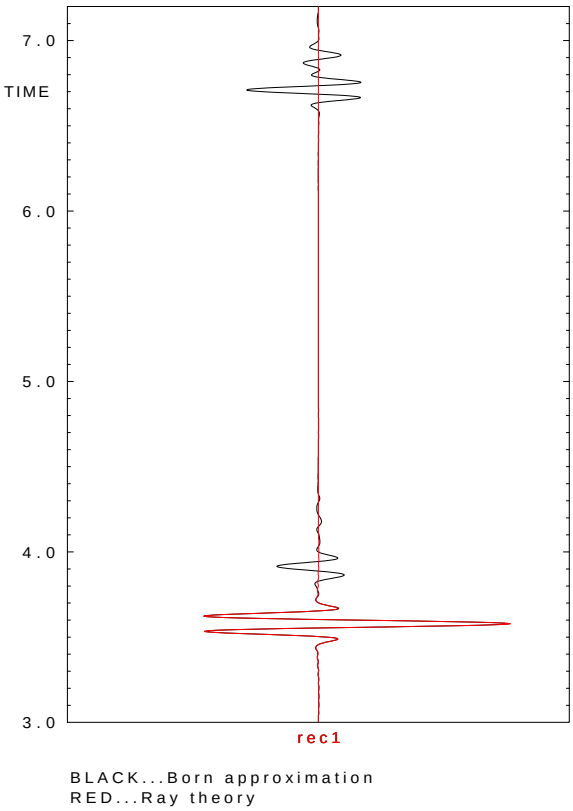

Figure 8: Model 1, grid $100 \times 100 \times 400$ gridpoints, enlarged time window.

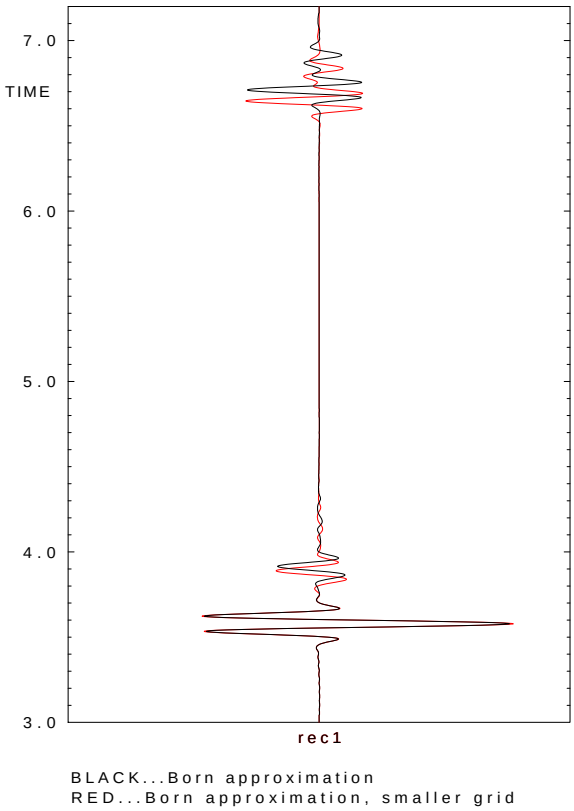

Figure 9: Model 1, grid $100 \times 100 \times 400$ gridpoints vs grid $96 \times 96 \times 392$ gridpoints.

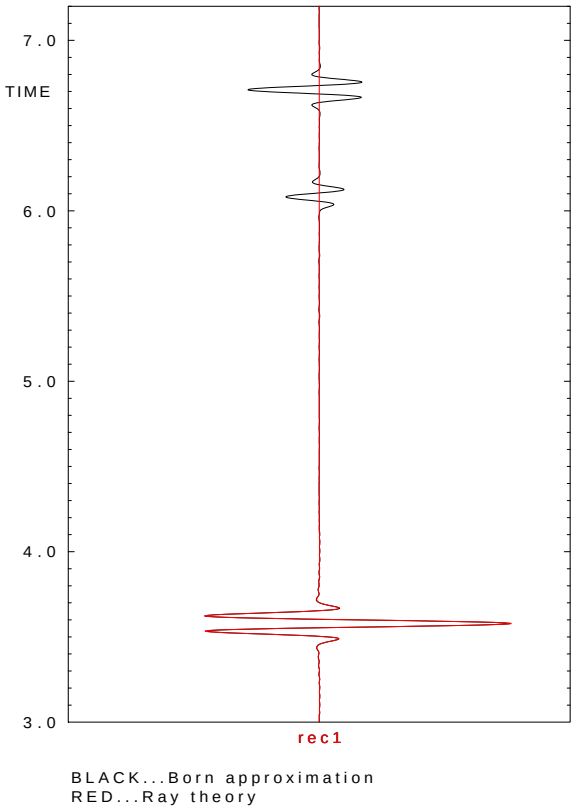

Figure 10: Extended Model 1, grid $300 \times 300 \times 400$ gridpoints.

$(-10\text{ km}, 20\text{ km}) \times (10\text{ km}, 20\text{ km})$, but now using a combination of two grids. The first grid is sparse and covers the whole volume except the middle part $(0\text{ km}, 10\text{ km}) \times (0\text{ km}, 10\text{ km}) \times (10\text{ km}, 20\text{ km})$. The second grid is dense and covers the middle part. SW3D programs work with regular rectangular grids. We thus have to compose the first grid of two rectangular grids. Grid A is sparse and covers the whole volume, grid B is also sparse and covers the middle part. The first grid is grid A minus grid B. The seismograms from the second grid and grid B are correct, but the seismogram from grid A is incorrect, see Figure 11. It is probable that constructive apart from destructive interference have occurred.

The second way of eliminating a spurious wave is to apply the cosine window at the artificial grid boundaries. The 1D cosine window starting at point x_s of length L is function

$$w(x) \begin{cases} = 0 & \text{for } x < x_s \\ = \frac{1}{2}\left(1 - \cos\left[\frac{\pi(x-x_s)}{L}\right]\right) & \text{for } x \in \langle x_s, x_s + L\rangle \\ = 1 & \text{for } x > x_s + L. \end{cases} \tag{14}$$

We introduce the following numbering of the model boundaries, see Table 2.

Axis perpendicular to the boundary	Assigned number
1st, negative direction	1
1st, positive direction	2
2nd, negative direction	3
2nd, positive direction	4
3rd, negative direction	5
3rd, positive direction	6

Table 2: Numbering of the model boundaries

If we apply the cosine window of length L to the 1st boundary at $(x_1^0, \bullet, \bullet)$, then the cosine window is function $w(x_1)$ defined by (14) with $x_s = x_1^0 - \frac{D_1}{2}$. Similarly for the other boundaries.

We apply the cosine windows of equal length to each grid boundary except the 5th, where we model the reflection. The tested lengths are $L = 1$ km, $L = 1.5$ km, $L = 2$ km, $L = 2.5$ km, $L = 3$ km The corresponding seismograms are displayed in Figures 12, 13, 14, 15, 16.

Notice that the amplitudes of the spurious waves decrease and the waves arrive earlier. The values of $L = 2.5$ km or $L = 3$ km are obviously too large; the spurious wave arrives so early that it interferes with the true wave. Another important fact is that the reflection from the bottom grid boundary is very well damped, while the diffractions from the side grid boundaries are damped less.

This phenomenon can be explained similarly as we derived formula (13). We change expression (14) for cosine window of length L to read

$$w(x) = \frac{1 - \cos\left(\pi\frac{x}{L}\right)}{2} = \frac{1}{2} - \frac{1}{4}\exp\left(i\pi\frac{x}{L}\right) - \frac{1}{4}\exp\left(-i\pi\frac{x}{L}\right). \tag{15}$$

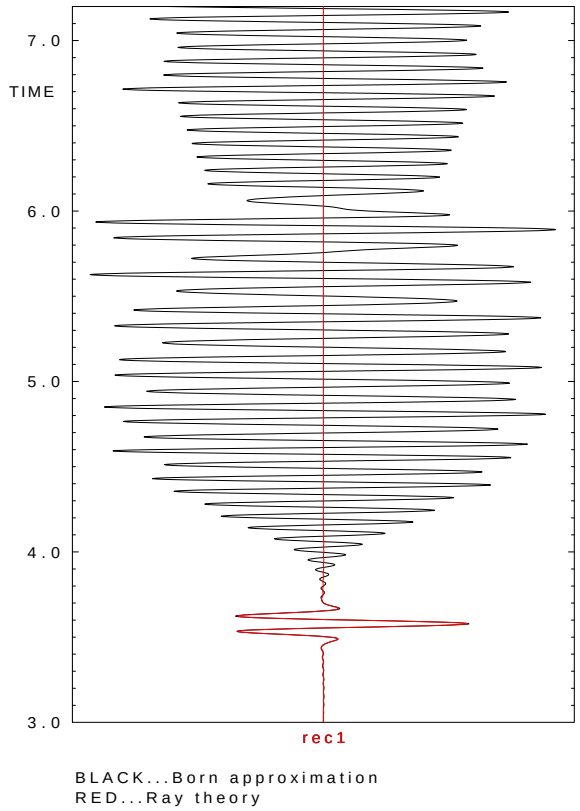

Figure 11: Extended Model 1, grid $75 \times 75 \times 400$ gridpoints.

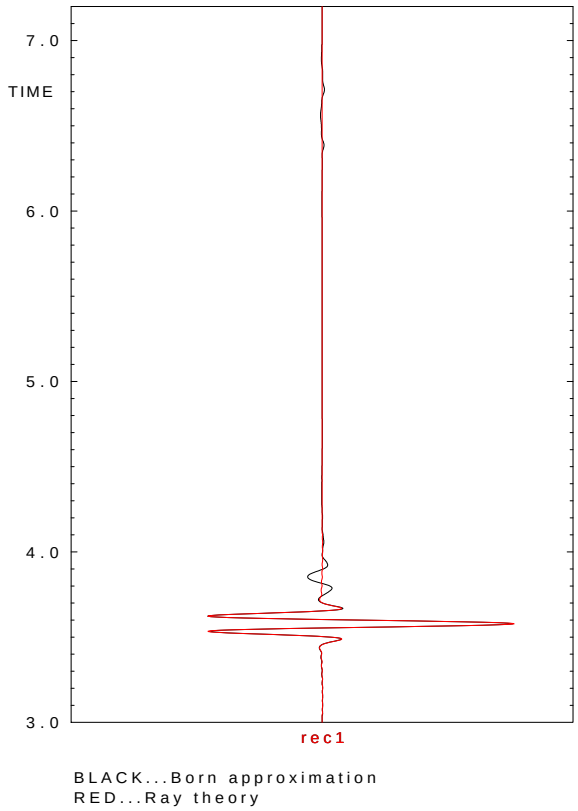

Figure 12: Model 1, grid $100 \times 100 \times 400$ gridpoints, cosine window of length 1 km applied to grid boundaries 1,2,3,4,6 (see Table 2).

The Born approximation with applied cosine window can be reduced to

$$
\begin{aligned}
I_1 &= \int_0^L w(x)\exp(i\omega\widehat{p_3}x_3)\mathrm{d}x_3 + \int_L^\infty \exp(i\omega\widehat{p_3}x_3)\mathrm{d}x_3 \\
&= \frac{1}{2i\omega\widehat{p_3}}\left[\exp(i\omega\widehat{p_3}L) - 1\right] - \frac{1}{4\left(i\frac{\pi}{L} + i\omega\widehat{p_3}\right)}\left[\exp(i\pi + i\omega\widehat{p_3}L) - 1\right] \\
&- \frac{1}{4\left(-i\frac{\pi}{L} + i\omega\widehat{p_3}\right)}\left[\exp(-i\pi + i\omega\widehat{p_3}L) - 1\right] - \frac{1}{i\omega\widehat{p_3}}\exp(i\omega\widehat{p_3}L),
\end{aligned}
$$

which can be expressed in factorized form:

$$
I_1 = \left[\frac{1}{4\left(i\omega\widehat{p_3} + i\frac{\pi}{L}\right)} + \frac{1}{4\left(i\omega\widehat{p_3} - i\frac{\pi}{L}\right)} - \frac{1}{2i\omega\widehat{p_3}}\right]\left[1 + \exp(i\omega\widehat{p_3}L)\right] \tag{16}
$$

$$
= \frac{\frac{1}{2}\left(\frac{\pi}{L}\right)^2}{i\omega\widehat{p_3}\left[(\omega\widehat{p_3})^2 - \left(\frac{\pi}{L}\right)^2\right]}\left[1 + \exp(i\omega\widehat{p_3}L)\right]. \tag{17}
$$

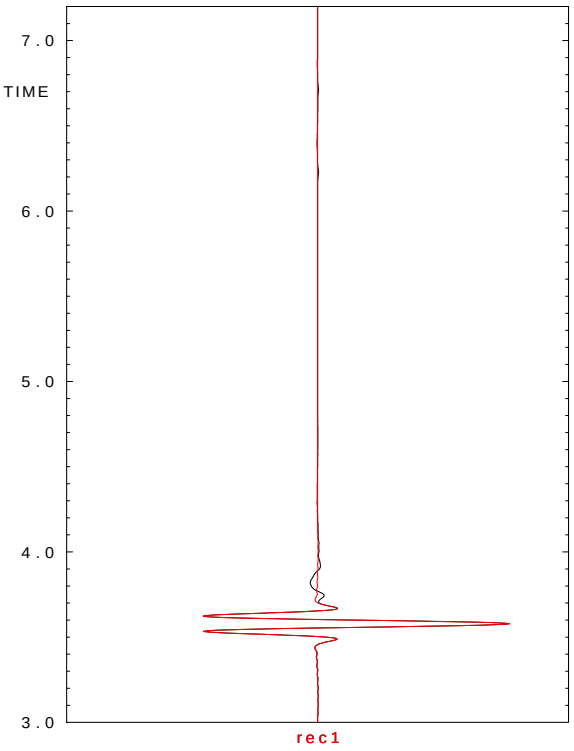

Figure 13: Model 1, grid $100 \times 100 \times 400$ grid-points, cosine window of length 1.5 km applied to grid boundaries 1,2,3,4,6.

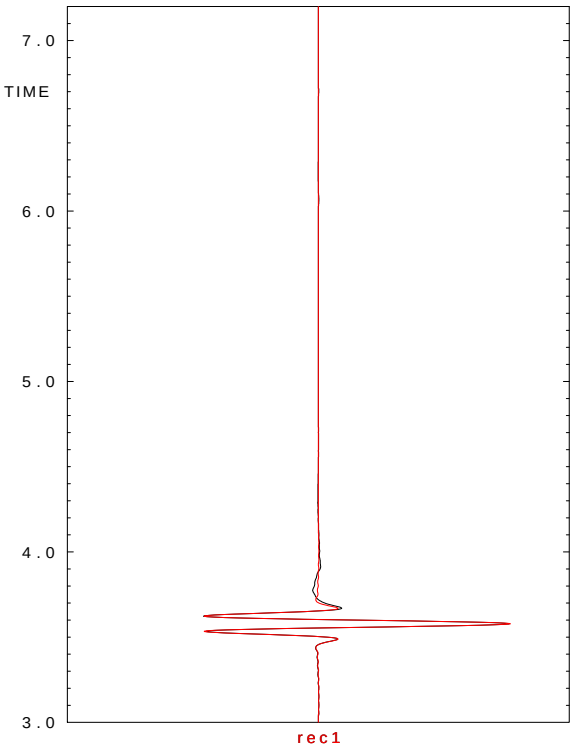

Figure 14: Model 1, grid $100 \times 100 \times 400$ grid-points, cosine window of length 2 km applied to grid boundaries 1,2,3,4,6.

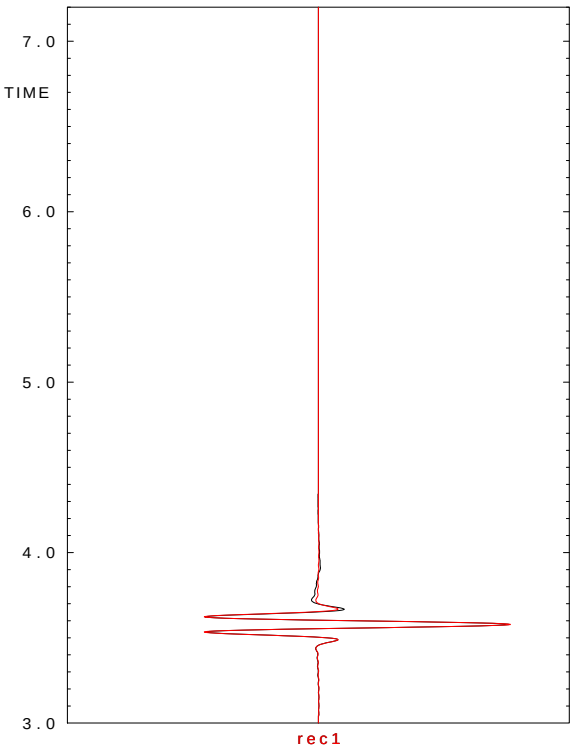

Figure 15: Model 1, grid $100 \times 100 \times 400$ grid-points, cosine window of length 2.5 km applied to grid boundaries 1,2,3,4,6.

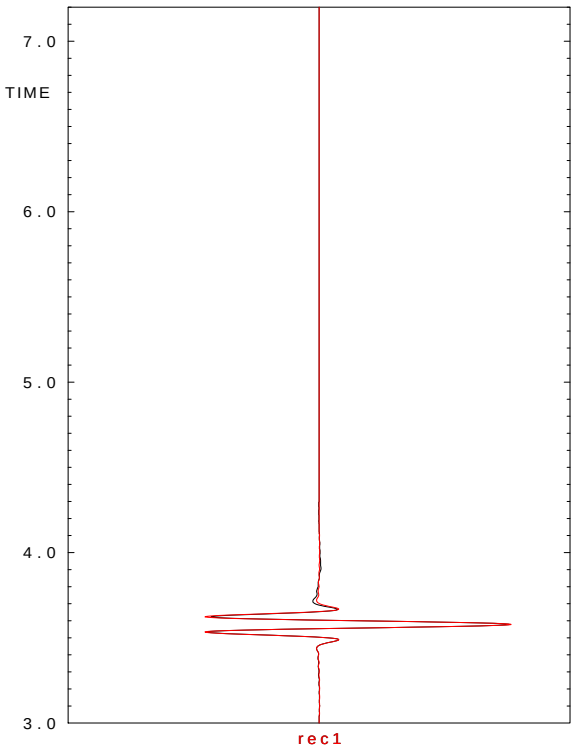

Figure 16: Model 1, grid $100 \times 100 \times 400$ grid-points, cosine window of length 3 km applied to grid boundaries 1,2,3,4,6.

Using expressions (8) and (17) we can put

$$\frac{I_1}{I_0} = \frac{\left(\frac{\pi}{L}\right)^2}{\left(\frac{\pi}{L}\right)^2 - (\omega\widehat{p}_3)^2} \frac{1 + \exp(i\omega\widehat{p}_3 L)}{2}. \tag{18}$$

If we assume that $\omega\widehat{p}_3 L \gg \pi$,

$$\left|\frac{I_1}{I_0}\right| < \left(\frac{\pi}{\omega\widehat{p}_3 L}\right)^2,$$

and finally, employing (9),

$$\left|\frac{I_1}{I_0}\right| < \left(\frac{\lambda}{4L\cos\alpha}\right)^2. \tag{19}$$

4.1.3 Modified Model 1 - Applicability of the ray-based Born approximation

We shall now study, how well the Born approximation behaves if medium perturbations increase. The grid is identical with the one used in the computation of the seismogram shown in Figure 7. The values of the elastic parameters in the lower layer are gradually increased to obtain the following perturbations of elastic parameters:

$$\Delta v_p = 0.1 \text{ km/s}, \qquad \Delta v_s = 0.1 \text{ km/s}, \qquad \Delta\rho = 100 \text{ kg/m}^3, \tag{20}$$

$$\Delta v_p = 0.5 \text{ km/s}, \qquad \Delta v_s = 0.5 \text{ km/s}, \qquad \Delta\rho = 500 \text{ kg/m}^3, \tag{21}$$

$$\Delta v_p = 1 \text{ km/s}, \qquad \Delta v_s = 1 \text{ km/s}, \qquad \Delta\rho = 1000 \text{ kg/m}^3. \tag{22}$$

The resulting seismograms are displayed in Figures 17, 18, 19. The scale is chosen in order to have practically equal ray-theory seismograms. It is interesting that, though perturbations (20) are 10 times greater than in the computation of the seismogram of Figure 7, the seismograms still appear to be quite satisfactory. Discrepancies appear and grow for larger perturbations. This is probably the consequence of the non-linearity of the reflection coefficient, see also Šachl (2011, sec. 3.2, fig. 22).

4.1.4 Model 1 - Other types of waves

So far we have tested the algorithm for P waves. Now we shall focus on other possible situations, i.e. incident P wave and scattered S wave (P-S for short), S-P and S-S. The resulting seismograms corresponding to the first two cases are displayed in Figures 20 and 21. Good agreement is observed. In the last case composed purely of S waves, discrepancies are observed, see Figure 22. Note that $v_p = 6$ km/s, $v_s = 3$ km/s and thus $\lambda_s = \frac{\lambda_p}{2}$. Therefore, the grid should be twice denser to be effectively the same as in the case of P waves. If the grid is twice denser in the vertical direction, the discrepancies disappear, see Figure 23.

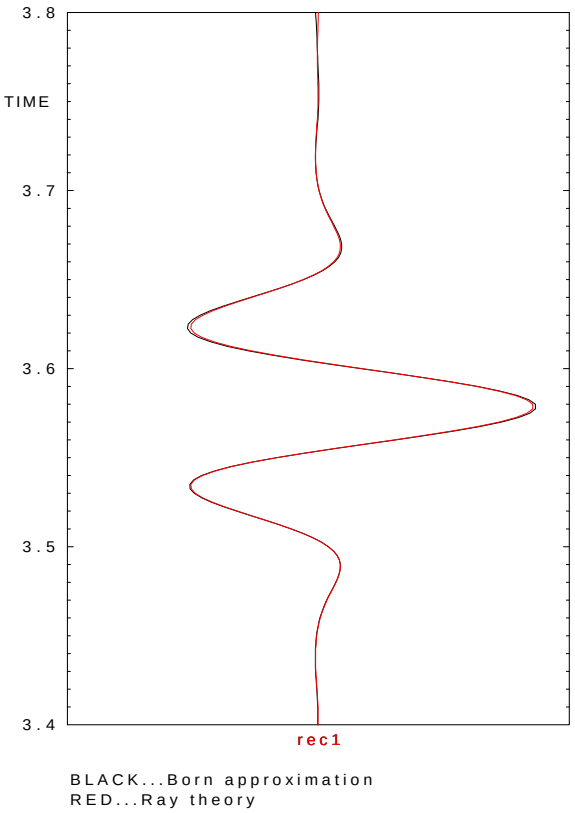

Figure 17: Model 1, grid $100 \times 100 \times 400$ grid-points, perturbations (20).

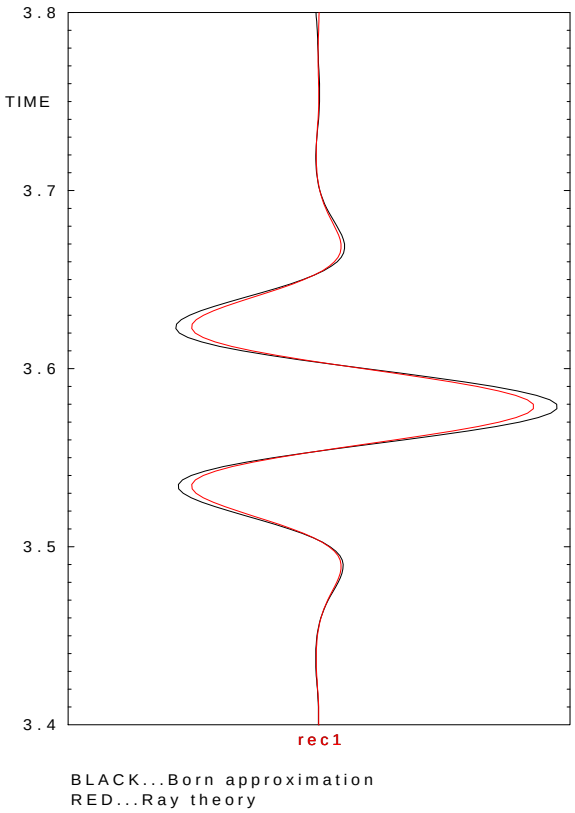

Figure 18: Model 1, grid $100 \times 100 \times 400$ grid-points, perturbations (21).

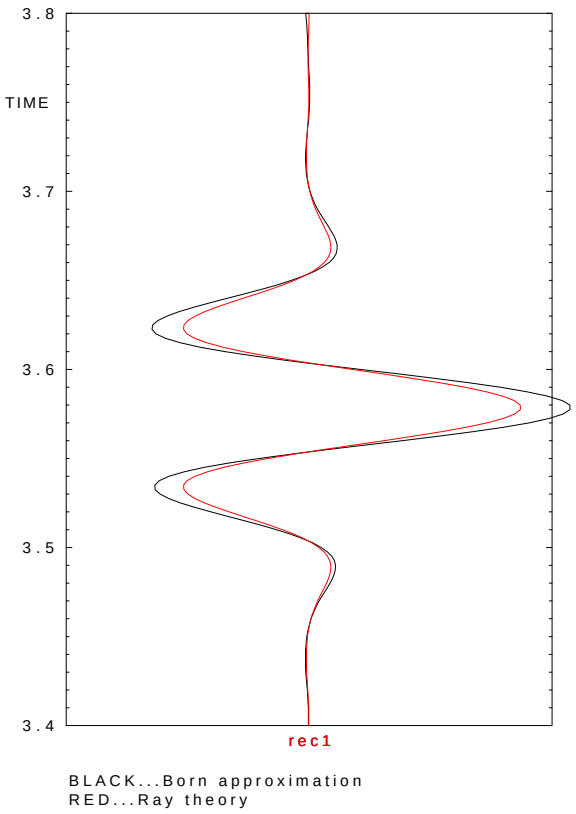

Figure 19: Model 1, grid $100 \times 100 \times 400$ grid-points, perturbations (22).

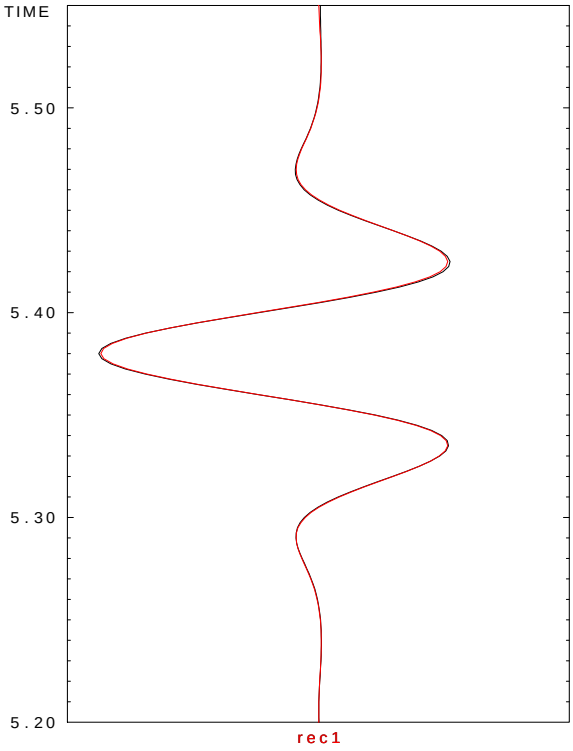

Figure 20: Model 1, incident P wave, scattered S wave, grid $100 \times 100 \times 400$ gridpoints.

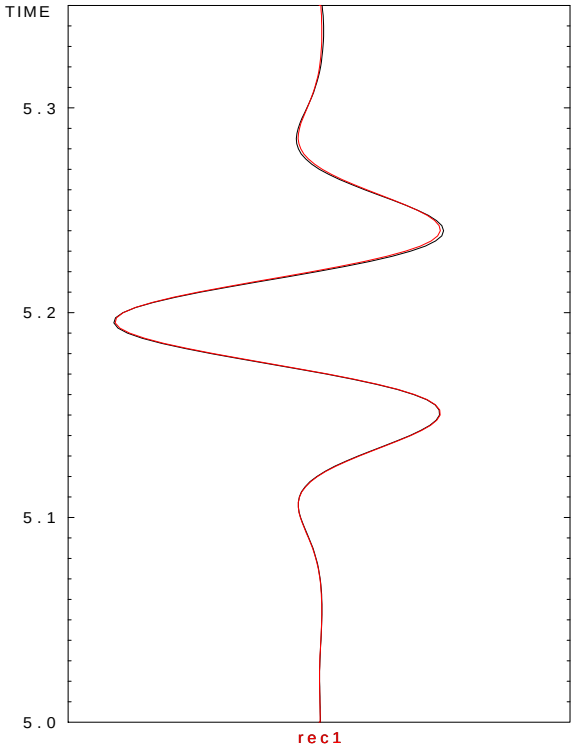

Figure 21: Model 1, incident S wave, scattered P wave, grid $100 \times 100 \times 400$ gridpoints.

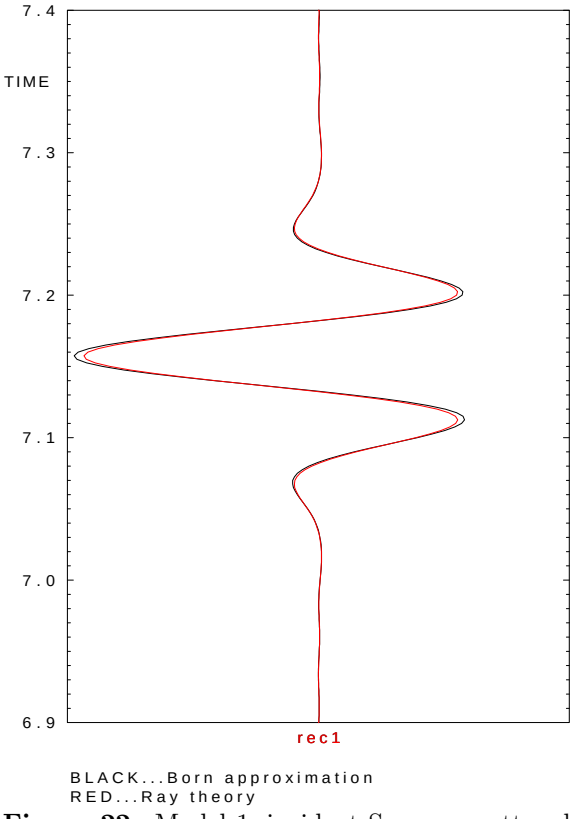

Figure 22: Model 1, incident S wave, scattered S wave, grid $100 \times 100 \times 400$ gridpoints.

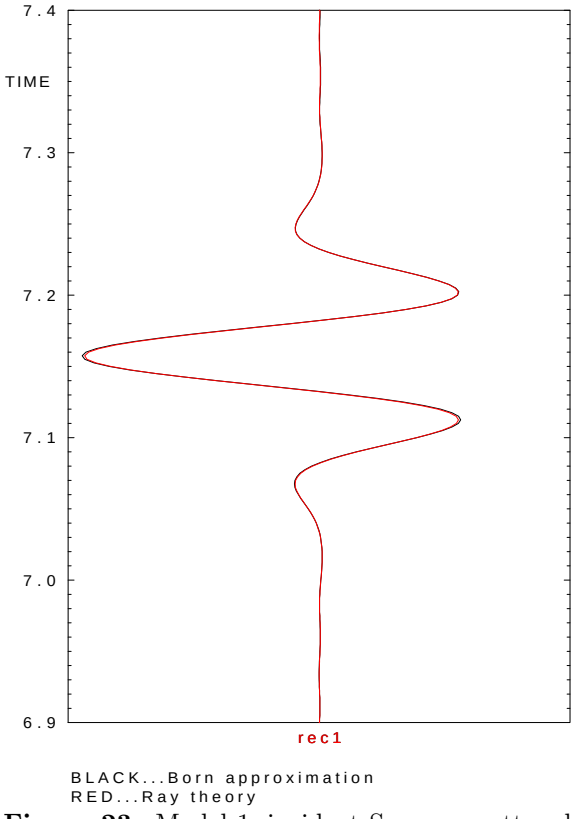

Figure 23: Model 1, incident S wave, scattered S wave, grid $100 \times 100 \times 800$ gridpoints.

4.2 Model 2

4.2.1 Model 2 - Grid

We choose $N_2 = 100$ for the computations in this 3D model. This number of gridpoints along the second coordinate axis is equal to the value used in Section 4.1. For the position of the coordinate axes, refer to Figure 2 in Section 3. The slope of the inclined interface is $\frac{2}{5}$. We choose the grid which fits the shape and position of the interface, i.e. the interface lies between two gridpoint planes, see Figure 24. We thus take

$$D_1 = \frac{5}{2} D_3 \tag{23}$$

We set $N_3 = 400$. The interface begins at the depth of 6 km, so that $D_3 = 0.034956$ km $\approx \frac{20-6}{N_3+0.5}$ km, therefore, $D_1 \approx 0.087391$ km and $N_1 = 171 \approx \frac{15 \text{ km}}{D_1}$.

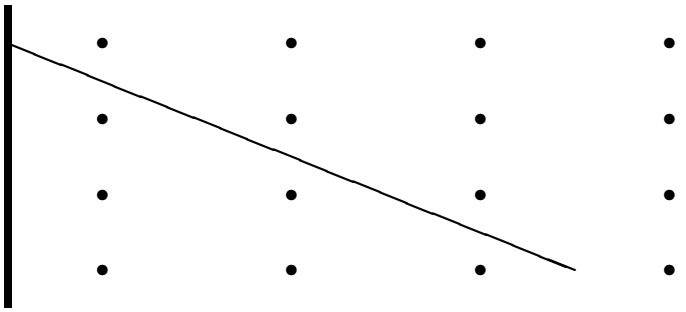

Figure 24: Grid which fits the shape and position of the interface in Model 2. Cross section in $x_1 - x_3$ plane. Bold line: Model boundary. Thin line: Interface.

Using this configuration, we calculate the seismogram displayed in Figure 25. The Born and ray-theory seismograms agree very well, although grid interval D_3 is larger than in the computation of the seismogram in Figure 5 and the discretization of the interface is worse, too. Indeed, in Model 1, the discretization is $h = D_3 = 0.025$ km. In Model 2, h is equal to the altitude in the right triangle with legs $D1$, $D3$,

$$h = \frac{D_1 D_3}{\sqrt{D_1^2 + D_3^2}}, \tag{24}$$

inserting (23) we obtain

$$h = \frac{5}{\sqrt{29}} D_3 \approx 0.0232 \text{ km}. \tag{25}$$

4.2.2 Model 2 - Spurious waves

Spurious waves are revealed in the same way as in Model 1, see Figure 26. They are suppressed by using cosine windows 0.5 km, 1 km and 1.5 km in length, respectively. The results are depicted in Figures 27, 28, 29.

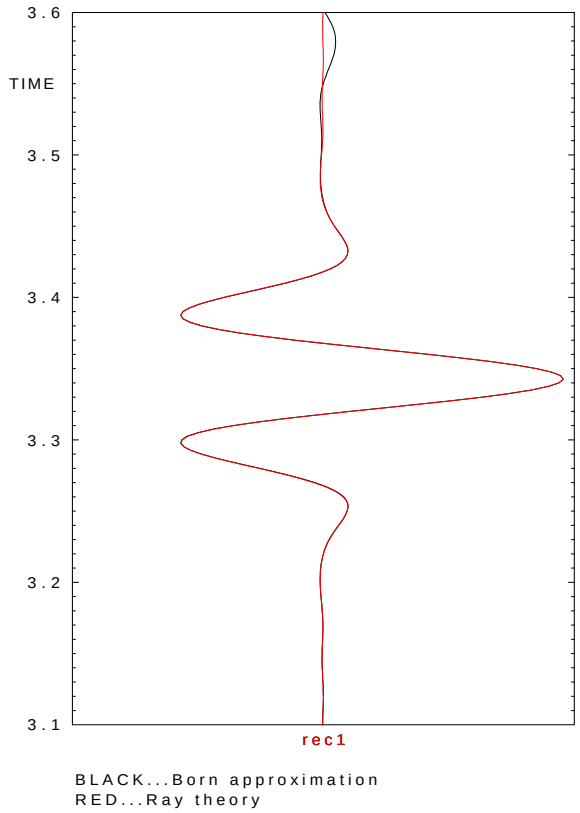

Figure 25: Model 2, grid 171 × 100 × 400 gridpoints.

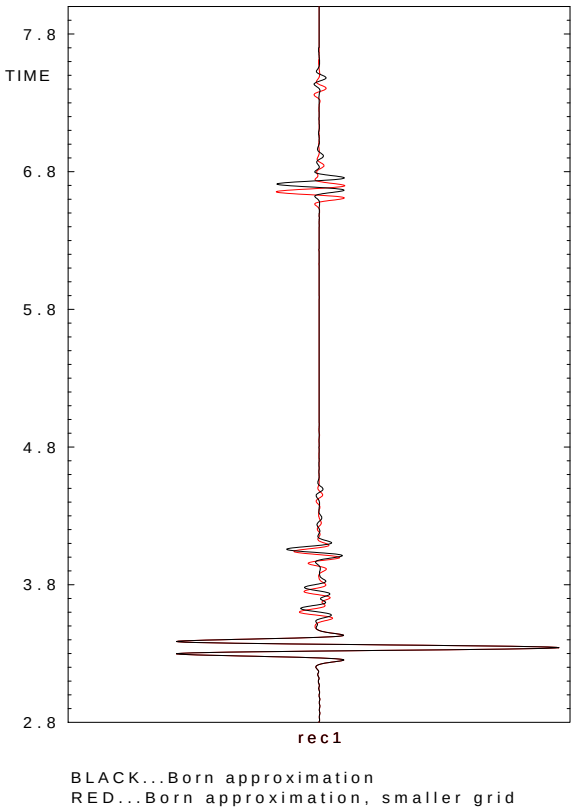

Figure 26: Model 2, grid 171 × 100 × 400 gridpoints, enlarged time window.

4.3 Model 3

For the position of the coordinate axes, refer to Figure 3 in Section 3. A grid of 300 × 100 × 800 points is chosen. The grid intervals are $D_1 = 0.066667$ km, $D_2 = 0.1$ km and $D_3 = 0.025$ km. The grid interval in the direction of the third axis is the same as in the computation of the seismogram in Figure 7. The shape of the interface does not depend on x_2, therefore, 100 gridpoints in the direction of the second coordinate axis would seem enough. The seismogram computed using this grid is displayed in Figure 30. We can see the differences between the Born and ray-theory seismogram in Figure 30, therefore, we compute the Born approximation with more precise grid values of the elastic parameters. We discretize the density, P-wave and S-wave velocity in the grid twice denser in the direction of the first and third axes. The quantities are then averaged to the grid described above. The density is averaged by taking its geometrical mean, which corresponds to the conservation of mass inside the volume determined by the averaged grid cell. The P-wave and S-wave velocities are averaged by taking their harmonic mean, which corresponds to the conservation of travel time inside the volume determined by the averaged grid cell. We obtain the seismogram in Figure 31. We can see the improvement in the first wave, but the more important effect is the reduction of the oscillations visible on the previous seismogram around 3.72 s, i.e. after the second wave. We further try to densify the grid used, interface is quite complicated in plane x_1-x_3 and, therefore, the discretization in the direction of the 1st axis could be insufficient. We then use the grid with 600 × 100 × 800

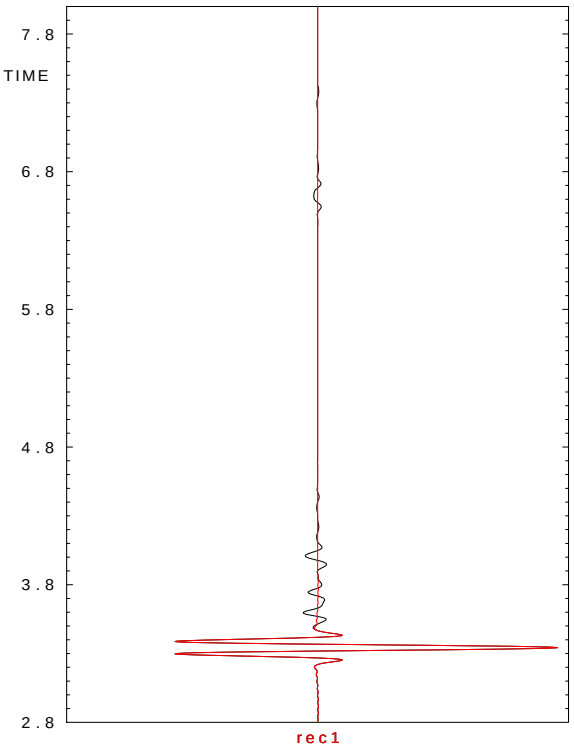

Figure 27: Model 2, grid 171 × 100 × 400 grid-points, cosine window 0.5 km in length applied to grid boundaries 1,2,3,4,6.

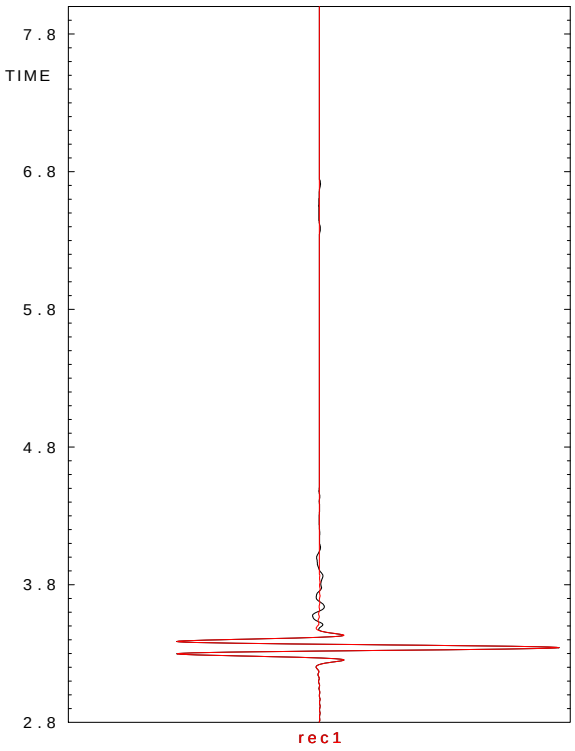

Figure 28: Model 2, grid 171 × 100 × 400 grid-points, cosine window 1 km in length applied to grid boundaries 1,2,3,4,6.

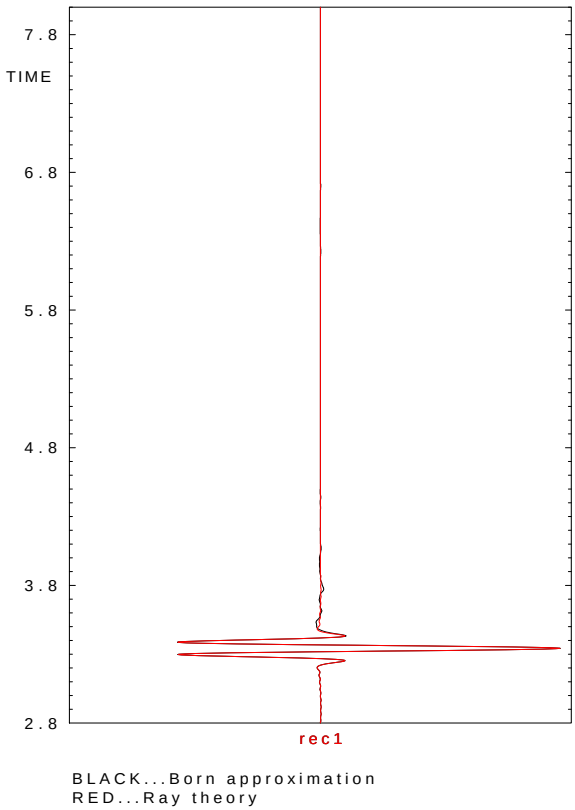

Figure 29: Model 2, grid 171 × 100 × 400 grid-points, cosine window 1.5 km in length applied to grid boundaries 1,2,3,4,6.

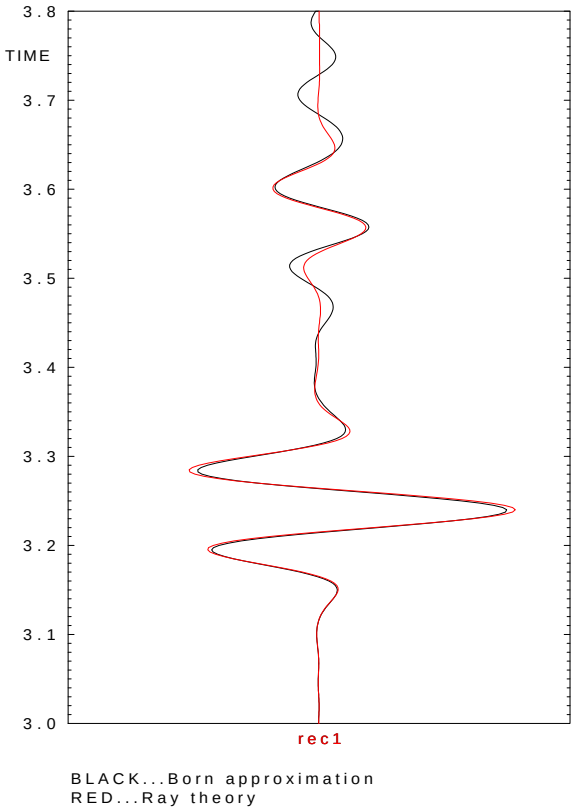

Figure 30: Model 3, grid 300 × 100 × 800 grid-points.

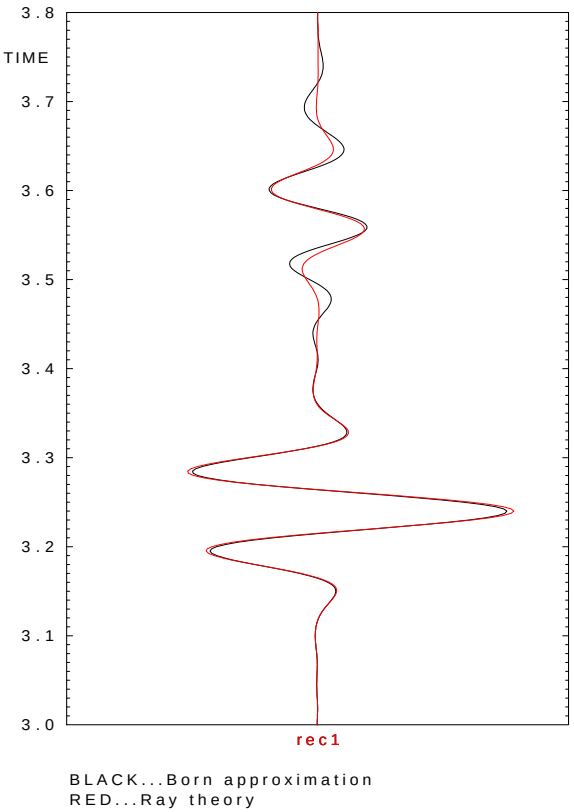

Figure 31: Model 3, grid $300 \times 100 \times 800$ gridpoints, averaged elastic parameters.

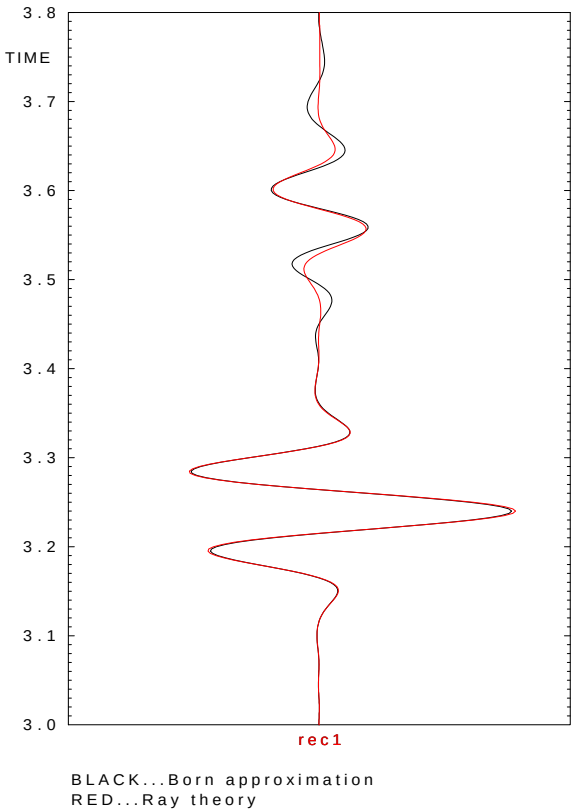

Figure 32: Model 3, grid $600 \times 100 \times 800$ gridpoints, averaged elastic parameters.

gridpoints, i.e. we densify it twice in the direction of the 1st axis. The elastic parameters are again computed in the grid twice denser in the direction of the first and third axes and then averaged as in the previous example. The resulting seismogram, see Figure 32, is satisfactory for lower arrival times, say until 3.4 s. But there is evidently something wrong with the waves which arrive later. This discrepancy radically improves after applying cosine window $L = 1.5$ km in length, see Figure 33. Our opinion is that it is caused by diffracted waves produced by introducing the grid needed for the numerical calculation. More precisely, we claim that these spurious waves come from the intersection between the grid boundary perpendicular to the second coordinate axis and the interface. The next computation provides the proof.

The grid contains $666 \times 100 \times 3200$ gridpoints. The elastic parameters are discretized in the same grid. We apply the cosine window only in the direction of the second coordinate axis. We obtain Figure 34, which is similar to Figure 33. The agreement between the Born and ray-theory seismograms is even slightly better. On the other hand, almost 4.5 times as many gridpoints are used (though elastic parameters are not computed in the denser grid and averaged). Notice also Figure 35 where we shift the grid boundary perpendicular to the second coordinate axis, i.e. we have made the grid smaller in the direction of the second coordinate axis. The shift is equal to 0.2 km, i.e. approximately $\frac{\lambda}{4}$ as in similar previous situations. The first wave in the seismogram is unaffected, while the second wavegroup is shifted. The wavegroup is distorted, which means that the wavegroup is a superposition of two waves. One wave shifts and the other does not. The reflected wave is mixed with the numerically diffracted wave.

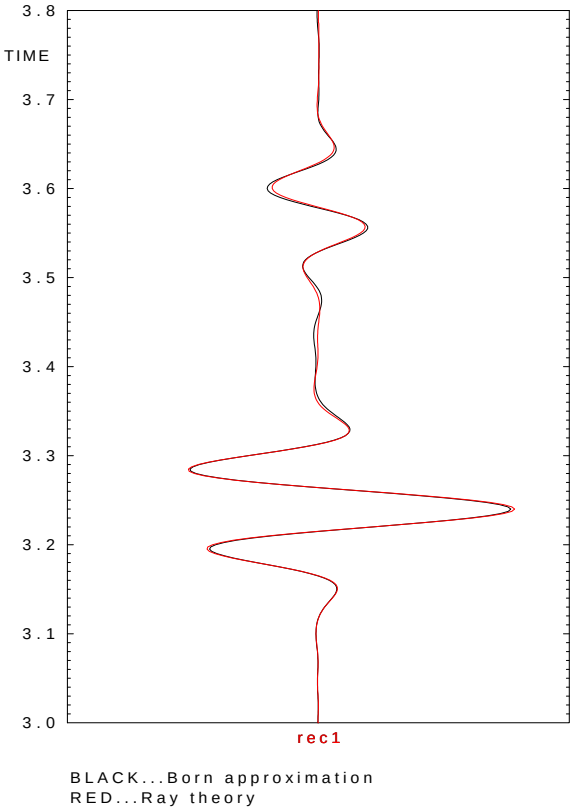

Figure 33: Model 3, grid $600 \times 100 \times 800$ gridpoints, averaged elastic parameters, cosine window 1.5 km in length applied to grid boundaries 1,2,3,4,6.

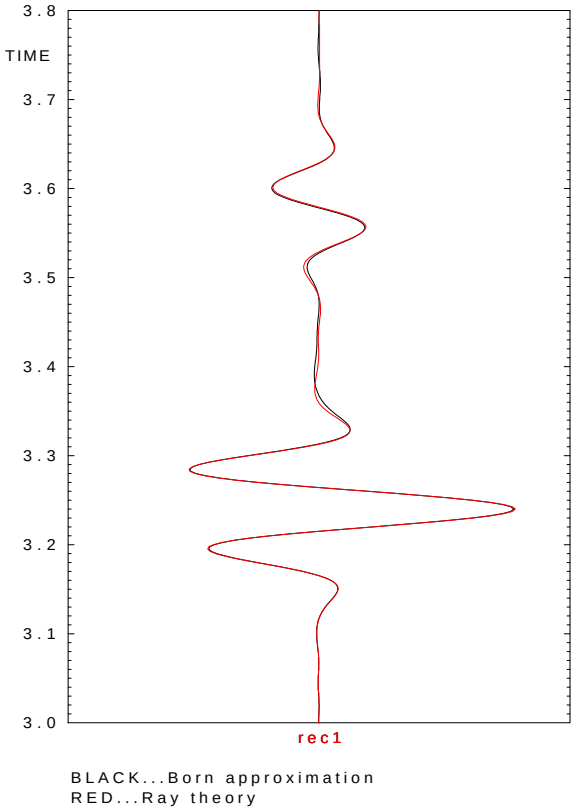

Figure 34: Model 3, grid $666 \times 100 \times 3200$ gridpoints, cosine window 1.5 km in length applied to grid boundaries 3,4.

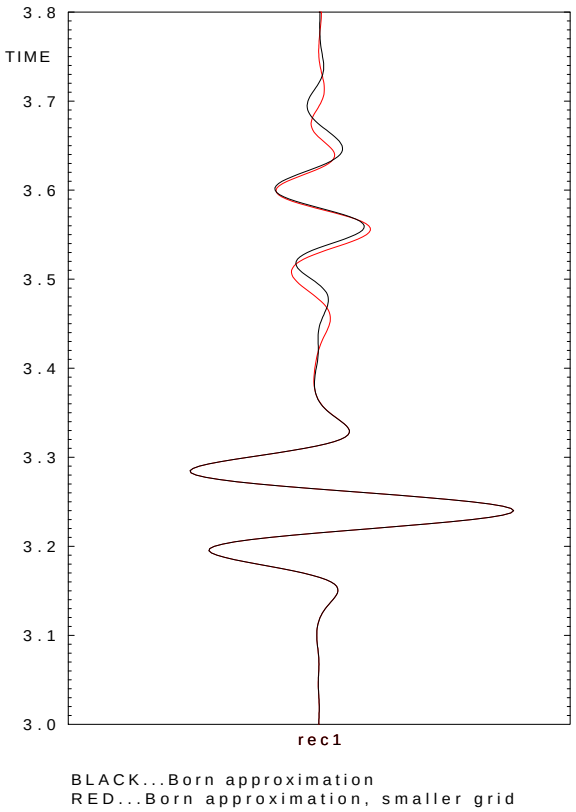

Figure 35: Model 3, grid $666 \times 100 \times 3200$ gridpoints vs grid $666 \times 96 \times 3200$ gridpoints.

5 Theory of 2D computations of 3D seismograms

If the source and receiver are situated in a symmetry plane of a 2D model, we can compute the Born approximation numerically in a 2D slice and perform the remaining one-dimensional integration in the direction perpendicular to the slice analytically (Červený & Coppoli, 1992). Of course, we do not know the values of the quantities present in the Born approximation there. We use paraxial approximation:

$$u_i(\mathbf{x}) = a_i(\mathbf{x}_0) \exp\left[i\omega\left(\tau_0 + \tau_{,i}\Delta x_i + \frac{1}{2}\tau_{,ij}\Delta x_i \Delta x_j\right)\right], \tag{26}$$

where $\mathbf{x}_0$ is a point in the slice, $\Delta\mathbf{x} = \mathbf{x} - \mathbf{x}_0$ and $\Delta\mathbf{x}$ is perpendicular to the slice, $\tau_0 = \tau(\mathbf{x}_0)$, $\tau_{,i} = \tau_{,i}(\mathbf{x}_0)$, $\tau_{,ij} = \tau_{,ij}(\mathbf{x}_0)$. Let us introduce the coordinate system in which all points in the slice have the second coordinate equal to zero. Then $\mathbf{x}_0 = (x_1, 0, x_3)$, $\Delta\mathbf{x} = (0, x_2, 0)$ and (26) takes the form

$$u_i(\mathbf{x}) = a_i(\mathbf{x}_0) \exp\left[i\omega\left(\tau_0 + \frac{1}{2}\tau_{,22}x_2^2\right)\right], \tag{27}$$

Notice that the first-order spatial derivative of travel time with respect to x_2 is not present, because it is equal to zero. The travel time is an even function of x_2. The derivative of an even function is an odd function and an odd function is zero for $x_2 = 0$. In fact, also the third-order spatial derivative of travel time with respect to x_2 is equal to zero, since the second-order spatial derivative of travel time with respect to x_2 is an even function. The spatial derivatives in the high-frequency approximation read

$$u_{i,j}(\mathbf{x}) = i\omega(\tau_{0,j} + \delta_{j2}\tau_{,22}x_2)a_i(\mathbf{x}_0) \exp\left[i\omega\left(\tau_0 + \frac{1}{2}\tau_{,22}x_2^2\right)\right], \tag{28}$$

where we have neglected $\frac{1}{2}\tau_{,22j}x_2^2 = \frac{1}{2}(\delta_{j1}\tau_{,221} + \delta_{j3}\tau_{,223})x_2^2$ (see the discussion following formula (43)). Similarly for the Green function:

$$G_{ij}(\mathbf{x}) = A_{ij}(\mathbf{x}_0) \exp\left[i\omega\left(T_0 + \frac{1}{2}T_{,22}x_2^2\right)\right], \tag{29}$$

$$G_{ij,k}(\mathbf{x}) = i\omega(T_{0,k} + \delta_{k2}T_{,22}x_2)A_{ij}(\mathbf{x}_0) \exp\left[i\omega\left(T_0 + \frac{1}{2}T_{,22}x_2^2\right)\right]. \tag{30}$$

Recall the Born approximation in an isotropic medium (2) and decompose it into three parts:

$$I_A = \omega^2 \int_\Omega \Delta\rho(\mathbf{x}')G_{mi}(\mathbf{x}', \mathbf{x}, \omega)u_m(\mathbf{x}', \omega)d^3\mathbf{x}', \tag{31}$$

$$I_B = \int_\Omega \Delta\lambda(\mathbf{x}')G_{ji,j}(\mathbf{x}', \mathbf{x}, \omega)u_{k,k}(\mathbf{x}', \omega)d^3\mathbf{x}', \tag{32}$$

$$I_C = \int_\Omega \Delta\mu(\mathbf{x}')G_{ki,j}(\mathbf{x}', \mathbf{x}, \omega)(u_{k,j}(\mathbf{x}', \omega) + u_{j,k}(\mathbf{x}', \omega))d^3\mathbf{x}'. \tag{33}$$

We insert (27) and (29) into the first part of Born approximation (31) with notation S for the slice and obtain:

$$I_1 = \omega^2 \int\limits_S \Delta\rho A_{ji} a_j \exp[i\omega(\tau_0 + T_0)] \left\{ \int\limits_{-\infty}^{\infty} \exp\left[i\frac{\omega}{2}(\tau_{,22} + T_{,22}) x_2^2 \right] dx_2 \right\} dx_1 dx_3, \tag{34}$$

The integral over slice S is calculated numerically; we focus on the integral in brackets. We call this integral I_{cor1}. We introduce a small imaginary part of the derivatives of the travel times and arrive at

$$I_{cor1} = \int\limits_{-\infty}^{\infty} \exp\left[i\left(\frac{\omega}{2}(\tau_{,22} + T_{,22}) + i\epsilon \right) x_2^2 \right] dx_2 = \int\limits_{-\infty}^{\infty} \exp\left[-(\epsilon - iA) x_2^2 \right] dx_2, \tag{35}$$

where $A = \frac{\omega}{2}(\tau_{,22} + T_{,22})$, $\epsilon > 0$, $\epsilon \ll 1$. We employ the expression for the integral of a complex Gaussian

$$\int\limits_{-\infty}^{\infty} \exp(-pt^2) dt = \sqrt{\frac{\pi}{p}}, \quad \forall p \in \mathbf{C} : Re(p) > 0 \tag{36}$$

to obtain

$$I_{cor1} = \sqrt{\frac{\pi}{\epsilon - iA}} \approx \sqrt{\frac{\pi}{-iA}} = \sqrt{\frac{2\pi}{A}} \frac{1}{1-i} = \sqrt{\frac{\pi}{\omega(\tau_{,22} + T_{,22})}} (1+i). \tag{37}$$

The second part of Born approximation (32) is more complicated due to spatial derivatives. Using (27), (28), (29) and (30)

$$I_2 = \int\limits_S \Delta\lambda A_{ji} P_{0j} a_k p_{0k} \exp[i\omega(\tau_0 + T_0)] \left\{ \int\limits_{-\infty}^{\infty} \exp\left[i\frac{\omega}{2}(\tau_{,22} + T_{,22}) x_2^2 \right] dx_2 \right\} dx_1 dx_3 \tag{38}$$

$$+ \int\limits_S \Delta\lambda A_{ji} P_{0j} a_2 \tau_{,22} \exp[i\omega(\tau_0 + T_0)] \left\{ \int\limits_{-\infty}^{\infty} x_2 \exp\left[i\frac{\omega}{2}(\tau_{,22} + T_{,22}) x_2^2 \right] dx_2 \right\} dx_1 dx_3 \tag{39}$$

$$+ \int\limits_S \Delta\lambda A_{2i} T_{,22} a_k p_{0k} \exp[i\omega(\tau_0 + T_0)] \left\{ \int\limits_{-\infty}^{\infty} x_2 \exp\left[i\frac{\omega}{2}(\tau_{,22} + T_{,22}) x_2^2 \right] dx_2 \right\} dx_1 dx_3 \tag{40}$$

$$+ \int\limits_S \Delta\lambda A_{2i} T_{,22} a_2 \tau_{,22} \exp[i\omega(\tau_0 + T_0)] \left\{ \int\limits_{-\infty}^{\infty} x_2^2 \exp\left[i\frac{\omega}{2}(\tau_{,22} + T_{,22}) x_2^2 \right] dx_2 \right\} dx_1 dx_3, \tag{41}$$

where $P_{0j} = T_{0,j}$ and $p_{0k} = \tau_{0,k}$. Integrals (39) and (40) are equal to zero because in the parentheses we integrate an odd function over a symmetrical interval. The integral in the

parentheses in (38) is equal to (37). To compute the integral in the parentheses in (41) we use formula

$$\int_{-\infty}^{\infty} t^{2k} \exp(-pt^2) dt = \frac{1.3 \ldots (2k-1)}{(2p)^k} \sqrt{\frac{\pi}{p}}, \quad \forall p \in \mathbf{C} : Re(p) > 0, \quad k = 1, 2, \ldots \tag{42}$$

and obtain

$$I_{cor2} \approx \frac{\sqrt{\pi}}{2(-iA)^{3/2}} = -\sqrt{\frac{\pi}{2A^3}} \frac{1}{1+i} = -\sqrt{\frac{\pi}{\omega^3(\tau_{,22} + T_{,22})^3}}(1-i). \tag{43}$$

Comparing (37) and (43) we see that

$$I_{cor2} \approx \frac{I_{cor1}}{\omega}, \tag{44}$$

therefore, in the high-frequency approximation we can neglect (41) and only (38) remains. In other words we can neglect corrections $\delta_{j2}\tau_{,22}x_2$ and $\delta_{k2}T_{,22}x_2$ in (28) and (30). Similarly using (42) it can be proved that it is possible to neglect terms $\frac{1}{2}\tau_{,22j}x_2^2$ and $\frac{1}{2}T_{,22j}x_2^2$, as we did in (28) and (30).

The third part of Born approximation (33) has a structure similar to the second part (32). Therefore, we can compute the Born approximation in the 2D grid in the same way as we did in the 3D grid, the only modification being the multiplication of the integrand in the Born integral by term I_{cor1}:

$$\begin{aligned} \Delta u_i(\mathbf{x}, \omega) = \int_S \sqrt{\frac{\pi}{\omega(\tau_{,22} + T_{,22})}}(1+i) \big[& \omega^2 \Delta\rho(\mathbf{x}') G_{mi}(\mathbf{x}', \mathbf{x}, \omega) u_m(\mathbf{x}', \omega) \\ & + \Delta\lambda(\mathbf{x}') G_{ji,j}(\mathbf{x}', \mathbf{x}, \omega) u_{k,k}(\mathbf{x}', \omega) \\ & + \Delta\mu(\mathbf{x}') G_{ki,j}(\mathbf{x}', \mathbf{x}, \omega)(u_{k,j}(\mathbf{x}', \omega) + u_{j,k}(\mathbf{x}', \omega)) \big] d^3\mathbf{x}'. \end{aligned} \tag{45}$$

6 Numerical examples of 2D computations of 3D seismograms

Models 1,2,3 are exactly the same as those used in the 3D computations of Section 4 and are described in Section 3, but the source and the receiver positions are different. We have moved the source and the receiver into the symmetry plane. Namely the explosive source is at point (1.5 km, 5 km, 1 km) and the receiver at point (8.5 km, 5 km, 0 km).

6.1 Model 1

Using the experience from the computations in the 3D version of Model 1, we start directly with the grid containing 100×400 gridpoints. The obtained seismogram displayed in Figure 36 shows good agreement with the reference solution. It is interesting to see how important correction (37) is. The seismogram in Figure 37 was computed without this correction. The magnification had to be 100 times smaller to visualize it.

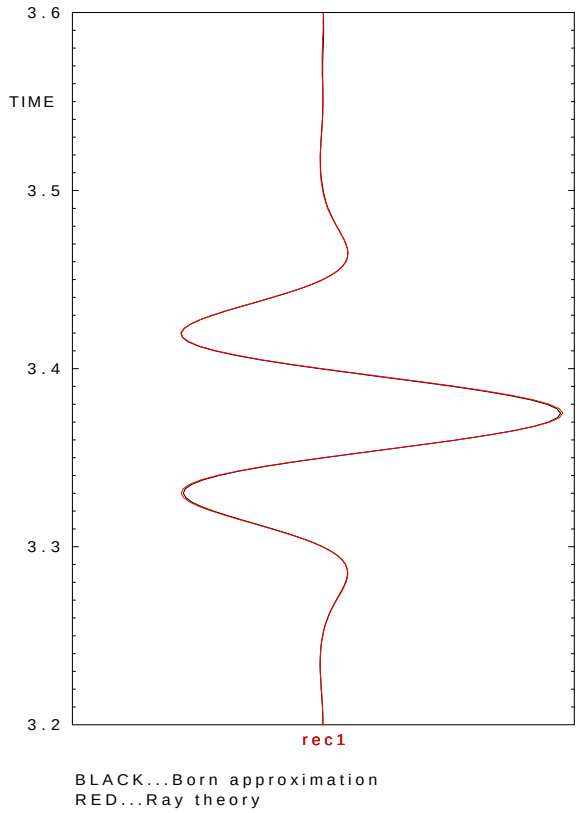

Figure 36: Model 1, 2D computation, grid 100×400 gridpoints.

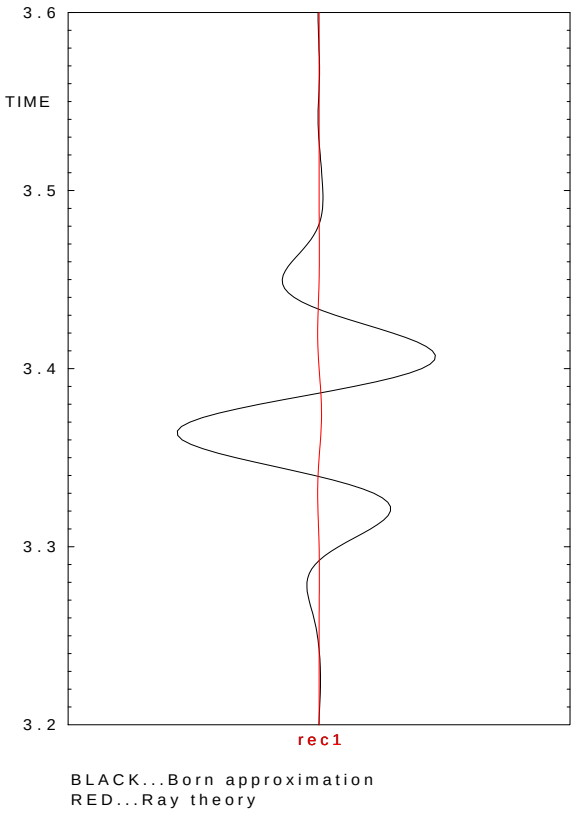

Figure 37: Model 1, 2D computation, grid 100×400 gridpoints, without correction (37), 100 times smaller magnification.

6.2 Model 2

According to the grid used in the computation of the seismogram in Figure 25, we firstly select a grid with 171×400 points. The resulting seismogram displayed in Figure 38 is slightly less accurate than the seismogram in Figure 25. For the denser grid with 343×800 points we get the excellent seismogram in Figure 39.

2D computations have undoubtedly one advantage compared to 3D computations. They are much faster. We used 100 times less points in Model 2. Therefore, one can easily experiment and get quick results. As an example, we try to shift the whole grid of 171×400 points downwards. The shift is smaller than $\frac{D_3}{2}$ but it is close to this value. Figure 40 shows the same seismograms as in Figure 38, but they are shifted against each other. That is correct. The interface is discretized between two gridpoint planes. We shift these planes downwards, so that the Born approximation shifts the interface downwards and the wave thus arrives later.

The second experiment shows what happens if the gridpoints lie exactly on the interface. This is obviously not a good choice, because one might expect seismogram shifts as in the previous experiment and in addition the rounding error can make the interface non-planar. The chosen grid covers the part of the model with vertical coordinate larger than 6 and it is quite dense, 375×875 gridpoints. Nevertheless, the seismogram in Figure 41 is much worse than the seismograms computed with more suitable grids.

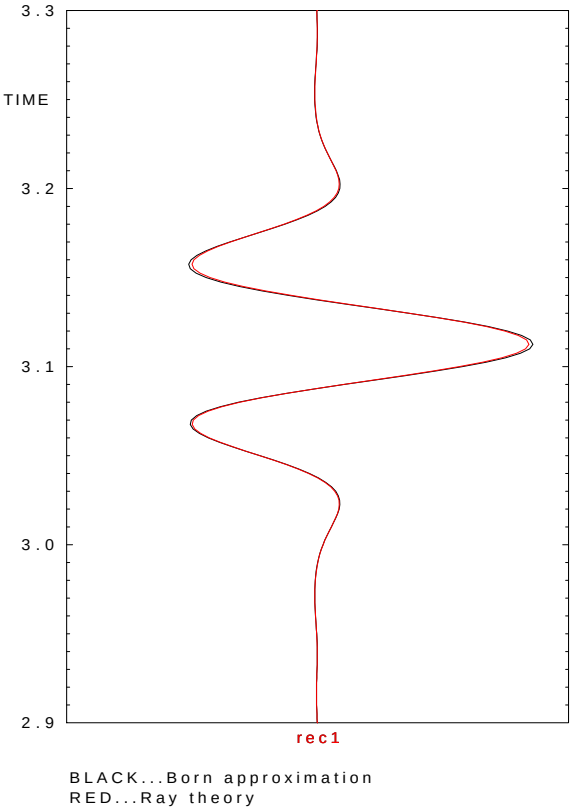

Figure 38: Model 2, 2D computation, grid 171 × 400 gridpoints.

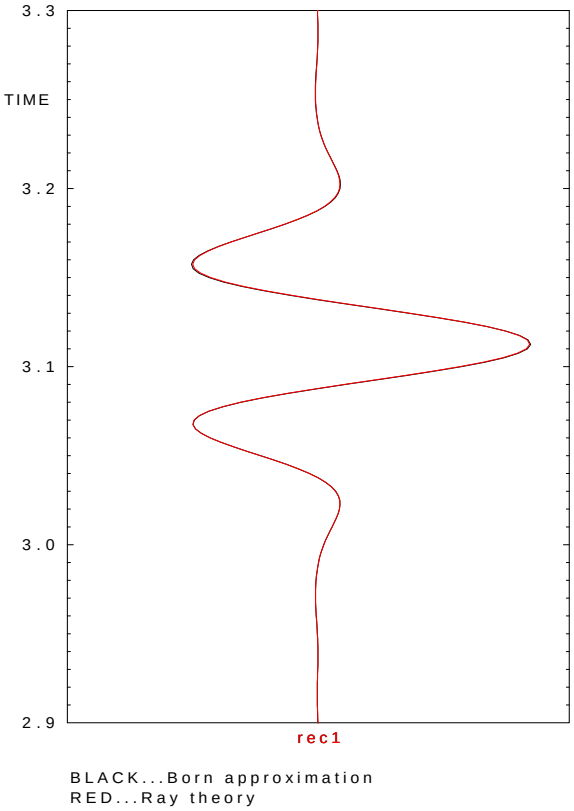

Figure 39: Model 2, 2D computation, grid 343 × 800 gridpoints.

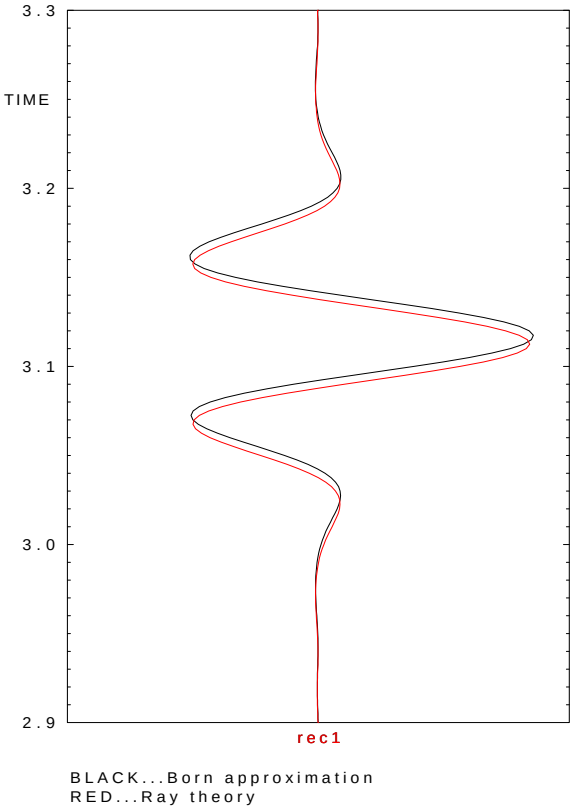

Figure 40: Model 2, 2D computation, grid 171 × 400 gridpoints, wrong discretization causes shift of the interface.

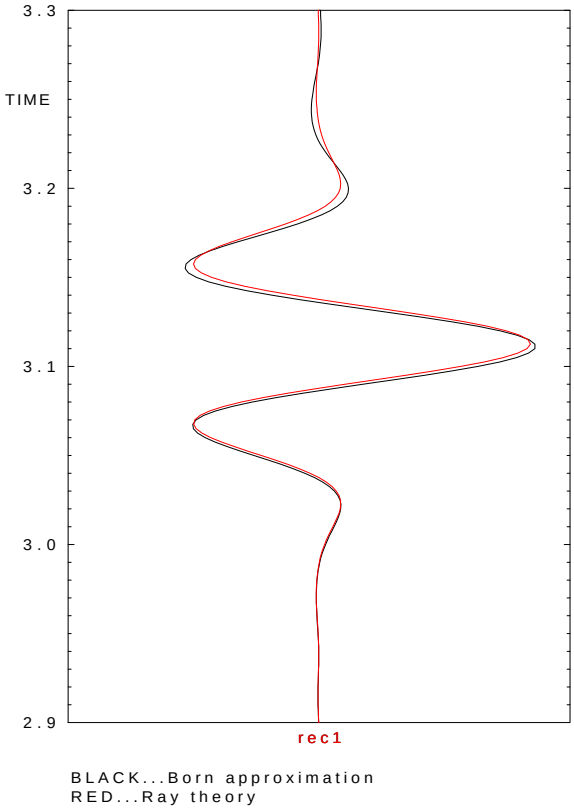

Figure 41: Model 2, 2D computation, grid 375 × 875 gridpoints, grid rectangles centred on the interface.

6.3 Model 3

Motivated by the computation of the seismogram in Figure 34 in Section 4.3, we choose a grid containing 600×3200 gridpoints. The calculated Born seismogram corresponds very well to the ray-theory seismogram, see Figure 42.

In the 2D computation, there is no grid boundary perpendicular to the second coordinate axis thanks to the numerical method used (analytical integration in the direction of the second coordinate axis). Remember that using an analogous grid in the 3D computation in Section 4.3, the Born and ray-theory seismograms did not agree until we applied cosine window $L = 1.5$ km in length in the direction of the second coordinate axis.

We shall also try a grid, which contains 600×800 gridpoints, see Figure 43. It is interesting that the first wave is already well resolved using this grid, while there are apparent wrong oscillations in the second wave.

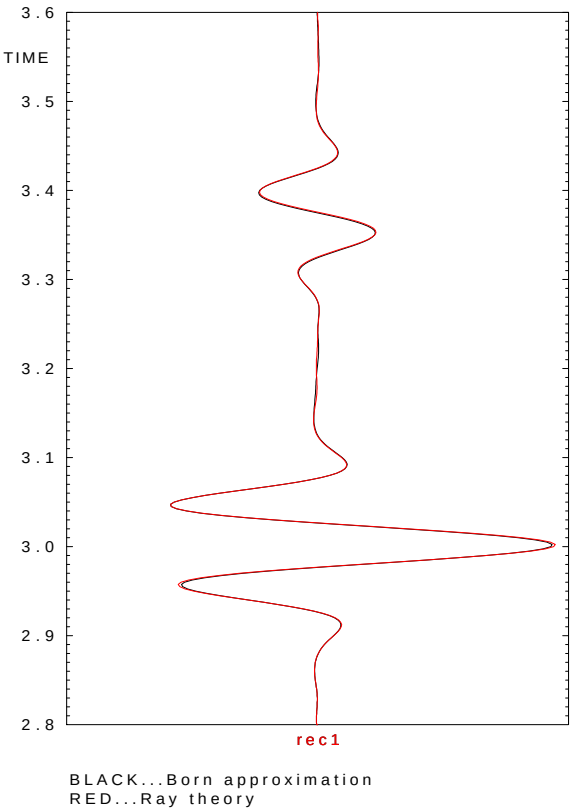

Figure 42: Model 3, 2D computation, grid 600×3200 gridpoints.

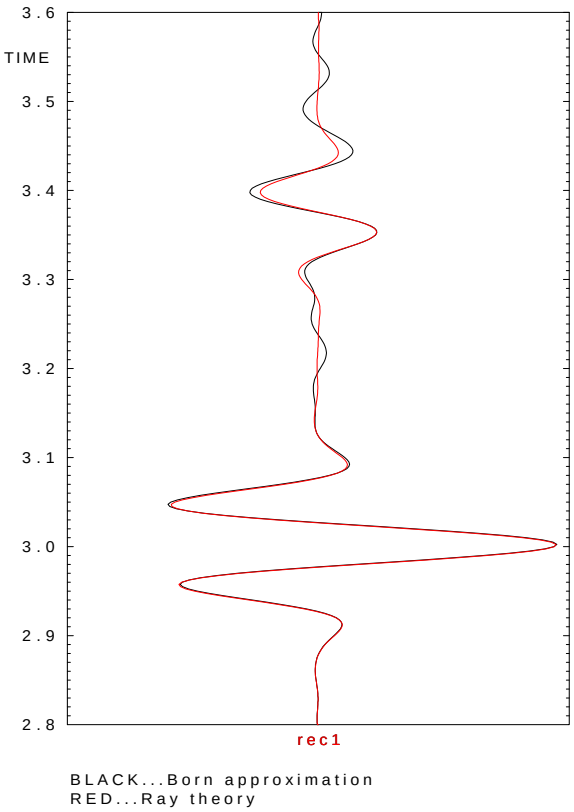

Figure 43: Model 3, 2D computation, grid 600×800 gridpoints.

7 Concluding remarks

We have tested the ray-based first-order Born approximation in homogenous background models. If the Born integral (2) is evaluated numerically using a computational grid, we should expect spurious waves to be introduced by the finite size of the grid. These waves are either reflections or diffractions from the grid boundaries. This effect was observed and suppressed by applying the cosine window of the appropriate length to the integrand of the Born integral, see Sections 4.1.2, 4.2.2 and 4.3. The effect of the cosine window on the spurious wave reflected from the grid boundary depends on the angle of incidence considerably. If the angle of incidence is large, application of the cosine window is problematic. This phenomenon was numerically observed and theoretically described in formula (19). Another possibility how to get rid of these spurious waves is to enlarge the computational volume, which is a safe but computationally expensive method. The discretization of the Born integral also introduces errors in the amplitude of the wave. Formulas (11) and (12) describe this effect.

The Born approximation is suitable for small differences in the elastic parameters between the perturbed and background model. In Model 1, see Section 3, we touched on the problem of growing perturbations. The elastic parameters in the background were $v_p =$ 6 km/s, $v_s = 3$ km/s and $\rho = 2000$ kg/m^3. If the perturbations of all elastic parameters were equal to (20) the seismogram was modelled correctly. For perturbations equal to (21) discrepancies were observed and they grew and became significant for perturbations equal to (22).

If the interface is shifted due to wrong discretization, the seismogram is shifted in time, see Figure 40.

We derived the form of the Born approximation usable if the source and receiver are situated in a symmetry plane of a 2D model. The integral is two-dimensional in the resulting formula (45). The formula works with 3D amplitudes of the incident wavefield and of the Green function. The formula was numerically tested in Sections 6.1, 6.2 and 6.3 with very good results.

Acknowledgements

First of all I would like to thank Luděk Klimeš, who greatly helped me with the work which led to this paper. I would also like to thank Václav Bucha who helped me with the figures of the models in Section 3.

The research has been supported by the Grant Agency of the Czech Republic under contract P210/10/0736, by the Ministry of Education of the Czech Republic within research project MSM0021620860, and by members of the consortium "Seismic Waves in Complex 3-D Structures" (see "http://sw3d.cz").

References

Červený, V. (2001): *Seismic ray theory.* Cambridge Univ. Press., Cambridge.

Červený, V. & Coppoli, A. D. M. (1992): Ray-Born synthetic seismograms for complex structures containing scatterers. In: *Journal of seismic exploration*, **1**, pp. 191-206.

Šachl, L. (2011): 2D computations of 3D synthetic seismograms using the ray-based Born approximation in heterogenous background model P1. In: Seismic Waves in Complex 3–D Structures, Report 21, pp. 99-114, Dep. Geophys., Charles Univ., Prague.

2D computations of 3D synthetic seismograms using the ray-based Born approximation in heterogenous model P1

Libor Šachl

Charles University, Faculty of Mathematics and Physics, Department of Geophysics,
E-mail: sachl@karel.troja.mff.cuni.cz

Summary

The accuracy of the ray-based Born approximation of the first order is tested in a smooth 2D heterogenous background model P1. Only P waves are considered. 3D synthetic seismograms are numerically calculated using the Born approximation in a 2D grid and are compared with the ray-theory seismograms. The Born seismograms contain reflected and diffracted waves. The individual reflected and diffracted waves are identified.

Key words: Born approximation, ray theory, velocity model, perturbation

1 Introduction

The Born approximation is a method which allows us to use quantities computed using the method of our choice, here the ray theory, in a simple background velocity model for calculating seismograms in a more complex velocity model. Let us call the more complex model perturbed. The requirement is that the background and perturbed models are "close" to each other.

This study was motivated by the synthetic seismogram computations of Bulant & Martakis (2011) in the 2D heterogenous model P1I, see Section 2, using the ray theory. We wished to compute the Born seismograms in this model and compare them with Bulant's & Martakis's (2011) results. We used smooth 2D background model P1. We performed the computations, but, unfortunately, the seismograms were very different and we were unable to explain the results. Therefore, we have simplified the model perturbations, and studied the differences between the Born and ray-theory seismograms. We have calculated the 3D wavefield using the 2D Born integral according to Červený & Coppoli (1992) and Šachl (2011, eq.45)

Seismic Waves in Complex 3-D Structures, Report 21, Charles University, Faculty of Mathematics and Physics, Department of Geophysics, Praha 2011, pp. 99-114

2 Models

2.1 Background model and model perturbations

Model P1 was created by Bulant & Martakis (2011). It is a 2D velocity model situated in a rectangle (0 km, 47.3 km) × (0 km, 6 km). The model has two versions. The smooth version of the model should be suitable for ray-theory computations. In our computations it serves as an background model for the ray-based Born approximation. We use the second version, model P1I, as our inspiration for the construction of simple perturbed models.

P-wave velocity v_p in smooth model P1 is depicted in Figure 1. The S-wave velocity $v_s = \frac{v_p}{\sqrt{3}}$. The density $\rho = 1000$ kg/m^3 everywhere. Figure 1 of the P-wave velocities is created using a grid which contains 4730×600 grid points. The largest value of the discretized P-wave velocities is $(v_p)_{max} \approx 5.93$ km/s.

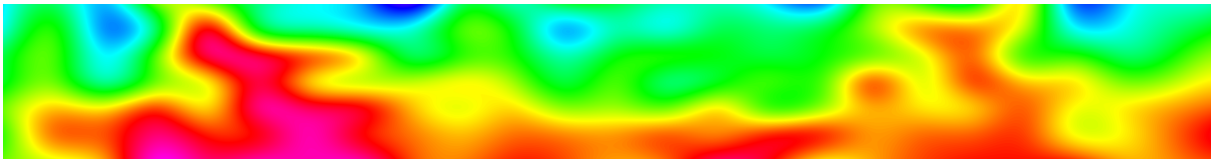

Figure 1: P-wave velocity in smooth model P1. The colour changes from blue to green and red as the P-wave velocity grows.

Model P1I is quite complicated because it is composed of 16 blocks and 13 surfaces, which form 15 interfaces where reflected waves may be generated. The blocks in model P1I are displayed in Figure 2. The colours are determined by the index of the block.

Figure 2: Blocks in model P1I. The colour of the block is determined by its index. The colour changes from green to red and blue. Block 1 is the leftmost green block.

The largest absolute value of the discretized P-wave perturbations is $|\Delta v_p|_{max} \approx 0.21$ km/s. See Figure 3 for the spatial distribution of the P-wave velocity perturbation and of the absolute value of the perturbation. The perturbation of the S-wave velocity is not depicted, because in the models, which we have constructed from model P1I, we have set $v_s = \frac{v_p}{\sqrt{3}}$ analogously to the background model.

2.2 Model P1-9-homo

This is the first of the 4 perturbed velocity models we have constructed. The density is the same as in smooth model P1 and equal to $\rho = 1000$ kg/m^3 everywhere. The S-wave

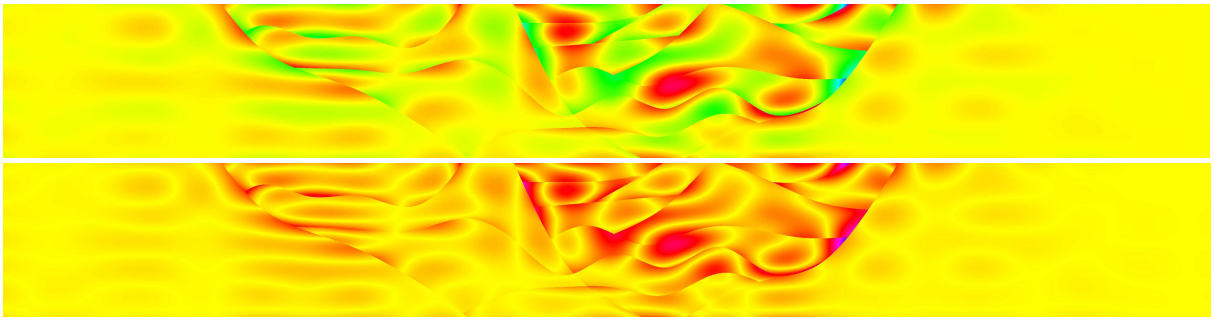

Figure 3: P-wave velocity perturbation in model P1; upper: without absolute value, lower: with absolute value. The extent of values corresponding to the whole colour circle RGB is set to 0.44 km/s. Positive perturbations are red, negative perturbations are green. Zero perturbations are drawn yellow.

velocity is related to the P-wave velocity by expression $v_s = \frac{v_p}{\sqrt{3}}$. The P-wave velocity is the same as in smooth model P1 except for the domain which corresponds to block 9 of model P1I. Block 9 is displayed in Figure 4. The distribution of the P-wave velocity in this domain is created by adding the homogenous perturbations of P-wave velocity $\Delta v_p = 0.01$ km/s to the smooth version of model P1.

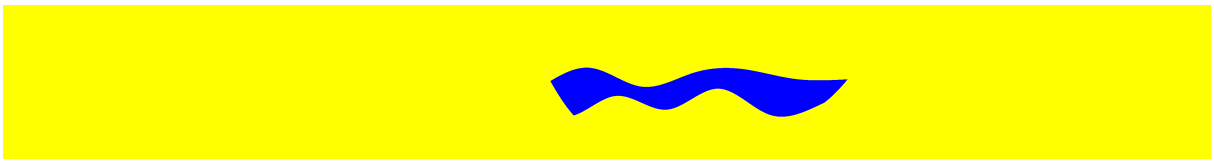

Figure 4: Block 9 in model P1I.

The P-wave velocity in the background model is specified on the bicubic-spline grid containing 24×7 points (from 0 km to 46 km steps of 2 km in the x_1 direction and from 0 km to 6 km in steps of 1 km in the x_3 direction); the values at the other points are determined by interpolation. If the grid were smaller, the values of the P-wave velocities would be different even at the interior points. In view of sidetracking this behaviour, we specified the P-wave velocity in block 9 in the same grid of 24×7 points.

2.3 Model P1-9-10%

Everything which we wrote about model P1-9-homo applies to model P1-9-10% except for the P-wave velocity in block 9. The distribution of the P-wave velocity in this domain is constructed as a linear combination of the distribution in smooth model P1 and model P1I:

$$v_p = 0.9(v_p)_{background} + 0.1(v_p)_{perturbed}. \tag{1}$$

2.4 Model P1-8-10%

This model is similar to model P1-9-10%, but perturbation (1) of the P-wave velocity is applied to block 8 rather than block 9. Block 8 is depicted in Figure 5.

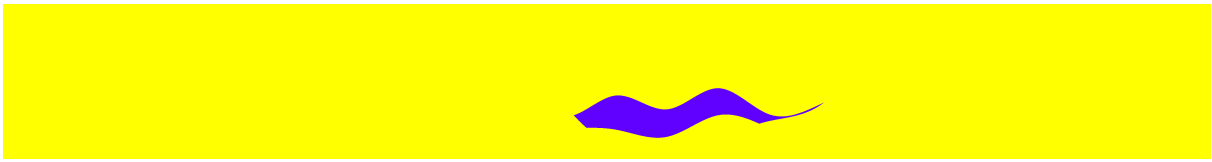

Figure 5: Block 8 in model P1I.

2.5 Model P1-8&9-10%

In this velocity model, P-wave velocity perturbation (1) is applied to both blocks 8 and 9.

3 2D computations of 3D seismograms

In all numerical examples we compute the ray-theory seismograms using once reflected P waves and compare them with the seismograms computed using the ray-based Born approximation of the first order. Only P waves are considered. The receiver is at point $(16\text{ km}, 0\text{ km}, 0\text{ km})$, the source is at point $(25\text{ km}, 0\text{ km}, 0\text{ km})$.

3.1 Shooting rays

First of all, it was necessary to decide how to shoot the rays. Bulant & Martakis (2011) shot rays in the angular interval $\langle -1.4, 1.4\rangle$ radians, where zero corresponds to a ray shot downwards, $-\frac{\pi}{2}$ to a ray shot horizontally to the left and $\frac{\pi}{2}$ to a ray shot horizontally to the right. They thus did not shoot rays into the whole lower half-plane. The reason is that otherwise they would calculate the direct wave as well, although they were interested in the once reflected waves only. In using the Born approximation, we shoot rays in the background medium, thus producing only direct waves, and we wish to cover the domain where the perturbations of the elastic parameters are nonzero with ray tubes. Shooting rays in the angular interval $\langle -1.4, 1.4\rangle$ radians is suitable, because the perturbations are present only in block 8 and block 9 in these computations.

The ray tubes cannot be "too wide", because the quantities in the specified grid are calculated by interpolation between them. Bulant & Martakis (2011) covered the angle, into which they shot the rays, by 11 rays. This basic system of rays is sufficient for two-point ray tracing, but probably insufficient for controlled initial-value ray tracing, which we are interested in. We have tried basic systems of rays composed of 11, 21, 46, 91, 121 rays for the rays shot from the position of the source. We have tried basic systems of rays composed of 11, 21, 46, 91, 121 rays for the rays shot from the position of the receiver. We propose to use interval $\langle -1.4, 1.4\rangle$ radians and 91 basic rays in shooting from the position of the source, see Figures 6 and 7. We propose to use interval $\langle -1.4, 1.4\rangle$ radians and 91 basic rays in shooting from the position of the receiver, see Figures 8 and 9.

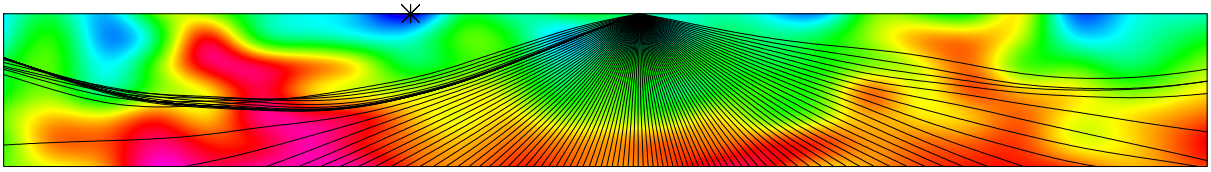

Figure 6: Coverage of smooth model P1 with the rays in shooting from the position of the source. The rays are depicted together with the P-wave velocity.

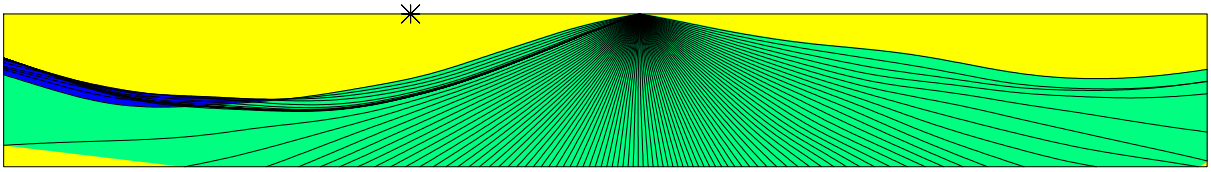

Figure 7: Coverage of smooth model P1 with the rays in shooting from the position of the source. The rays are depicted together with the number of arrivals.

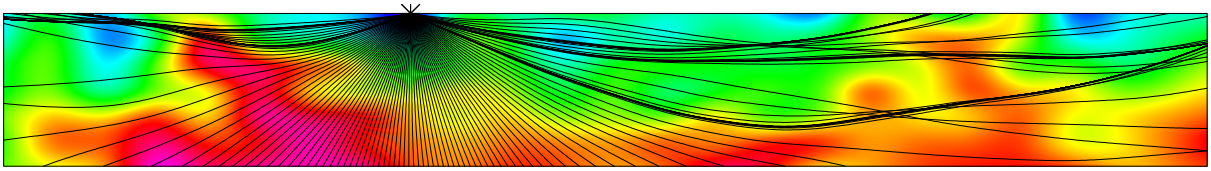

Figure 8: Coverage of smooth model P1 with the rays in shooting from the position of the receiver. The rays are depicted together with the P-wave velocity.

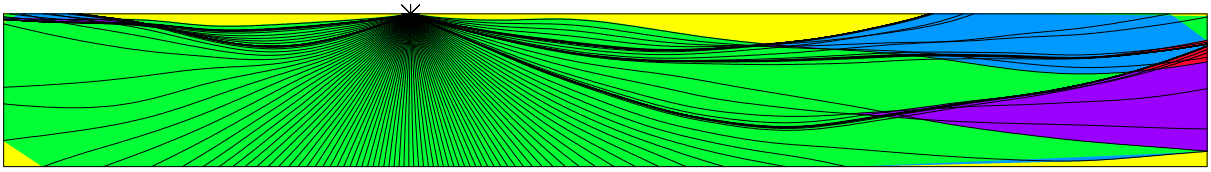

Figure 9: Coverage of smooth model P1 with the rays in shooting from the position of the receiver. The rays are depicted together with the number of arrivals.

3.2 Model P1-9-homo

In the SW3D programs, the following specification of the grid is used: O_1, O_2, O_3 are the coordinates of the origin of the grid. N_1, N_2, N_3 are the numbers of gridpoints along the x_1, x_2, x_3 coordinate axes, and D_1, D_2, D_3 are the grid intervals in the directions of the x_1, x_2, x_3 coordinate axes. We use this notation also in this paper.

The minimum P-wave velocity at the grid points is equal to $(v_p)_{min} = 4.65235$ km/s (the maximum is $(v_p)_{max} = 5.91815$ km/s). In the 2D models, which we have used previously, see Šachl (2011), the grids used had the smallest value of the grid interval in vertical direction. The best values of the vertical grid interval were $D_3 = 0.025$ km in Model 1, $D_3 = 0.017489$ km in Model 2 and $D_3 = 0.00625$ km in Model 3. If we recalculate these values using $(v_p)_{min}$, we obtain values $D_3 = 0.019$ km, $D_3 = 0.014$ km

and $D_3 = 0.0048$ km, respectively. Therefore, we choose grid intervals $D_1 = 0.005$ km, $D_3 = 0.005$ km.

Note that a grid, which covers the whole model is too large for computing the Born approximation, because the perturbations are non-zero only in block 9. In the case of model P1-9-homo, we use a smaller grid, given by parameters $N_1 = 2500$, $D_1 = 0.005$ km, $O_1 = 21.0025$ km, $N_3 = 500$, $D_3 = 0.005$ km, $O_3 = 2.005$ km, which covers the part of the model displayed in Figure 10.

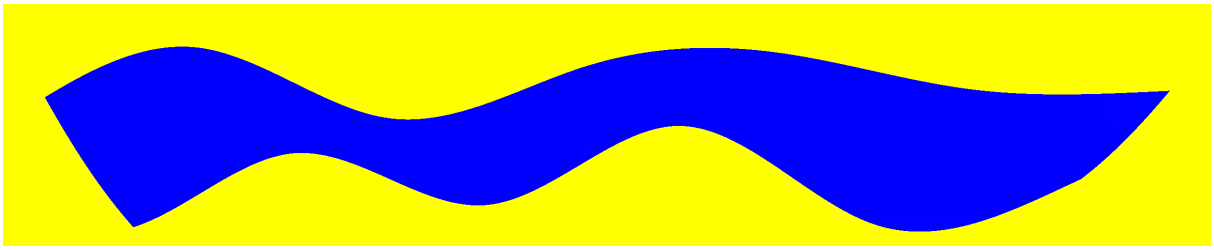

Figure 10: Small grid with 2500×500 points used in the computations with block 9 covers only the displayed part of model P-9-homo in Figure 13.

After applying all the discussed options and parameters, we calculate the seismogram displayed in Figure 11. The seismogram contains 2 reflected waves computed by the ray theory, as one can see from Figure 13. The ray reflected from the upper interface arrives first, at approximately 2.06 s. The ray reflected from the lower interface arrives, as one would expect, later, at approximately 2.93 s. The agreement between the Born and ray-theory seismograms is not bad, but there are some discrepancies and we are interested in the reasons for the difference. We thus subtract the ray-theory seismogram from the Born seismogram, see Figure 12. The abscissae in Figures 11 and 12 are travel times which correspond to the waves diffracted from 4 edges of block 9. The travel times of the individual diffracted waves are given in Table 1, where each diffracted wave is described by the edge, from which it is diffracted. In Figures 14, 15, 16 and 17, we see the isochrones

Edge	left upper	left lower	right upper	right lower
Travel time [s]	2.12	2.45	5.05	4.80

Table 1: The travel times of the waves diffracted from the edges of block 9

of the travel times which correspond to the travel times of these diffracted waves. We think that the major discrepancies can be explained by the absence of the diffracted waves in the ray-theory seismogram. Note that, to determine the travel time of the diffraction, we firstly make a rough guess of the position of the edge from Figure 2. The numbers of blocks in the dense rectangular grid centred at our guessed position are computed. The edge is determined using this grid, with a discretization error of the order of D_1. The position of the edge is entered into the computation of the isochrone with an accuracy of 2 decimal places.

If the P-wave perturbation is small and homogenous, we are able to compare both seismograms and we think that we know, more or less, what causes the differences. But in the original version of the P1 model, the perturbations are larger, see Section 2.1. It

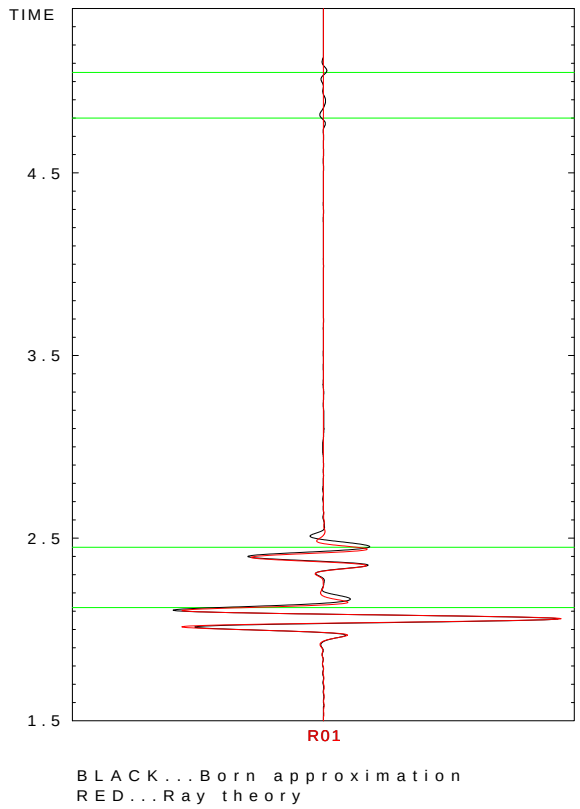

Figure 11: Model P1-9-homo, grid with grid intervals 0.005 km × 0.005 km.

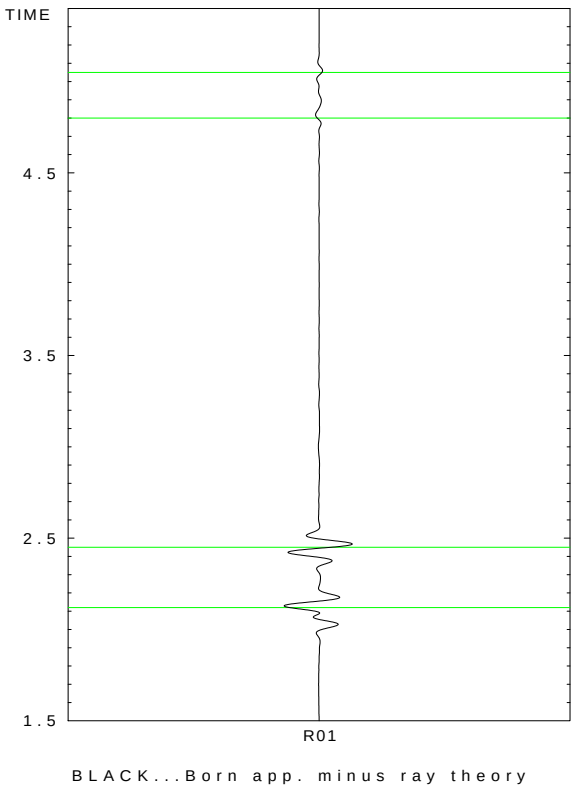

Figure 12: Model P1-9-homo, grid intervals 0.005 km × 0.005 km, the Born seismogram minus the ray-theory seismogram.

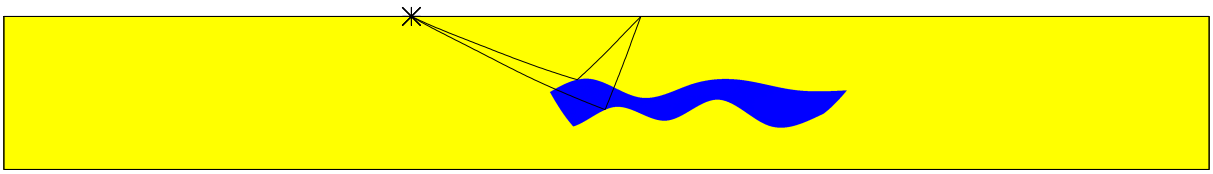

Figure 13: The reflected rays in model P1-9-homo.

is, therefore, necessary to acquire insight into how much perturbations can be increased without loss of accuracy. We tested the values of P-wave velocity perturbations 0.02 km/s, 0.04 km/s, 0.08 km/s, 0.1 km/s, 0.2 km/s and 0.3 km/s. The results are shown only for 0.02 km/s, 0.1 km/s, 0.2 km/s and 0.3 km/s, see Figures 18, 19, 20 and 21, where the time window is shortened in order to see the effect better. The figures are scaled with respect to the largest value in the ray-theory seismogram to compare them easily. In case of the first wave, reflected from the upper interface, the discrepancies in amplitude grow. In case of the second wave this happens too, but moreover we observe a time shift. The reason is that there are no perturbations of material parameters (except the interface itself) along the path of the first ray, whereas the perturbations in block 9 are present along the path of the second ray. We see that we cannot increase the perturbations too much. If we take the largest amplitude in absolute value in the seismogram computed using the Born approximation for P-wave velocity perturbations equal to 0.01 km/s and perform a linear prediction with respect to the perturbations, which matches the behaviour of the Born approximation, we obtain the blue curve in Figure 22. But the ray-theory result is slightly

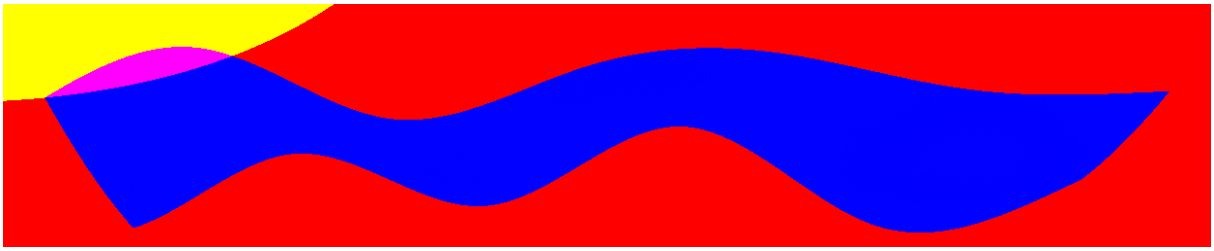

Figure 14: Isochrone of travel time 2.12 s in background model P1.

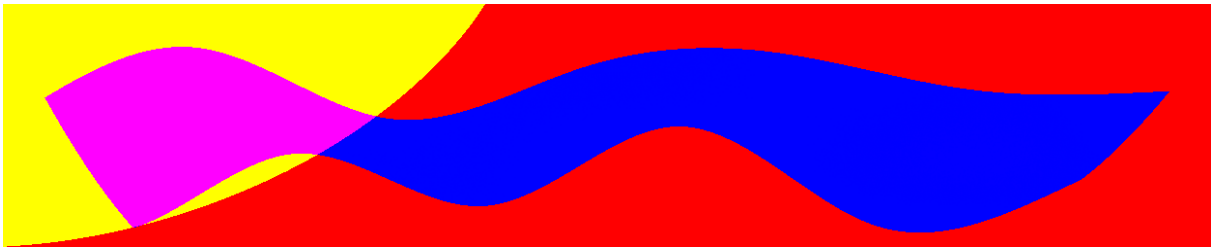

Figure 15: Isochrone of travel time 2.45 s in background model P1.

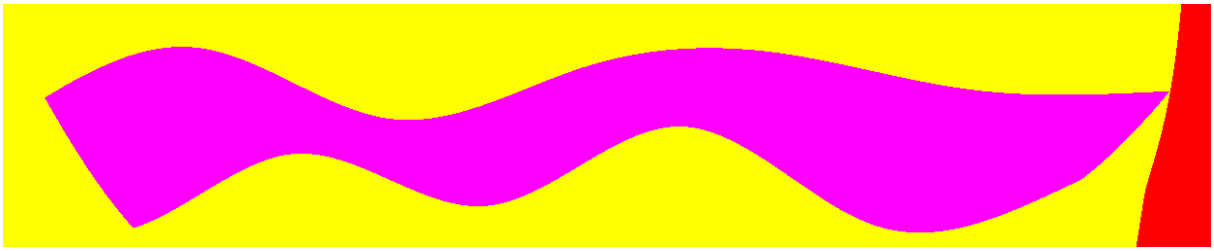

Figure 16: Isochrone of travel time 5.05 s in background model P1.

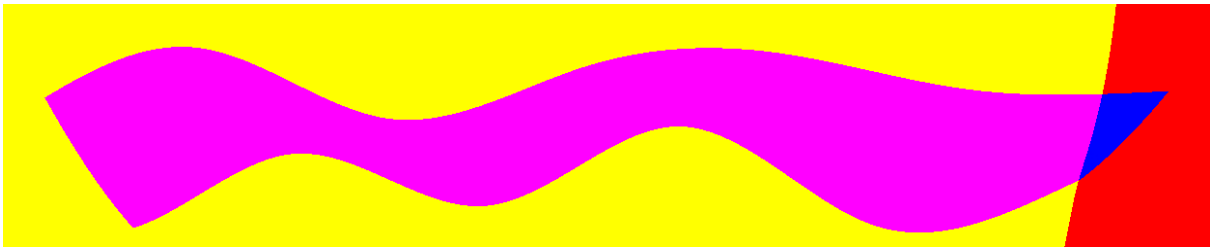

Figure 17: Isochrone of travel time 4.80 s in background model P1.

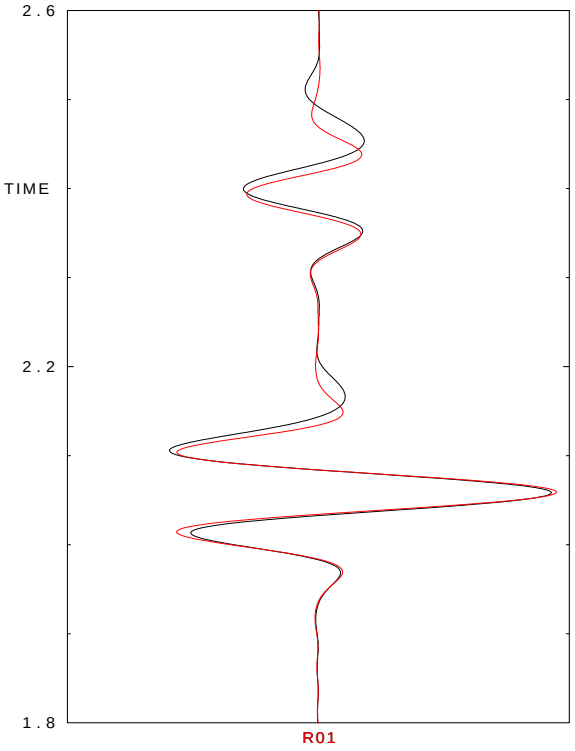

Figure 18: Model P1-9-homo, grid intervals 0.005 km × 0.005 km, $\Delta v_p = 0.02$ km/s

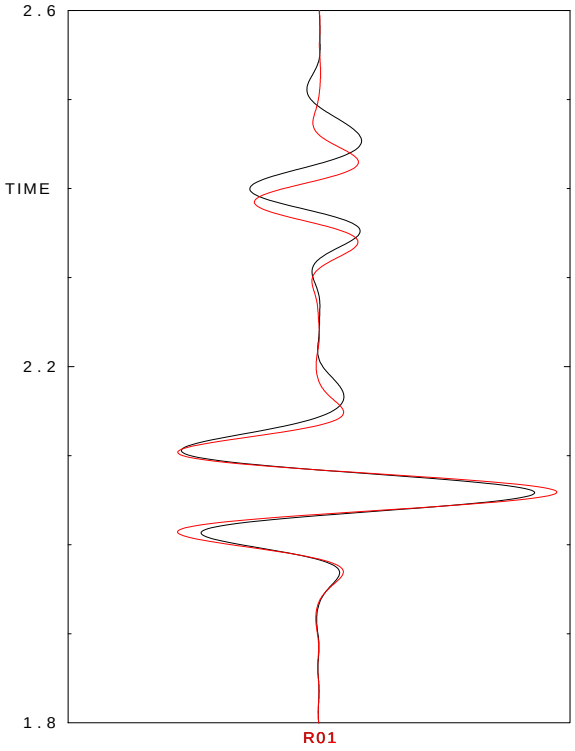

Figure 19: Model P1-9-homo, grid intervals 0.005 km × 0.005 km, $\Delta v_p = 0.1$ km/s

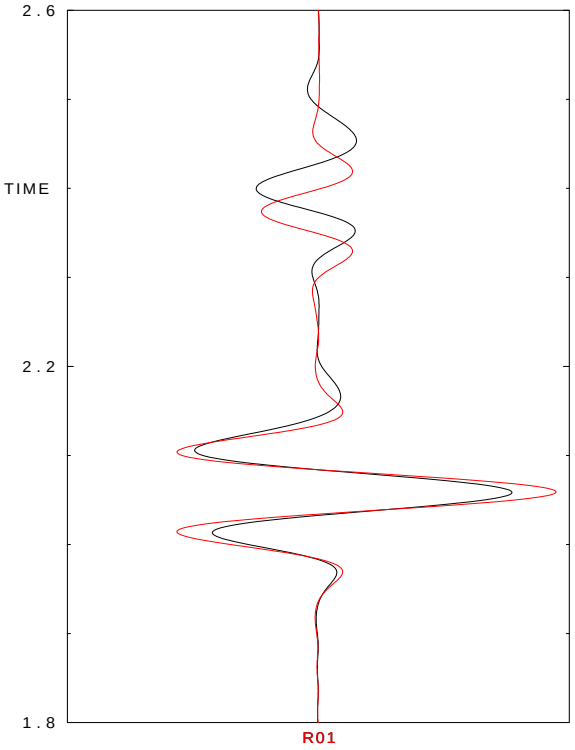

Figure 20: Model P1-9-homo, grid intervals 0.005 km × 0.005 km, $\Delta v_p = 0.2$ km/s

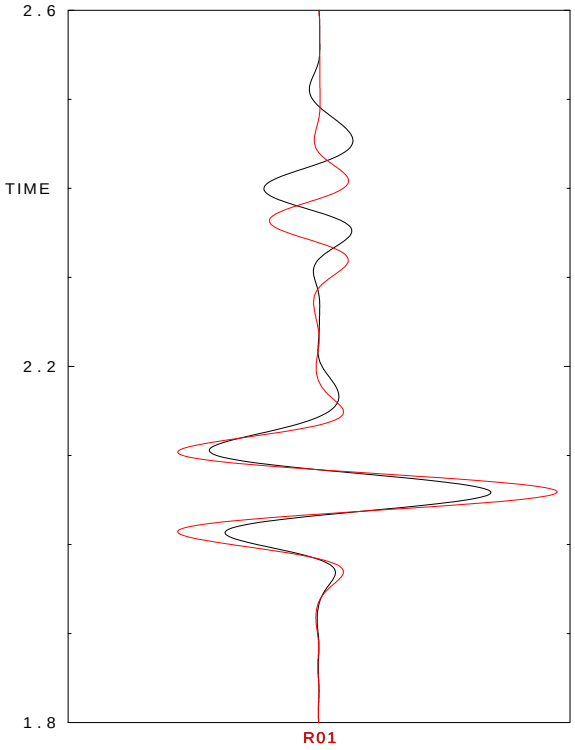

Figure 21: Model P1-9-homo, grid intervals 0.005 km × 0.005 km, $\Delta v_p = 0.3$ km/s

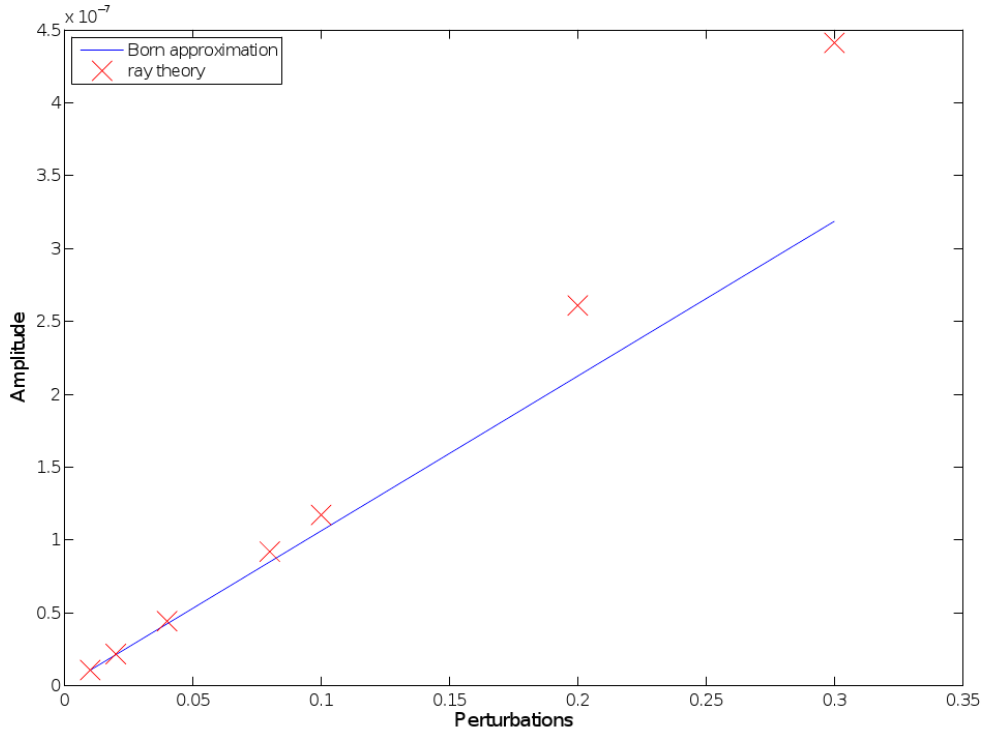

Figure 22: Maximum amplitudes in absolute values in the Born and ray-theory seismograms for growing perturbations.

different, see the red points. We conclude that this is the consequence of non-linearity of the reflection coefficient, because the largest value in the seismogram belongs to the reflection from the upper interface. In principle, we see its Taylor expansion with respect to the perturbations. Only the linear term is important for very small values, further the quadratic term plays the role and so on. Table 2 summarizes the relative amplitude difference ΔA between the ray-theory amplitude A_{rt} and the Born amplitude A_{Ba}. The formula for ΔA reads

$$\Delta A = \frac{A_{rt} - A_{Ba}}{A_{Ba}} 100\%. \tag{2}$$

Δv_p [km/s]	0.01	0.02	0.04	0.08	0.1	0.2	0.3
ΔA [%]	1.22	2.17	4.10	8.19	10.36	22.79	38.42

Table 2: The evolution of the relative amplitude difference ΔA with respect to the P-wave velocity perturbations.

3.3 Model P1-9-10%

Due to what was shown and said, we questioned the use of model P1I because the maximum measured perturbations were $|\Delta(v_p)|_{max} \approx 0.21$ km/s, and Figure 20 indicated some

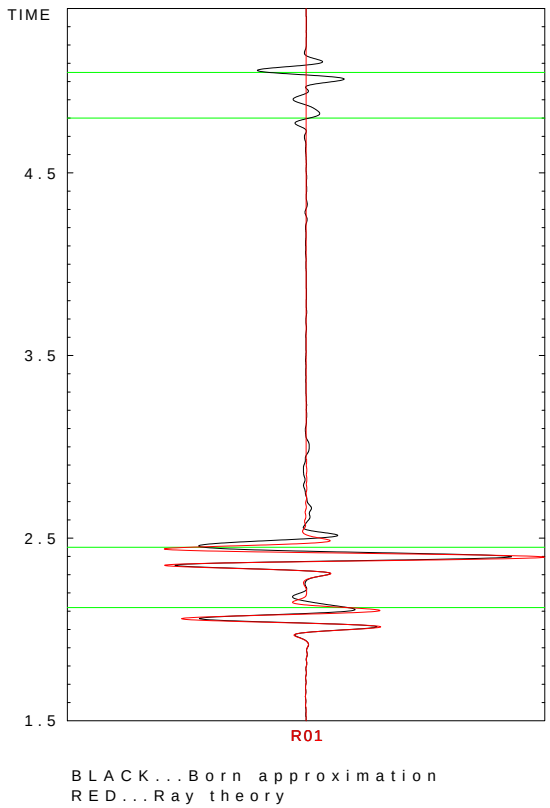

Figure 23: Model P1-9-10%, grid intervals 0.005 km × 0.005 km

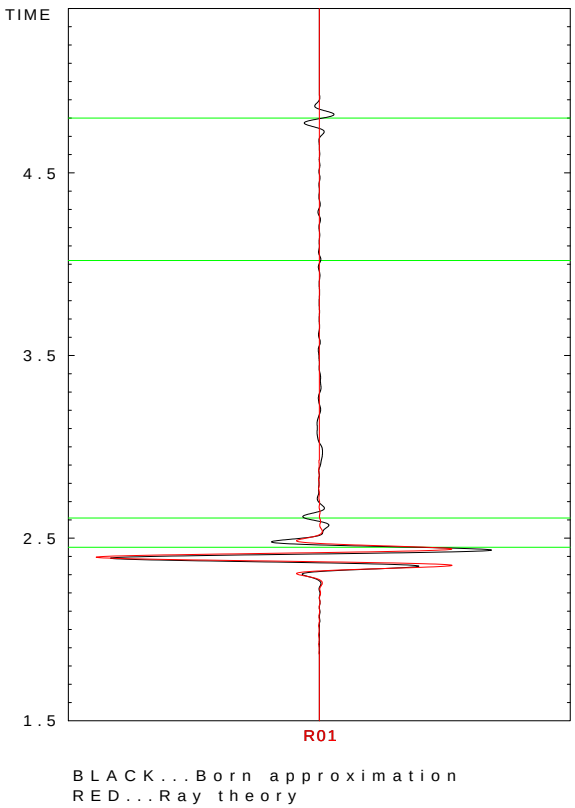

Figure 24: Model P1-8-10%, grid intervals 0.005 km × 0.005 km

problems. Therefore, we prepared a model with suitably low perturbations, see Sec. 2.3. The perturbations in this model are ten times smaller than in the original model P1I. With regard to Figure 18 this seems sufficient.

We obtained the seismograms displayed in Figure 23. The differences between the Born and ray-theory seismograms are larger in Figure 23 than with the homogenous perturbation displayed in Figure 11. Nevertheless, the drawn diffractions again play a role. We see that the differences between the seismograms appear in both wavegroups at later times.

3.4 Model P1-8-10%

The Born seismogram computed in this model is compared with the ray-theory seismogram in Figure 24. Similarly to the previous cases, the times of the diffracted waves are computed and marked. The travel times of the individual diffracted waves are given in Table 3. There is only one reflected wave, see Figure 25, but the displayed features are common with the previous example.

Edge	left upper	left lower	right upper	right lower
Travel time [s]	2.45	2.61	4.80	4.02

Table 3: The travel times of the waves diffracted from the edges of block 8

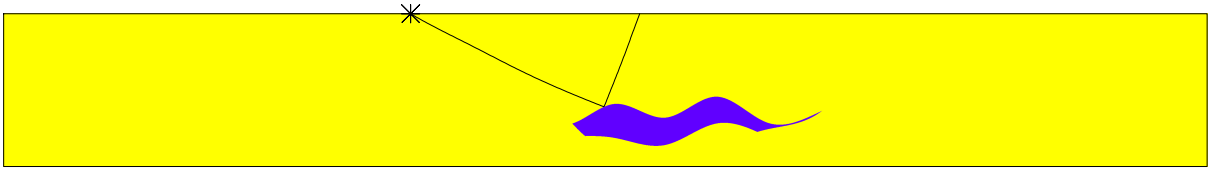

Figure 25: The reflected ray in model P1-8-10%

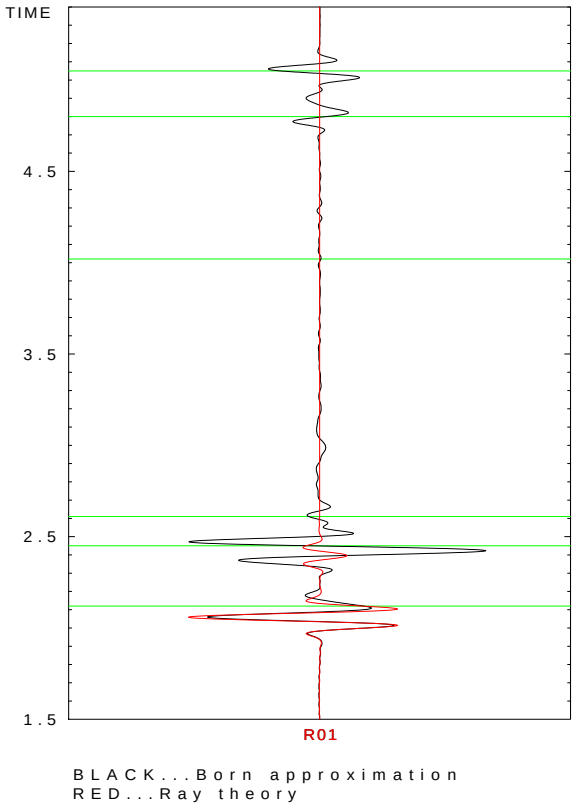

Figure 26: Model P1-8&9-10%, grid intervals 0.005 km × 0.005 km

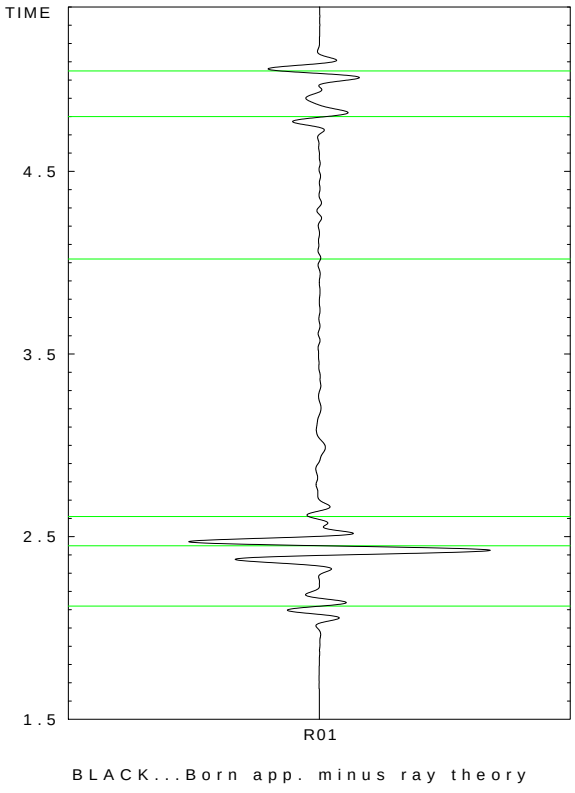

Figure 27: Model P1-8&9-10%, grid intervals 0.005 km × 0.005 km, the Born seismogram minus the ray-theory seismogram

3.5 Model P1-8&9-10%

In this computation, we applied the perturbations to both block 8 and block 9. The travel times of the individual diffracted waves are given in Table 4. Considering the separate

Edge	left upper	left middle	left lower	right upper	right middle	right lower
Travel time [s]	2.12	2.45	2.61	5.05	4.80	4.02

Table 4: The travel times of the waves diffracted from the edges of block 8 and block 9

computations in these blocks, we expect to obtain a seismogram similar to the ray-theory result. Figure 26 is, therefore, quite a surprise. There is a significant discrepancy in

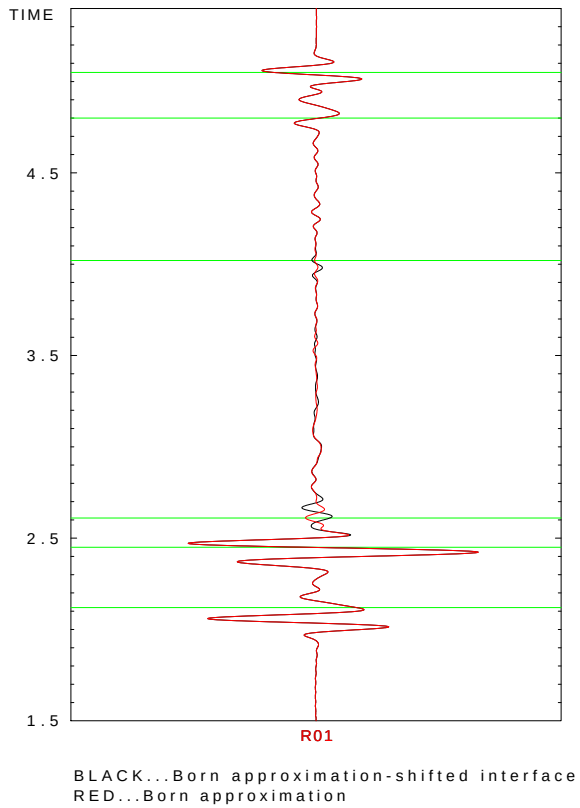

Figure 28: Model P1-8&9-10%, grid intervals 0.01 km × 0.01 km, $\frac{\lambda}{4}$ shift of the lower interface

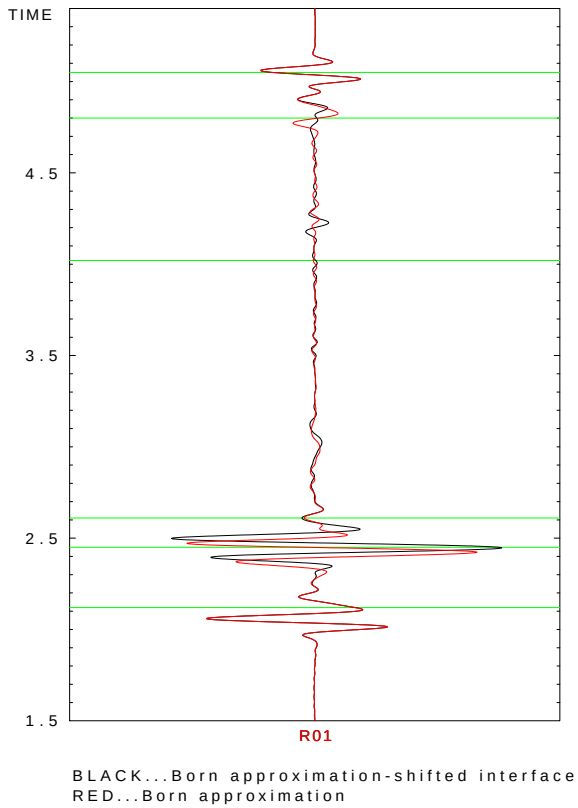

Figure 29: Model P1-8&9-10%, grid intervals 0.01 km × 0.01 km, $\frac{\lambda}{4}$ shift of the middle interface

the second wavegroup. To see the discrepancy precisely, we subtracted the ray-theory seismogram from the Born seismogram, see Figure 27. Now it appears that the difference is again caused by diffraction, but why is it so strong?

In order to get some hint, we tried to slightly ($\frac{\lambda}{4}$) shift each of 5 interfaces (4 outer and one between blocks). The left interface was shifted to the right, the right to the left and the lower, middle and upper interfaces downwards. These computations employ a coarser grid which covers the whole model volume with grid intervals $D_1 = D_2 = 0.01$ km. We want to study the shifts of the waves on the seismogram, and this should not interfere our conclusions. Let us observe Figures 28, 29, 30, 31 and 32. The first wavegroup marked by the abscissa at 2.12 s reacts to the shift of the upper interface, because it is the reflection from this interface. The first wavegroup is also sensitive to the shift of the left interface; we observe signal deformation. This sensitivity is caused by the diffracted wave superposed on the reflected wave. Similarly, the second wavegroup marked by the abscissa at 2.45 s is sensitive to the shift of the middle and left interface. The wave marked by the abscissa at 2.61 s is sensitive to the shift of the lower and left interface. The wave marked by the abscissa at 4.02 s is sensitive to the shift of the lower interface and it should be sensitive to the shift of the right interface, but this is not apparent. Two significant waves at the end of the seismogram are sensitive to the shift of the right interface. The wave marked by the abscissa at 4.80 s is sensitive to the shift of the middle interface. The wave marked by the abscissa at 5.05 s is sensitive to the shift of the upper interface.

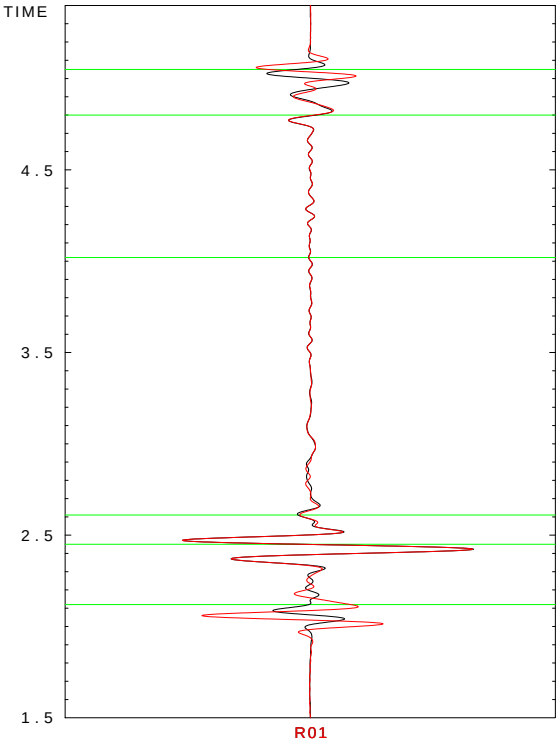

BLACK...Born approximation-shifted interface
RED...Born approximation

Figure 30: Model P1-8&9-10%, grid intervals 0.01 km $\times$ 0.01 km, $\frac{\lambda}{4}$ shift of the upper interface

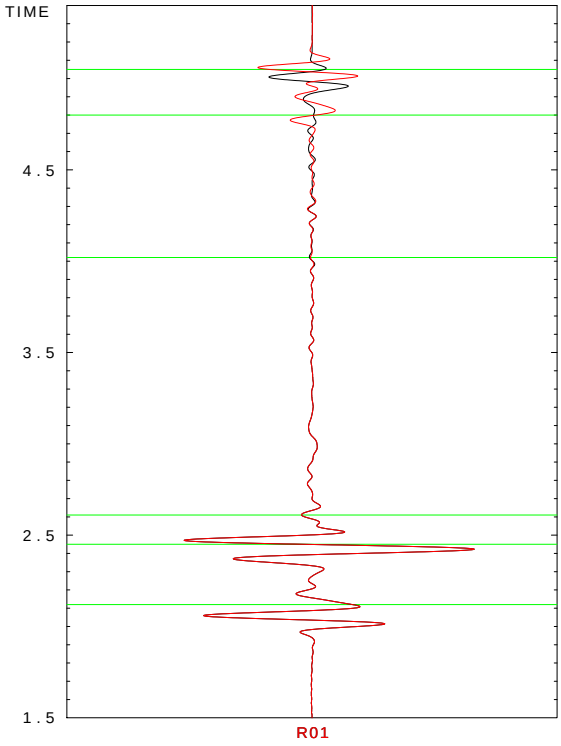

BLACK...Born approximation-shifted interface
RED...Born approximation

Figure 31: Model P1-8&9-10%, grid intervals 0.01 km $\times$ 0.01 km, $\frac{\lambda}{4}$ shift of the right interface

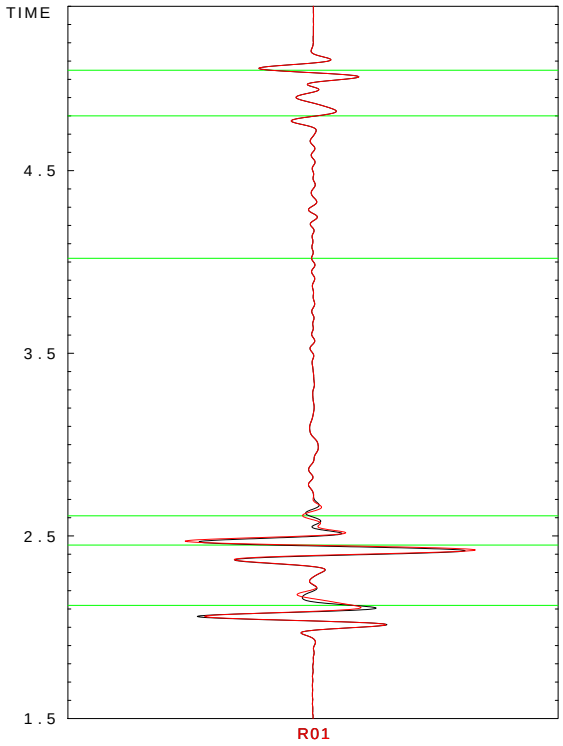

BLACK...Born approximation-shifted interface
RED...Born approximation

Figure 32: Model P1-8&9-10%, grid intervals 0.01 km $\times$ 0.01 km, $\frac{\lambda}{4}$ shift of the left interface

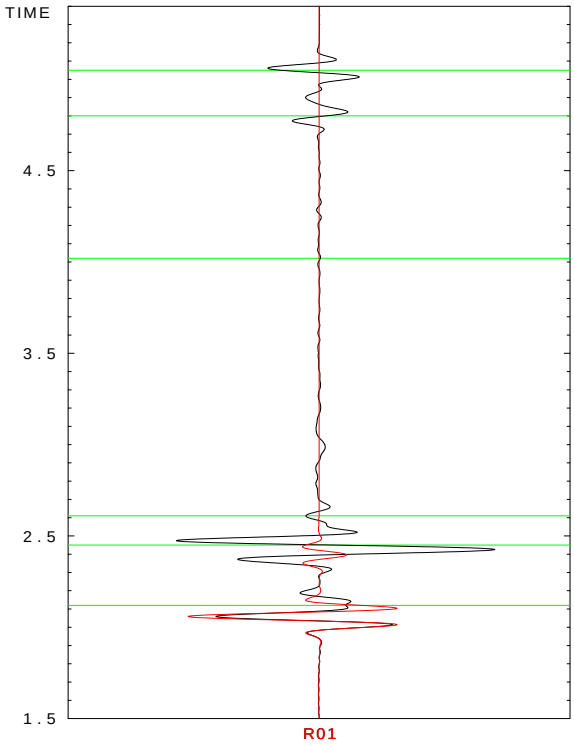

BLACK...Born approximation
RED...Ray theory

Figure 33: Model P1-8&9-10%, grid intervals 0.005 km $\times$ 0.005 km, shift of 0.1 km of the left interface to the left

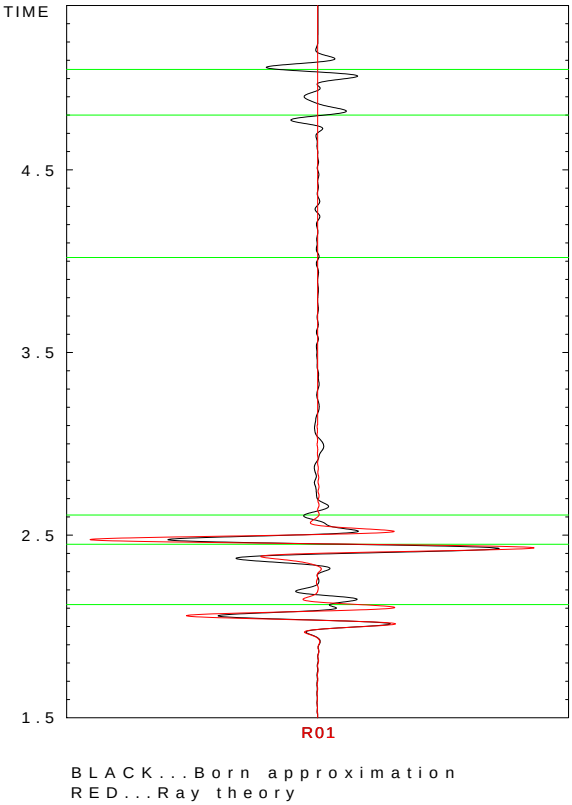

Figure 34: Model P1-8&9-10%, grid intervals 0.005 km × 0.005 km, shift of 0.15 km of the left interface to the left

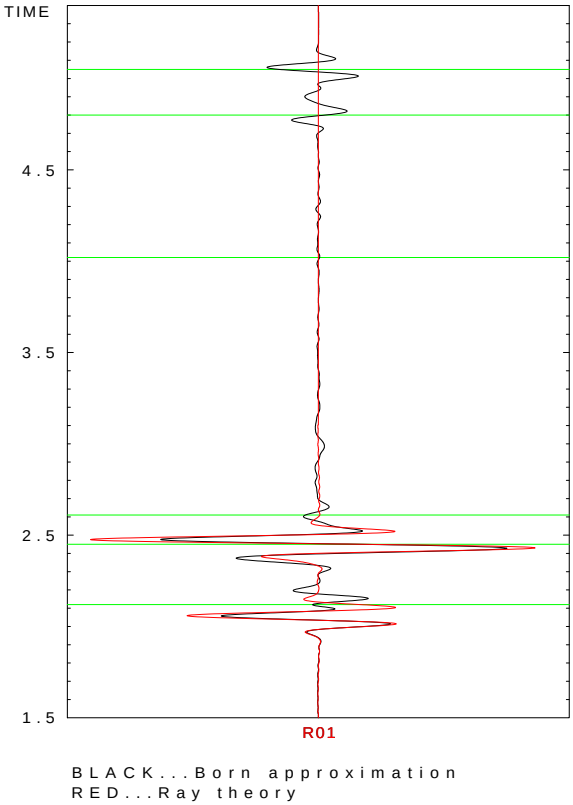

Figure 35: Model P1-8&9-10%, grid intervals 0.005 km × 0.005 km, shift of 0.2 km of the left interface to the left

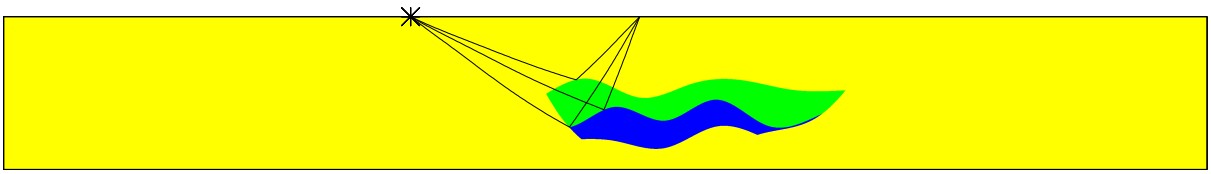

Figure 36: The reflected rays in model P1-8&9-10% with the left interface shifted by 0.15 km.

This motivated us to shift the left interface not only to the right, but also to the left by 0.1 km, 0.15 km and 0.2 km; the corresponding seismograms are displayed in Figures 33, 34 and 35. One thing is obvious. A very dramatic change of the ray-theory seismogram occurs if the shift is increased from 0.1 km to 0.15 km. Figure 36 demonstrates that a new reflected ray is generated. From the ray-theory point of view this change is immediate, but in the Born approximation this process is different. The diffraction contains the reflection and grows gradually. That is why the diffraction is so strong. In addition, we observe that the first wavegroup is really composed of 2 waves. Their separation is apparent and grows, because the reflected wave does not change its position, while the diffracted wave does.

4 Concluding remarks

In this paper we have compared the seismograms of once reflected waves computed by the ray theory with the seismograms obtained using the ray-based first-order Born approximation. Both the background and perturbed models are heterogenous and isotropic. We observed differences between the seismograms computed using the two methods mentioned. The differences are caused by several factors:

(a) The absence of the diffracted waves in the ray-theory seismograms.

(b) The Born approximation breaks down if the perturbations of the medium parameters are too large. One of the reasons is that the Born approximation is linear with respect to the medium perturbations, while the reflection coefficient is non-linear. Another is the time shift in the Born seismograms, because they are computed in the background medium.

(c) If a ray is reflected from an interface close to the edge of the interface, a next close ray need not be reflected and the reflected wave suddenly disappears from the ray-theory seismogram. In the Born seismogram, the wave diffracted at the edge provides a smooth transition from the reflected wave to the shadow.

Acknowledgements

First of all I would like to thank Luděk Klimeš, who greatly helped me with the work which led to this paper. I would also like to thank Petr Bulant because he provided me with model P1 and the history files, which he used for seismogram computation and visualization of the medium parameters. Hence, if I wanted to compute the reference seismogram or to visualize some quantities, I used parts of these history files (or the whole history files) and adjusted them as necessary.

The research has been supported by the Grant Agency of the Czech Republic under contract P210/10/0736, by the Ministry of Education of the Czech Republic within research project MSM0021620860, and by members of the consortium "Seismic Waves in Complex 3-D Structures" (see "http://sw3d.cz").

References

Bulant, P. & Martakis, N. (2011): Constructing model P1I for reflection studies. In: Seismic Waves in Complex 3–D Structures, Report 21, pp. 17-26, Dep. Geophys., Charles Univ., Prague.

Červený, V. & Coppoli, A. D. M. (1992): Ray-Born synthetic seismograms for complex structures containing scatterers. In: *Journal of seismic exploration*, **1**, pp. 191-206.

Šachl, L. (2011): 3D and 2D computations of 3D synthetic seismograms using the ray-based Born approximation in simple models. In: Seismic Waves in Complex 3–D Structures, Report 21, pp. 69-98, Dep. Geophys., Charles Univ., Prague.

Effect of caustics to the ray-based Born approximation

Libor Šachl

Charles University, Faculty of Mathematics and Physics, Department of Geophysics,
E-mail: sachl@karel.troja.mff.cuni.cz

Summary

The seismograms in several 2D isotropic heterogenous models are computed using the first-order ray-based Born approximation and the ray theory. Only P waves are considered. The seismograms are computed for the total number of 37 receivers. The weird wavegroups are observed in the Born seismograms. The explanation that these problems are caused by caustics on the direct wave is presented. Possible solutions are suggested. Seismograms corrected using one of these solutions are shown. Furthermore, particular wavegroups present in the Born seismograms and missing in the ray-theory seismograms are discussed.

Key words: Born approximation, ray theory, velocity model, caustic

1 Introduction

Common approaches to calculate synthetic seismograms in complex structures are either methods based on direct numerical solution of the elastodynamic equation or approximate high-frequency methods using asymptotic solutions of the elastodynamic equation. The first group represents finite-difference or finite-element methods. The most important representative of the second group is the ray method which is based on the asymptotic ray theory. The ray method has several important advantages when compared with e.g. finite differences: Large models and high frequencies do not represent any problem, the wavefield is separated into individual types of waves and so on. On the other hand there are also disadvantages: The models must be smooth (not changing rapidly with respect to the wavelength), the wavefield does not contain several types of waves (e.g. diffracted waves) and it fails in the singular regions (shadow zones, caustics etc.) (Brokešová, 2006).

It is desirable to benefit from the advantages of the ray method mentioned above and try to fix its disadvantages. One possibility is to use some perturbation method. Červený et al. (2007) describes them: We assume that a model, in which we wish to study wave propagation, differs only little from another model called the background or reference model. If only the first term of the series is considered, which is often the case, we speak of the first-order perturbation expansion.

We use the first-order ray-based Born approximation. We use the ray method to compute and discretize the appropriate quantities in the computational grid in the background model. The Born approximation uses these quantities to compute the seismograms. The method is slower than the ray method but it should be faster than the finite difference method. The separation of the wavefield into the individual types of waves is not possible. It is possible to model the P-P (the incident P wave, the reflected P wave), P-S, S-P and

S-S reflections only. On the other hand, the method is applicable to the larger class of models than the ray method because it requires the background model not the original (perturbed) model to be smooth. Furthermore, the method models diffracted waves, see e.g. Šachl (2011).

In this paper we show that also the first-order ray-based Born approximation can have problems in some situations.

2 Perturbed models and the background model

The models where we would like to obtain seismograms (perturbed models) are called P1-j-10%, j $\in \{1, 2, 3, 4, 5, 6, 7, 8, 9, 10, 15\}$. They are constructed from model P1I, which is described in Bulant & Martakis (2011). The background model is smooth model P1 described in the same paper. All models are 2D isotropic heterogenous velocity models situated into rectangle (0 km, 47.3 km) $\times$ (0 km, 6 km).

The density in the perturbed models is the same as in the background model and equal to $\rho = 1000$ kg/m^3 everywhere. The S-wave velocity $v_s = \frac{v_p}{\sqrt{3}}$. The P-wave velocity in each model is the same as in the background model except for one domain. The P-wave velocity in each of these domains is equal to the P-wave velocity in the background model plus 10% of the perturbation between the background model and model P1I. The perturbation is reduced to 10% in order to satisfy sufficiently small differences between the perturbed and the background model. This is the requirement of the Born approximation. The P-wave velocity perturbation between model P1-j-10% and the background model is depicted for each model P1-j-10%, j $\in \{1, 2, 3, 4, 5, 6, 7, 8, 9, 10, 15\}$, in Figures 1 to 11.

Figure 1: P-wave velocity perturbation between model P1-1-10% and the background model. Positive perturbations are red, negative perturbations are green. Zero perturbations are drawn yellow.

Figure 2: P-wave velocity perturbation between model P1-2-10% and the background model. Positive perturbations are red, negative perturbations are green. Zero perturbations are drawn yellow.

Figure 3: P-wave velocity perturbation between model P1-3-10% and the background model. Positive perturbations are red, negative perturbations are green. Zero perturbations are drawn yellow.

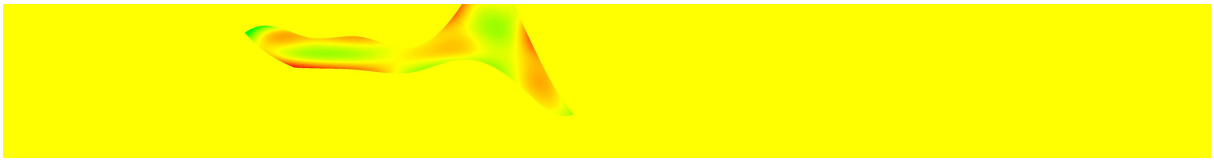

Figure 4: P-wave velocity perturbation between model P1-4-10% and the background model. Positive perturbations are red, negative perturbations are green. Zero perturbations are drawn yellow.

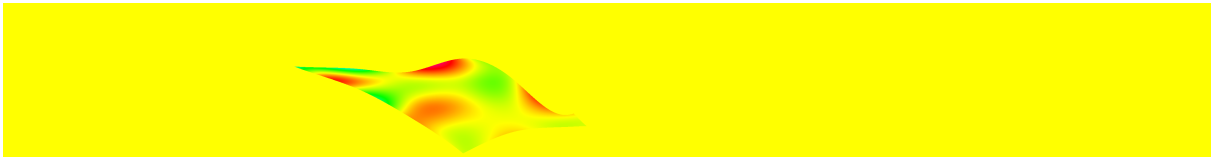

Figure 5: P-wave velocity perturbation between model P1-5-10% and the background model. Positive perturbations are red, negative perturbations are green. Zero perturbations are drawn yellow.

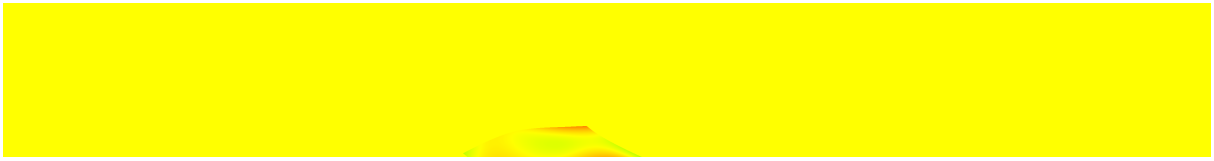

Figure 6: P-wave velocity perturbation between model P1-6-10% and the background model. Positive perturbations are red, negative perturbations are green. Zero perturbations are drawn yellow.

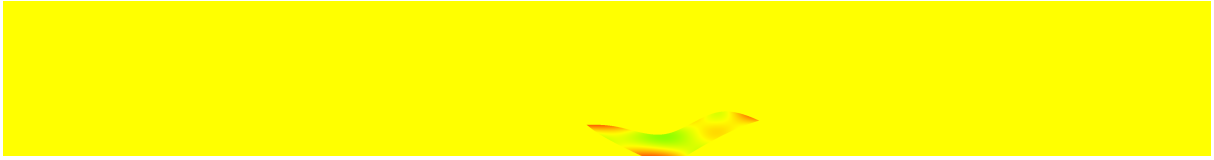

Figure 7: P-wave velocity perturbation between model P1-7-10% and the background model. Positive perturbations are red, negative perturbations are green. Zero perturbations are drawn yellow.

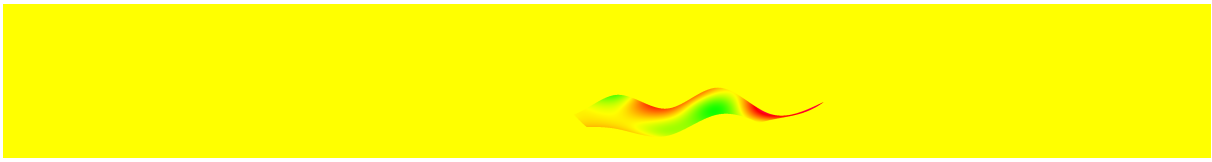

Figure 8: P-wave velocity perturbation between model P1-8-10% and the background model. Positive perturbations are red, negative perturbations are green. Zero perturbations are drawn yellow.

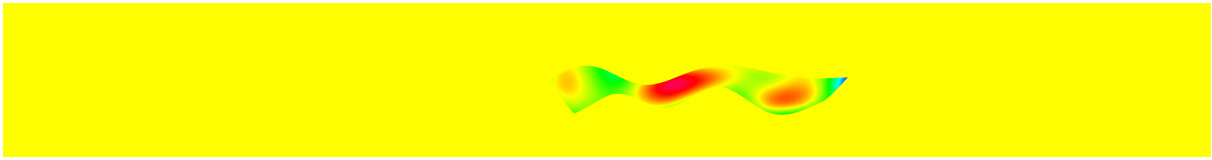

Figure 9: P-wave velocity perturbation between model P1-9-10% and the background model. Positive perturbations are red, negative perturbations are green. Zero perturbations are drawn yellow.

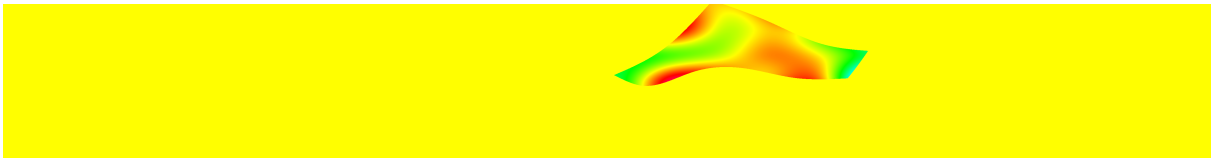

Figure 10: P-wave velocity perturbation between model P1-10-10% and the background model. Positive perturbations are red, negative perturbations are green. Zero perturbations are drawn yellow.

Figure 11: P-wave velocity perturbation between model P1-15-10% and the background model. Positive perturbations are red, negative perturbations are green. Zero perturbations are drawn yellow.

3 Computation of the seismograms

The x_1 coordinate is the horizontal coordinate, it grows from the left to the right. The x_3 coordinate is the vertical coordinate, it grows downwards. The origin of the coordinate system is in the upper left corner of the model.

Motivated by Bulant & Martakis (2011) we choose 37 receivers placed at the upper model boundary. The first receiver has the horizontal coordinate $x_1 = 16$ km. The spacing between the receivers is 0.5 km, therefore, the last receiver has the horizontal coordinate $x_1 = 34$ km.

The explosive source is also placed at the upper model boundary, $x_1 = 25$ km, $x_3 = 0$ km. Its position is the same as the position of the 19th receiver. The source time function is a Gabor signal with a prevailing frequency 10 Hz, filtered by a frequency filter which is non-zero only for frequencies f, 1 Hz $< f <$ 20 Hz. There is a cosine tapering for 1 Hz $< f <$ 2 Hz and 19 Hz $< f <$ 20 Hz while for 2 Hz $< f <$ 19 Hz the filter is equal to one. Only P waves are considered.

The rays are shot into the whole lower half plane. We use the basic system of rays containing 121 rays, which covers the straight angle into which the rays are shot.

The Born seismograms are computed using these settings . The reference solution is the ray-theory seismogram. The detailed analysis of the seismograms is not presented in this paper. We try to do it in Šachl (2011b). Here we focus just on the effects caused by the caustics.

4 Caustics on the direct wave

Let us start with the seismograms computed in models P1-5-10% and P1-6-10%. The seismograms are depicted in Figure 12 and Figure 13 respectively.

There are apparent some weird wavegroups in the computed seismograms. They are marked by ghost green in Figures 12 and 13. Let us have several close receivers. If the weird wavegroups are present in the seismograms computed for these receivers, they usually differ significantly among themselves, see Figure 12. The amplitude is different, the phase can change, sometimes the signals are not similar at all. On the other hand, the wavegroups present in several close receivers have similar travel times. Our explanation is that these wavegroups are caused by the caustics on the direct wave.

We focus on the seismograms computed in model P1-6-10%. There are just two weird wavegroups in the seismograms for the receivers with horizontal coordinates $x_1 = 33.0$ km and $x_1 = 33.5$ km. The Born approximation is computed using the grid, in which the needed quantities are discretized. The computation of the quantities at the gridpoints of the computational grid is following: The model volume is decomposed into ray cells on the direct wave using the controlled initial-value ray tracing. The interpolation within these ray cells follows. The algorithm is described in Bulant (1999). Thus, it is desirable to check the rays and the ray coverage of block 6. The Born approximation uses both the Green function from the source and from the receiver. The Green function from the source is the same for all receivers, therefore, if there are any problems, they should be caused by the Green function from the receiver. The Figures 14, 15, 16, 17 depict the ray coverage of block 6 in shooting rays from the receivers at $x_1 = 32.5$ km, $x_1 = 33.0$ km, $x_1 = 33.5$ km, $x_1 = 34.0$ km.

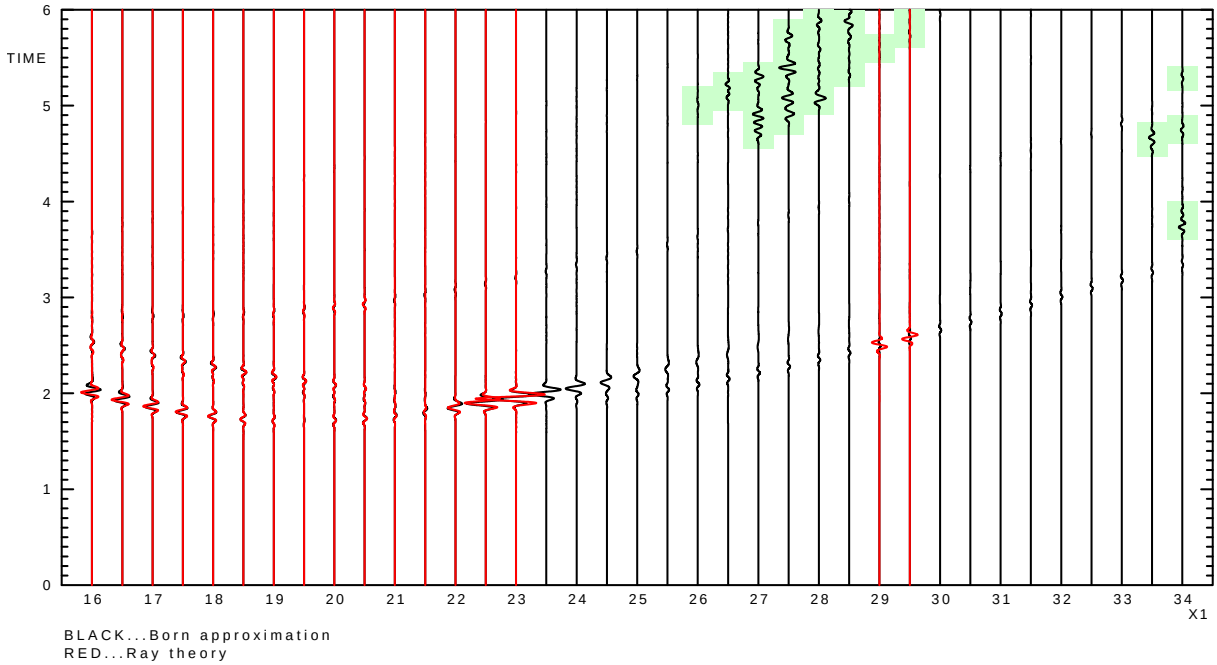

Figure 12: Born and ray-theory seismograms computed in model P1-5-10%

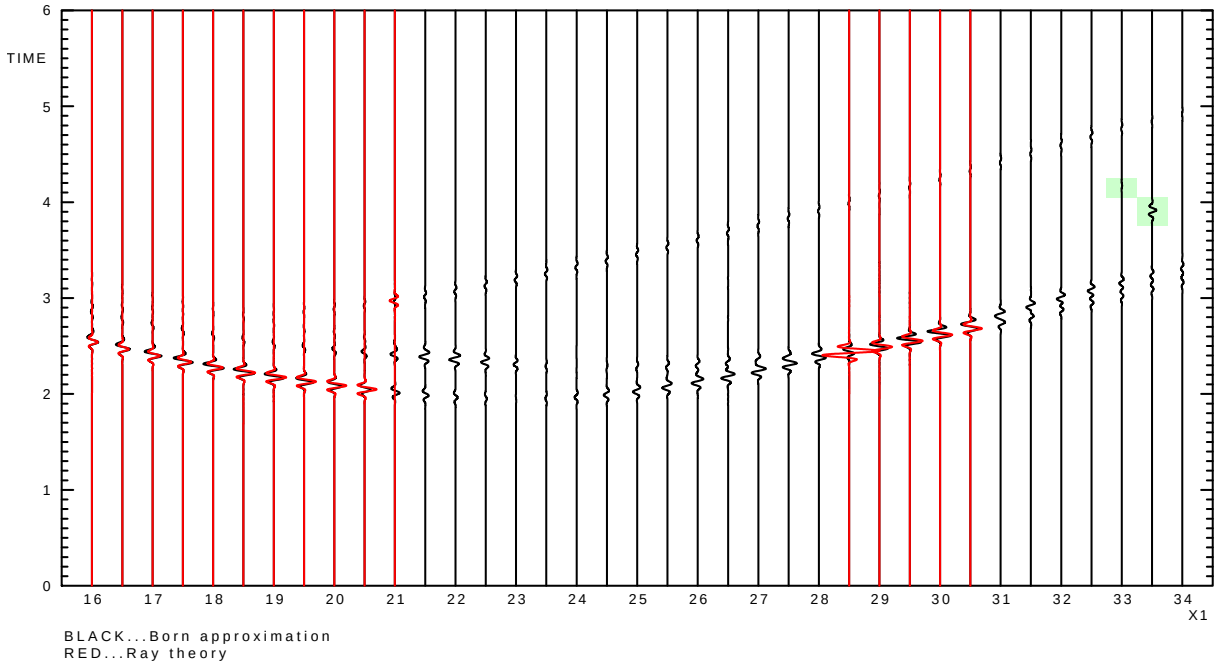

Figure 13: Born and ray-theory seismograms computed in model P1-6-10%

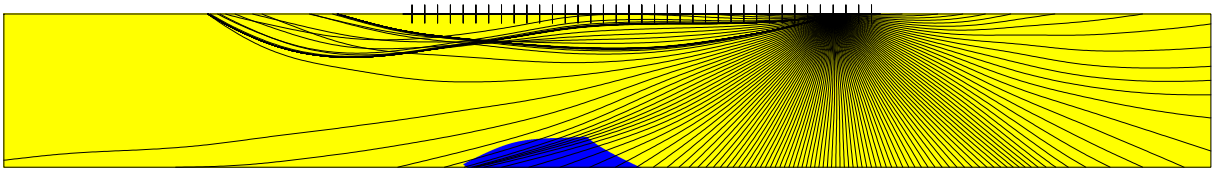

Figure 14: Coverage of the background model with the rays in shooting from the position of the receiver at $x_1 = 32.5$ km

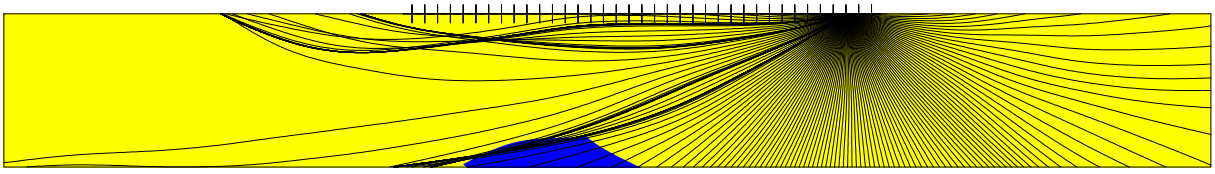

Figure 15: Coverage of the background model with the rays in shooting from the position of the receiver at $x_1 = 33.0$ km

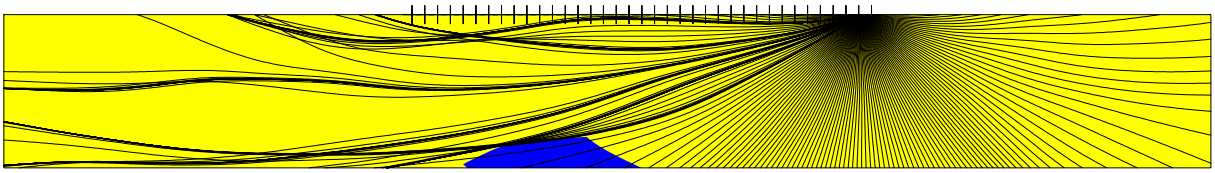

Figure 16: Coverage of the background model with the rays in shooting from the position of the receiver at $x_1 = 33.5$ km

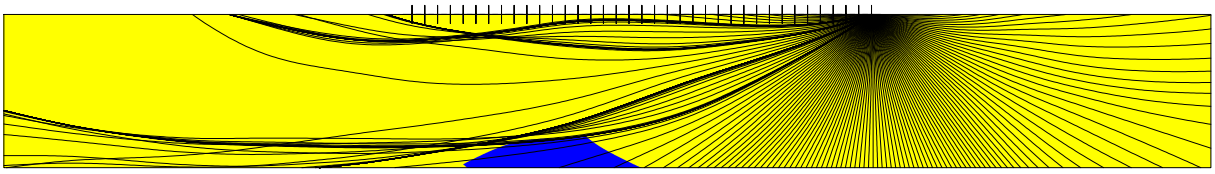

Figure 17: Coverage of the background model with the rays in shooting from the position of the receiver at $x_1 = 34.0$ km

The intersection of rays is observed in Figure 15 and Figure 16. These figures correspond to the receivers with the weird wavegroups in the seismograms.

The places where two neighbouring rays intersect are called caustics. Vavryčuk (2002) warns that caustics often cause difficulties in modelling wavefields. They produce infinite ray amplitudes, phase shifts of signals and triplications of the wave front. Caustics usually appear in wavefields propagating in inhomogenous media such as gradient media or media with curved interfaces.

We mostly worry about the infinite ray amplitudes. This problem is typical for the ray theory and is caused by zero ray Jacobian (and its square root called the geometrical spreading), see Červený (2001, sec. 3.10.5). We perform the following experiment:

First, we find the "biggest values" in the file containing the discretized amplitudes of the Green function. We analyze component G_{11} of Green function G_{ij}. The Green function is discretized in the grid with the grid intervals 0.005 km. The "biggest values" of the amplitudes are one order larger than the typical values of the amplitude. The gridpoints with the "biggest values" are marked in Figures 18 and 19 by red crosses. Note that only gridpoints which lie in block 6 are shown.

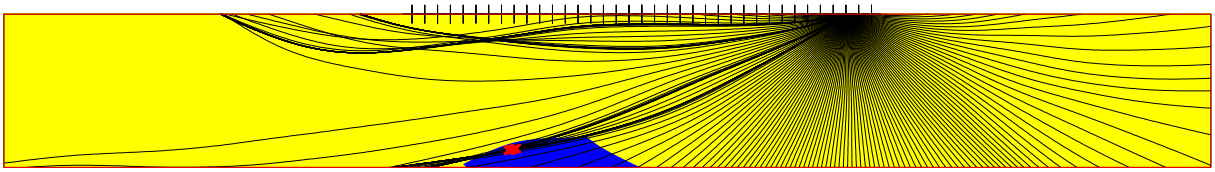

Figure 18: Positions of the "biggest values" of the amplitudes of component G_{11} of the Green function marked by red crosses. The rays are shot in the background model from the position of the receiver at $x_1 = 33.0$ km.

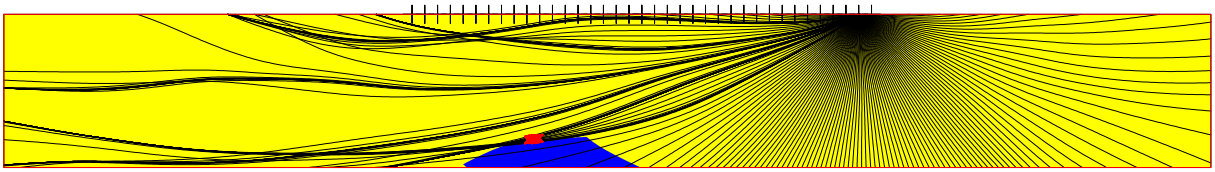

Figure 19: Positions of the "biggest values" of the amplitudes of component G_{11} of the Green function marked by red crosses. The rays are shot in the background model from the position of the receiver at $x_1 = 33.5$ km.

The red crosses in Figures 18 and 19 correspond to the position of the caustic. Do not be misleaded by the position of the crossing of thicker lines created by several near rays. They have a bit different meaning. The caustic is located closer to the source.

Second, we compute the Born seismograms for the receivers at $x_1 = 33.0$ km and $x_1 = 33.5$ km using 2 small grids. The first small grid is a grid for the receiver at $x_1 = 33.0$ km, it contains the gridpoints marked by the red crosses in Figure 18. The second small grid is a grid for the receiver at $x_1 = 33.5$ km, it contains the gridpoints marked by the red crosses in Figure 19. The original grid is a regular rectangular grid which covers block 6 (not the whole model). The second small grid is composed of only approximately 2 % of the original gridpoints. The first small grid is even smaller, it contains about 0.3 % of the original gridpoints. The newly computed Born seismograms

are compared with the original seismograms in Figure 20. The seismograms are ten times enlarged to see the details better.

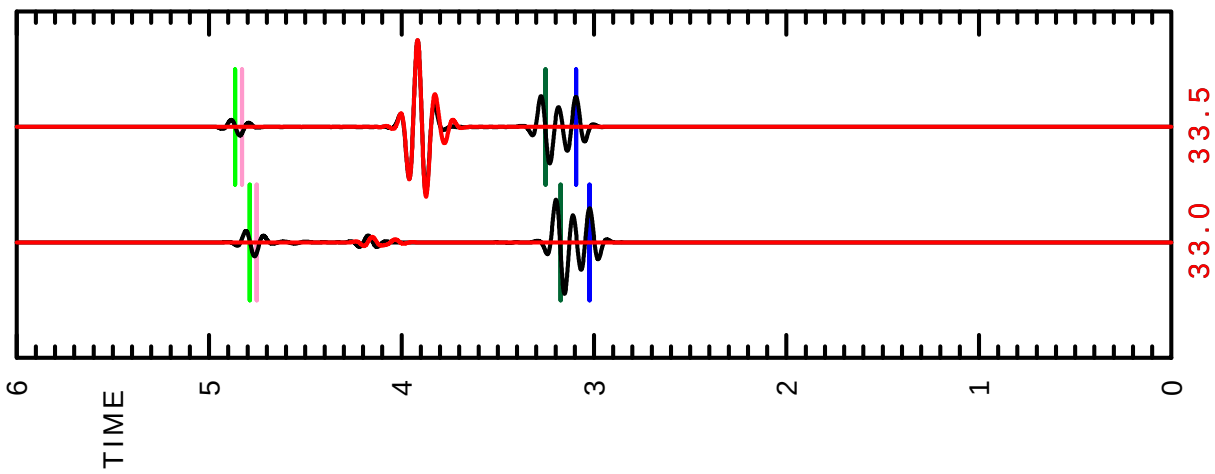

Figure 20: The Born seismograms computed using the grid which covers whole block 6 (black) and using the small grid which contains gridpoints with the "biggest values" of the amplitude of component G_{11} of the Green function (red). The seismograms are computed for the receivers at $x_1 = 33.5$ km and at $x_1 = 34.0$ km.

Figure 20 shows that the Born seismograms computed using the small grids do not contain the waves diffracted from the edges of block 6. That is nothing surprising, none of the two small grids covers these edges. However, the weird wavegroups do not differ too much. There are some differences, but they can be caused by the diffractions at the boundaries of the small grid.

4.1 Possible solutions of the problem

We have at least 3 possibilities how to solve the observed problem:

1. Use smoother background model, where caustics are not present.
2. Dampen the "biggest amplitudes" choosing an appropriate cut-off.
3. Use the Gaussian wave packets, which do not suffer by infinite amplitudes in the caustics.

The first possibility could work in some models. However, too violent smoothing is not desirable, because the Born approximation requires the background model to be close to the perturbed model.

The second possibility is easy to accomplish, but the value of the cut-off depends on the user.

The third possibility sounds interesting and it is probably the only right solution. Unfortunately, it requires new attitude to the computation of the Born approximation, new programs etc..

4.2 Corrected seismograms

We tested the second possibility. The seismograms computed in models P1-5-10% and P1-6-10% using appropriate cut-offs are depicted in Figures 22 and 24 respectively. Figure 21 and Figure 23 are the same as Figure 12 and Figure 13. We repeat them for a better comparison with the figures displaying the seismograms computed using the amplitude cut-offs.

The choice of the value of the cut-off is not unique. We choose the value in order to preserve the genuine waves and dampen the weird waves. The genuine waves are the waves reflected from the interfaces of the block and the diffracted waves, see also Šachl (2011b).

The weird wavegroups in the seismograms computed in model P1-5-10% are still visible, but their amplitudes are much smaller now. The weird wavegroups virtually disappeared from the seismograms computed in model P1-6-10%.

The discussed problem is observed also in the seismograms computed in models P1-1-10%, P1-2-10%, P1-3-10%, P1-4-10%, P1-10-10%, P1-15-10%. The coresponding seismograms computed using no amplitude cut-off and using the amplitude cut-offs are depicted in Figures 25 and 26, Figures 27 and 28, Figures 29 and 30, Figures 31 and 32, Figures 33 and 34, Figures 35 and 36 respectively.

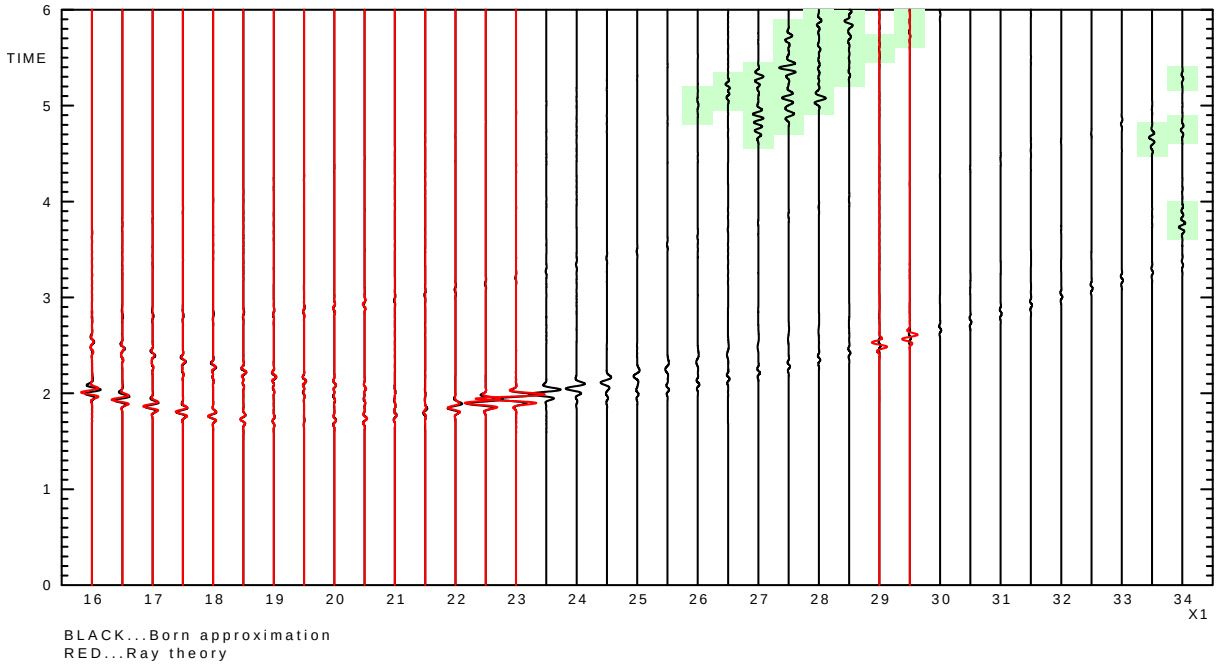

Figure 21: Born and ray-theory seismograms computed in model P1-5-10% using no amplitude cut-off.

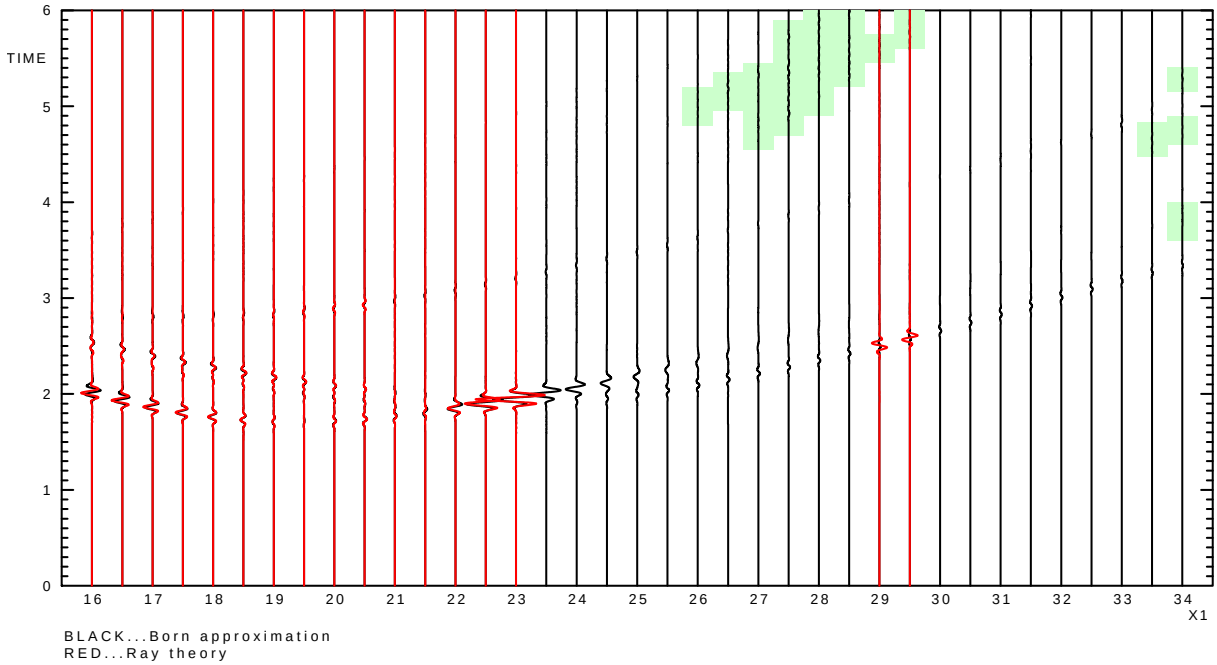

Figure 22: Born and ray-theory seismograms computed in model P1-5-10% using the amplitude cut-offs.

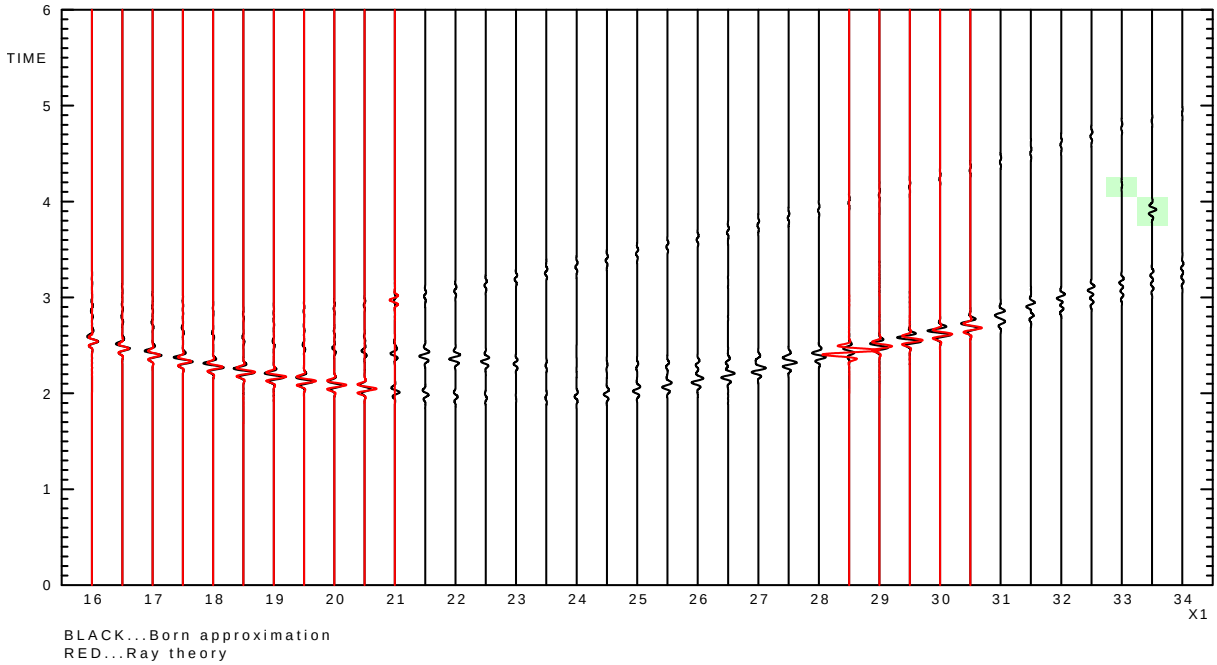

Figure 23: Born and ray-theory seismograms computed in model P1-6-10% using no amplitude cut-off.

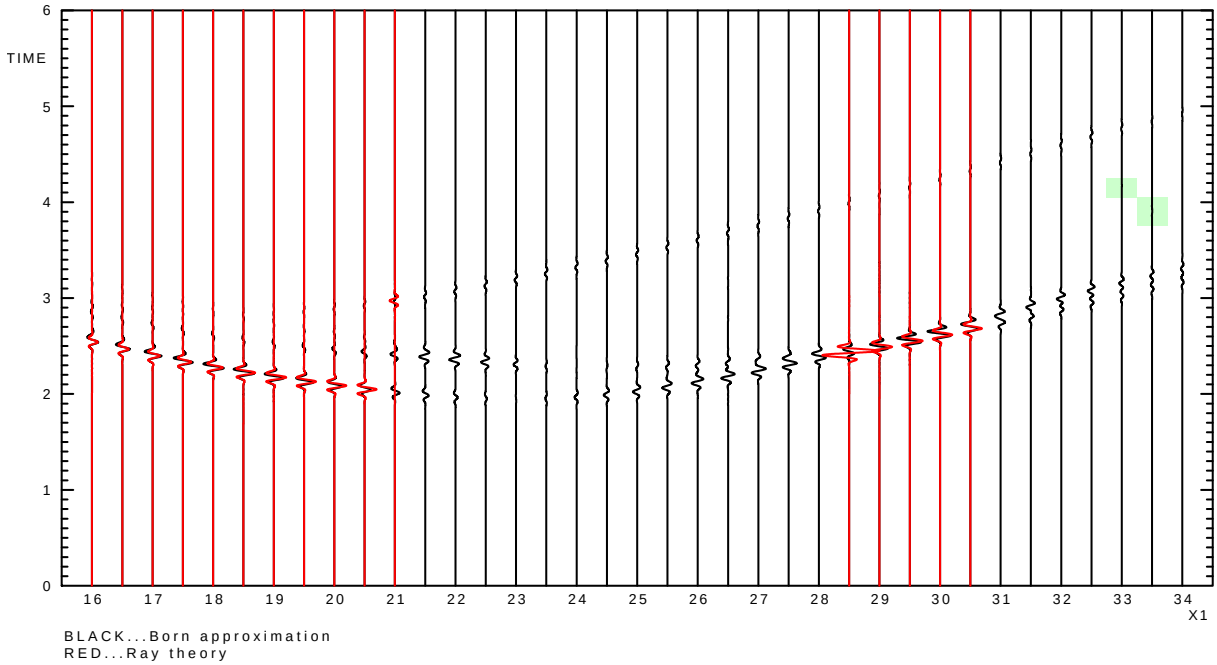

Figure 24: Born and ray-theory seismograms computed in model P1-6-10% using the amplitude cut-offs.

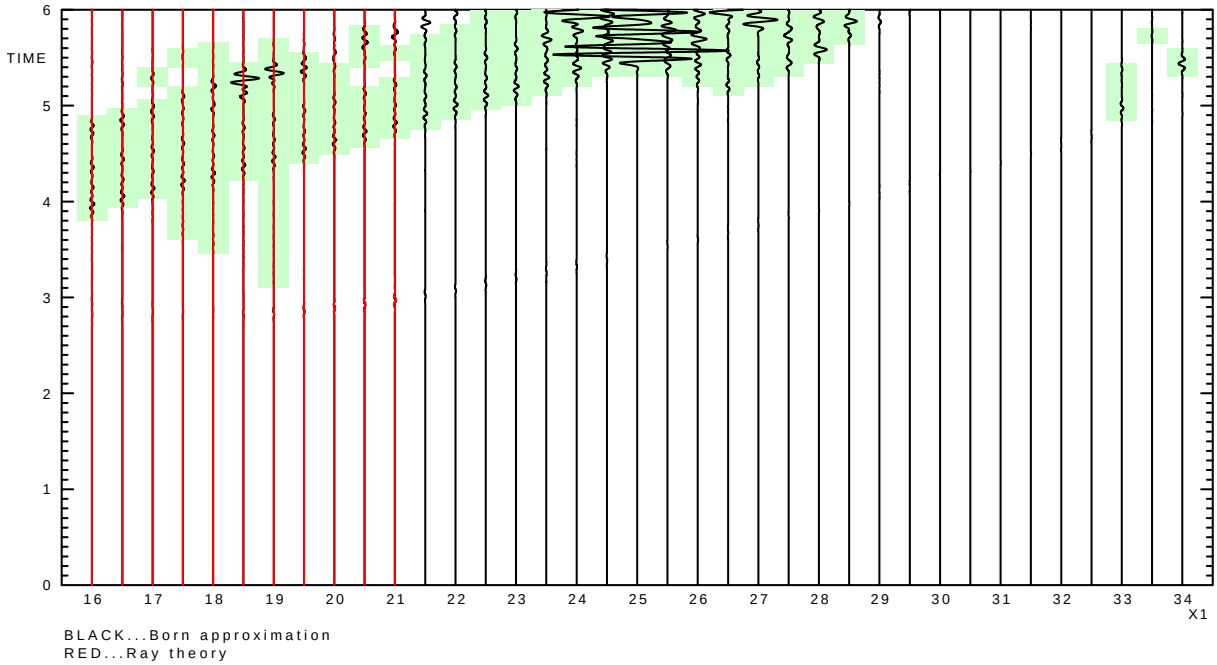

Figure 25: Born and ray-theory seismograms computed in model P1-1-10% using no amplitude cut-off.

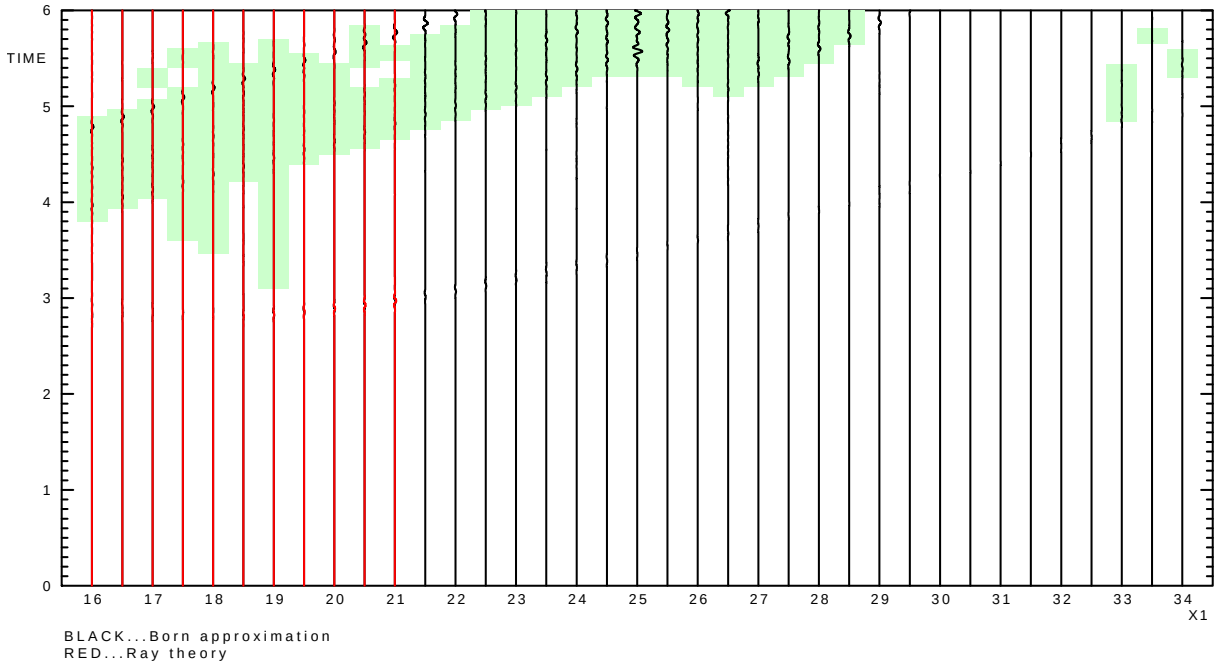

Figure 26: Born and ray-theory seismograms computed in model P1-1-10% using the amplitude cut-offs.

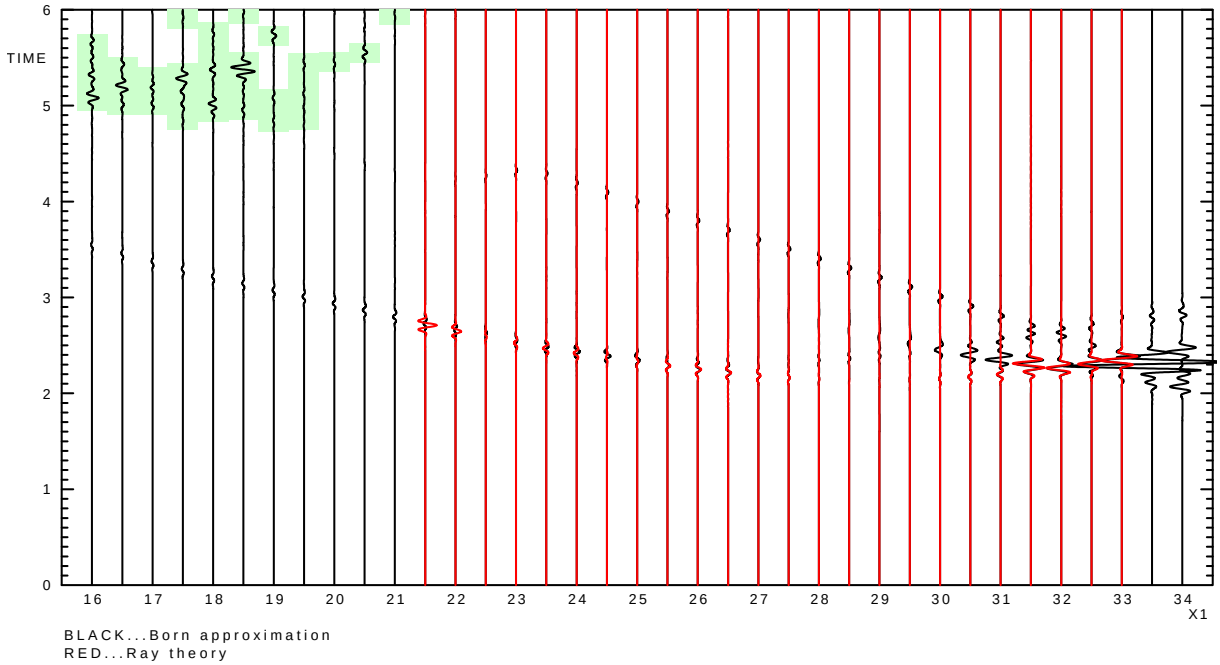

Figure 27: Born and ray-theory seismograms computed in model P1-2-10% using no amplitude cut-off.

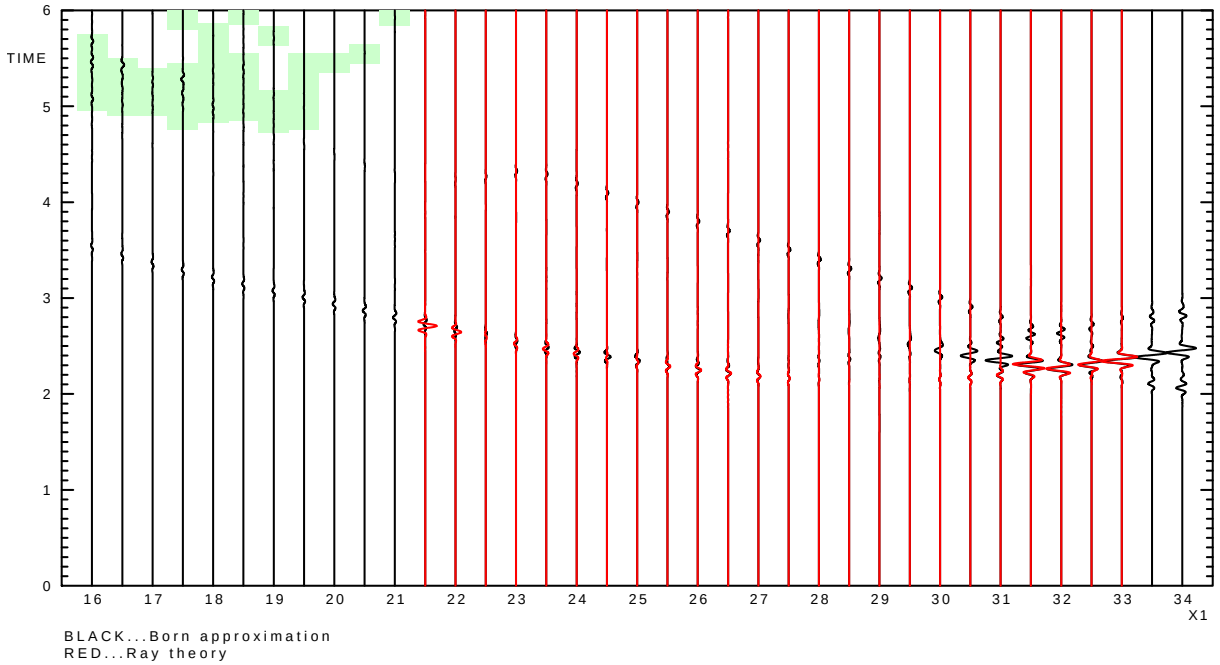

Figure 28: Born and ray-theory seismograms computed in model P1-2-10% using the amplitude cut-offs.

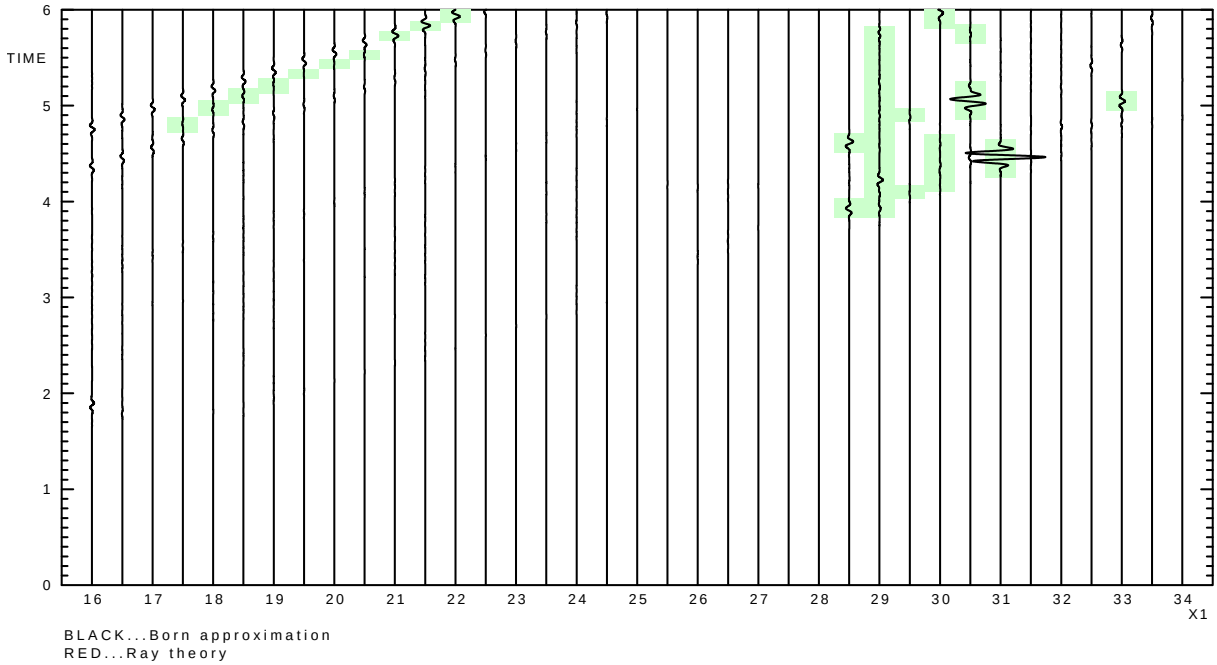

Figure 29: Born and ray-theory seismograms computed in model P1-3-10% using no amplitude cut-off.

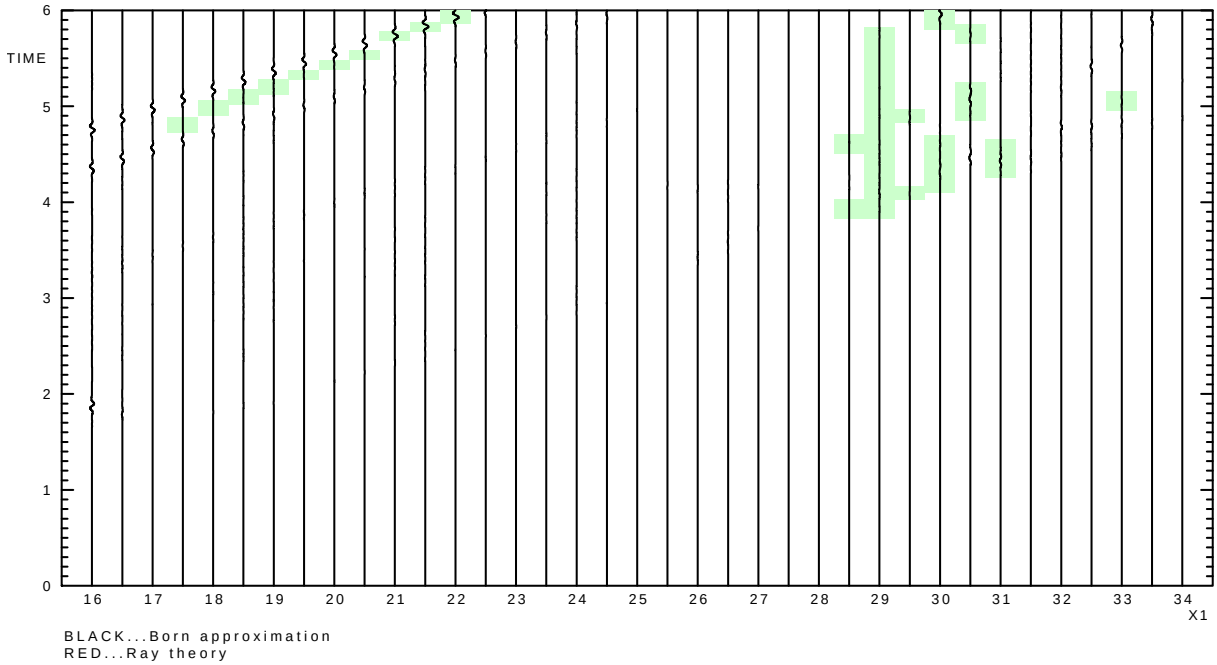

Figure 30: Born and ray-theory seismograms computed in model P1-3-10% using the amplitude cut-offs.

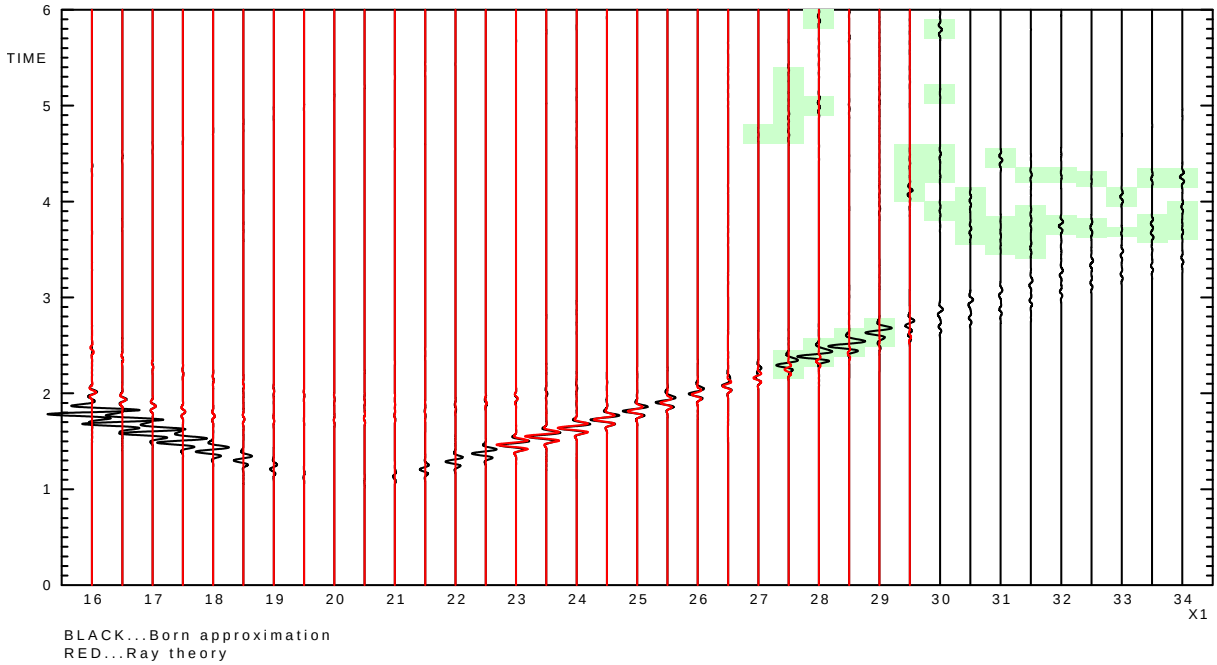

Figure 31: Born and ray-theory seismograms computed in model P1-4-10% using no amplitude cut-off.

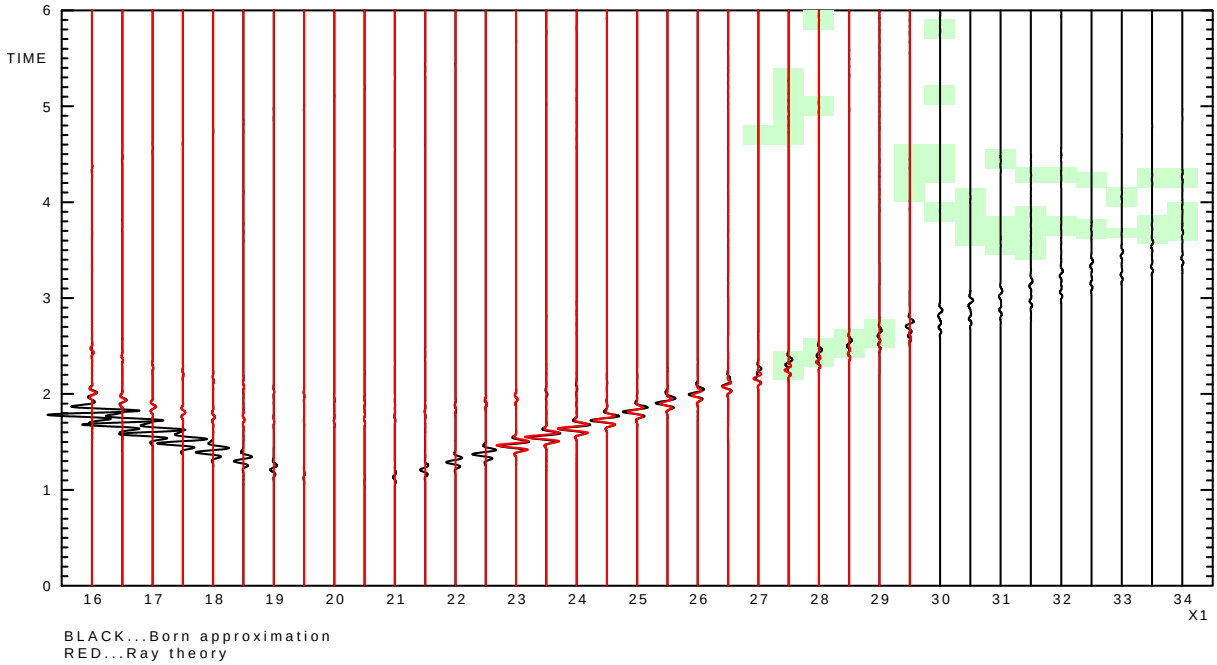

Figure 32: Born and ray-theory seismograms computed in model P1-4-10% using the amplitude cut-offs.

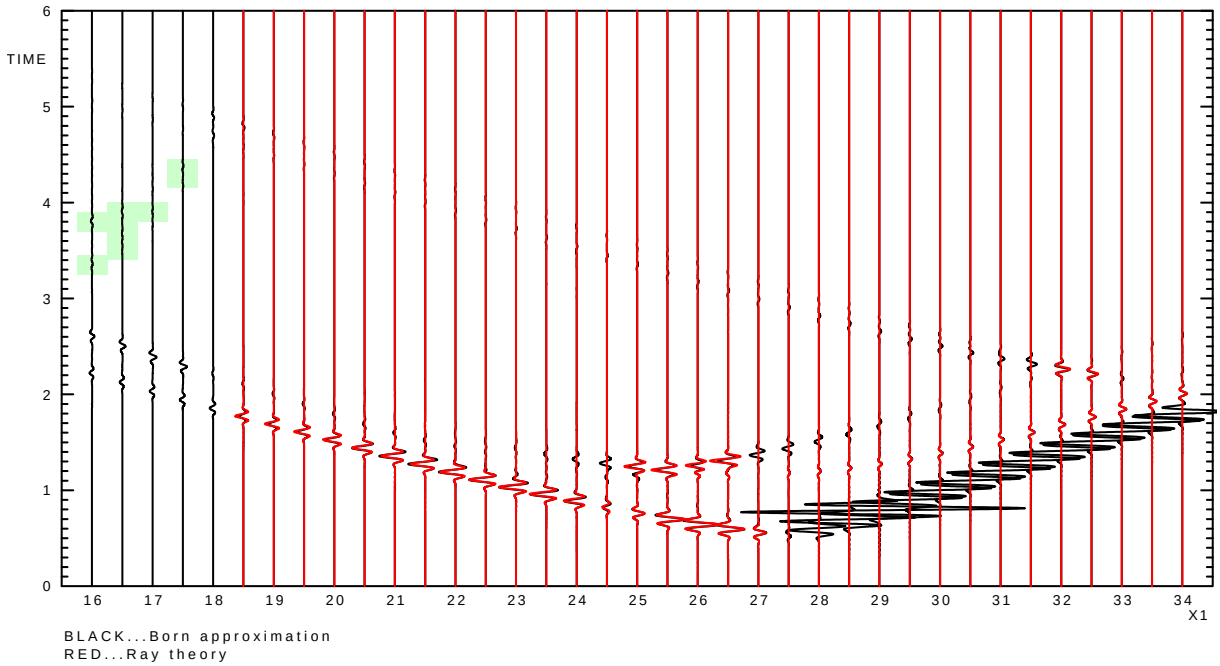

Figure 33: Born and ray-theory seismograms computed in model P1-10-10% using no amplitude cut-off.

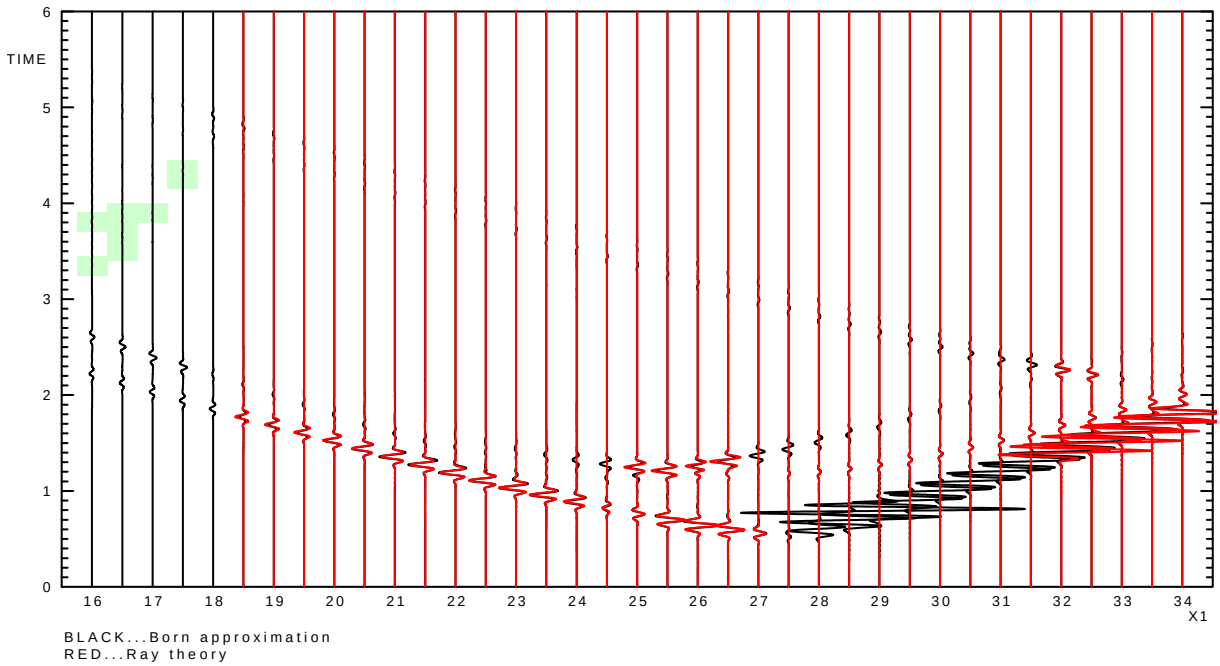

Figure 34: Born and ray-theory seismograms computed in model P1-10-10% using the amplitude cut-offs.

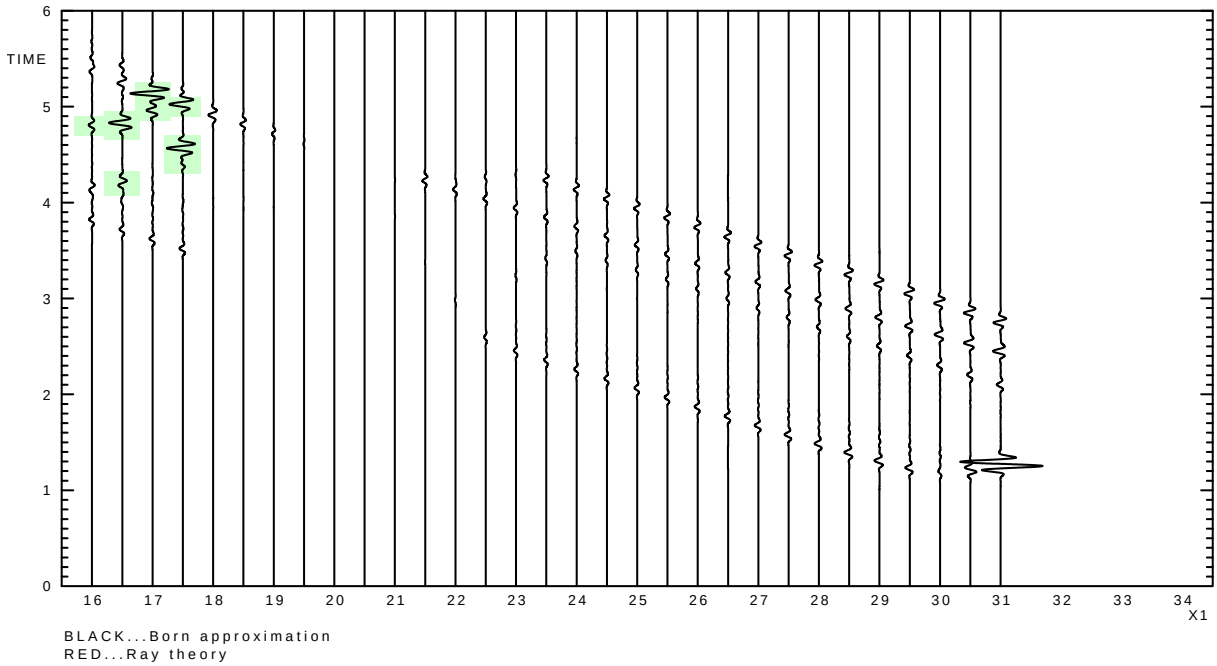

Figure 35: Born and ray-theory seismograms computed in model P1-15-10% using no amplitude cut-off.

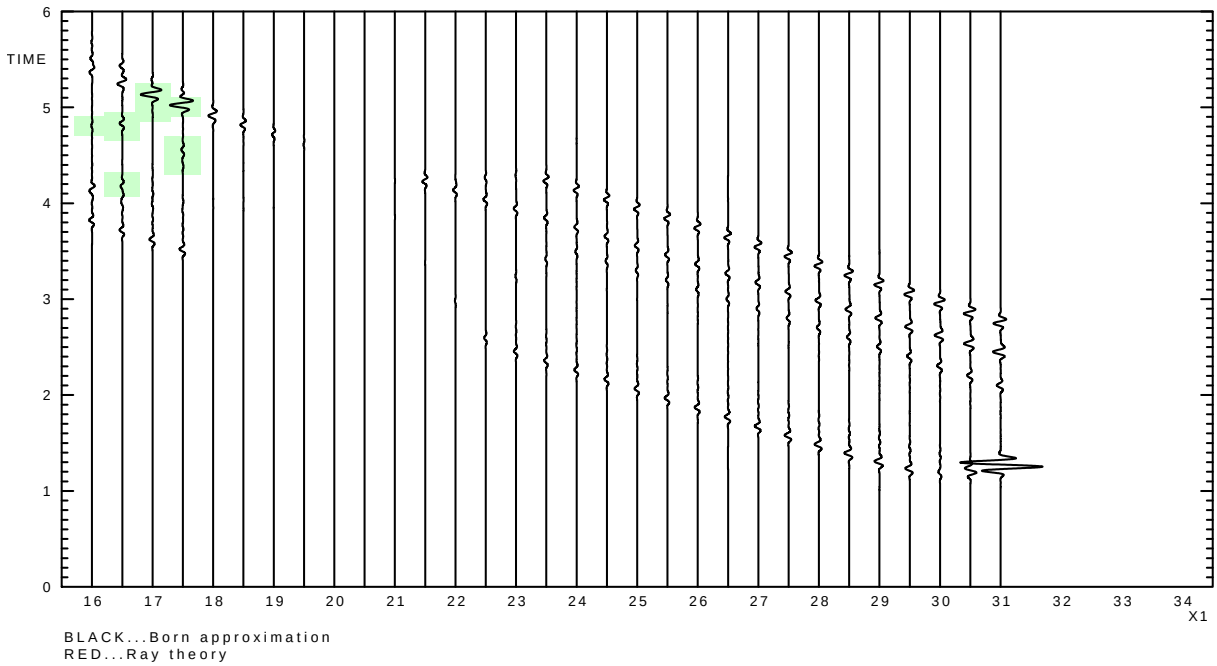

Figure 36: Born and ray-theory seismograms computed in model P1-15-10% using the amplitude cut-offs.

5 Caustics on the reflected wave

So far, we discussed the problems caused by caustics on the direct wave. However, another effect caused by caustics is still contained in the computed seismograms. The caustics can be present on the reflected wave. The ray-theory seismograms could have significant problems if the receiver is situated at the caustic or in its close vicinity. The seismogram could be greatly magnified. On the other hand, the Born approximation may not suffer from this problem, because it is computed in the background model where no caustics on the direct wave could be present. Moreover, the ray-theory seismograms are zero for the receivers located in the shadow zone. The Born seismograms are nonzero. We observe the diffractions from the caustic.

We present 6 examples. We comment 3 of them:

In the first example, the seismograms are computed in model P1-2-10%. The seismograms are depicted in Figure 38, light yellow highlights the first and last receiver where we observe the triplication. The Born seismograms computed for the close receivers continue with the waves diffracted from the caustic. The ray diagram is depicted in Figure 37, the triplication is perfectly visible. The rays shot closer and closer to the upper model boundary incident more and more to the right, then they return back to the left, and again incident more to the right.

In the second example, the seismograms are computed in model P1-5-10%. The seismograms are depicted in Figure 41. Notice the strong wavegroup in the seismogram for the receiver at $x_1 = 23$ km highlighted by light yellow. Figures 39 and 40 depict the ray diagrams. There are two arrivals for the receivers beween $x_1 = 16$ km and $x_1 = 23$ km. This is the consequence of the caustic. We would probably observe a triplication if the interface did not end suddenly. The ray-theory seismograms depicted in Figure 41 are zero for the receivers with the horizontal coordinate $x_1 \geq 23.5$ km. The Born seismograms smoothly continue to the shadow zone, the amplitudes of the wavegroups gradually decrease.

In the third example, the seismograms are computed in model P1-7-10%. The seismograms are depicted in Figure 44. Quite complicated ray diagrams are depicted in Figure 42 and Figure 43. Two occurences of the triplications are observed. The first and last receiver where we observe the triplication are highlighted by light yellow in the first case and light blue-green in the second case.

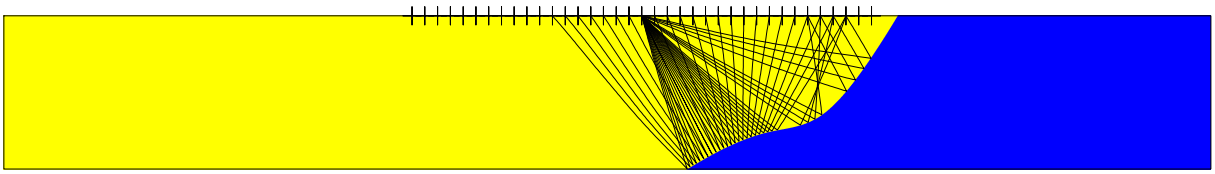

Figure 37: Model P1-2-10%, the first elementary wave

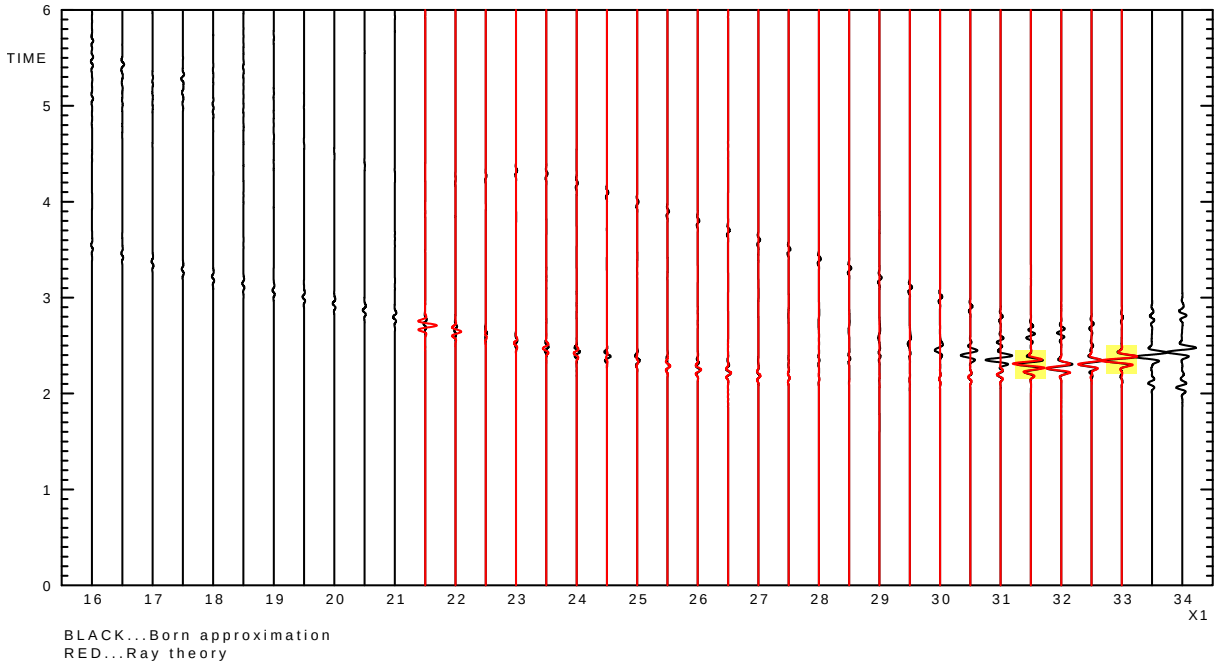

Figure 38: Born and ray-theory seismograms computed in model P1-2-10% using amplitude cut-offs. The wavegroups highlighted by light yellow continue to the shadow zone with the waves diffracted from the caustic.

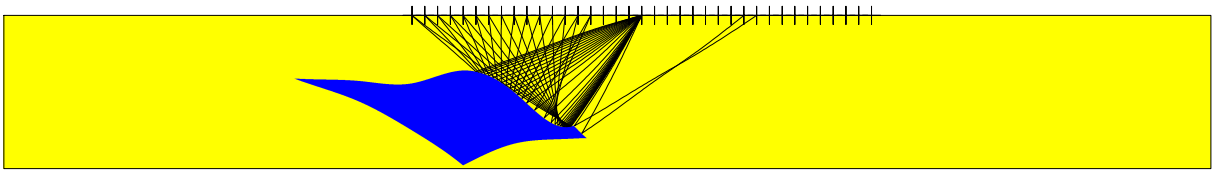

Figure 39: Model P1-5-10%, the first elementary wave

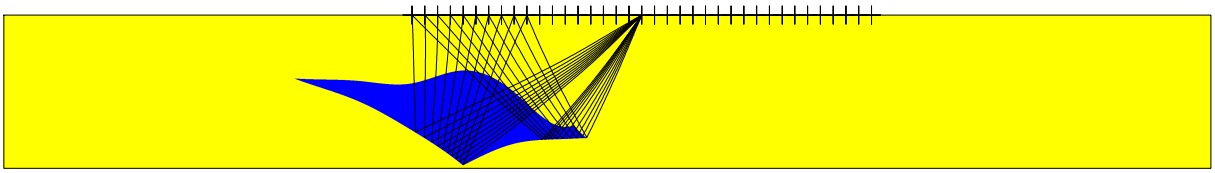

Figure 40: Model P1-5-10%, the second elementary wave

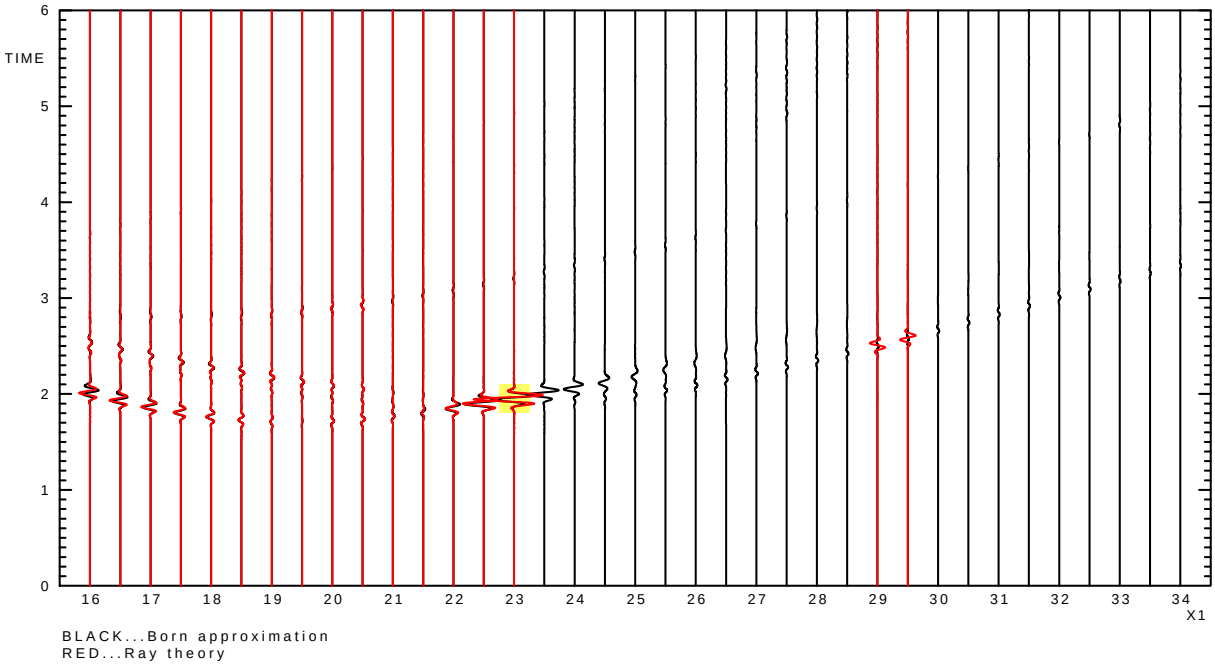

Figure 41: Born and ray-theory seismograms computed in model P1-5-10% using amplitude cut-offs. The wavegroups highlighted by light yellow continue to the shadow zone with the waves diffracted from the caustic.

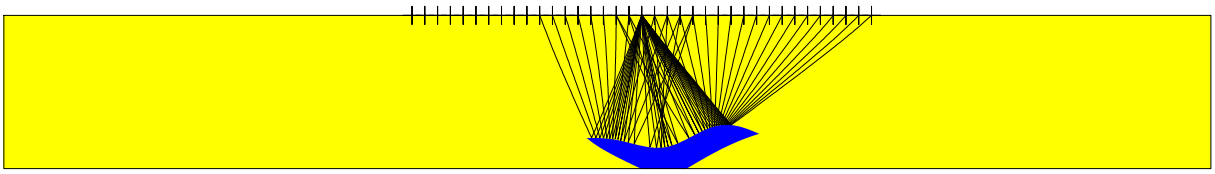

Figure 42: Model P1-7-10%, the first elementary wave

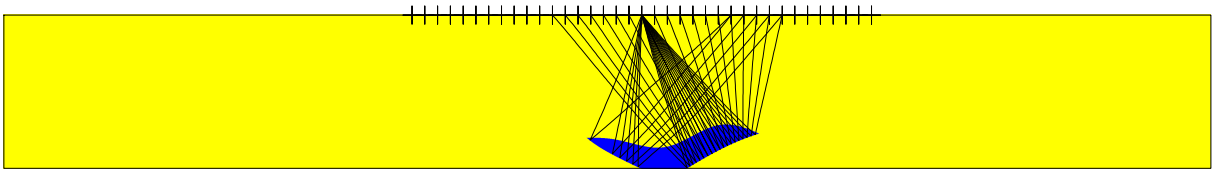

Figure 43: Model P1-7-10%, the second elementary wave

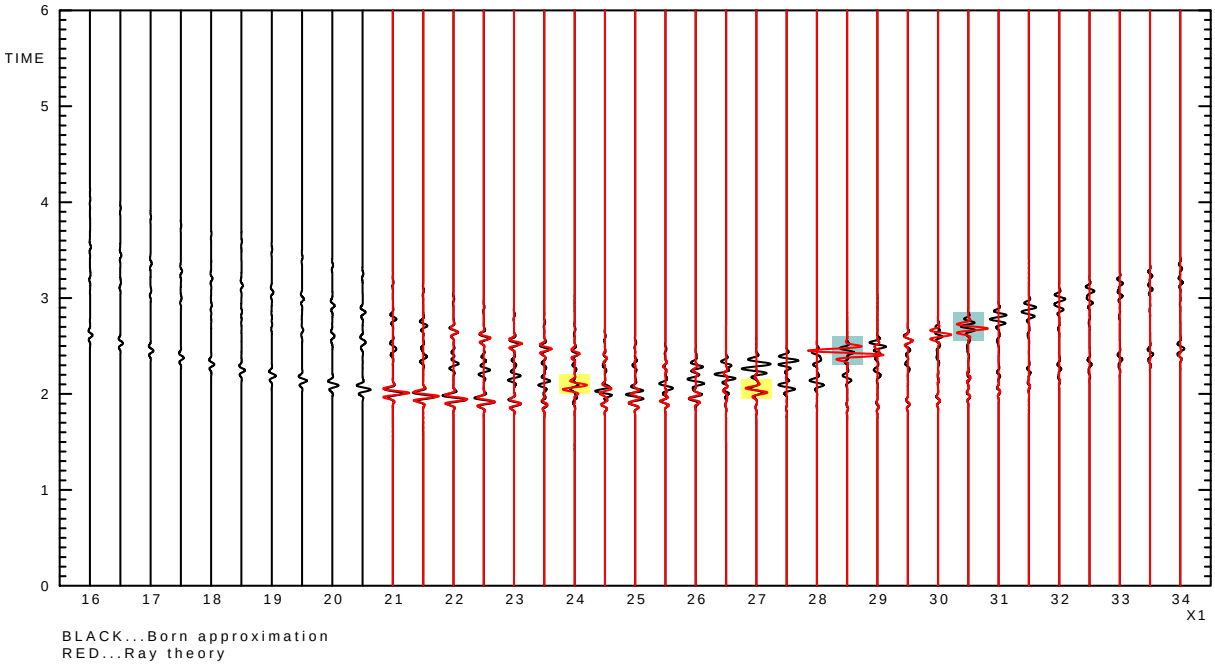

Figure 44: Born and ray-theory seismograms computed in model P1-7-10% using amplitude cut-offs. The wavegroups highlighted by light yellow and light blue-green continue to the shadow zones with the waves diffracted from the caustics.

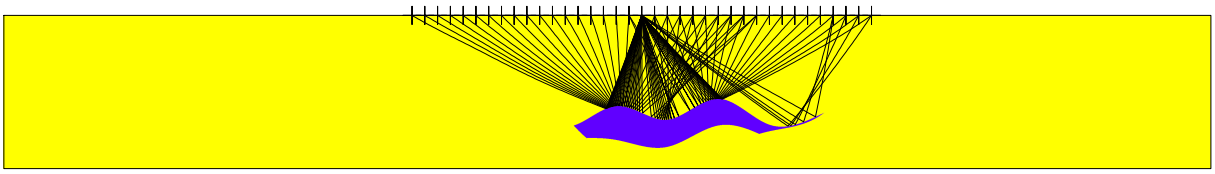

Figure 45: Model P1-8-10%, the first elementary wave

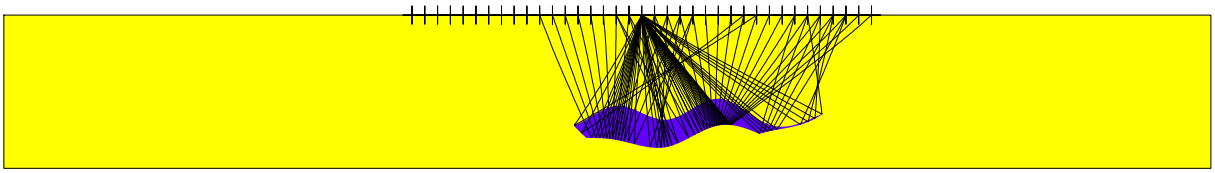

Figure 46: Model P1-8-10%, the second elementary wave

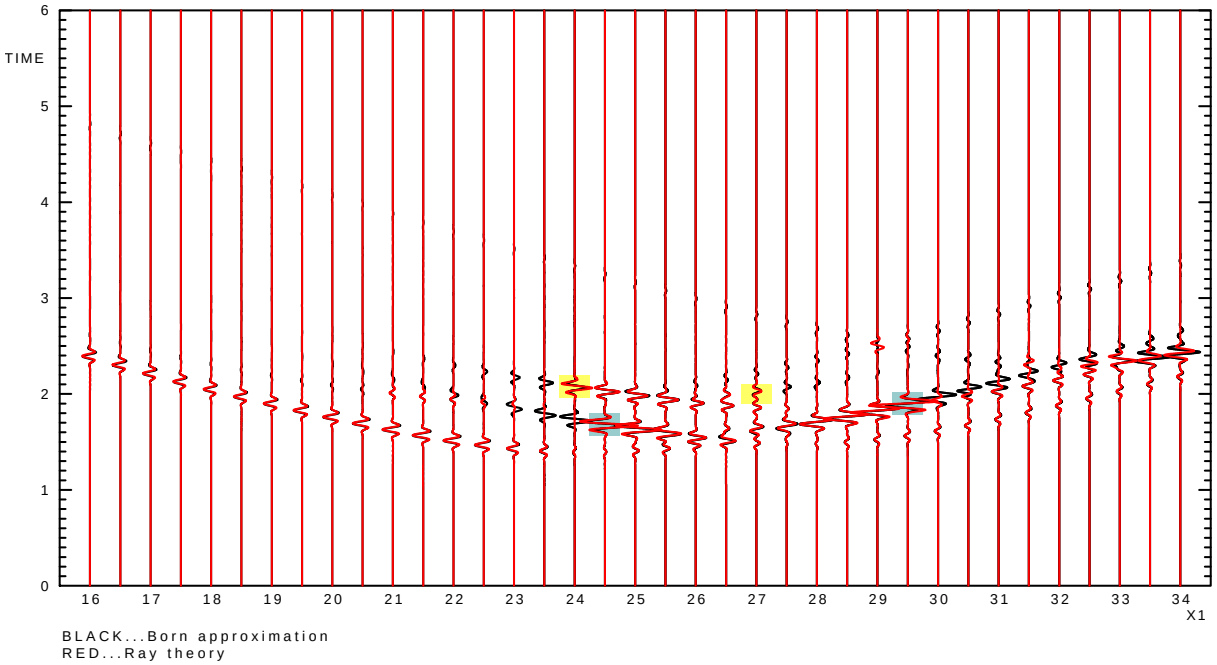

Figure 47: Born and ray-theory seismograms computed in model P1-8-10% using amplitude cut-offs. The wavegroups highlighted by light yellow and light blue-green continue to the shadow zones with the waves diffracted from the caustics.

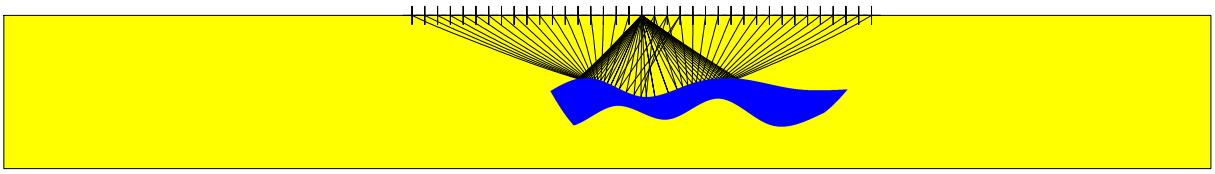

Figure 48: Model P1-9-10%, the first elementary wave

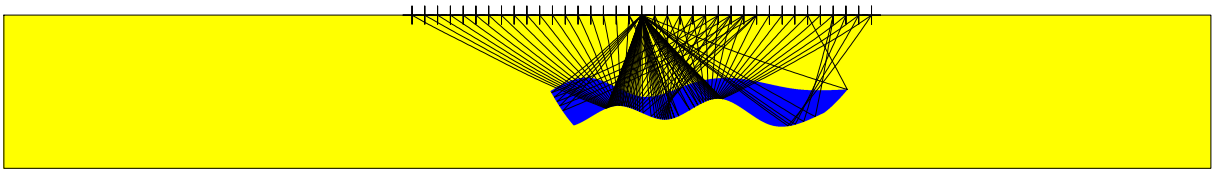

Figure 49: Model P1-9-10%, the second elementary wave

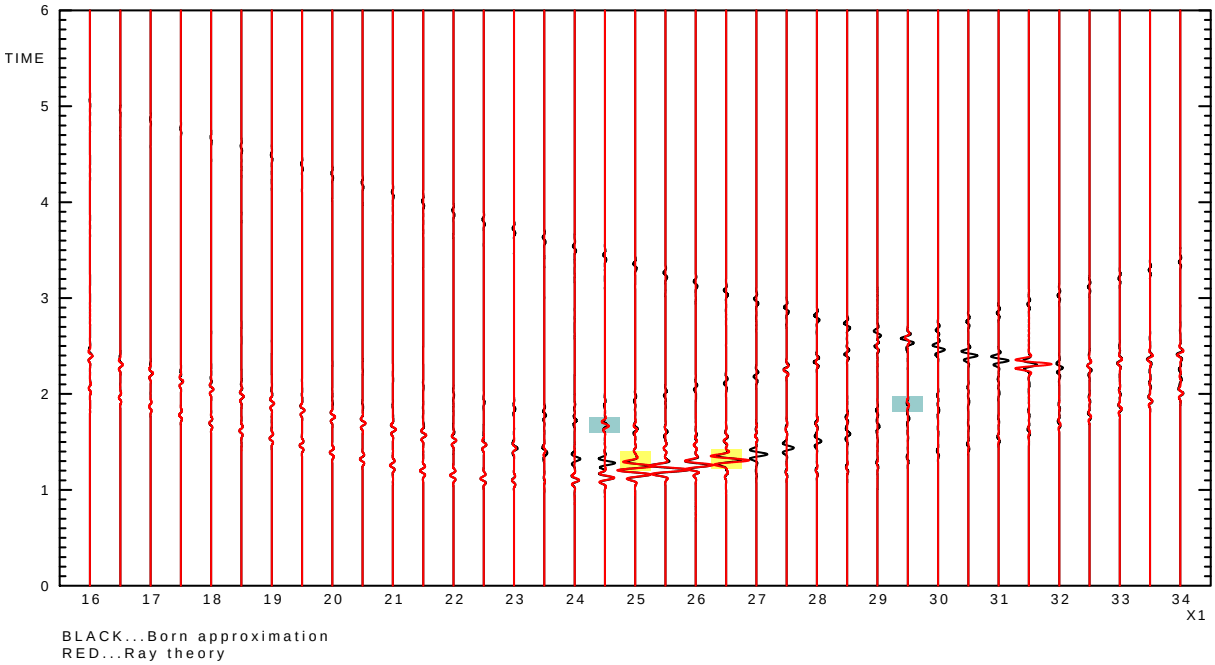

Figure 50: Born and ray-theory seismograms computed in model P1-9-10% using amplitude cut-offs. The wavegroups highlighted by light yellow and light blue-green continue to the shadow zones with the waves diffracted from the caustics.

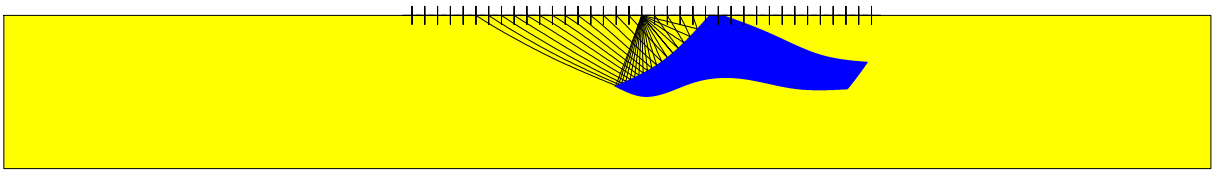

Figure 51: Model P1-10-10%, the first elementary wave

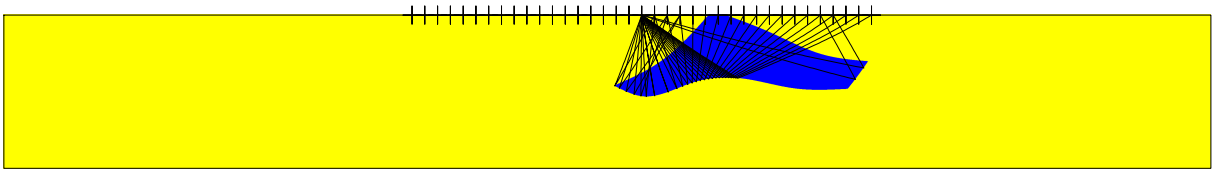

Figure 52: Model P1-10-10%, the second elementary wave

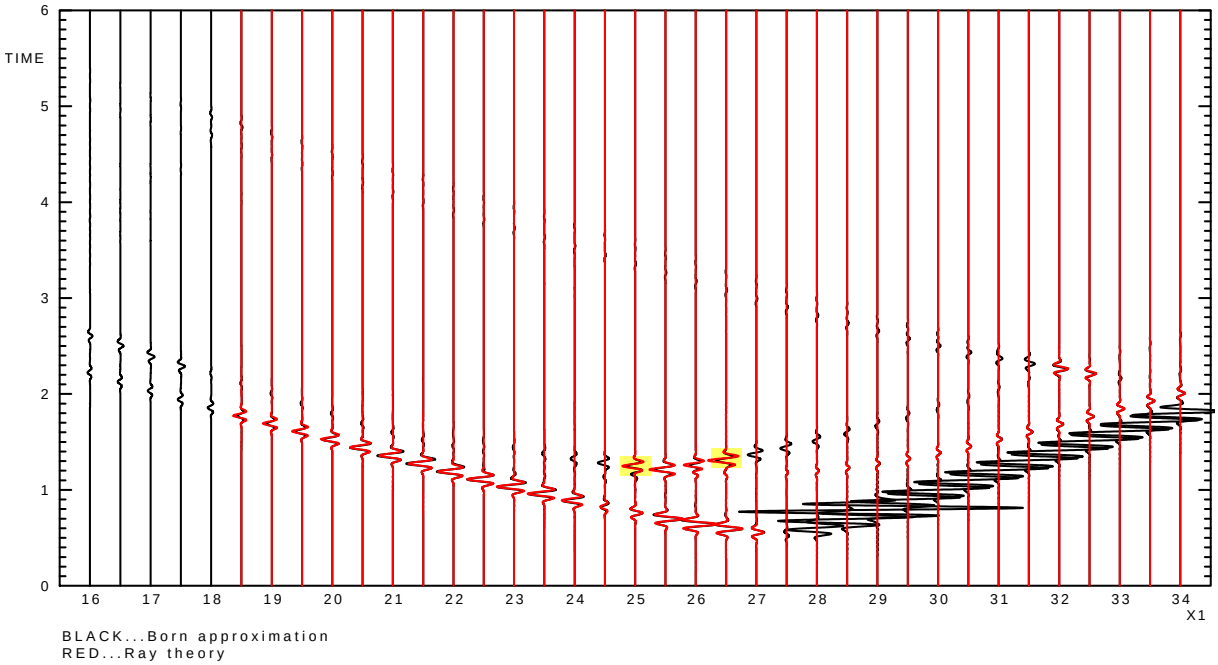

Figure 53: Born and ray-theory seismograms computed in model P1-10-10% using amplitude cut-offs. The wavegroups highlighted by light yellow continue to the shadow zone with the waves diffracted from the caustic.

6 Concluding remarks

The ray-based Born approximation overcomes some difficulties of the ray theory such as required smoothness of the model. Unfortunately, also this method has certain problems. One such problem is the generation of the weird waves, if the caustics are present in the background model. The possible solution consists in cutting the biggest amplitudes of the Green function discretized in the computational grid. However, the solution is not fully satisfactory and other possibilities should be studied in the future.

The caustics can also be present on the reflected wave in the perturbed model. The Born approximation is computed in the background model, but the diffractions from the caustics can be observed in the Born seismograms. These diffracted wavegroups are visible also for the receivers in the shadow zone, where the ray-theory seismogram is zero.

Acknowledgements

First of all I would like to thank Luděk Klimeš, who greatly helped me with the work which led to this paper. I would also like to thank Petr Bulant because he provided me model P1 and the history files, which he used for seismogram computation and visualization of the medium parameters. Hence if I wanted to compute the reference seismogram or to visualize some quantities I used parts of these history files (or the whole history files) and adjusted them as necessary.

The research has been supported by the Grant Agency of the Czech Republic under contract P210/10/0736, by the Ministry of Education of the Czech Republic within research project MSM0021620860, and by the members of the consortium "Seismic Waves in Complex 3-D Structures" (see "http://sw3d.cz").

References

Brokešová, J. (2006): *Asymptotic ray method in seismology: A tutorial.* Matfyzpress, Prague.

Bulant, P. (1999): Two-point ray-tracing and controlled initial-value ray-tracing in 3-D heterogeneous block structures. In: *J. seism. Explor.*, **8**, pp. 57-75.

Bulant, P. & Martakis, N. (2011): Constructing model P1I for reflection studies. In: Seismic Waves in Complex 3–D Structures, Report 21, pp. 17-26, Dep. Geophys., Charles Univ., Prague.

Červený, V. (2001): *Seismic ray theory.* Cambridge University Press, Cambridge.

Červený, V.– Klimeš, L. & Pšenčík, I. (2007): Seismic ray method: Recent developments. *Advances in Geophysics*, **48**, pp. 1-126.

Šachl, L. (2011): 2D computations of 3D synthetic seismograms using the ray-based

Born approximation in heterogenous background model P1. In: Seismic Waves in Complex 3–D Structures, Report 21, pp. 99-114, Dep. Geophys., Charles Univ., Prague.

Šachl, L. (2011b): Born and ray-theory seismograms in 2D heterogenous isotropic models. Send to print in Seismic Waves in Complex 3–D Structures

Vavryčuk, V. (2003): Parabolic lines and caustics in homogenous weakly anisotropic solids. In: *Geophys. J. Int.*, **152**, pp. 318-334

Born and ray-theory seismograms in 2D heterogenous isotropic models

Libor Šachl

Charles University, Faculty of Mathematics and Physics, Department of Geophysics,
E-mail: sachl@karel.troja.mff.cuni.cz

Summary

The seismograms computed using the first-order ray-based Born approximation in the 2D heterogenous background model with the 2D heterogenous perturbation are presented. The Born seismograms are compared with the ray-theory seismograms computed in the perturbed model. The seismograms are computed for a set of receivers in order to see how the seismograms change. The rays in the perturbed model are computed to be able to identify the wavegroups in the seismograms. Similarly, the travel times of the diffracted waves are computed and highlighted in the seismograms.

Key words: Born approximation, ray theory, velocity model, perturbation

1 Introduction

This paper follows Šachl (2011) and Šachl (2011b). All three papers concern the computation of the Born approximation in the perturbed models constructed using model P1I. This last paper attempts, in a sense, to conclude this task. The first paper is dedicated to the choice of the P-wave velocity perturbation and the seismogram computation for one receiver in 2 (3) perturbed models. The second paper deals with the effects of caustics. Now we present the seismograms and ray diagrams computed in 16 perturbed models for 37 receivers. Some of them are presented also in Šachl (2011b). Here they appear again because first, they constitute one collection with the other seismograms and second, there remain pieces of information which were not mentioned yet, because they have no connection with the caustics.

2 Perturbed models and the background model

We have 16 models where we would like to obtain seismograms (perturbed models). The models are called P1-1-10%, P1-2-10%, ..., P1-16-10%. They are constructed using model P1I, which is described in Bulant & Martakis (2011). The background model is smooth model P1 described in the same paper. All models are 2D isotropic heterogenous velocity models situated into rectangle (0 km, 47.3 km) × (0 km, 6 km).

The density in the perturbed models is the same as in the background model and equal to $\rho = 1000$ kg/m^3 everywhere. The S-wave velocity $v_s = \frac{v_p}{\sqrt{3}}$. The P-wave velocity in each model is the same as in the background model except for one domain. The domain corresponds to "block j" of model P1I in the case of model P1-j-10%, see Figure 1. The

P-wave velocity in each of these domains is equal to the P-wave velocity in the background model plus 10% of the perturbation between the background model and model P1I. The perturbation is reduced to 10% in order to satisfy sufficiently low differences between the perturbed and the background model. This is the requirement of the Born approximation.

Figure 1: Blocks in model P1I. The colour of the block is determined by its index. The colour changes from green to red and blue. Block 1 is the leftmost green block.

3 Numerical computations

The x_1 coordinate is the horizontal coordinate, it grows from the left to the right. The x_3 coordinate is the vertical coordinate, it grows downwards. The origin of the coordinate system is in the upper left corner of the model.

Motivated by Bulant & Martakis (2011) we choose 37 receivers placed at the upper model boundary. The first receiver has the horizontal coordinate $x_1 = 16$ km. The spacing between the receivers is 0.5 km, therefore, the last receiver has the horizontal coordinate $x_1 = 34$ km.

The explosive source is also placed at the upper model boundary, $x_1 = 25$ km, $x_3 = 0$ km. Its position is the same as the position of the 19th receiver. The source time function is a Gabor signal with a prevailing frequency 10 Hz, filtered by a frequency filter which is non-zero only for frequencies f, 1 Hz $< f <$ 20 Hz. There is a cosine tapering for 1 Hz $< f <$ 2 Hz and 19 Hz $< f <$ 20 Hz while for 2 Hz $< f <$ 19 Hz the filter is equal to one. Only P waves are considered.

The two-point ray tracing in models P1-1-10%, ..., P1-16-10% is performed first. The two-point rays computed in these models are depicted in Figures 4,...,27. The rays from the first elementary wave reflect at the first reached interface. The rays from the second elementary wave transmit through the first and reflect at the second reached interface.

The rays are shot into the whole lower half plane in computing the Born seismograms. We use the basic system of rays containing 121 rays, which covers the straight angle into which the rays are shot.

We use the appropriate amplitude cut-off applied to the Green function in computing the Born seismograms. For more details see Šachl (2011b).

We computed the Born seismograms using these settings . The reference solution is the ray-theory seismogram. The seismograms computed in models P1-1-10%, ..., P1-16-10% are depicted in Figures 28, ..., 47 respectively. The first component is shown. Each set of seismograms computed in one model is scaled by one number, which is written in the caption under the figure depicting the seismogram.

The abscissas in the seismograms denote the travel times of the diffracted waves. The waves are diffracted from the edges of the block containing the perturbation of the elastic parameters. The travel times are computed in the background model, because the Born

approximation uses quantities from the background model. Most blocks in model P1I have 4 edges. The colours associated with the edges are in Table 1.

Edge	left upper	left lower	right upper	right lower
Color	green	pink	forest green	blue

Table 1: The edges of the block and the colours of the corresponding abscissas highlighting the travel times of the waves diffracted from the edges.

Three blocks are exceptional. Block 3 and block 16 have only 3 edges, block 10 has 5 edges: In block 3, there are no diffracted waves (computed by the ray theory) from the rightmost edge. The remaining two edges are taken as the left upper and left lower edges. In block 16, there are no diffracted waves from the leftmost edge. The remaining two edges are taken as the right upper and right lower edges. In block 10, there are no diffracted waves from the two edges located at the upper model boundary. The two edges at the right hand side are taken as the right upper and right lower edges, the remaining edge is taken as the left lower edge.

We shall describe the computed seismograms now. The weird wavegroups described in Šachl (2011b) and the diffractions from the caustics are no more discussed.

4 Description of the computed seismograms

4.1 Model P1-1-10%

The seismograms are depicted in Figure 28. The ray diagrams of the first elementary wave are depicted in Figure 4. The reflected waves in the ray-theory seismograms are weak until $x_1 = 19$ km. They end at $x_1 = 21$ km. The ray reflects very close to the right lower edge of the block, see Figure 4. The Born seismograms continue with the diffracted waves highlighted by the blue abscissas. This phenomenon is often observed also in other the seismograms.

The waves diffracted from the right upper edge are visible for the receivers between $x_1 = 16$ km and $x_1 = 22$ km. These waves arrive too late for the other receivers. The waves diffracted from the left upper and left lower edges are not visible. They arrive later. The first diffracted wave from these edges does not arrive earlier then in approximately 7.9 s.

4.2 Model P1-2-10%

The seismograms are depicted in Figure 29. The ray diagrams of the first elementary wave are depicted in Figure 5. The ray-theory seismograms are non-zero for the receivers between $x_1 = 21.5$ km and $x_1 = 33$ km. Concerning the diffracted waves, only the waves diffracted from the left upper and left lower edge are visible, similarly as in model P1-1-10%. For example: The last ray, which incidents to the receiver at $x_1 = 21.5$, reflects very close to the left lower edge, see the ray diagram displayed in Figure 5. The Born seismograms are therefore nonzero for the receivers between $x_1 = 16$ km and $x_1 = 21$ km and smoothly continue with the diffractions from the left lower edge highlighted by the pink abscissas.

This model is discussed in Šachl (2011b).

4.3 Model P1-3-10%

The seismograms are depicted in Figure 30. There are no any two-point rays in this model, therefore, there is neither a ray diagram nor ray-theory seismograms. There are diffracted waves in the Born seismogram. The wavegroups visible in the seismogram for the receiver at $x_1 = 16$ km in approximately 1.9 s and also slightly for the receiver at $x_1 = 16.5$ km are discussed below.

4.4 Model P1-4-10%

The seismograms are depicted in Figure 31. The ray diagrams of the first and second elementary wave are depicted in Figure 6 and Figure 7 respectively. There are waves penetrating to the shadow in the Born seismograms, some diffracted waves (Notice that the reflections visible in the ray-theory seismograms e.g. between $x_1 = 16$ km and $x_1 = 18$ km have virtually the same travel times as the diffractions from the right lower edge highlighted by the blue abscissas.), but the most interesting are the strong wavegroups in the Born seismograms for the receivers between $x_1 = 16$ km and $x_1 = 19$ km.

The Born approximation computed in the background model contains not only the reflected and the diffracted waves but also the corrections of the direct waves. The ray diagram of the direct wave computed in the background model is depicted in Figure 2 together with the blocks in model P1I. The rays in Figure 2 travel through blocks 10, 12, 14, 15, 16.

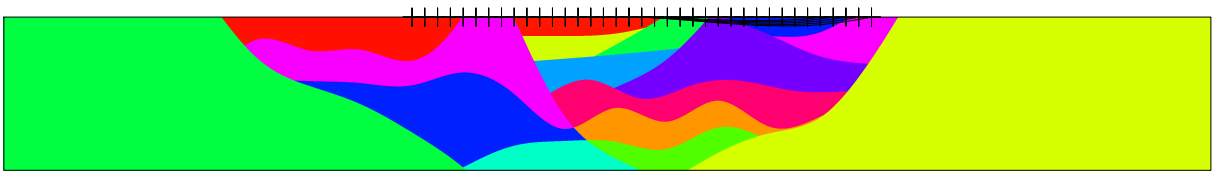

Figure 2: The ray diagram of the direct wave computed in the background model depicted together with the blocks in model P1I.

Thus, we expect the most important contribution to the correction of the direct wave in models P1-10-10%, P1-12-10%, P1-14-10%, P1-15-10%, P1-16-10%, because in these models the perturbation of the elastic parameters is nonzero in some of the listed blocks. This behaviour is really observed, see the seismograms computed in these models. It seems that these corrections of the direct waves are generated also in models P1-3-10% and P1-4-10%. The corrections are rather weak in the seismograms computed in model P1-3-10% but the positions of these wavegroups correspond to the already mentioned strong wavegroups in the Born seismograms computed in model P1-4-10%.

There are no rays crossing block 3 or block 4 in Figure 2. All two-point rays incident to the receivers situated on the right hand side of the model. However, there would be probably also rays incident to the receivers situated on the left hand side of the model if the model was defined for $x_3 < 0$ km. Notice that the amplitude of the wavegroups grow from $x_1 = 19.5$ km to $x_1 = 16$ km in both Figure 30 and Figure 31. This behaviour is expected as the length of the ray effected by the perturbation of the elastic parameters grows. Our conclusion is that the strong wavegroups observed in the Born seismograms in model P1-4-10% for the receivers between $x_1 = 16$ km and $x_1 = 19$ km and much weaker wavegroups observed in model P1-3-10% are the corrections of the direct waves.

4.5 Model P1-5-10%

The seismograms are depicted in Figure 32. The ray diagrams of the first and second elementary wave are depicted in Figure 8 and Figure 9 respectively. There are 4 arrivals for the receivers between $x_1 = 16$ km and $x_1 = 20.5$ km, 2 arrivals for the receivers between $x_1 = 21$ km and $x_1 = 23$ km and 1 arrival for the receivers at $x_1 = 29$ km and $x_1 = 29.5$ km, see the ray diagrams. Four waves visible at $x_1 = 20.5$ km are:

The first two waves are from the first elementary wave. The stronger wave is the reflection from the upper part of the block. The weaker wave is reflected close to the right upper edge.

The next two waves are from the second elementary wave. The wave which arrives earlier is the reflection from the right lower interface. This wave continues for the receivers at $x_1 \geq 21$ km with the diffractions from the right lower edge highlighted by the blue abscissas. The wave which arrives later is reflected from the left lower interface. This wave continues for the receivers at $x_1 \geq 21$ km with the diffractions from the left lower edge highlighted by the pink abscissas.

A similar continuation to the shadow zone is observed in case of the waves visible at $x_1 = 29$ km and $x_1 = 29.5$ km.

This model is discussed in Šachl (2011b).

4.6 Model P1-6-10%

The seismograms are depicted in Figure 33. The ray diagrams of the first and second elementary wave are depicted in Figure 10 and Figure 11 respectively. The ray-theory seismograms contain mainly the rays from the first elementary wave. Only one ray from the second elementary wave incidents to the receiver at $x_1 = 21$ km. There is a stronger wavegroup in the ray theory seismogram for the receiver at $x_1 = 28.5$ km. This wavegroup is a superposition of two waves as we can see from the diagram in Figure 10. We observe the diffracted waves in the seismogram. The remaining unexplained waves distinguishable between the dark green and the blue abscissas for the receivers between $x_1 = 16$ km and $x_1 = 23$ km seem to be the reflections from the lower boundary of the computational grid. This problem is discussed in Šachl (2011c).

4.7 Model P1-7-10%

The seismograms are depicted in Figure 34. The ray diagrams of the first and second elementary wave are depicted in Figure 12 and Figure 13 respectively. We observe the diffracted waves which provide smooth transition to the shadow zone in the Born seismograms. One example: The single wave visible in the ray-theory seismogram for the receiver at $x_1 = 21$ km reflects very close to the left upper edge of block 7, see Figure 12. The receivers between $x_1 = 16$ km and $x_1 = 20.5$ km record the waves diffracted from the left upper edge highlighted by the green abscissas.

This model is discussed in Šachl (2011b).

4.8 Model P1-8-10%

The seismograms are depicted in Figure 35. Quite complicated ray diagrams of the first and second elementary wave are depicted in Figure 14 and Figure 15 respectively. There

are only waves from the first elementary wave in the seismograms for the receivers between $x_1 = 16$ km and $x_1 = 20.5$ km. Further, we see that the ray from the second elementary wave reflects from the lower interface of block 8 close to the left lower edge and incidents to the receiver at $x_1 = 21$ km at 2 s. The receivers placed at $x_1 \leq 21$ km detect the waves diffracted from the left lower edge. The waves are highlighted by the pink abscissas in the Born seismograms. A similar situation is observed for 2 rays from the second elementary wave, which reflect from the left interface of block 8, see the ray diagram and the seismograms for the receivers at $x_1 = 29$ km and $x_1 = 29.5$ km at approximately 2.6 s. And notice also the wavegroups highlighted by the forest green abscissas in the Born seismograms for the receivers between $x_1 = 30$ km and $x_1 = 31$ km. These wavegroups should be the transition of the waves reflected close to the right upper edge to the shadow zone.

4.9 Model P1-9-10%

The seismograms are depicted in Figure 36. The ray diagrams of the first and second elementary wave are depicted in Figure 16 and Figure 17 respectively. The ray diagrams are quite complicated similarly to the ray diagrams in model P1-8-10%. We observe a triplication on both elementary waves, see Šachl (2011b) too. We can also see several diffracted waves. One example: The waves arriving last to the receivers between $x_1 = 27.5$ km and $x_1 = 29.5$ km in the ray-theory seismograms are the reflections from the left interface of block 9. They continue as the diffracted waves in the Born seismograms.

4.10 Model P1-10-10%

The seismograms are depicted in Figure 37. The ray diagrams of the first and second elementary wave are depicted in Figure 18 and Figure 19 respectively. The locations of these waves in the seismograms are following. The waves from the first elementary wave are visible for the receivers between $x_1 = 18$ km and $x_1 = 27$ km, they arrive first. There is a triplication on the second elementary wave apparent in the ray diagram in Figure 19. The triplication is visible in the seismograms for the receivers between $x_1 = 25$ km and $x_1 = 26.5$ km at approximately 1.3 s. The rays from the second elementary wave reflected from the right interface of block 10 arrives to the receivers at $x_1 = 32$ km and $x_1 = 32.5$ km at approximately 2.3 s. The remaining waves in the ray-theory seismograms are the waves from the second elementary wave.

We point out that the Born seismograms coincide well with the ray-theory seismogram in the whole set of seismograms (with the exception of the correction of the direct wave, see below). However, the Born seismograms are nonzero even in the shadow zone. See e.g. the wavegroups in the Born seismograms for the receivers between $x_1 = 16$ km and $x_1 = 18$ km highlighted by the pink abscissas. These wavegroups are the diffractions from the left lower edge of block 10.

The strong wavegroups in the seismograms are the corrections of the direct waves. The seismograms for the receivers between $x_1 = 28$ km and $x_1 = 34$ km are depicted once more separately using smaller scale in Figure 44. The ray-theory signal is computed by subtracting the direct wave computed in the background model from the direct wave computed in the perturbed model. If we compare the ray-theory and Born corrections, the travel times coincide well, but there are some differences in the amplitudes.

4.11 Model P1-11-10%

The seismograms are depicted in Figure 38. The ray diagrams of the first and second elementary wave are depicted in Figure 20 and Figure 21 respectively. The waves from the first elementary wave arrive first in the ray-theory seismograms. The waves from the second elementary wave reflected from the left interface of block 11 are detected by the receivers between $x_1 = 24$ km and $x_1 = 27.5$ km. These waves arrive last in the ray-theory seismograms. Notice that these signals continue in the Born seismograms by the waves diffracted from the left upper and left lower edge of block 11. The remaining wavegroups in the ray-theory seismograms are the reflections from the right and lower interface. The diffracted waves which continue these waves are again observed in the Born seismograms.

4.12 Model P1-12-10%

The seismograms are depicted in Figure 39. The ray diagrams of the first and second elementary wave are depicted in Figure 22 and Figure 23 respectively. The waves from the first elementary wave incident to the receivers between $x_1 = 16$ km and $x_1 = 25.5$ km. The waves from the second elementary wave incident to the receivers between $x_1 = 20.5$ km and $x_1 = 27$ km. The receivers between $x_1 = 20.5$ km and $x_1 = 25.5$ km detect waves from both elementary waves. The waves from the first elementary wave arrive earlier.

The strong wavegroups in the Born seismograms are the corrections of the direct waves similarly as in model P1-10-10%. The seismograms for the receivers between $x_1 = 26$ km and $x_1 = 34$ km are depicted once more separately using smaller scale in Figure 45.

The waves diffracted from the left lower edge of block 12 are observed in the Born seismograms. The waves are highlighted by the pink abscissas for the receivers between $x_1 = 16$ km and $x_1 = 20$ km. The waves diffracted from the other edges of block 12 are probably also computed by the Born approximation. Unfortunately, they are not clearly visible due to the corrections of the direct waves.

4.13 Model P1-13-10%

The seismograms are depicted in Figure 40. The ray diagrams of the first and second elementary wave are depicted in Figure 24 and Figure 25 respectively. We recognize the waves from the second elementary wave reflected from the left interface. These waves are visible in the seismograms for the receivers between $x_1 = 22.5$ km and $x_1 = 23.5$ km, they arrive at about 1.5 s.

It is interesting, that we observe significant discrepancy between the ray-theory and Born seismograms for the receivers between $x_1 = 19.5$ km and $x_1 = 21$ km, although the ray-theory and Born seismograms coincide well for the receivers between $x_1 = 22.5$ km and $x_1 = 23.5$ km.

The waves from the second elementary wave continue with the waves diffracted from the left lower edge of block 13 for the receivers at $x_1 \leq 22$ km and from the left upper edge of block 13 for the receivers at $x_1 \geq 24$ km. The waves diffracted from the right upper and right lower edge of block 13 are virtually not observed. They are probably weak.

4.14 Model P1-14-10%

The seismograms are depicted in Figure 41. The ray diagram of the first elementary wave is depicted in Figure 26. There are no two-point rays from the second elementary wave. Despite the fact that the ray diagram in Figure 26 is not difficult, we observe discrepancies between the ray-theory and Born seismograms. There is one exception. The strong waves in the Born seismograms for the receivers between $x_1 = 25.5$ km and 34 km are probably the corrections of the direct waves. The ray-theory correction does not appear in so many seismograms but if it appears, it is similar to the correction predicted by the Born approximation.

4.15 Model P1-15-10%

The seismograms for the receivers between $x_1 = 16$ km and $x_1 = 31$ km are depicted in Figure 42. The seismograms for the receivers between $x_1 = 31.5$ km and $x_1 = 34$ km are depicted separately in Figure 46. The reason is that the Born seismograms for the receivers between $x_1 = 31.5$ km and $x_1 = 34$ km contain big corrections of the direct waves. In other words, we need two scales for one set of seismograms computed in model P1-15-10%. Unfortunately, due to the smaller scaling in the seismograms in Figure 46 we do not see anything else than the corrections of the direct waves. However, we do not miss anything. The seismograms for the receivers between $x_1 = 31.5$ km and $x_1 = 34$ km are similar to the seismograms for the receivers between $x_1 = 16$ km and $x_1 = 31$ km. The only new thing, apart from the corrections of the direct waves, is one arrival for the receiver at $x_1 = 33$ km. The corresponding ray is depicted in the ray diagram in Figure 27.

The seismograms displayed in Figure 46 depict the corrections of the direct waves. The highest amplitudes are in the seismograms for the receivers at $x_1 = 33.5$ km and $x_1 = 34$ km. The ray-theory seismogram for the receiver at $x_1 = 31.5$ is zero, but the Born approximation predicts some correction even for this receiver.

Still opened question is what are the other wavegroups.

4.16 Model P1-16-10%

The seismograms computed in this model are similar to the seismograms computed in the previous model. There are no any two-point rays in this model, therefore, there is neither a ray diagram nor ray-theory seismograms. The seismograms for the receivers between $x_1 = 16$ km and $x_1 = 28.5$ km are depicted in Figure 43. They contain diffracted waves and some other unknown wavegroups. The seismograms for the receivers between $x_1 = 29$ km and $x_1 = 34$ km are depicted in Figure 47. The seismograms for the receiver at $x_1 = 31.5$ km are not shown. The ray-theory seismogram contains huge correction of the direct wave. The reason is that there arise a new ray of the direct wave, which incidents to this receiver in the perturbed model. This sudden change is not correct. The amplitude should change smoothly as in the Born approximation.

As you see, we understand the main features of the presented seismograms. However, there still remains some unrecognized wavegroups or differences between the ray-theory and Born seismograms.

One possibility is that the unrecognized wavegroups are the diffracted waves arisen due to the imperfect coverage of the block which contains nonzero perturbations. Figure 3 depicts how the ray shot close to the upper model boundary can bend downwards. Blocks 2, 10, 12, 14, 15, 16 are not covered perfectly. New incorrect edges and waves diffracted from these edges arise.

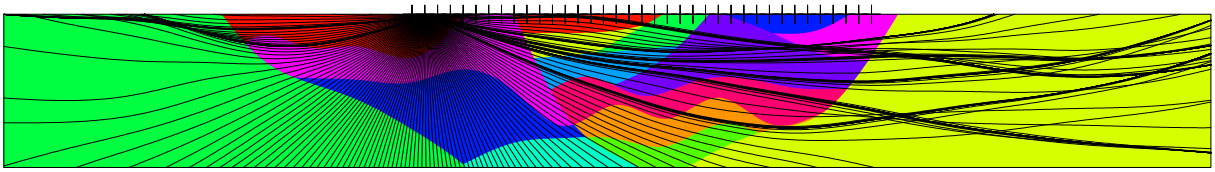

Figure 3: Coverage of smooth model P1 with the rays in shooting from the position of the 2nd receiver. The rays are depicted together with the blocks in model P1I.

5 Concluding remarks

The ray-theory and Born seismograms are computed and compared in heterogenous 2D models. We try to identify and discuss the individual wavegroups. We state that the Born seismograms contain, apart from the reflected waves, the diffracted waves and the corrections of the direct waves. The ray-theory seismograms computed in the perturbed model are zero in the shadow zone. The Born seismograms are nonzero. The reflected waves often continue with the diffracted waves.

Acknowledgements

First of all I would like to thank Luděk Klimeš, who greatly helped me with the work which led to this paper. I would also like to thank Petr Bulant because he provided me model P1 and the history files, which he used for seismogram computation and visualization of the medium parameters. Hence if I wanted to compute the reference seismogram or to visualize some quantities I used parts of these history files (or the whole history files) and adjusted them as necessary.

The research has been supported by the Grant Agency of the Czech Republic under contract P210/10/0736, by the Ministry of Education of the Czech Republic within research project MSM0021620860, and by the members of the consortium "Seismic Waves in Complex 3-D Structures" (see "http://sw3d.cz").

References

Bulant, P. & Martakis, N. (2011): Constructing model P1I for reflection studies. Seismic Waves in Complex 3–D Structures, Report 21, pp. 17-26, Dep. Geophys., Charles Univ., Prague.

Šachl, L. (2011): 2D computations of 3D synthetic seismograms using the ray-based

Born approximation in heterogenous background model P1. In: Seismic Waves in Complex 3–D Structures, Report 21, pp. 99-114, Dep. Geophys., Charles Univ., Prague.

Šachl, L. (2011b): Effect of caustics to the ray-based Born approximation. Send to print in Seismic Waves in Complex 3–D Structures.

Šachl, L. (2011c): 3D and 2D computations of 3D synthetic seismograms using the ray-based Born approximation in simple models. In: Seismic Waves in Complex 3–D Structures, Report 21, pp. 69-98, Dep. Geophys., Charles Univ., Prague.

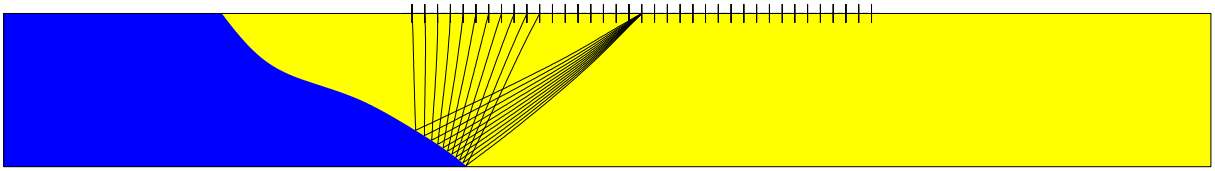

Figure 4: The first elementary wave computed in model P1-1-10%.

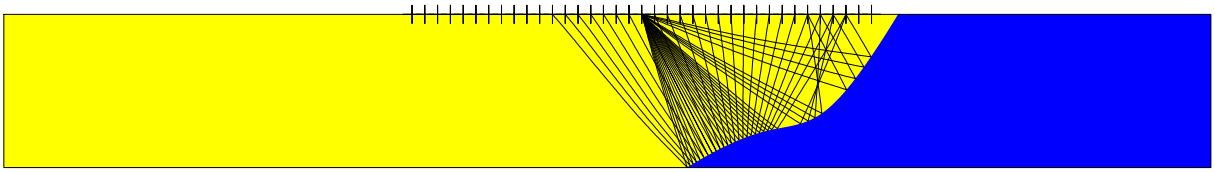

Figure 5: The first elementary wave computed in model P1-2-10%.

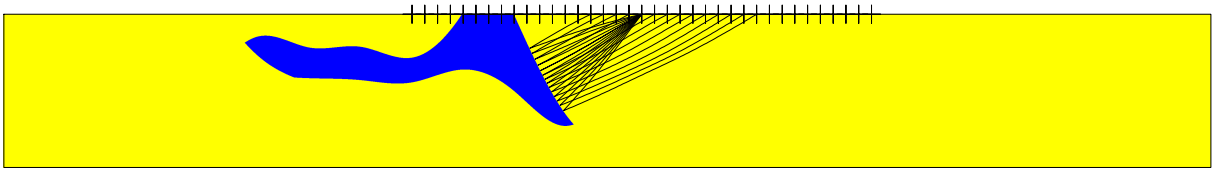

Figure 6: The first elementary wave computed in model P1-4-10%.

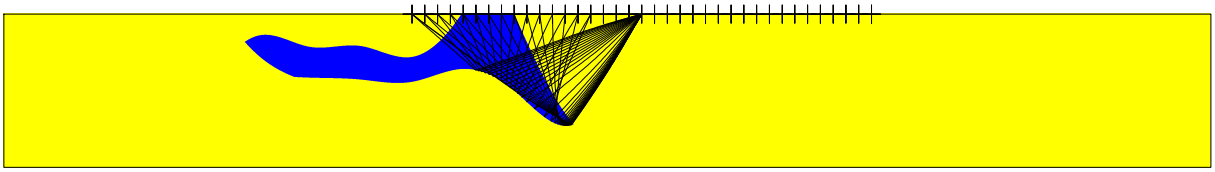

Figure 7: The second elementary wave computed in model P1-4-10%.

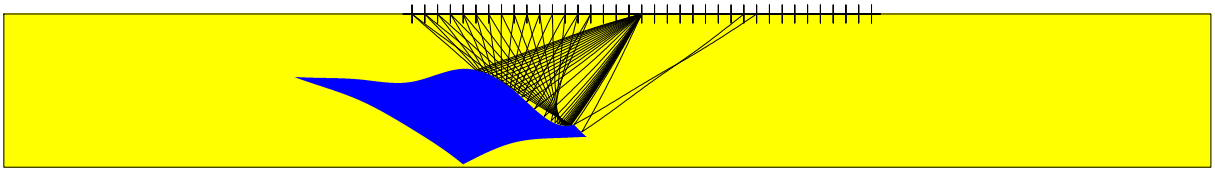

Figure 8: The first elementary wave computed in model P1-5-10%.

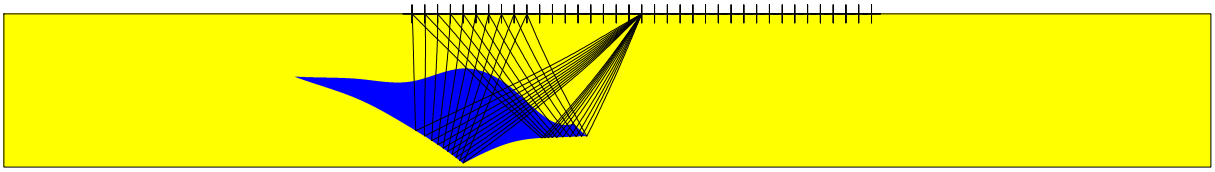

Figure 9: The second elementary wave computed in model P1-5-10%.

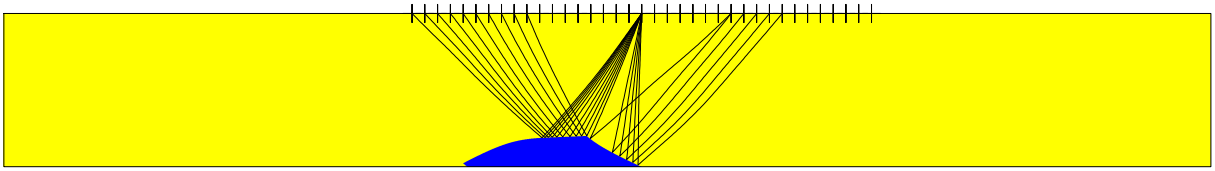

Figure 10: The first elementary wave computed in model P1-6-10%.

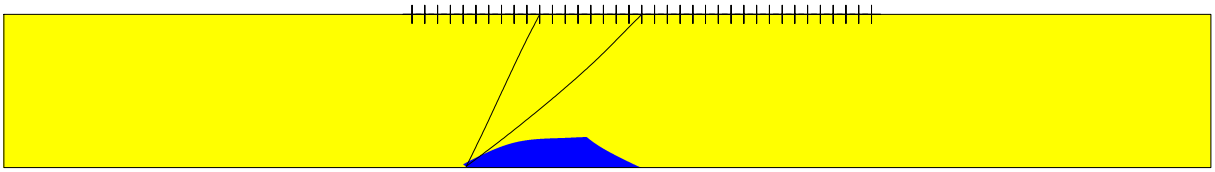

Figure 11: The second elementary wave computed in model P1-6-10%.

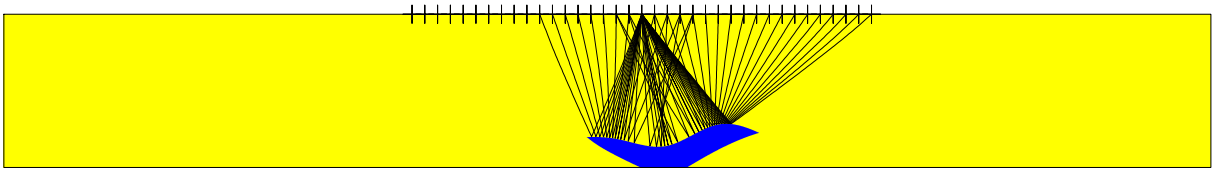

Figure 12: The first elementary wave computed in model P1-7-10%.

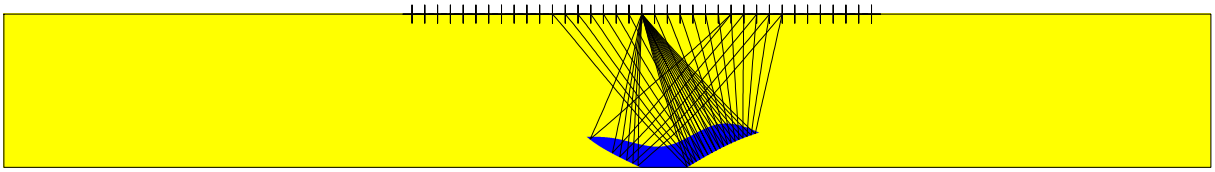

Figure 13: The second elementary wave computed in model P1-7-10%.

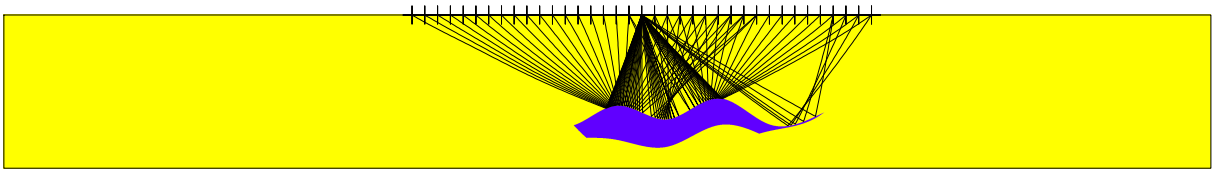

Figure 14: The first elementary wave computed in model P1-8-10%.

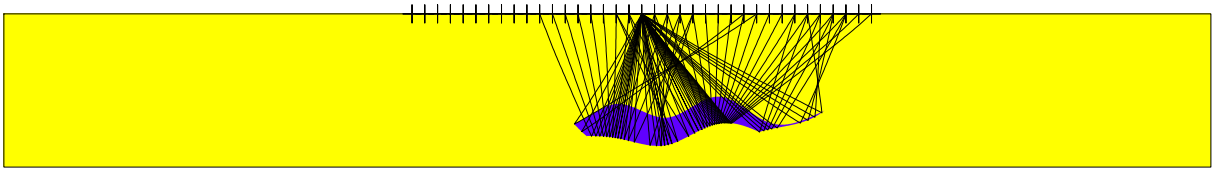

Figure 15: The second elementary wave computed in model P1-8-10%.

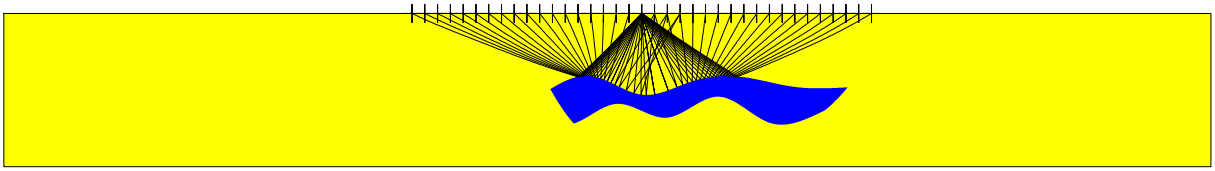

Figure 16: The first elementary wave computed in model P1-9-10%.

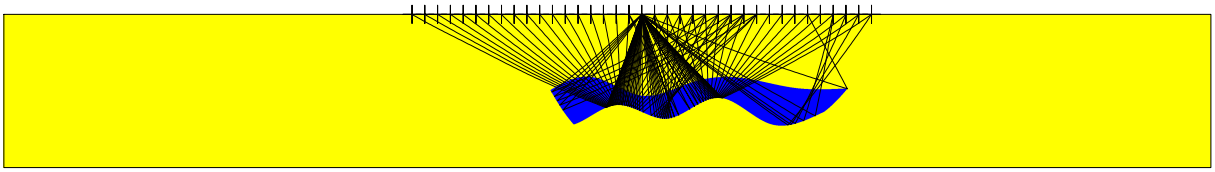

Figure 17: The second elementary wave computed in model P1-9-10%.

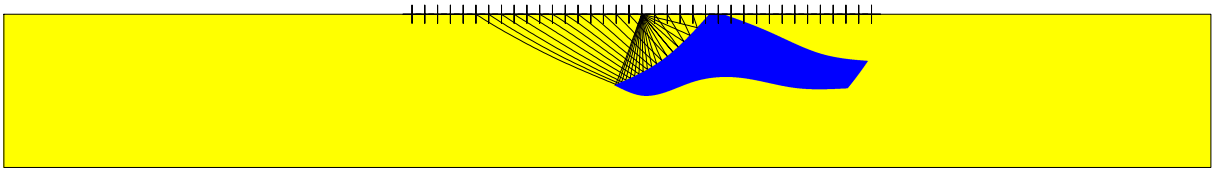

Figure 18: The first elementary wave computed in model P1-10-10%.

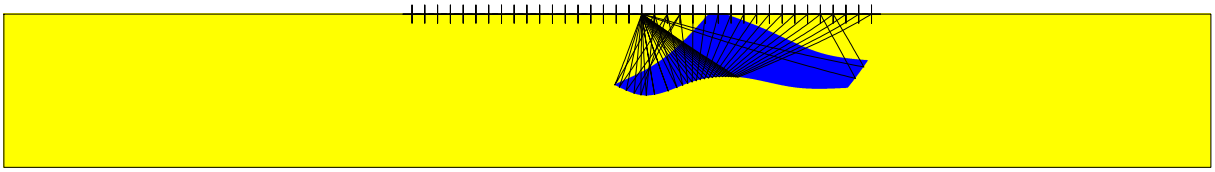

Figure 19: The second elementary wave computed in model P1-10-10%.

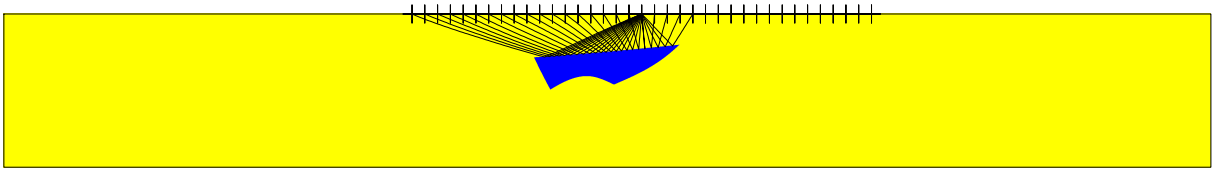

Figure 20: The first elementary wave computed in model P1-11-10%.

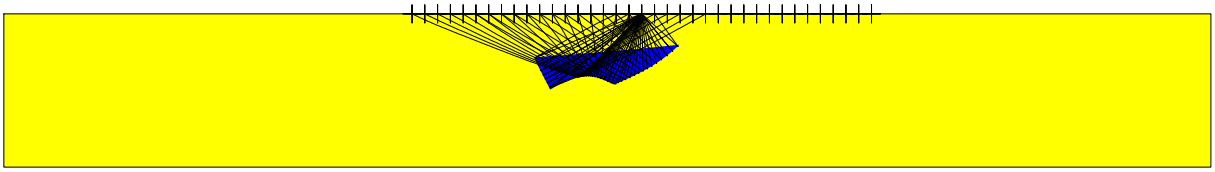

Figure 21: The second elementary wave computed in model P1-11-10%.

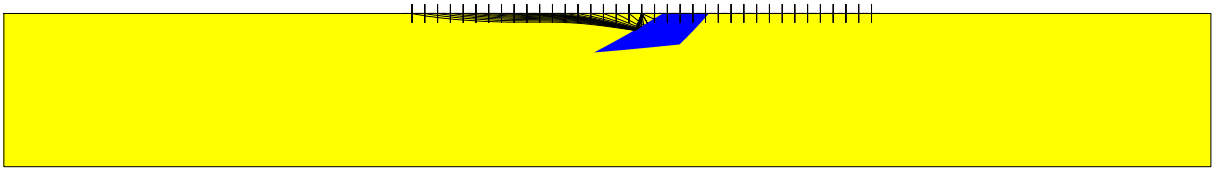

Figure 22: The first elementary wave computed in model P1-12-10%.

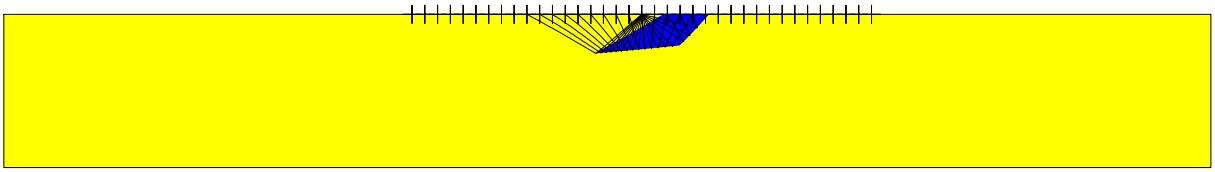

Figure 23: The second elementary wave computed in model P1-12-10%.

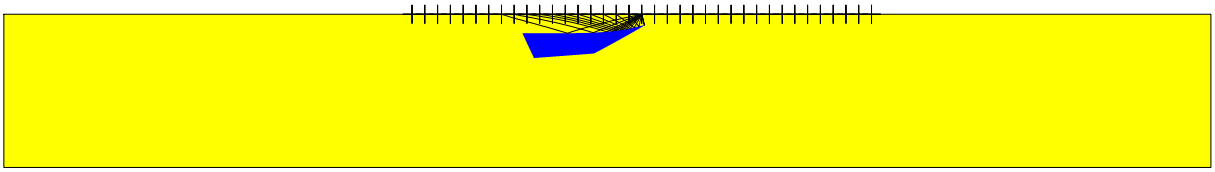

Figure 24: The first elementary wave computed in model P1-13-10%.

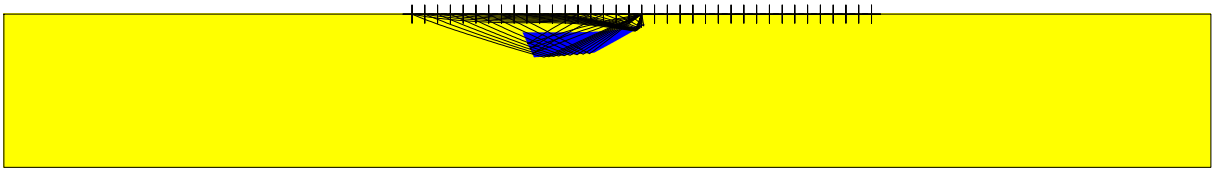

Figure 25: The second elementary wave computed in model P1-13-10%.

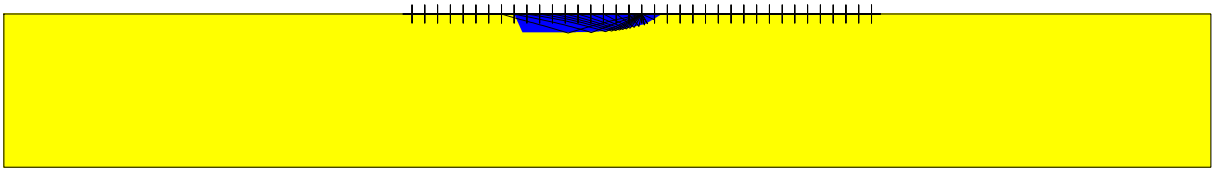

Figure 26: The first elementary wave computed in model P1-14-10%.

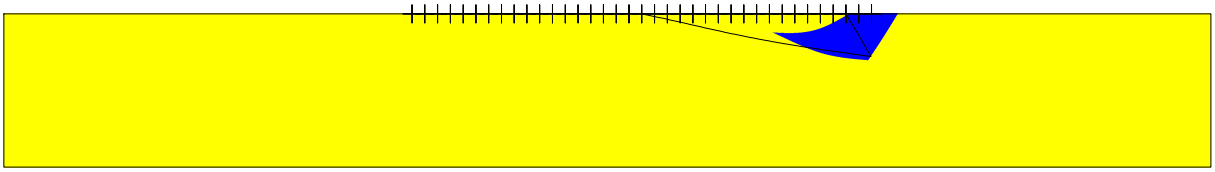

Figure 27: The second elementary wave computed in model P1-15-10%.

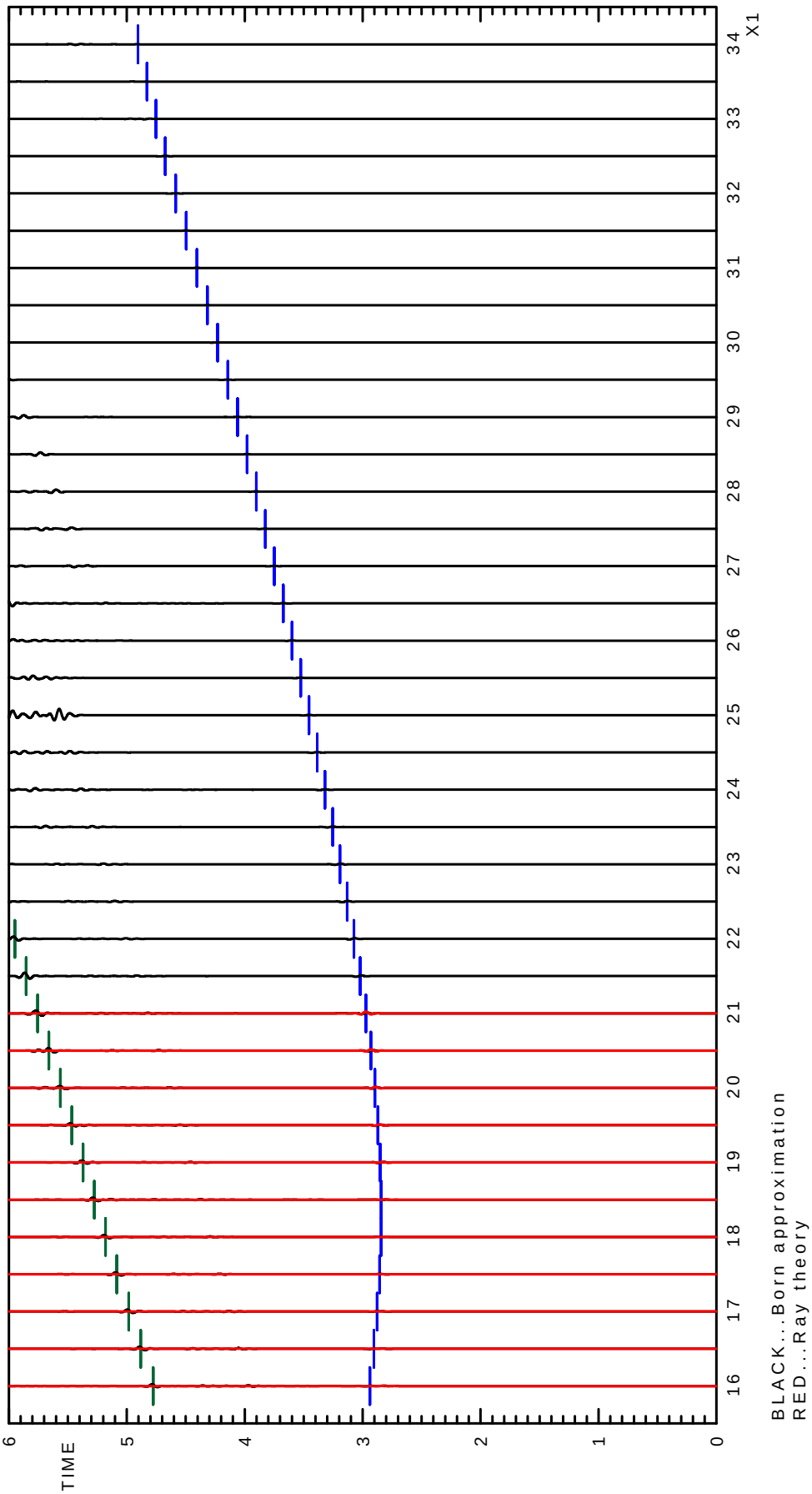

Figure 28: Born and ray-theory seismograms computed in model P1-1-10% scaled by 2×10^5.

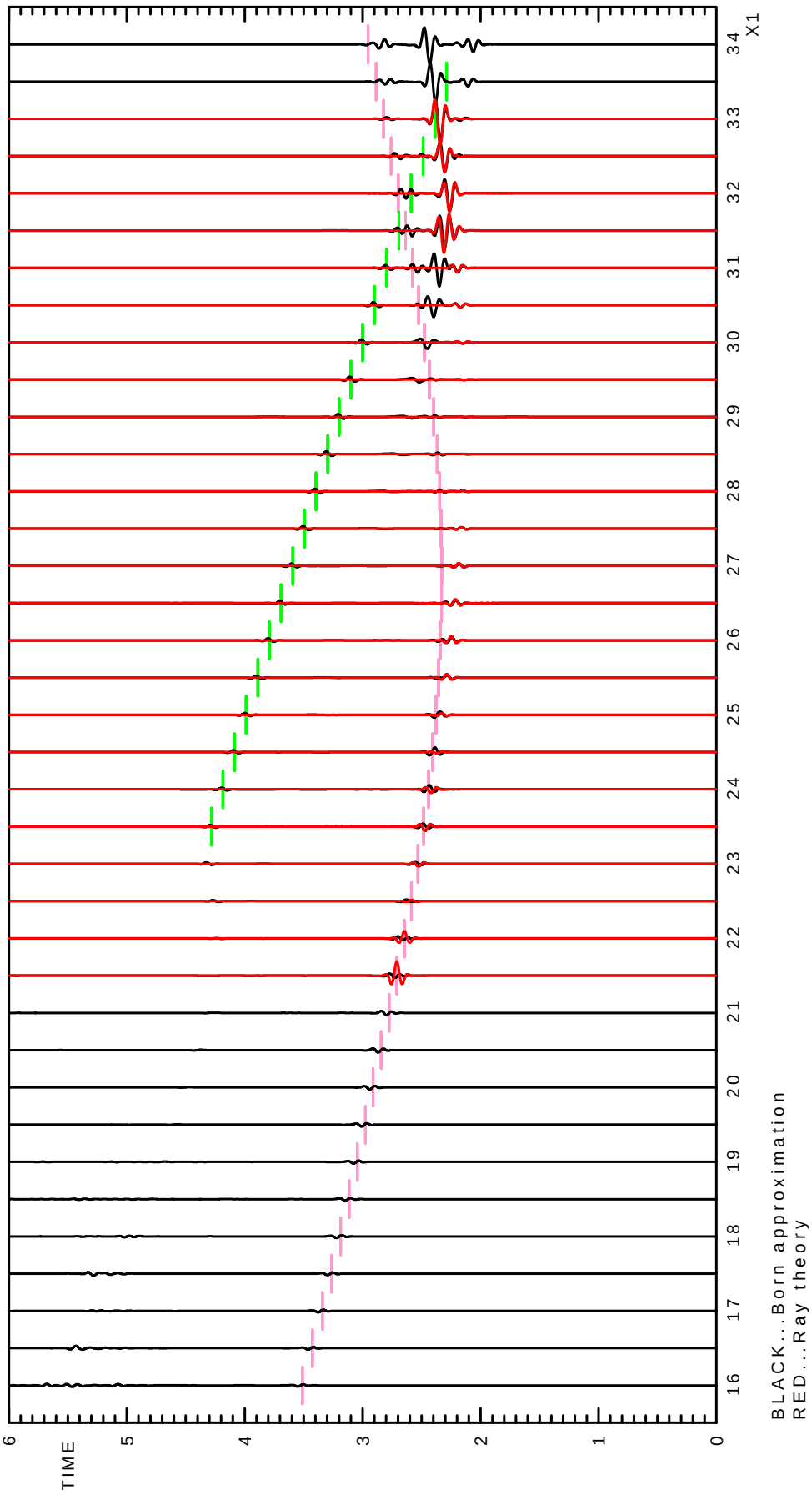

Figure 29: Born and ray-theory seismograms computed in model P1-2-10% scaled by 2×10^5.

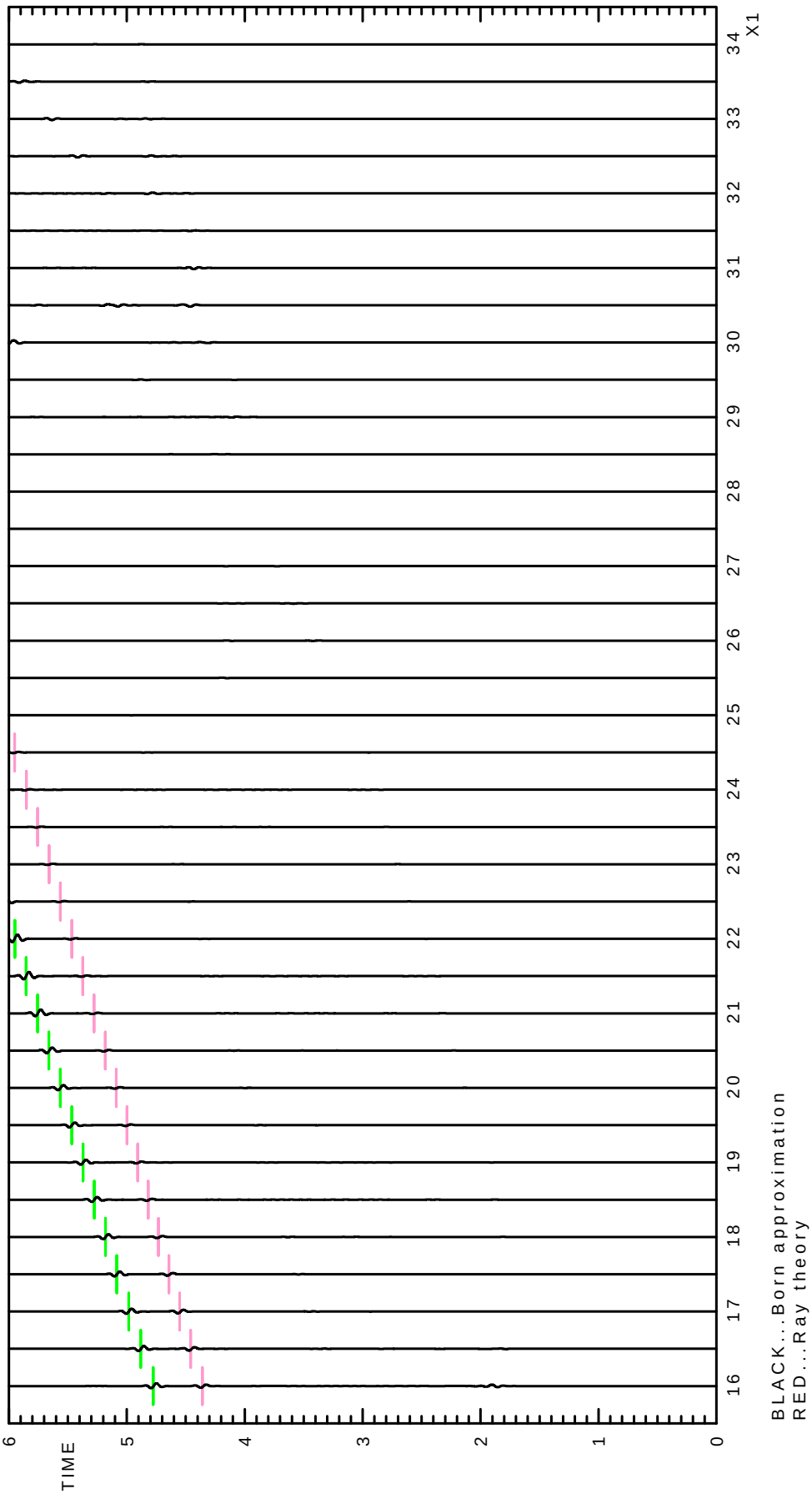

Figure 30: Born and ray-theory seismograms computed in model P1-3-10% scaled by 2×10^5.

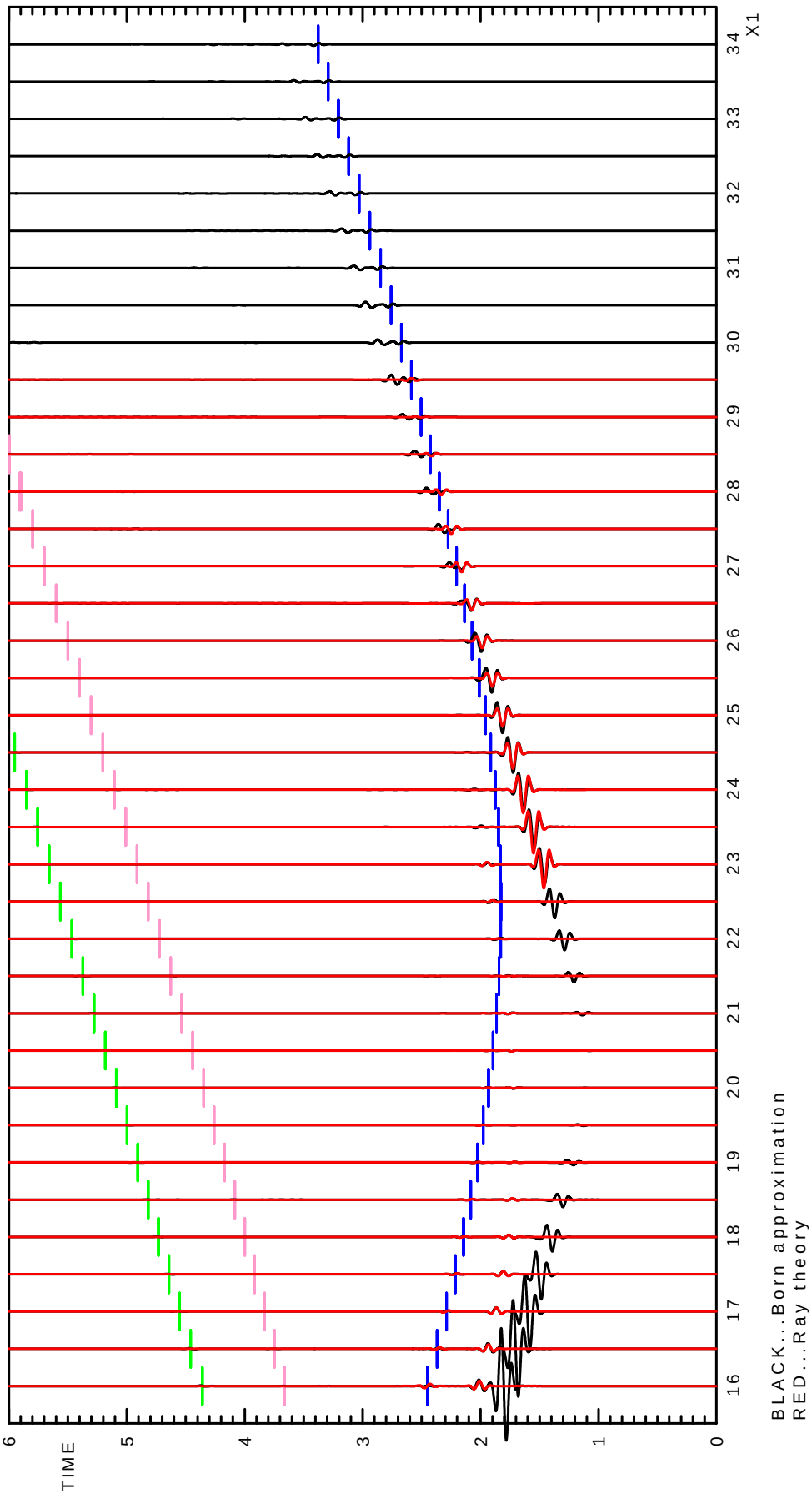

Figure 31: Born and ray-theory seismograms computed in model P1-4-10% scaled by 3×10^4.

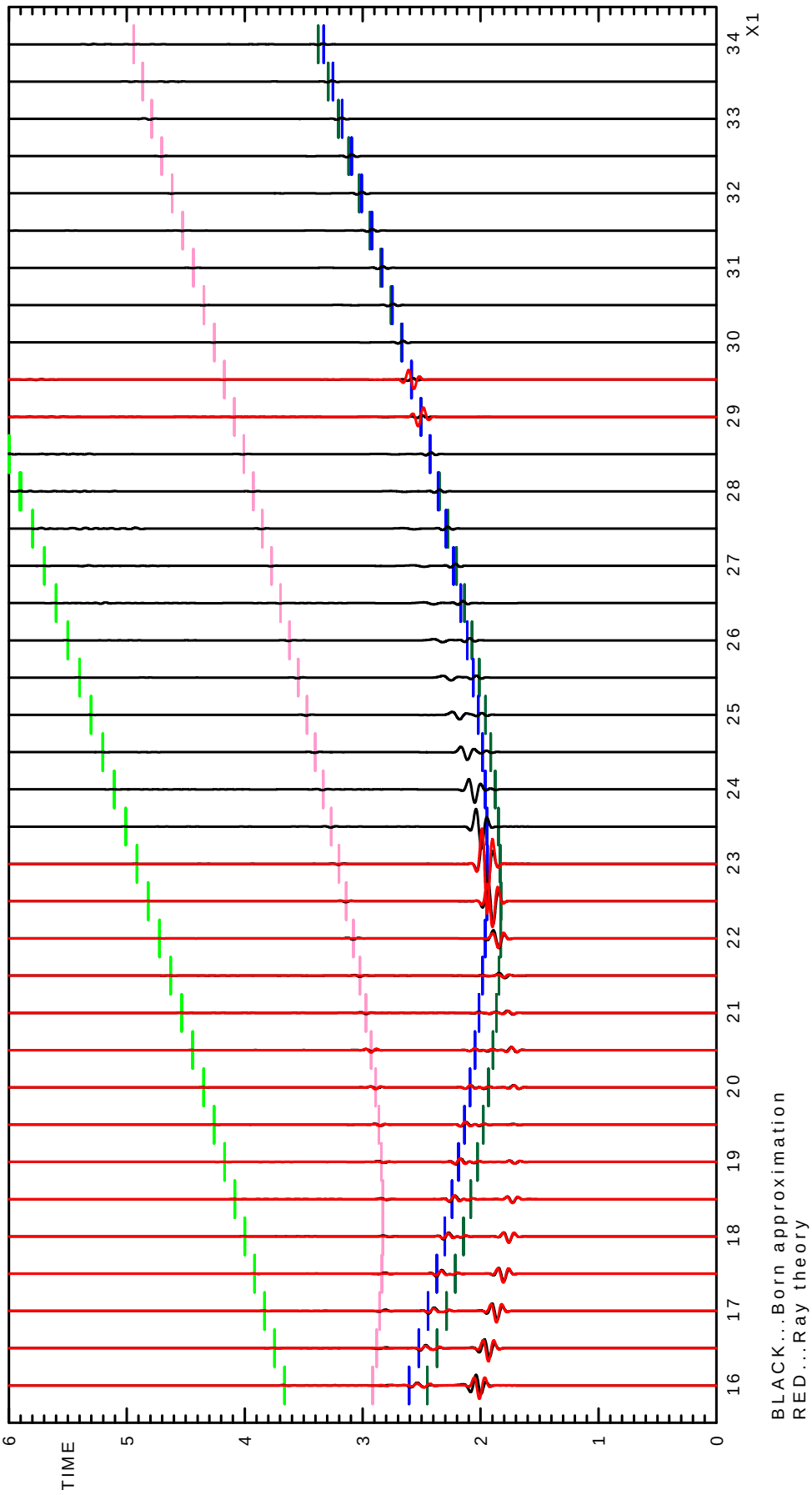

Figure 32: Born and ray-theory seismograms computed in model P1-5-10% scaled by 2×10^5.

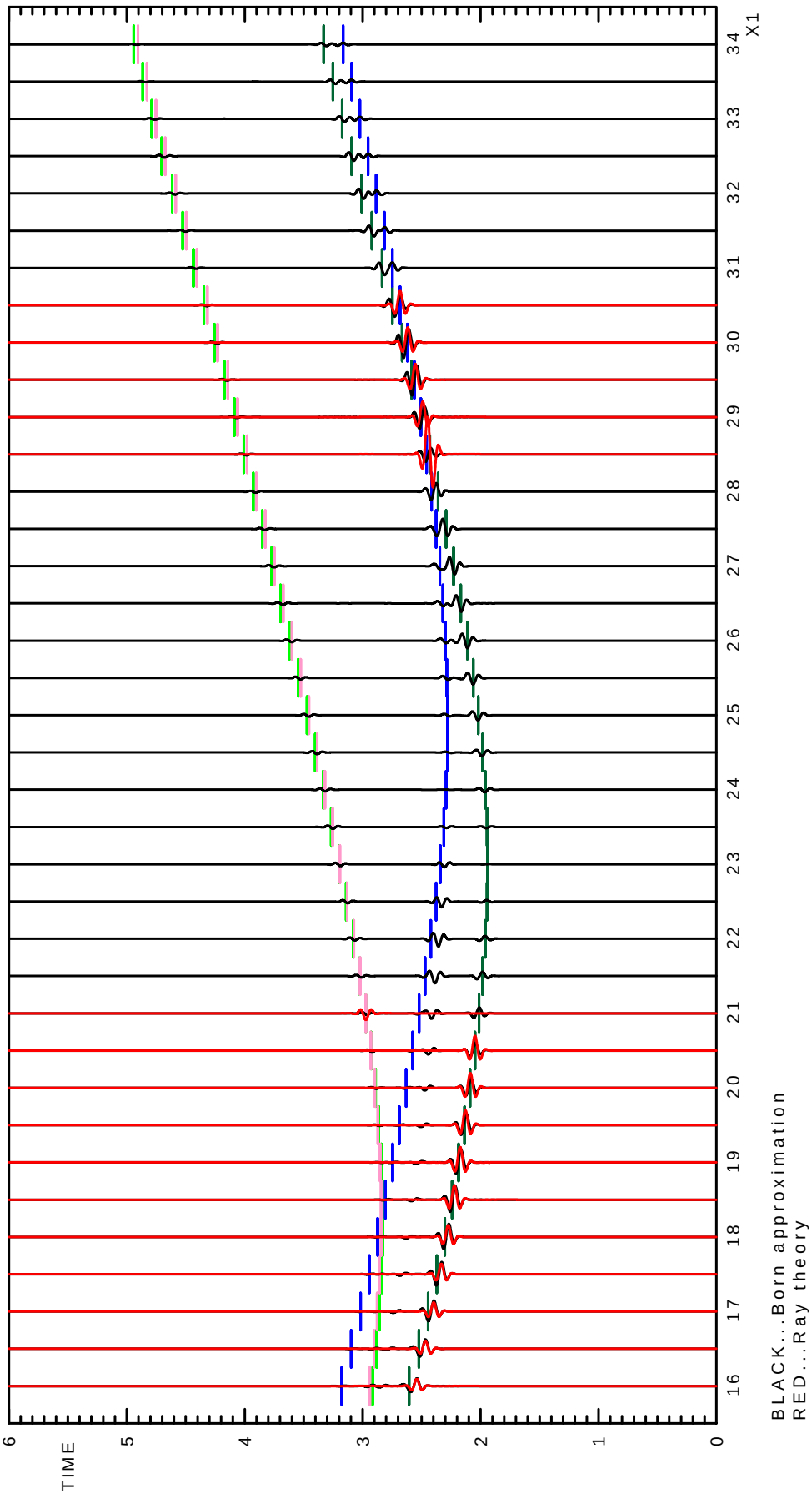

Figure 33: Born and ray-theory seismograms computed in model P1-6-10% scaled by 2×10^5.

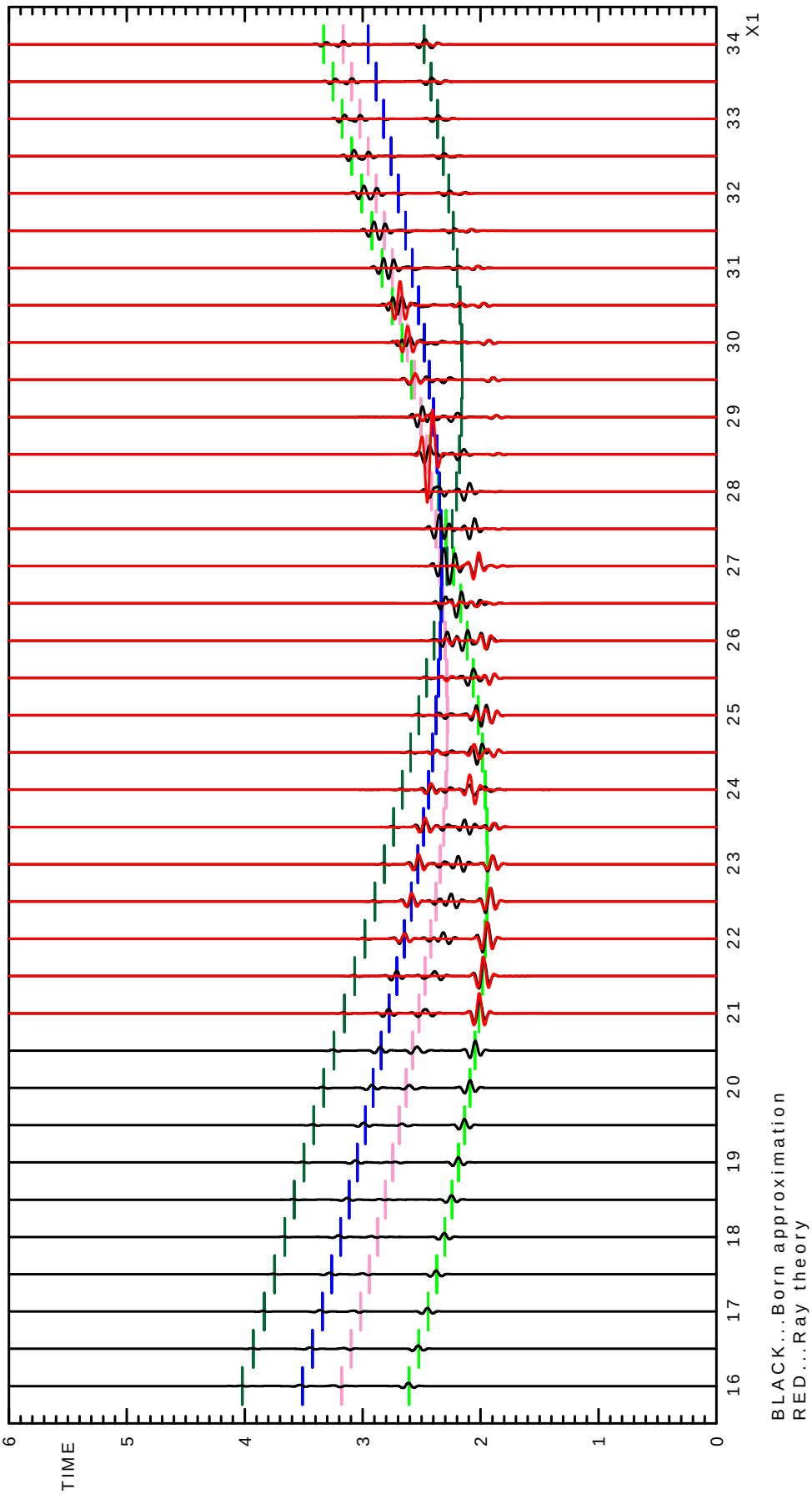

Figure 34: Born and ray-theory seismograms computed in model P1-7-10% scaled by 2×10^5.

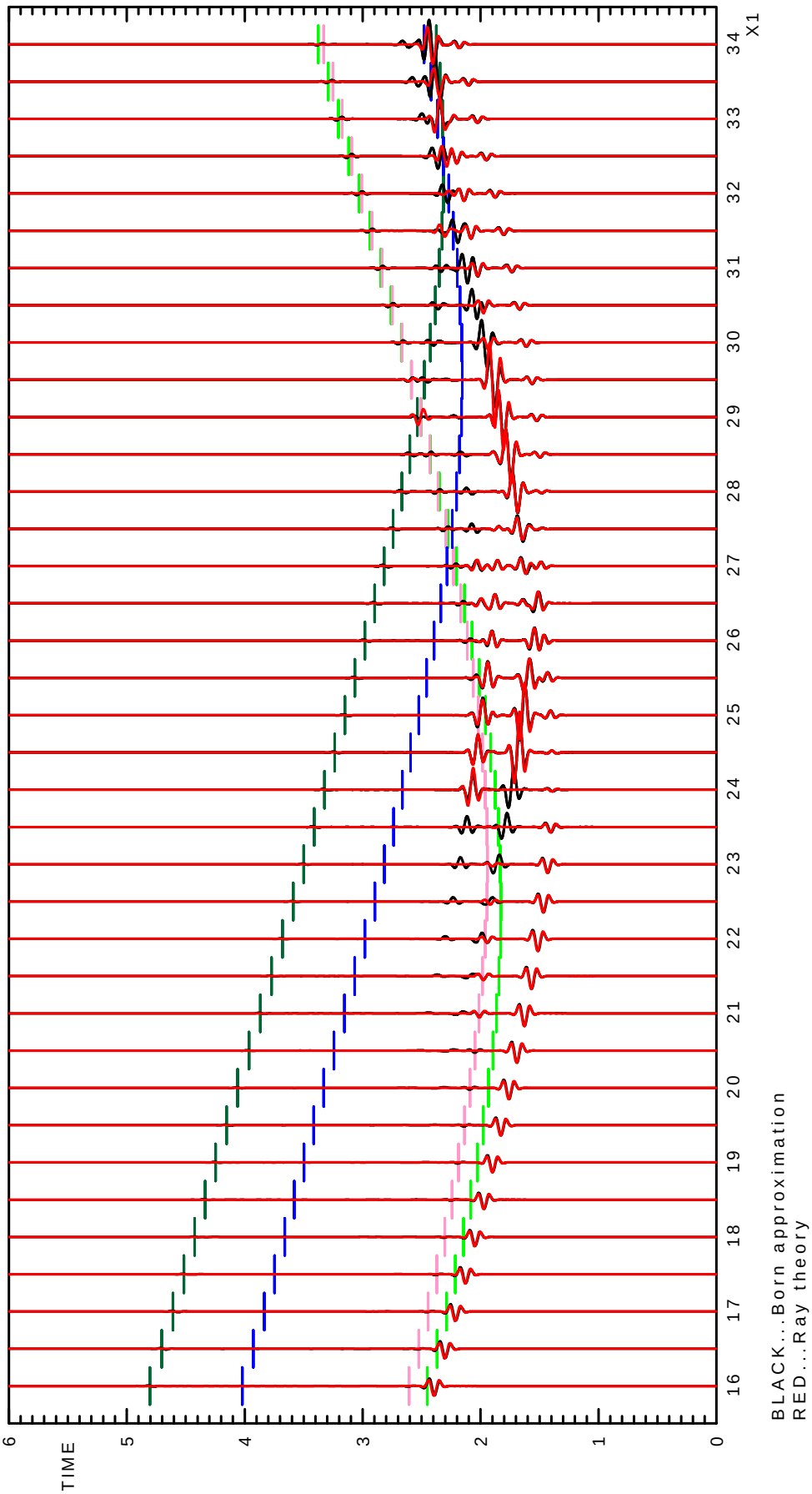

Figure 35: Born and ray-theory seismograms computed in model P1-8-10% scaled by 1×10^5.

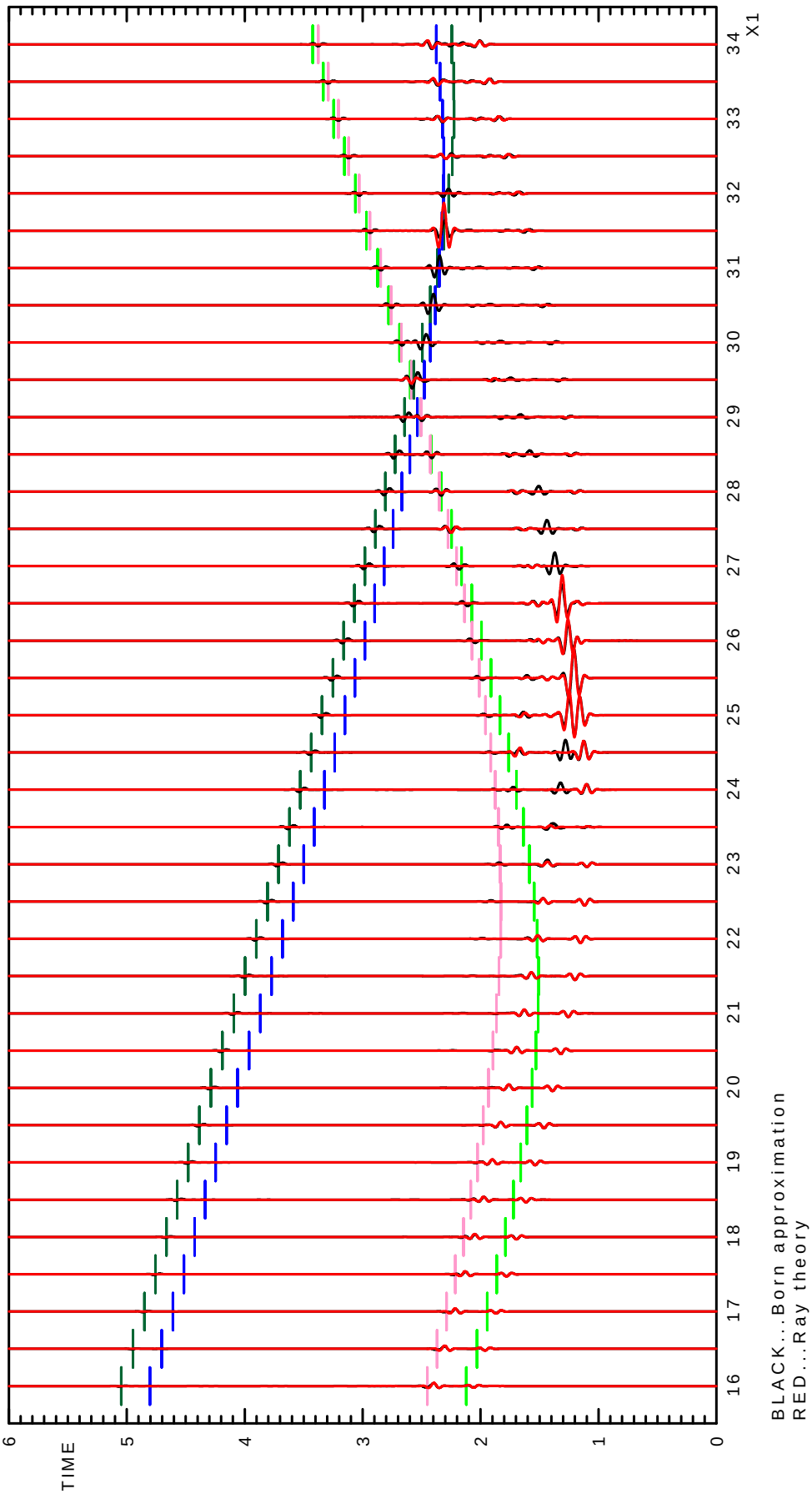

Figure 36: Born and ray-theory seismograms computed in model P1-9-10% scaled by 3×10^4.

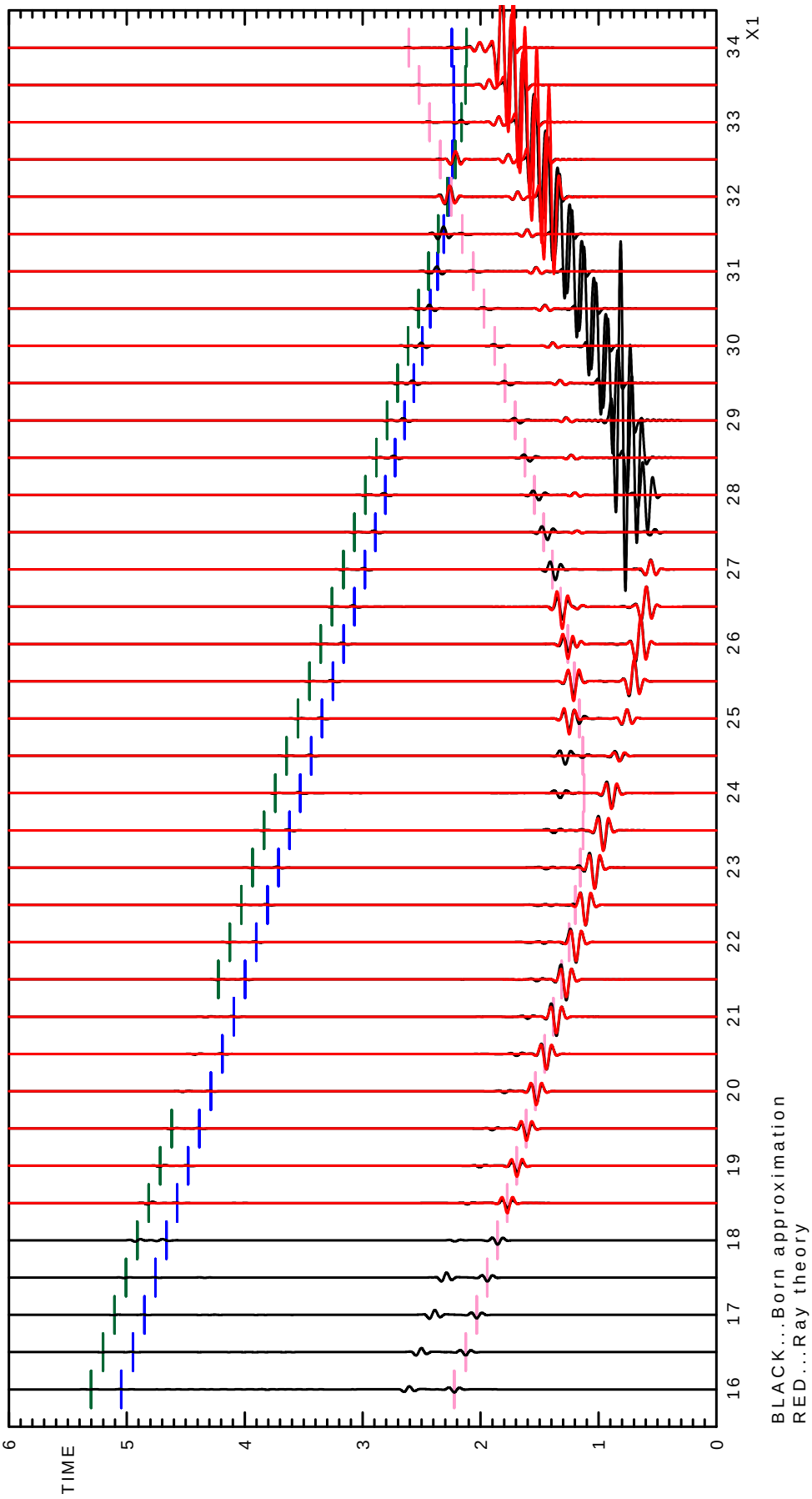

Figure 37: Born and ray-theory seismograms computed in model P1-10-10% scaled by 2×10^4.

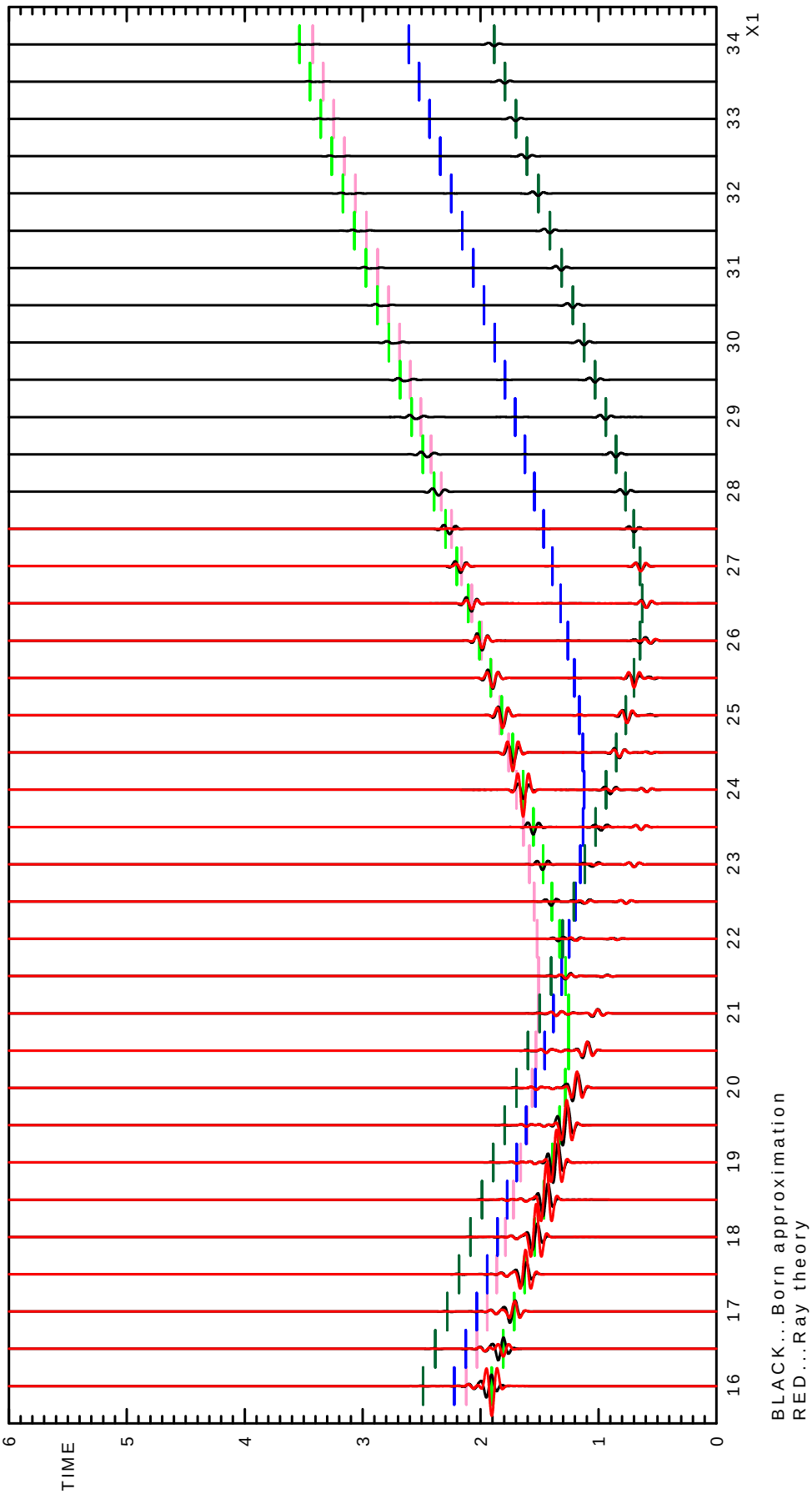

Figure 38: Born and ray-theory seismograms computed in model P1-11-10% scaled by 1×10^4.

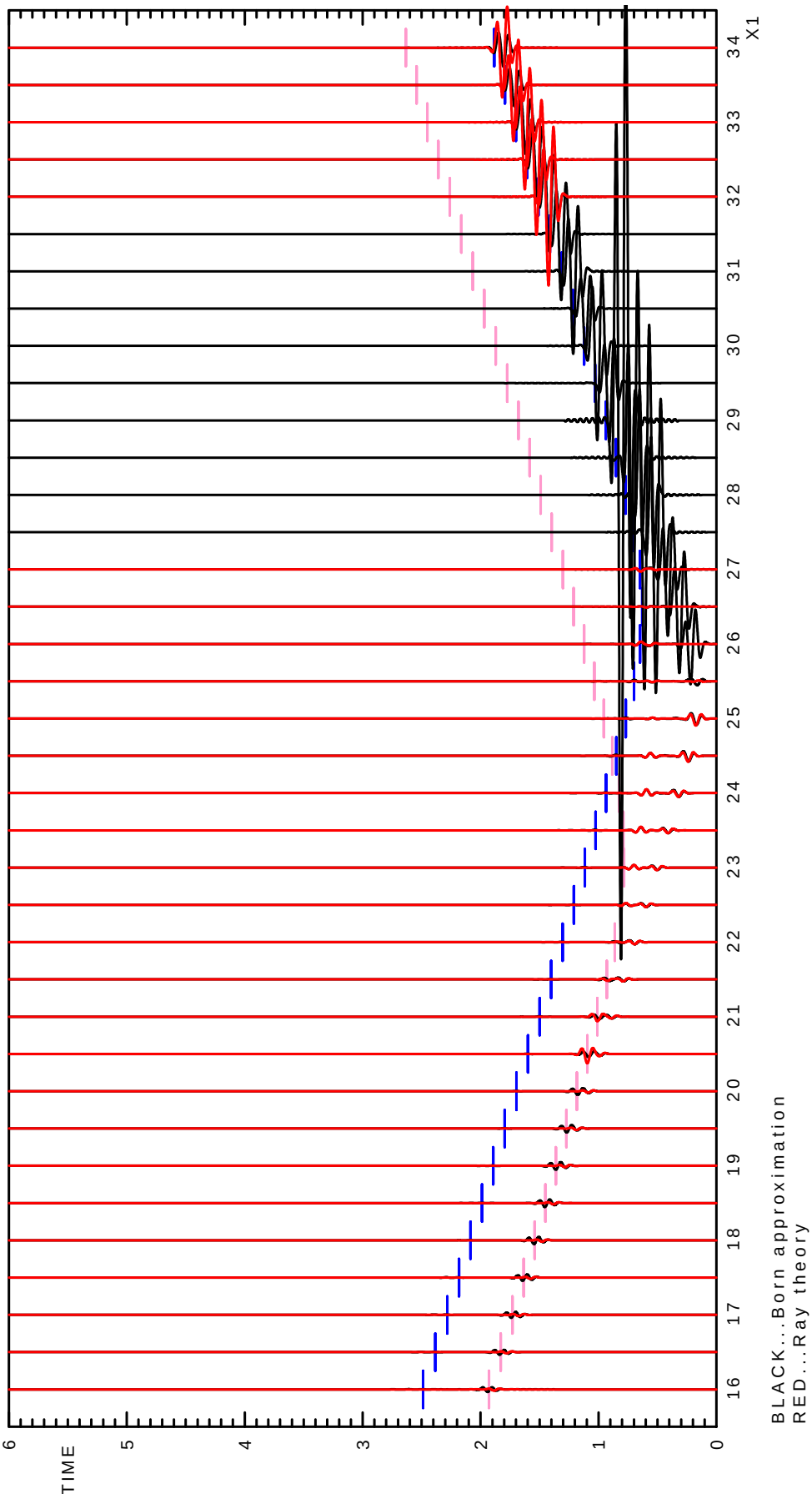

Figure 39: Born and ray-theory seismograms computed in model P1-12-10% scaled by 6×10^3.

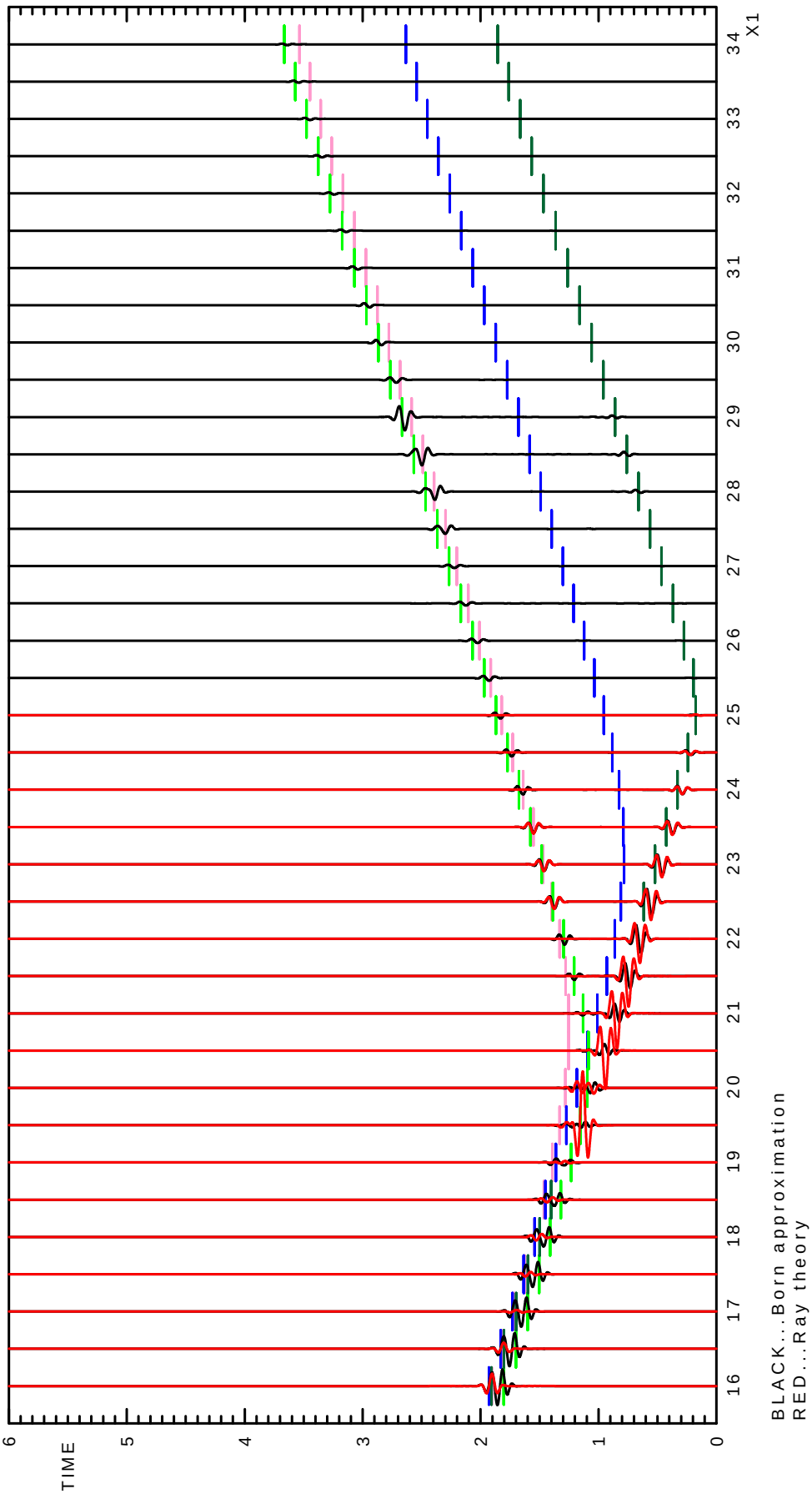

Figure 40: Born and ray-theory seismograms computed in model P1-13-10% scaled by 4×10^3.

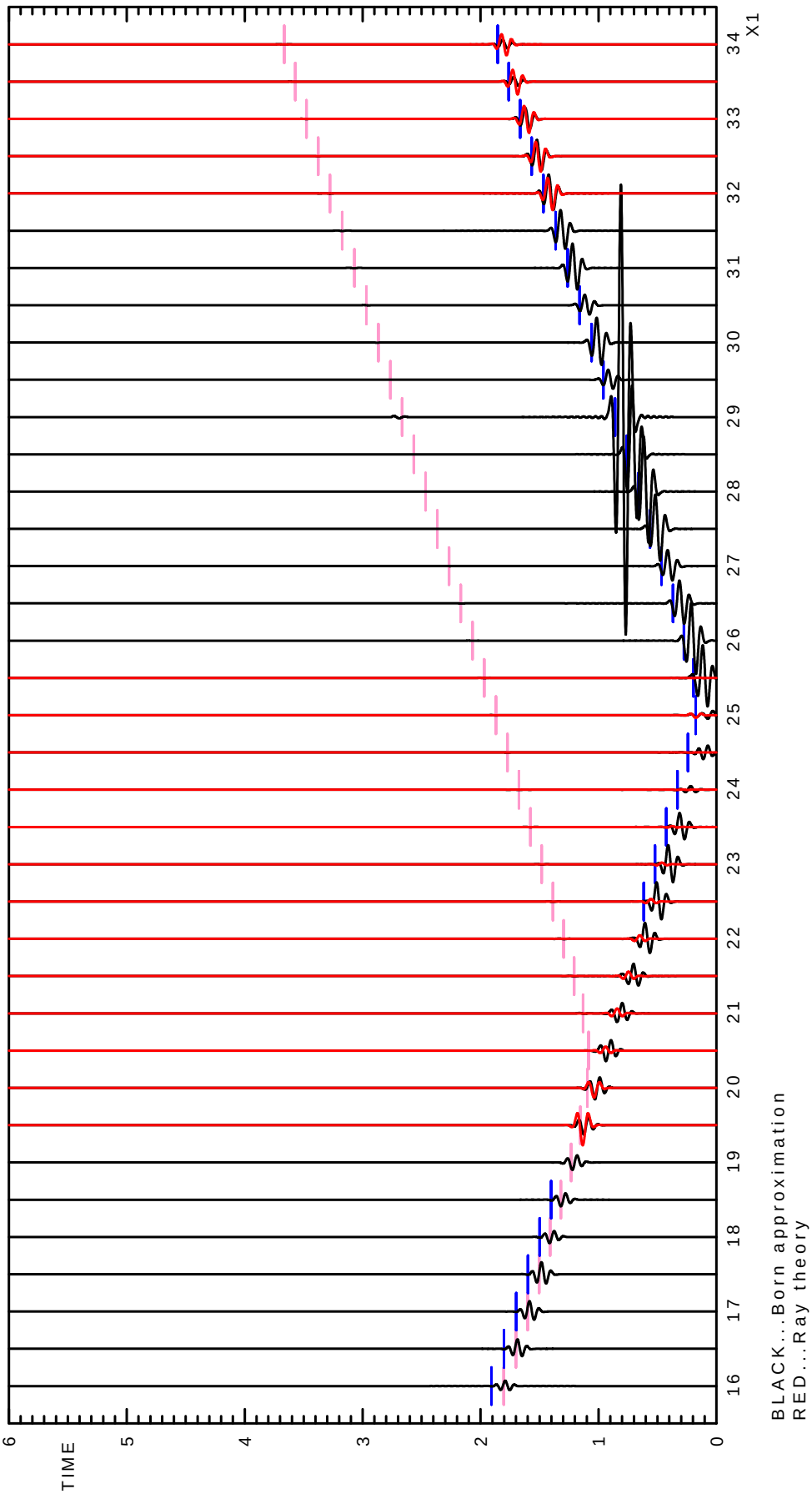

Figure 41: Born and ray-theory seismograms computed in model P1-14-10% scaled by 2×10^3.

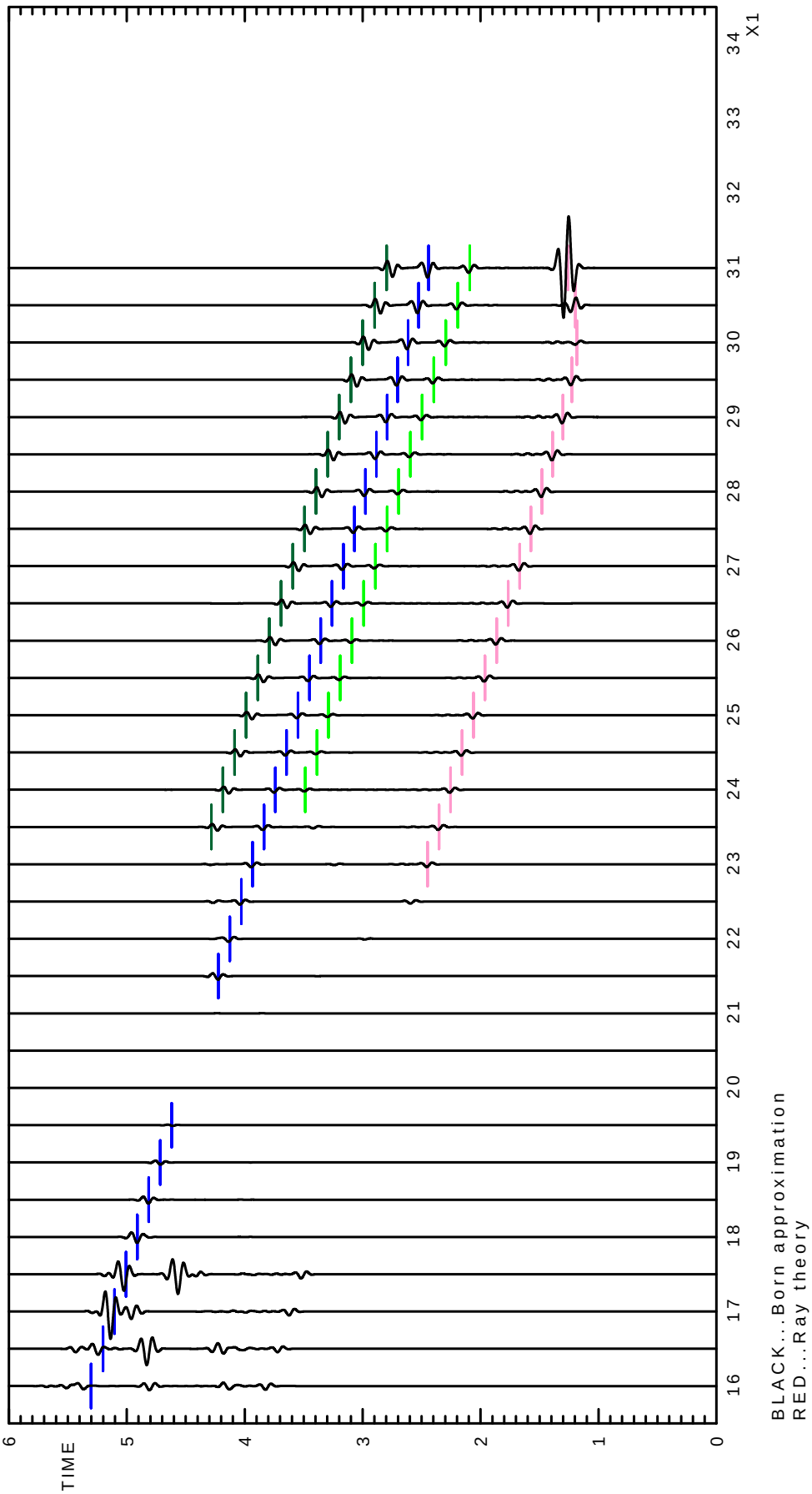

Figure 42: Born and ray-theory seismograms computed in model P1-15-10% scaled by 2×10^5.

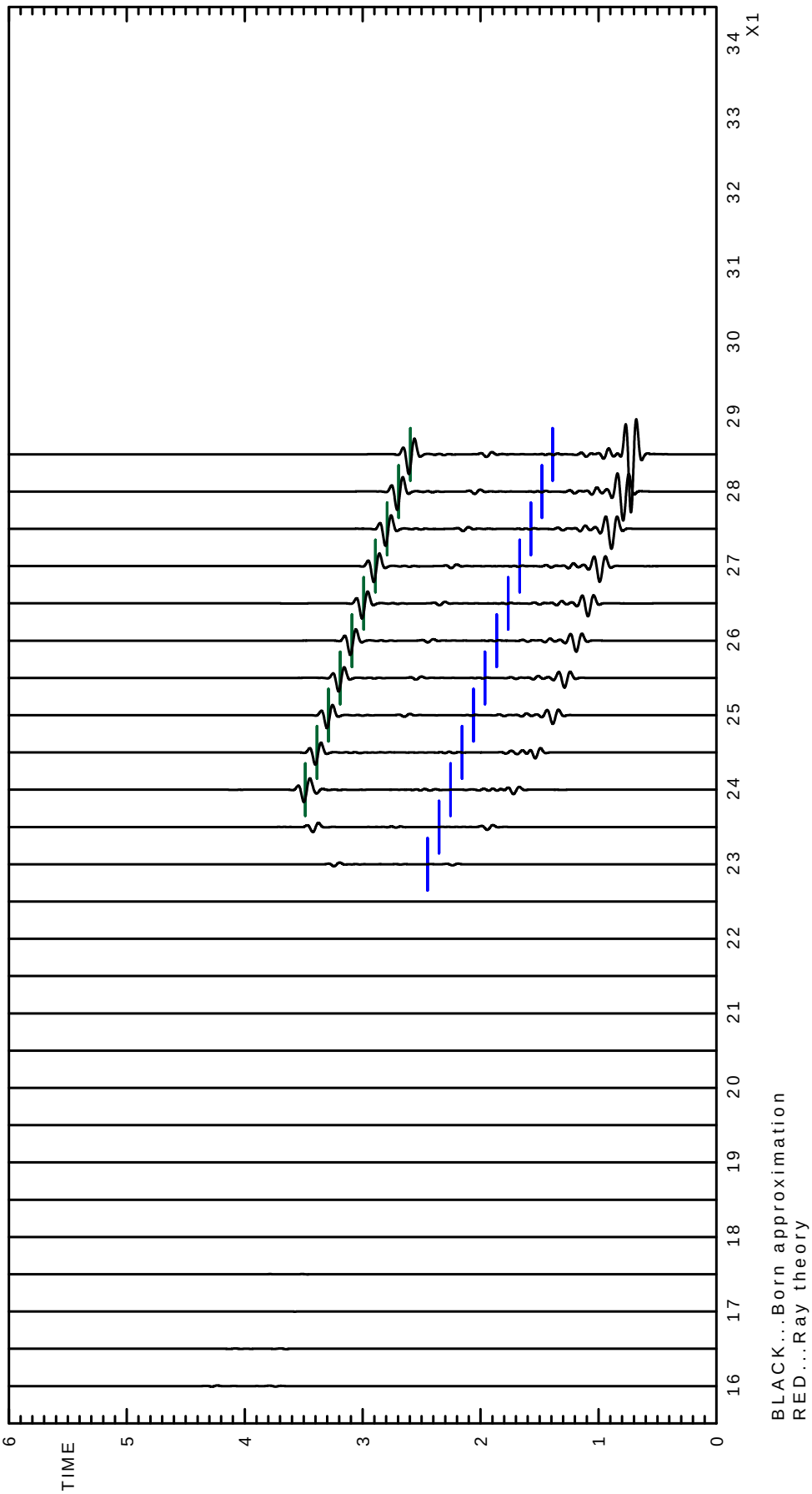

Figure 43: Born and ray-theory seismograms computed in model P1-16-10% scaled by 6×10^5.

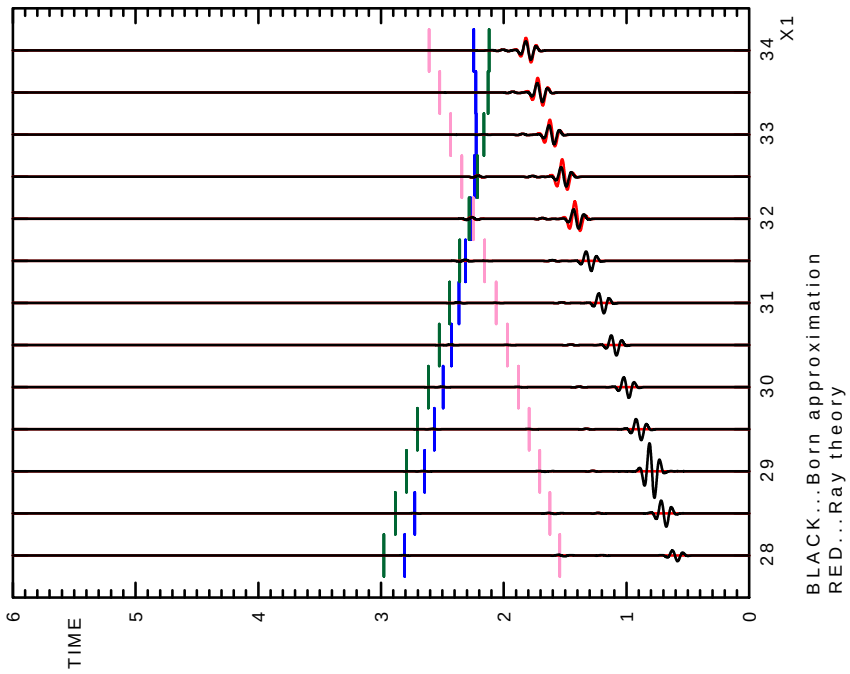

Figure 44: Born and ray-theory seismograms computed in model P1-10-10% scaled by 3×10^3. Only the seismograms for the receivers between $x_1 = 28$ km and $x_1 = 34$ km are depicted.

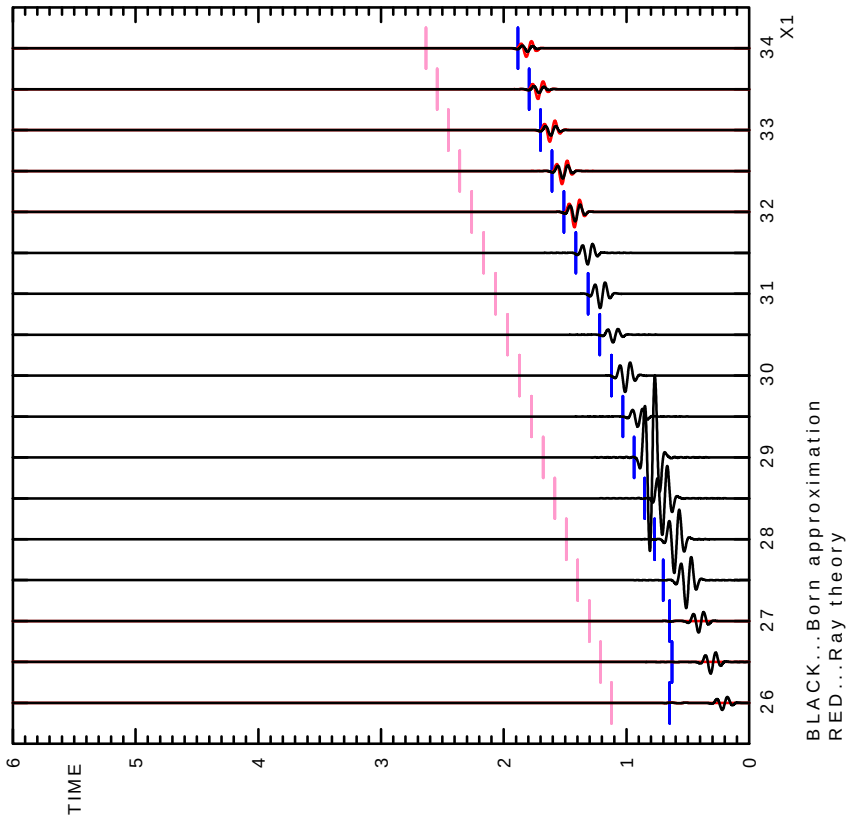

Figure 45: Born and ray-theory seismograms computed in model P1-12-10% scaled by 10^3. Only the seismograms for the receivers between $x_1 = 26$ km and $x_1 = 34$ km are depicted.

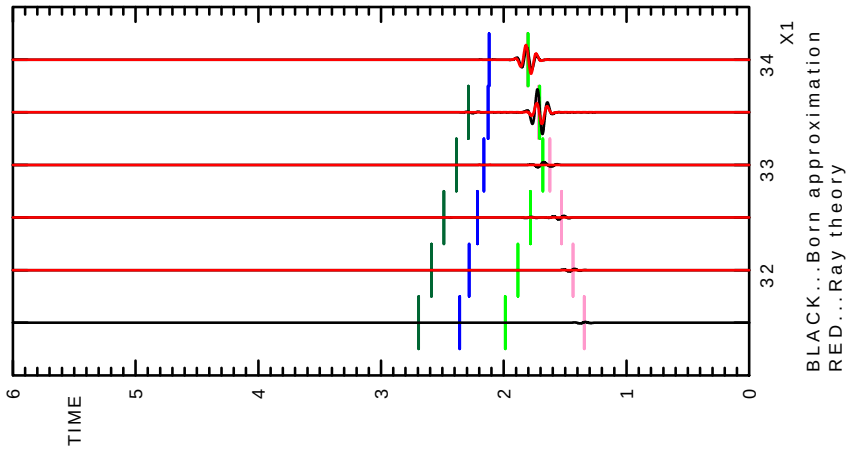

Figure 46: Born and ray-theory seismograms computed in model P1-15-10% scaled by 10^3. Only the seismograms for the receivers between $x_1 = 31.5$ km and $x_1 = 34$ km are depicted.

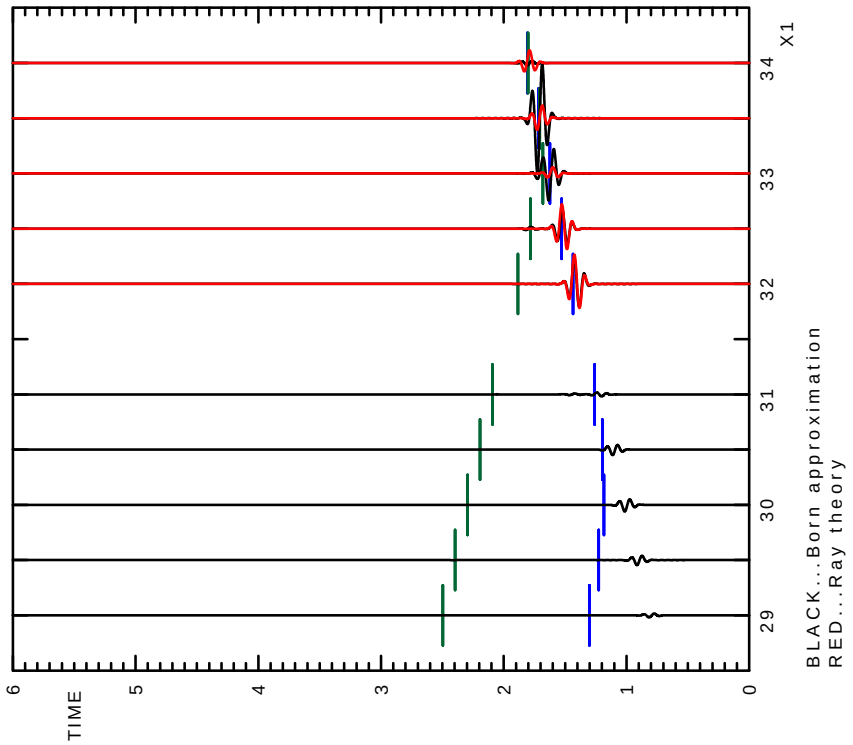

Figure 47: Born and ray-theory seismograms computed in model P1-16-10% scaled by 10^3. Only the seismograms for the receivers between $x_1 = 29$ km and $x_1 = 34$ km are depicted.

Appendix A

Software used in the numerical computations

The computations were performed using the SW3D consortium programs. The documentation is available on consortium web page `http://sw3d.cz/`. Namely, we speak about these programs:

- Package FORMS: *grdcal.for*, *grdps.for*, *pictures.for*, *ss.for*, *sp.for* and alternatively *grdnorm.for* apart from newly programmed auxiliary program *average.for*.
- Package MODEL: *grid.for*, *modchk.for*.
- Package CRT *crt.for*, *crtray.for*, *crtpts.for mtt.for*, *green.for*, *greenss.for*.

Apart from the already existing SW3D programs, we used several programs, which we have newly coded. These programs are, as well as the SW3D programs, coded in FORTRAN 77. The description of the parameters governing each program's performance is present at the begining of the code. A short presentation of the coded programs follows.

grdborn.for

The coding of program *grdborn.for*, which computes the Born approximation, was one of the aims of this master thesis. The theory is presented in the first chapter and the first paper. The numerical implementation is described in Appendix B.

pprf.for

This program is designed to **P**ost **P**rocess files in the **RF** output format, see

`http://sw3d.cz/software/sw3dcd15/forms/ss.for#RF`

The program can be used e.g. if someone wants to subtract two seismograms or add two or more seismograms. The seismograms are, in the SW3D programs, stored in the GSE data exchange format, see

`http://sw3d.cz/software/sw3dcd15/forms/gse.for#data`

The GSE format is a bit complicated, so it was easier to code a program which works with the RF format files, from which the seismograms are computed using program *ss.for*.

The program reads the input files containing the seismograms and coefficients. The output is a file containing the seismogram created as a linear combination of the seismograms with the given coefficients.

The program checks the input data. The error is generated if the hypocentre, the lowest frequency, frequency step, number of frequencies or coordinates of each receiver are not the same in the given files. The warning is generated, if there are different receiver names in the given files. The warning is also generated if there are different header sections in the given files. The header section from the first file is used.

average.for

The program averages quantities stored in the input VEL file. The type of averaging is given by parameter ITYPE. Available is the geometric or harmonic mean. The input are numbers N_1, N_2, N_3, L_1, L_2, L_3. The program reads $N_1N_2N_3L_1L_2L_3$ values from the data file VEL. The first to $L_1L_2L_3$th value, $(L_1L_2L_3+1)$th to $2L_1L_2L_3$th value and so on are averaged. The averaged data are stored in the VEL file. They rewrite the old data.

The program can be used in computing the Born approximation using the grid containing $N_1 \times N_2 \times N_3$ grid points. The elastic parameters can be discretized in the same grid, or they can be discretized in the finer grid with $N_1L_1 \times N_2L_2 \times N_3L_3$ gridpoints and then averaged using this program. The parameters L_1, L_2, L_3 have the meaning of the refinements of each gridpoint of the original grid in the directions of the x_1, x_2, x_3 coordinate axes respectively.

grdmak.for

A frequent computation of the parameters of the grid arisen during computations, especially in Model 3 in the first paper. In the SW3D programs, these parameters are usually the coordinates O_1, O_2, O_3 of the origin of the grid, the grid intervals D_1, D_2, D_3 and the numbers N_1, N_2, N_3 of gridpoints along the x_1, x_2, x_3 coordinate axes. Nevertheless, we usually know the domain to be covered with the grid and the needed grid interval.

Moreover some grids contain so many gridpoints that we have to split them up into more subgrids, compute the Born approximation using these subgrids and add the results using program *pprf.for*, which is correct thanks to the linearity of the Born approximation.

Program *grdmak.for* solves these two problems. The program firstly computes the parameters of the subgrids which have no more than NPTSMX gridpoints from the known domain specification and grid spacings. Secondly, the program reproduce the given history file and subsequently writes the parameters of each single subgrid into the copies. This information is written after the line which contains the same string as the one specified by parameter EXPR.

ttdif.for

The program computes the travel times of the diffracted waves. The input file PTS is supposed to be generated by program *crtpts.for* using the option KALL=-2. We use program *ttdif.for* in computing the travel times of the diffracted waves in the fourth paper. We perform the ray tracing using the edge of the block as the source. Then we run program *ttdif.for*. The program searches for the receiver name identical with the name of the real source, which is specified by input parameter SRCNAM. The error is generated, if there is no such receiver. Otherwise, this travel time is added to all travel times from the input file PTS. The resulting travel times are stored in the output file TTDIF together with the name of the receiver and real source. The output file is in the FTT format, see

`http://sw3d.cz/software/sw3dcd15/forms/formsdat.htm#FTT`

posbig.for

The program reads the input files FNAME and NUM. These files are supposed to be generated by program *mtt.for*. File FNAME is supposed to contain the amplitudes, file NUM is supposed to contain the number of arrivals at each gridpoint. Program *posbig.for* searches file FNAME and if there is a number

bigger than the value of input parameter BIG, the coordinates of that grid point are written into the output file FOUT. The coordinates are computed using the input grid dimensions. The output file has the PTS format, see

`http://sw3d.cz/software/sw3dcd15/forms/formsdat.htm#PTS`

Appendix B

Program grdborn.for

B.1 Numerical implementation of the governing formulas

Program *grdborn.for* is designed to compute the first-order Born approximation in the isotropic medium using the high frequency approximation of the derivatives at certain specified receivers.

We start with formula (7) from the first paper. We evaluate the integral numerically because all quantities (perturbations of the elastic parameters, amplitudes of the Green functions and so on) are known in one particular grid (the grid is the same for each quantity) containing N_1, N_2, N_3 gridpoints with D_1, D_2, D_3 grid intervals along x_1, x_2, x_3 coordinate axes respectively. We replace the integration by summation[1].

Furthermore, we have to realize that, due to caustics, there could be more arrivals to each particular gridpoint. On the other hand, it can also happen that no arrival is present. This fact holds for the incident wavefield and the Green function as well, but the number of arrivals at one particular gridpoint could be different. The reason is that despite the fact that both the wavefield and the Green function incident in the chosen grid, the wavefield emanates from the point source but the Green function emanates from the receiver. Let us denote the number of arrivals of the incident wavefield and the Green function at I-th gridpoint by $N_{wf}(I)$ and $N_{gr}(I)$ respectively.

[1]The Born integral is indefinite, therefore use of e.g. the trapezoidal rule or Simpson's rule is not desirable.

Altogether formula (7) from the first paper has the form

$$\Delta u_i(\mathbf{x},\omega) = \omega^2 D_{123} \sum_{I=1}^{N_{123}} \sum_{o=1}^{N_{wf}(I)} \sum_{q=1}^{N_{gr}(I)} \Big\{ \exp\left[i\omega\left(\tau^{(I,o)} + T^{(I,q)}\right)\right] \Big[\Delta\rho^{(I)} A_{ji}^{(I,q)} a_j^{(I,o)} + \Delta\lambda^{(I)} A_{ji}^{(I,q)} P_j^{(I,q)} a_k^{(I,o)} p_k^{(I,o)} + \Delta\mu^{(I)} A_{mi}^{(I,q)} P_j^{(I,q)} \left(a_m^{(I,o)} p_j^{(I,o)} + a_j^{(I,o)} p_m^{(I,o)} \right) \Big] \Big\}, \quad \text{(B.1)}$$

where index I stands for I-th gridpoint, index o stands for the o-th arrival at the I-th gridpoint of the incident wavefield and index q stands for the q-th arrival at the I-th gridpoint of the Green function, $N_{123} = N_1 N_2 N_3$ and $D_{123} = D_1 D_2 D_3$.

From the numerical point of view, it is useful to remark that the integrand of (B.1) is composed of the following parts:

3 vectors

$$A_{ji}^{(I,q)} a_j^{(I,o)}, \qquad A_{ji}^{(I,q)} P_j^{(I,q)}, \qquad A_{ji}^{(I,q)} p_j^{(I,o)}, \quad \text{(B.2)}$$

3 dot products

$$a_k^{(I,o)} p_k^{(I,o)}, \qquad a_k^{(I,o)} P_k^{(I,q)}, \qquad P_k^{(I,q)} p_k^{(I,o)}, \quad \text{(B.3)}$$

the phase term

$$\exp\left[i\omega\left(\tau^{(I,o)} + T^{(I,q)}\right)\right] \quad \text{(B.4)}$$

and the term

$$\omega^2 D_{123}. \quad \text{(B.5)}$$

From the physical point of view, formula (B.1) is composed of the 3 terms. They correspond to the perturbations of density ρ and Lamé's elastic moduli λ and μ. Each of these 3 terms is composed of some combinations of the above mentioned vectors and dot products. The combinations are written in Table (B.1).

Formula (B.1) is evaluated for n_f frequencies in program *grdborn.for*. The lowest frequency is f_{min} the frequency step is f_{step}. Terms (B.2), (B.3) are frequency independent. The computation of (B.5) is straightforward. Computation of (B.4) for frequency $f = f_{min} + n f_{step}$ can be done straightforward too, but it

Vector/dot product	Term number
$A_{ji}^{(I,q)} a_j^{(I,o)}$	1,3
$A_{ji}^{(I,q)} P_j^{(I,q)}$	2
$A_{ji}^{(I,q)} p_j^{(I,o)}$	3
$a_k^{(I,o)} p_k^{(I,o)}$	2
$a_k^{(I,o)} P_k^{(I,q)}$	3
$P_k^{(I,q)} p_k^{(I,o)}$	3

Table B.1: Combinations of vectors and dot products in each term of the Born approximation

is more efficient to rewrite it in the following way:

$$\begin{aligned}
&\exp\left[i\omega\left(\tau^{(I,o)}+T^{(I,q)}\right)\right] = \exp\left[i2\pi(f_{min}+nf_{step})\left(\tau^{(I,o)}+T^{(I,q)}\right)\right] = \\
&= \exp\left[i2\pi f_{min}\left(\tau^{(I,o)}+T^{(I,q)}\right)\right]\exp\left[i2\pi n f_{step}\left(\tau^{(I,o)}+T^{(I,q)}\right)\right] = \\
&= \exp\left[i2\pi f_{min}\left(\tau^{(I,o)}+T^{(I,q)}\right)\right]\left(\exp\left[i2\pi f_{step}\left(\tau^{(I,o)}+T^{(I,q)}\right)\right]\right)^n
\end{aligned} \tag{B.6}$$

As we can see, it is sufficient to compute $\exp\left[i2\pi f_{min}\left(\tau^{(I,o)}+T^{(I,q)}\right)\right]$ for frequency $f = f_{min}$ and then multiply it by $\exp\left[i2\pi f_{step}\left(\tau^{(I,o)}+T^{(I,q)}\right)\right]$ for each following frequency. The advantage is that the computation of the exponential is reduced to one complex multiplication, i.e. 4 multiplications and 2 adds.

If the source and receiver are situated in a symmetry plane of a 2D model (identical with the plane x_1-x_3), we can compute the Born approximation numerically in a 2D slice according to formula (45) in the first paper:

$$\begin{aligned}
\Delta u_i(\mathbf{x},\omega) = \omega^{\frac{3}{2}} D_{13}\pi^{\frac{1}{2}}(1+i)\sum_{I=1}^{N_{13}}\sum_{o=1}^{N_{wf}(I)}\sum_{q=1}^{N_{gr}(I)}\Bigg\{&\exp\left[i\omega\left(\tau^{(I,o)}+T^{(I,q)}\right)\right] \\
&\Big[\Delta\rho^{(I)} A_{ji}^{(I,q)} a_j^{(I,o)} + \Delta\lambda^{(I)} A_{ji}^{(I,q)} P_j^{(I,q)} a_k^{(I,o)} p_k^{(I,o)} \\
&+ \Delta\mu^{(I)} A_{mi}^{(I,q)} P_j^{(I,q)}\left(a_m^{(I,o)} p_j^{(I,o)} + a_j^{(I,o)} p_m^{(I,o)}\right)\Big] \\
&\frac{1}{\sqrt{\tau_{,22}^{(I,o)} + T_{,22}^{(I,q)}}}\Bigg\},
\end{aligned} \tag{B.7}$$

where $N_{13} = N_1 N_3$.

The spurious wavegroups can arise due to the finite size of the grid. We met this situation in the first paper. We suggested to apply the cosine window at the grid boundaries. The formula (B.1) is modified:

$$\Delta u_i(\mathbf{x},\omega,0) = \omega^2 D_{123} \sum_{I=1}^{N_{123}} w_1(I)w_2(I)w_3(I)w_4(I)w_5(I)w_6(I) \sum_{o=1}^{N_{wf}(I)} \sum_{q=1}^{N_{gr}(I)} \Big\{ \dots \Big\},$$

where $w_1(I), \dots, w_6(I)$ are the values of the cosine windows applied at grid boundaries $1, \dots, 6$ (see Table 2 in the first paper) at the particular grid point. Similarly with formula (B.7).

B.2 Skim through program, comments and discussion

First of all, the data directly specified in the history file are read. The very first are read the specifications of the input grid because we can calculate N_{123} and check the size of computing array RAM for storing $N_{wf}(I)$, $\Delta\rho$, $\Delta(\rho v_p^2)$, $\Delta(\rho v_s^2)$.

Then the data stored in some particular files are read. At first, the data specifying the material perturbations and the incident wavefield are read. The order is following: $N_{wf}(I)$, material perturbations, $\tau^{(I,o)}$, $p_i^{(I,o)}$, $\tau_{,22}^{(I,o)}$ (in 2D model), $Re\left(a_i^{(I,o)}\right)$, $Im\left(a_i^{(I,o)}\right)$. $N_{wf}(I)$ are read preferentially, because then we know the total number of arrivals and we can check our size of array RAM for storing the other quantities. You may wonder why the perturbations $\Delta(\rho v_p^2)$, $\Delta(\rho v_s^2)$ are read instead of perturbations $\Delta\lambda$, $\Delta\mu$. In our opinion, it is more common to specify the isotropic medium by the density and the P-wave, S-wave velocities. It stands

$$\rho v_p^2 = \lambda + 2\mu, \qquad \rho v_s^2 = \mu, \tag{B.8}$$

therefore, both attitudes are equivalent.

The data specifying the Green functions are read at last. Program *grdborn.for* is designed to compute the Born approximation for one source but possibly more receivers, i.e. the incident wavefield is the same for different receivers but not the Green functions.

As far as the computational structure goes, the outermost loop is over receivers. Following (B.1) or (B.7), the next loop is over gridpoints. Further, there should be one loop over the arrivals of the Green functions and one loop over the arrivals of the incident wavefield. It is better to choose the loop over the arrivals

of the Green functions as the outer loop because the program copies the values from array RAM into the auxiliary variables with the suitable names and the Green functions are specified by more parameters. The innermost loop is over frequencies. We use (B.6).

Terms (B.2), (B.3) which compose the 3 terms in (B.1) as described in Table B.1 are computed only if the appropriate perturbations are present. If any of parameters RHOPER, VPPER or VSPER is blank on input, it is supposed that this particular perturbation is zero in the whole model. It can also happen that there are material perturbations in the model, but at some gridpoint they are equal to zero. Both possibilities are tested. The only problem is that due to (B.8), $\Delta(\rho v_p^2)$ can be zero in the whole model, which implies $\Delta\lambda = -2\Delta\mu$ in the whole model. That does not mean $\Delta\lambda$ is zero in the whole model.

Appendix C

Sample computations

Generally speaking, any computation consists of the used programs, input data files and history files. The used programs are the topic of Appendix A. Term data file is clear. The data files which are output of some program are named *.out, the data files which are prepared by user are named *.dat.

Internet page `http://www.sw3d.cz/software/sw3dcd15/forms/sep.htm` describes the history files in details. The main points are: The history files are designed to contain both the data and the information how to execute the programs. The history files may be executed by Perl script *go.pl*. The following items are recognized in the history files:

- # Comments: Everything from a # (hash mark) to the end of line is assumed to be a comment and is ignored.
- =Data: Each = (equal sign) immediately preceded by a string is interpreted as the PARAMETER=VALUE couple specifying the value of the parameter named PARAMETER. For example, N1=27 means that the value of the parameter named N1 is 27.
- :Programs: Each : (colon) immediately preceded by a string is interpreted as the instruction to execute a program.

C.1 Introduction and description of the structure of the first sample computation

We present the computation of the 3D seismograms using the 2D ray-based Born approximation in heterogenous model P1-8-10%. The background model is

heterogenous smooth model P1 without interfaces. The reference seismogram is computed using the ray theory. The observed differences between the Born and ray-theory seismogram are caused by the diffracted waves. Their travel times are marked by the green abscissas. The computation consists of the following 7 history files:

1. History file *p1-main.h* is the leading history file. It runs history files *p1-grid.h*, *p1-mtt.h*, *p1-iwf.h*, *p1-born.h*, *p1-ss2.h* and *p1-ss.h*.
2. History file *p1-grid.h* computes the perturbations of the elastic parameters between the perturbed and background medium. The history file also generates several pictures.
3. History file *p1-mtt.h* computes the Green functions from the source and from the receiver, slowness vectors, travel times and other quantities at the gridpoints.
4. History file *p1-iwf.h* computes the incident wavefield necessary for the Born approximation using the representation theorem.
5. History file *p1-born.h* computes the 2D Born approximation. The output file is in the RF format.
6. History file *p1-ss2.h* generates the ray-theory seismogram.
7. History file *p1-ss.h* generates the Born seismogram from the RF format file computed by history file *p1-born.h* and visualize it together with the ray-theory seismogram computed by history file *p1-ss2.h*.

C.2 Detailed analysis of the first sample computation

There are comments of the parameters and the program itself at the beginning of each program's code. We used some of these sentences in the following text.

p1-mod1c.dat

In this file, there are defined model boundaries, surfaces, simple blocks, complex blocks and the distribution of the elastic parameters in the perturbed model. The original 16 simple blocks from model P1I are united into one complex block except simple block 8. This simple block is also the second complex block.

p1-mod2.dat

The file containing the definition of the background model. One simple block, one complex block. Smooth distribution of the elastic parameters.

History file *p1-grid.h*

Perturbations $\Delta(\rho v_p^2)$, $\Delta(\rho v_s^2)$, $\Delta\rho$ could be input by manually created files in some simplified cases, e.g. Model 1 in the first paper. This is not possible in a heterogenous model with curved interfaces. The P-wave velocity, S-wave velocity and density are gridded in the perturbed and background model using program *grid.for*. Parameter MPAR specifies the quantity to be discretized. The output files are input for program *grdcal.for* to compute the perturbations using script *pert2.cal*. The resulting output files containing perturbations $\Delta(\rho v_p^2)$, $\Delta(\rho v_s^2)$, $\Delta\rho$ are named *p1-vpper.out*, *p1-vsper.out* and *p1-rhper.out* respectively.

The computational grid covers just block 8. The P-wave velocity perturbation, indices of the blocks and P-wave velocity in the background model should be visualized in the whole model. Thus, it is necessary to redefine the grid dimensions and discretize the P-wave velocity and indices of the blocks in this grid. Note that in the "computational part" of this history file, the parameter ICB which defines the output file with indices of the blocks is not specified. The plotting is in all 3 cases performed by program *grdps.for*. The input and output files are specified by parameters GRD and PS respectively. Different are the settings of parameters VREF, CREF, VCIRC, VMIN, VMAX, R, G, B. Let us explain how it works when plotting indices of the blocks. Value VREF corresponds to colour CREF and VCIRC is the extent of values corresponding to the whole colour circle RGB. Values less than or equal to VMIN or greater than or equal to VMAX are drawn in colour specified by R, G, B. VREF=2 and CREF corresponds to blue colour. This ensures to plot block 8, specified as the second complex block in *p1-mod1c.dat*, in blue colour. All other complex blocks are drawn in default colour specified by R, G, B due to VMIN=1.9, VMAX=2.1. There are two complex blocks in this model. The first complex block, which unites all simple blocks except the 8-th simple (and also complex) block, is drawn in default yellow colour.

p1-rec.dat

The data file containing the name and coordinates of the receiver.

p1-src.dat

The data file containing the name and coordinates of the source.

p1-pts.dat

The data file containing the names and coordinates of various points. It contains the name and coordinates of the source and receiver in this computation.

History file *p1-mtt.h*

The file performs controlled initial-value ray tracing and interpolation inside ray tubes. The travel times, amplitudes and other quantities of the Green functions from the receiver and from the source are computed at the gridpoints.

The history file computes the Green functions from the receiver first. Then it plots several pictures with the rays. The same process is repeated for the Green functions from the source.

The model is specified by the MODEL file. File *p1-mod2.dat* specifies the background model, file *p1-mod1c.dat* specifies the perturbed model.

The SRC file specifies the position of the seismic source for the ray tracing. The SRC file contains the position of the receiver when computing the Green functions from the receiver. The SRC file contains position of the real source when computing the Green functions from the source.

WRIT='writall.dat' is a setting suitable for the controlled initial-value ray tracing. All rays are stored.

The code, i.e. the specification of the types of waves we are interested in, is specified by parameter CODE. We use direct P waves, CODE=*p1-codep.dat*, because the Born approximation is computed in the background model without interfaces. The reflection-transmission code was chosen, because it is simple but sufficient.

Parameters DCRT and RPAR specify the files that control the complete ray tracing, and the take-off parameters of the desired rays. The files have different names in shooting the rays from the position of the receiver and source. This is left for the future extension. The both files have the same content in this computation.

Azimuthal equidistant projection of a unit sphere is used to parametrize rays (INIPAR=3). This option, if compared with geographic-like spherical coordinates, has the advantage of only one singularity in the upward direction (Sphe-

rical coordinates have 2 singularities, in both downward and upward directions). The source is at the surface, therefore these coordinates are useful.

The computational grid and the grid for plotting are, of course, the same as in history file *p1-grid.h*.

The ray tracing is performed by program *crt.for*. The output data are post processed by program *mtt.for* which interpolates travel times, amplitudes and other quantities with respect to the gridpoints.

Program *crtray.for* is used to convert the unformatted output of program *crt.for* into formatted file *p1-r01.tmp* with rays. The file is suitable for plotting. File *r01.out* with the quantities at the initial points of rays and file *r01i.out* with the quantities stored along rays are used. We wish to plot all rays not just two point rays, therefore KALL=1.

The rays together with the boundaries of the model and the positions of the receivers are plotted by program *pictures.for*. The information for plotting is read from file *picdat.tmp* specified by parameter PICDAT. File *picdat.tmp* controls the type and size of markers, the names of files with lines and points to be plotted and so on. The output file specified by parameter PICTURE is called *p1-ray.ps*.

Perl script *copy.pl* is used to copy file *p1-vep.ps* into new file *p1-v-g.ps* and to copy file *p1-icb.ps* into new file *p1-cov-g.ps*. The rays are appended to these newly created files using Perl script *append.pl*.

Plotting the number of arrivals is similar to the plots in history file *p1-grid.h*.

p1-crt-g.dat

The DCRT and RPAR data are merged in this data file.

DCRT

Parameters KSTORE, NEXPS, NHLF and MODCRT are left to their default values: No amplitude conversion coefficients, the travel time as an independent variable, the maximum of 5 allowed bisections of the initial increment of the independent variable during the numerical integration.

Parameter STORE controls the step of the independent variable for storing the computed quantities along a ray. In fact it sets the size of a ray cell used for the interpolation in program *mtt.for*. STORE=0.02 seems to be the appropriate value. The Born seismogram would be inaccurate if we use insufficiently small ray cells.

The initial increment of the independent variable for the numerical integration is set to STEP=0.02.

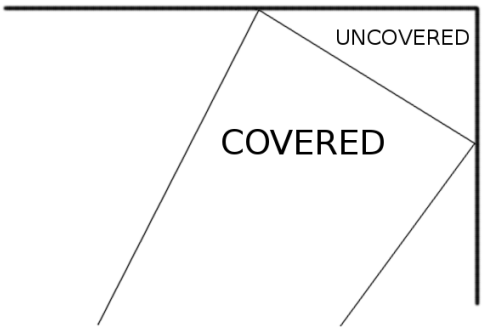

Figure C.1: Problems with uncovered corners when using PRMO(3)=1

The computational volume is the whole volume. This setting is not ideal. We use PRMO(3)=1. The thin spaces uncovered by ray tubes are limited, because the boundaries of the computational volume do not influence ray histories. This option is suitable for the controlled initial-value ray tracing, however, problems occur in the corners of the computational volume. Two rays that are incident at the different boundaries of the computational volume have the same histories, which causes the uncovered corners of the computational volume, see Fig. C.1. The solution is to define the computational volume larger than the model volume. Thus, it is useful to define the elastic parameters also in the neighbourhood of the model boundaries. We do not want to change model p1-8-10%, but we used this idea in the first sample computation.

RPAR

The reference surface, specified by parameter ISRFR, is the upper model boundary.

The first coordinate is the same as the horizontal coordinate, therefore, ISRFX1=1.

We perform one parametric ray tracing and thus ISRFX2=0.

XERR is not used in the controlled initial-value ray tracing. AERR is the accuracy of the determination of the boundary rays between the different ray histories.

The ray parameters domain is, in the case of one parametric ray tracing, degenerated from a rectangle to a line. We shoot rays in the angular interval $\langle -1.4, 1.4 \rangle$ radians and we use 91 basic rays, to sufficiently cover the whole block 8.

p1-bnd.dat

The file defining the lines that form the bounding box of the model.

History file *p1-iwf.h*

The history file computes the amplitudes of the incident wavefield using the amplitudes and slowness vectors of the Green functions according to

$$u_m(\mathbf{x}', \omega) \approx G_{mi}(\mathbf{x}', \mathbf{x}_0, \omega) M_{ij}\, s_M(\omega)\, p_j(\mathbf{x}_0), \tag{C.1}$$

where $s_M(\omega)$ is the frequency–domain source–time functions and M_{ij} is the moment tensor. The formula is derived using the representation theorem with applied high frequency approximation. It is valid for a points source at point $\mathbf{x}_0$ (Klimeš, 2009).

The amplitudes of the incident wavefield is computed by program *grdcal.for* using script *iwf.cal*. The moment tensor is prescribed directly in the history file. It has the form of the explosive source (when dealing with P waves).

Program *grdcal.for* was available in version 6.40 when this history file was created. There is a limitation to this version. It can work with only 9 files at a time. Unfortunately, we need 18 files containing real and imaginary parts of the amplitudes of the Green function from the source to the gridpoints and 3 files containing slowness vectors at the source point. One more file for output is necessary. A total of 22 files, which is too many. If we computed each component separately, we would still need 10 files (6 files with amplitudes, 3 files with slowness vectors plus 1 output file). Hence, it is necessary to compute even real and imaginary parts separately. In this case 7 files are needed in each of the 6 runs. The disadvantage of this approach is that the slowness vectors have to be loaded repeatedly which slows down the computation.

The appropriate quantities used in the runs are specified in Table C.1.

Remark that the vector opposite to the slowness vector in the source instead of the slowness vector itself is loaded. The minus sign has to be present in the script *iwf.cal* then. Unfortunately, program *mtt.for* does not allow to discretize directly the slowness vector in the source.

History file *p1-born.h*

The file runs program *grdborn.for* which computes the Born approximation.

The Born approximation is gradually computed for the receivers specified in file BORN. Data file BORN contains the names of the files, which contain

Parameter name	6 runs, file specified by parameter contains					
GRD1	$-p_1$	$-p_1$	$-p_1$	$-p_1$	$-p_1$	$-p_1$
GRD2	$-p_2$	$-p_2$	$-p_2$	$-p_2$	$-p_2$	$-p_2$
GRD3	$-p_3$	$-p_3$	$-p_3$	$-p_3$	$-p_3$	$-p_3$
GRD4	$\mathrm{Re}(A_{11})$	$\mathrm{Re}(A_{21})$	$\mathrm{Re}(A_{31})$	$\mathrm{Im}(A_{11})$	$\mathrm{Im}(A_{21})$	$\mathrm{Im}(A_{31})$
GRD5	$\mathrm{Re}(A_{12})$	$\mathrm{Re}(A_{22})$	$\mathrm{Re}(A_{32})$	$\mathrm{Im}(A_{12})$	$\mathrm{Im}(A_{22})$	$\mathrm{Im}(A_{32})$
GRD6	$\mathrm{Re}(A_{13})$	$\mathrm{Re}(A_{23})$	$\mathrm{Re}(A_{33})$	$\mathrm{Im}(A_{13})$	$\mathrm{Im}(A_{23})$	$\mathrm{Im}(A_{33})$
GRD7	$\mathrm{Re}(u_1)$	$\mathrm{Re}(u_2)$	$\mathrm{Re}(u_3)$	$\mathrm{Im}(u_1)$	$\mathrm{Im}(u_2)$	$\mathrm{Im}(u_3)$

Table C.1: Quantities specified by parameters GRD1-GRD7 in each of 6 runs of program *grdcal.for* launched by history file *p1-iwf.h*. p_i are the components of the slowness vector in the source, A_{ij} are the amplitudes of the Green function and u_i are the components of the incident wave field. Indices $i, j \in \{1, 2, 3\}$

the parameters of the Green functions belonging to the particular receiver. The receiver is specified in data file BORN by its name. The receiver coordinates can be found in datafile REC.

There is one receiver in this computation, therefore the index of the line corresponding to the first receiver is IREC=1 and the number of the receivers is NREC=1. So, parameters IREC and NREC are left to their defaults.

Parameters FMIN, FLOW, FHIGH and FMAX common with program *ss.for* are only used to determine the frequencies for which the Born approximation is computed. In fact, only parameters FMIN and FMAX are used.

Program *grdborn.for* allows the cosine smoothing applied to the grid boundaries. There is no cosine smoothing in this computation. Parameters CSWIN, CSWIN1,CSWIN2, CSWIN3, CSWIN4, CSWIN5 and CSWIN6 are left to their default values.

Files SRC and REC are not necessary for the computation of the Born approximation. They are used in generating the output file in the RF format. The coordinates of the source and the name and coordinates of the receiver are written.

The history file works with the data files generated by the previously described history files. The data files are summarized in Table C.2

Output is a frequency-domain response function in the RF format, which is input for program *ss.for* in history file *p1-ss.h*.

Quantity	Input	Program	Parameter name in the program
$\Delta(\rho v_p^2)$	VPPER	*grid.for + grdcal.for*	VEL, MPAR=1 (grid.for)
$\Delta(\rho v_s^2)$	VSPER	*grid.for + grdcal.for*	VEL, MPAR=2 (grid.for)
$\Delta\rho$	RHOPER	*grid.for + grdcal.for*	VEL, MPAR=3 (grid.for)
$N_{wf}(I)$	NUM	*mtt.for*	NUM
$\tau^{(I,o)}$	MTT	*mtt.for*	MTT
$p_i^{(I,o)}$	MPi	*mtt.for*	MPi
$\tau_{,22}^{(I,o)}$	MTTXX	*mtt.for*	MTT22
$Re\left(a_i^{(I,o)}\right)$	AURi	*mtt.for + grdcal.for*	AMPRij (*mtt.for*)
$Im\left(a_i^{(I,o)}\right)$	AUIi	*mtt.for + grdcal.for*	AMPIij (*mtt.for*)
$N_{gr}(I)$	BORN	*mtt.for*	NUM
$T^{(I,q)}$	BORN	*mtt.for*	MTT
$P_i^{(I,q)}$	BORN	*mtt.for*	MPi
$T_{,22}^{(I,q)}$	BORN	*mtt.for*	MTT22
$Re\left(A_{ij}^{(I,q)}\right)$	BORN	*mtt.for*	AMPRij
$Im\left(A_{ij}^{(I,q)}\right)$	BORN	*mtt.for*	AMPIij

Table C.2: Input data files for history file *p1-born.h*. The notation used in appendix B and the first paper is used. Indices $i, j \in \{1, 2, 3\}$, I ranges the number of gridpoints, o,q range the number of arrivals of the Green functions from the source and from the receiver at each gridpoint respectively.

History file p1-ss2.h

The history file firstly runs program *crt.for*, which performs two-point ray tracing, i.e. the rays from the source to the receiver are traced. The setting of parameters for program *crt.for* is similar as in history file *p1-mtt.h*, where we performed controlled initial-value ray tracing, but there are some important differences.

The DCRT file *p1i-crt.dat* defers from *p1-crt-g.dat* (or *p1-crt-u.dat*) by the definition of one storing surface. The upper model boundary, where the receiver is placed, is the storing surface.

The CODE file *p1i-cod.dat* specifies the once reflected P waves.

The RPAR file *test5-rpa2.dat* is also a bit different. Parameter PRMO(3)=0 not PRMO(3)=1. The rays terminating at different boundaries of the computational volume have different histories. This option is suitable for two-point ray tracing. Parameter IPOINT is not left to its default value 999999, but

IPOINT=1. Otherwise all rays would be unsuccessful. It is also important that IPOINT> 0. The successful ray does not have to satisfy the whole code.

There is WRIT='writ.dat' in this history file apart from WRIT='writall.dat' used in history file *p1-mtt.h*. Not all rays but only two-point rays are stored now.

The rays are plotted similarly as in history file *p1-mtt.for*. The difference is that we plot only two point rays, due to default KALL=0.

Program *crtpts.for* converts the unformatted output of program *crt.for* into a formatted file containing coordinates, travel times, slowness vectors, and amplitudes at the endpoints of two-point rays. The program may be used to determine the indices of the reflected waves.

The ray-theory elastodynamic Green function is computed using program *green.for*. Computing the response function follows, but now it is not performed by *grdborn.for* but by *greenss.for*. The computation of the synthetic seismograms in the GSE data exchange format from the response function is done by *ss.for*.

The source time function is a Gabor signal, filtered by a frequency filter which is nonzero only for frequencies f, FMIN=1 Hz $< f <$ FMAX=20 Hz. There is a cosine tapering for FMIN=1 Hz $< f <$ FLOW=2 Hz and FHIGH=19 Hz $< f <$ FMAX=20 Hz while for FLOW=2 Hz $< f <$ FHIGH=19 Hz the filter is equal to one.

Time step DT has been chosen in order to plot a smoothly looking seismogram. Its choice depends on the length of plotting interval, i.e. on the details we would like to study. We are choosing the time step, the number of time intervals NFFT is set to the value covering the whole desired time interval.

Note that program *greenss.for* reads the complex-valued seismic force or moment from the input file specified by parameter SOURCE. This parameter is left to its default value, SOURCE=*source.dat*. This setting corresponds to the explosive source used in history file *p1-iwf.h*.

Program *sp.for* visualize the seismograms.

Parameters SPTLEN and SPXLEN control the length of the vertical time axis and horizontal axis. Parameters SPTDIV, SPTSUB, SPXDIV, SPXSUB control the number of intervals and subintervals along the vertical and horizontal axes. In the following examples KODESP=0, so that the horizontal axis represents the index of the receiver corresponding to the receiver position in file REC and, due to SPXDIV>0, the horizontal axis is denoted by the names of the receivers. The values SPTDIV and SPTSUB are chosen to divide the whole time interval reasonably. Parameter SPAMP is the amplitude scale for all 3 components. Its value is chosen to cover the whole figure in the horizontal direction with the seismogram.

SP1, SP2 and SP3 set the names of the output files with the first, second and third components of the seismogram.

History file *p1-ss.h*

Two seismograms are drawn into one figure using program *sp.for*. The Born and ray-theory seismograms are specified by parameter SS and SS1 respectively. The Born seismogram is drawn black, due to KOLOR=1, the ray-theory seismogram is drawn red, due to KOLOR1=2. The green lines marking the travel times of the diffractions are read from SPTTC file. This file specifies the names of the FTT files containing the list of travel times to be highlighted. The FTT files are named *p1-edge2.dat*, *p1-edge4.dat*, *p1-edge5.dat*, *p1-edge6.dat* Parameter KOLORTT specifies the colour to plot the travel times and SPHIWI the length of the lines. The other settings are similar as in history file *p1-ss2.h*

Bibliography

[1] AKI, K.– RICHARDS, P. *Quantitative seismology.* 2nd edition. San Francisco: Freeman, 2002. ISBN 0-935702-96-2.

[2] BULANT, P. *Two-point ray tracing in 3-D.* Pure appl. Geophys., 148, 421-447, 1996.

[3] BULANT, P. *Two-point ray-tracing and controlled initial-value ray-tracing in 3-D heterogeneous block structures.* J. seism. Explor., 8, 57-75, 1999.

[4] ČERVENÝ, V. *Seismic rays and ray intensities in inhomogeneous anisotropic media*, Geophys. J. R. astr. Soc., 29, 1-13, 1972.

[5] ČERVENÝ, V. *Seismic ray theory.* Cambridge University Press, 2001. ISBN 0-521-36671-2.

[6] ČERVENÝ, V.– KLIMEŠ L. & PŠENČÍK I. *Seismic ray method: Recent developments.* Advances in Geophysics, 48, 1-126, 2007

[7] EVANS, L. C. *Partial differential equations.* USA: American Mathematical Society, 1998. ISBN 0-8218-0772-2

[8] JEFFREYS, H.– JEFFREYS, B. S. *Methods of mathematical physics.* 3rd edition. Cambridge (GB): Cambridge University Press, 1956. ISBN 0-521-66402-0.

[9] KLIMEŠ, L. *Second–order and higher–order perturbations of travel time in isotropic and anisotropic media.* Stud. geophys. geod., 46, 213-248, 2002

[10] KLIMEŠ, L. *Theoretical foundations of ray methods.* Lecture notes, 2009.

[11] KLIMEŠ, L. *Zero-order ray-theory Green tensor in a heterogeneous anisotropic medium.* Seismic Waves in Complex 3–D Structures, Report 21, 17-26, 2011

[12] MATYSKA, C. *Personal communication*. 2011.

[13] REKTORYS, K. *The method of discretization in time and partial differential equations*. Prague: SNTL, 1982. ISBN 90-277-1342-1